Quasiparticle interference in strongly correlated electronic systems

Philip G. Derry

Department of Chemistry
University of Oxford

A thesis submitted for the degree of
Doctor of Philosophy

Balliol College

April 2017

Acknowledgements

I would like to thank my supervisor David Logan for his assistance, insight and advice over the past four years, and thank him for giving me the freedom and independence to pursue my research. I would also like to thank Andrew Mitchell and Martin Galpin for their extensive guidance and support throughout. Along with other members of the Logan group, past and present, they have been responsible for a great atmosphere of friendship and camaraderie which has proved invaluable over the years. In particular, my thanks go to Adam and Fred for welcoming me to the group – even if it was only so I could fill the kettle – and to Max, for putting up with me in the past few months.

I would like to thank my family and friends for an immense amount of love and encouragement during my time in the department. They have been there throughout the tough times and the good times, and their unconditional support has been vital throughout. Many thanks are due: to my parents Sheena and John, who have been given me everything, and my brother Chris who has been a constant companion, advisor and friend throughout my life, and more recently to Ruth for her sage wisdom and friendship; to my oldest friends, Dom, Seamus and Harry, for sticking with me; and to Emrys, Seb, Rich, Steve and Adam for sharing the journey through Oxford from start to finish.

Most importantly, my eternal thanks and love go to Lottie, for keeping me sane, happy and healthy. Without her support and encouragement, none of this would have been possible.

Abstract

We investigate the manifestation of strong electronic correlations in the quasiparticle interference (QPI), arising from the scattering of conduction electrons from defects and impurities in an otherwise translationally-invariant host. The QPI may be measured experimentally as the Fourier transform of the spatial modulations in the host surface density of states that result, which are mapped using a scanning tunnelling microscope.

We calculate the QPI for a range of physically relevant models, demonstrating the effect of strong local electronic correlations arising in systems of magnetic impurities adsorbed on the surface of non-interacting host systems. In the first instance the effect of these magnetic impurities is modelled via the single Anderson impurity model, treated via numerical renormalization group (NRG) calculations. The scattering of conduction electrons, and hence the QPI, demonstrate an array of characteristic signatures of the many-body state formed by the impurity, for example due to the Kondo effect.The effect of multiple impurities on the QPI is also investigated, with a numerically-exact treatment of the system of two Anderson impurities via state-of-the-art NRG calculations. Inter-impurity interactions are found to result in additional scattering channels and additional features in the QPI.

The QPI is then investigated for the layered transition metal oxide Sr_2RuO_4, for which strong interactions in the host conduction electrons give rise to an unconventional triplet superconducting state at $T_c \sim 1.5$K. The detailed mechanism for this superconductivity is still unknown, but electron-electron or electron-phonon interactions on are believed to play a central role. We simulate the QPI in Sr_2RuO_4, employing an effective parametrized model consisting of three conduction bands derived from the Ru $4d$ t_{2g} orbitals that takes into account spin orbit coupling and the anisotropy of the Ru t_{2g} orbitals. Signatures of such interactions in the normal state are investigated by comparing these model calculations to experimental results. We also calculate the QPI in the superconducting state, and propose how experimental measurements may provide direct evidence of the anisotropy and symmetry of the superconducting gap, and thus offer insight into the pairing mechanism and the superconducting state.

Table of contents

List of figures

List of publications

Some of the material described in Chapters 3, 4 and 5 (respectively) has been published or submitted for publication in the following papers:

P. G. Derry, A. K. Mitchell, and D. E. Logan. "Quasiparticle interference from magnetic impurities". In: *Phys. Rev. B* **92** (2015), p. 035126.

A. K. Mitchell, P. G. Derry, and D. E. Logan. "Multiple magnetic impurities on surfaces: Scattering and quasiparticle interference". In: *Phys. Rev. B* **91** (2015), p. 235127.

Z. Wang et al. "Quasiparticle interference and strong electron-mode coupling in the quasi-one-dimensional bands of Sr_2RuO_4". *Nat. Phys.* (2017). (*Accepted for publication - preprint arXiv:1701.02773*).

Chapter 1

Introduction

Strong correlations between electrons in condensed matter systems give rise to a plethora of interesting phenomena, in which the collective behaviour of electrons does not admit a complete description in terms of simple, single-particle states. As a result, these systems are of fundamental scientific interest, and the theoretical treatment of strong correlations in a variety of forms has been a central challenge for over half a century. Experimental investigations have evolved from the observation and measurement of such effects towards their manipulation and possible exploitation for practical applications; a detailed understanding of the electronic states giving rise to these effects is of great importance in order to harness them effectively.

In the past decade, for example, theoretical study of correlated magnetic systems has informed the development of nanoscale spintronic devices. Similarly, progress in understanding the mechanism of superconductivity in unconventional superconductors, typically driven by electron-electron interactions, helps to direct the search for materials displaying superconductivity at higher temperatures, but also sheds light on the nature and properties of the superconducting state. The development of a theoretical framework for the classification and understanding of the topological nature of electronic states has perhaps had the most profound impact on the study of strongly-correlated condensed matter electronic systems in recent years, with the proposal of topologically non-trivial states arising due to strong correlations as the basis for quantum information processing and computation. Accurate characterization of these states is therefore a key goal of theoretical and experimental investigations in such exotic materials.

In this thesis, we investigate how the effects of strong correlations are manifest in the scattering of electronic states from impurities, in particular considering the resultant effect on the quasiparticle interference (QPI). The QPI depicts the magnitude of this scattering in reciprocal space, as we explain briefly below, before a more

detailed introduction in Chapter 2. The QPI is considered for several systems in which electron-electron interactions affect significantly the physics, and we demonstrate how these interactions impact on the QPI in each case. As a number of different interacting systems are considered, the scope of the material covered in this thesis is quite broad, touching on several different fields within condensed matter theory, and thus several different bodies of literature. We therefore do not undertake a discussion of the background material at the outset, but instead give a more detailed introduction to the important concepts in each chapter. Here we provide an overview of the material covered in the thesis, placed within the context of a more general investigation of the QPI in strongly-correlated electronic systems.

The delocalized states of a translationally-invariant material are scattered by defects that break the translational symmetry; the scattered states thus contain information about both the nature of host material and the nature and distribution of defects or impurities. The interference between these scattered states gives rise to spatial fluctuations in the electronic density of states at the surface of the material, which may be measured experimentally using a scanning tunnelling microscope (STM): the Fourier transform of these spatially-mapped fluctuations yields the QPI. Chapter 2 serves as a detailed introduction to the QPI, presenting a formal derivation in terms of the scattered electronic states of the host material, and comparing this with the experimental protocol, and the commonly-used phenomenological interpretation of the QPI that is pervasive throughout the literature. We demonstrate how the electronic structure of both the host and the impurity (or impurities) enter the QPI. The presence of electron-electron interactions between states of either the host or adsorbed impurities is also considered; the detailed formulation is carried out for a non-interacting host material with a single 2D conduction band in the first instance, but we subsequently address the additional formalism in the case of correlated electronic states of the host material. Moreover, we consider a range of complicating factors that are relevant in the QPI for more realistic materials, including the presence of multiple conduction bands and the effect of coupling between the surface electronic states and those of the bulk for 3D host materials.

Magnetic atoms adsorbed on the surface of a host material provide a simple realization of an interacting system for which the QPI may be calculated, and for which experimental measurements are possible. Such systems are typically well-described by quantum impurity models, which consist of a small subsystem of interacting degrees of freedom coupled to a bath of non-interacting, delocalized electronic states. In Chapter 3 we consider the QPI for magnetic adatom systems, focusing on the case of

a single magnetic impurity adsorbed on a range of representative host lattices. The magnetic adatom is modelled as a single-level Anderson impurity model, for which the electron-electron interaction term is an on-site Hubbard interaction. We demonstrate that the scattering of conduction electrons and modulation of the density of states can be expressed in terms of the impurity electron dynamics, calculated via the numerical renormalization group (NRG) method. These quantities display clearly the effect of many-body correlations (in this case due to the Kondo effect). In order to calculate the spatial modulations of the density of states, the propagation of conduction electrons in the absence of the impurity must also be known. In Appendix A we derive a computationally-efficient method for the calculation of the lattice Green functions in hypercubic tight binding models, which we use in Chapter 3 and throughout the thesis.

Chapter 4 studies the case of multiple magnetic impurities embedded on a metallic host surface, described by multiple Anderson impurities. We begin by considering in detail the two-impurity case, the Anderson Alexander model, as a minimal model displaying inter-impurity interactions. A careful investigation of the Anderson Alexander model is presented, demonstrating the interplay of intra- and inter-impurity correlations, which give rise to a richer range of physics than the simpler single-impurity case. These effects are shown to have a potentially profound impact on the scattering of conduction electrons, and hence the QPI, giving rise to additional non-local scattering channels as well as more complex local impurity electron dynamics – again, calculated using NRG. Exact results for the AAM allow us to establish an effective range of inter-impurity interactions in real space, beyond which impurities become essentially independent. Using this information we establish a controlled "independent cluster approximation" for the QPI in the experimentally-relevant many-impurity case, comparing with a simpler independent impurity approximation, valid only in the dilute limit.

Having focused on the QPI in systems of interacting impurities embedded in hosts with non-interacting conduction electron bands in Chapters 3 and 4, we turn our attention in Chapter 5 to a material for which strong electronic correlations are of fundamental importance in the electronic structure. In this chapter we study the QPI for Sr_2RuO_4, a strongly-correlated transition metal oxide for which electron-electron (and electron-phonon) interactions, the interplay of spin and orbital degrees of freedom, and the presence of multiple conduction electron bands are all of vital importance for the physics of the system. Of primary interest is the unconventional superconducting state exhibited by Sr_2RuO_4 below $T_c \sim 1.5$K. Experimental evidence points to a *triplet* superconducting state with a chiral, p-wave order parameter, which may also be topologically non-trivial and thus be of interest for applications in topological

quantum computation and information processing. However, the detailed nature of the superconducting state and the underlying mechanism giving rise to it are still not well understood. It is hoped that theoretical and experimental QPI measurements may help to resolve the controversy surrounding the pairing mechanism, which is thought to be driven by strong electron-electron interactions, themselves readily observed to result in significant magnetic fluctuations in the normal state.

In the first instance, we study the QPI in the normal state of Sr_2RuO_4, using a non-interacting effective model, in order to interpret experimental measurements carried out by collaborators. Careful account must be taken of the more complicated nature of the material in comparison with the simpler, idealized hosts considered in Chapters 3 and 4, including the multi-band structure of Sr_2RuO_4, the detailed surface electronic structure of the surface compared to the bulk, and the nature of the scattering from defects. As outlined previously in Chapter 2, these effects are expected to have a significant qualitative impact on the QPI, and thus a detailed comparison with experimental measurements requires a full consideration of these effects. By examining the deviation of experimental measurements from the calculated QPI for the non-interacting model, the effect of interactions on the electronic structure of the conduction bands in the normal state is revealed. Furthermore, these interactions are thought to be relevant for the superconducting pairing mechanism; measurements of interactions in the normal state may therefore indirectly offer insight into the superconducting state. We also calculate the QPI for the superconducting state, which reflects the anisotropy in the magnitude of the superconducting gap around the Fermi surface, directly related to the superconducting order parameter and thus indicative of the pairing mechanism. Comparison of such calculations to future experimental measurements may yield further information on the anisotropic superconducting gap function and hence the pairing mechanism in Sr_2RuO_4, which may help to confirm or refute the topologically non-trivial nature of the superconducting state.

Chapter 2

Imaging electron standing waves & probing band structure via STM

In this chapter we present the basic theory behind the quasiparticle interference (QPI), which is measured experimentally via scanning tunnelling microscopy (STM), where it has largely been used to map the electronic structure of the host material under study. However, this interpretation of the QPI, based on very basic phenomenological arguments about the joint density of states detailed in Section 2.2, is greatly over-simplified. We carefully examine the QPI from a more rigorous theoretical perspective, demonstrating the pitfalls of the more simplistic approach, and attempt to develop an intuitive physical picture of the processes giving rise to the QPI. In anticipation of calculations in later chapters, we consider several important effects relevant to the QPI in more complex systems in Sections 2.2 and 2.3.

2.1 Spectroscopic STM measurements & Fourier transform STS

Since its development 35 years ago [22, 23], the scanning tunnelling microscope has provided scientists with a non-destructive technique to image surfaces and their features directly at atomic resolution. The tunnelling current depends (via the electron tunnelling amplitude) exponentially on the separation of STM tip and sample, and thus STM measurements are extremely sensitive to the physical geometry of the surface; by rastering the STM tip over the surface and adjusting the tip height to maintain a constant tunnelling current ("constant-I mode"), the sample surface features are mapped on the atomic scale. In addition, the electronic structure of the material is

also critical in controlling tunnelling – STM measurements over adsorbed molecules in constant-I mode may show an increase or a decrease in tip height [38, 25]. The topographical maps generated by constant-I STM measurements in fact image the local density of states (LDOS) of electrons at the surface.

Theoretical treatments of the tunnelling process demonstrate that, neglecting the effects of the tunnelling matrix element and the tip density of states, the differential conductance dI/dV at a given tip-sample bias voltage V is proportional to the surface LDOS at a particular energy, eV [192]. The complicating factors of tip-sample separation and bias may be partially mitigated by considering the normalized (dimensionless) conductance $(dI/dV)/(I/V)$ which more accurately reflects the sample LDOS [52, 25, 38]:

$$\left(\frac{(dI/dV)}{(I/V)}\right)(\mathbf{r}) \propto \rho(\mathbf{r}, \omega = eV)\,. \tag{2.1}$$

Measuring the (normalized) conductance between tip and sample as a function of bias voltage thus offers detailed spectroscopic information about the electronic state of the sample surface with high spatial and energetic resolution. So-called scanning tunnelling spectroscopy (STS) has been widely used to study the electronic structure of metallic [93] and insulating materials [52], as well as that of adsorbed adatoms [118, 128, 129].

Mapping LDOS features in real space allows direct imaging of the quantum mechanical interference caused by defects and impurities in the sample material. Such defects break the translational symmetry of the underlying host, scattering conduction electrons: the resultant interference between incoming and outgoing electron wavefunctions gives rise to electronic "standing waves", visible as spatial modulations in the LDOS [42, 40]. The spatial structure of these modulations reflects the shape (and distribution) of the scatter(s) in space as illustrated in Figure 2.1, reproduced from Ref. 41. A single point defect (e.g. an adatom) gives a circular modulation in the LDOS, Figure 2.1 (left panel), while more elaborately engineered structures can cause interference of scattered electronic states, for example in the creation of confined wavefunctions in a "quantum corral", Figure 2.1 (right panel).

These spatial modulations in the LDOS, as measured by STS, contain information not only about the nature and distribution of scatterers but also about the underlying electronic states of the host material:

$$\rho(\mathbf{r}, \omega) = -\pi^{-1}\mathrm{Im}\; G(\mathbf{r}, \mathbf{r}, \omega + \mathrm{i}0^+) = -\pi^{-1}\mathrm{Im}\; \left[G^0 + G^0 T G^0\right](\mathbf{r}, \mathbf{r}, \omega + \mathrm{i}0^+)\,, \tag{2.2}$$

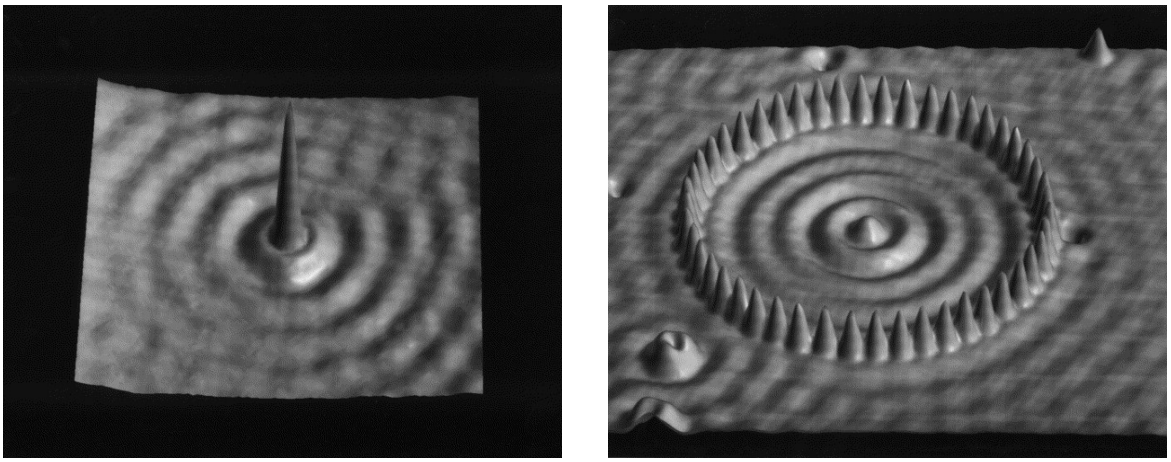

Fig. 2.1 Constant-I images of electron standing waves due to Fe adatoms on Cu(111) surface, which hosts a 2DEG-like surface band. Reproduced from Ref. 41. *Left:* Circular standing waves due to scattering of surface electrons from a single Fe adatom. *Right:* Interference of standing waves confined in a corral of 48 Fe adatoms

where $G(\mathbf{r}, \mathbf{r}, \omega + \mathrm{i}0^+)$ is the local retarded Green function of the host conduction electrons (G^0 denotes the Green function for the free system, in the absence of scattering centres). T is the t-matrix, which generically describes all effects of scattering due to defects, including multiple scattering processes, and the effect of interactions [74]. As we shall only consider retarded Green functions (and other quantities where appropriate) in this thesis, we specify $G(\omega) \equiv G(\omega + \mathrm{i}0^+)$ as implicit henceforth for notational simplicity; on occasion, the (complex) frequency argument is stated explicitly where it is appropriate and relevant. As such, measured LDOS maps can be thought of as the outcome of an "in-situ scattering experiment", in which both the scattering particles and the scattering centres are investigated. The scattered particles are the states of the clean (defect-free) host, which have well defined momentum due to translational symmetry in the absence of defects. The spatial LDOS modulations therefore contain scattering of amplitude and momenta characteristic of the underlying host material. The Fourier transform of these modulations depicts the sum of all such scattering events for a particular vector in momentum space, written generically as

$$\rho(\mathbf{q}, \omega) = \sum_i \mathrm{e}^{-\mathrm{i}\mathbf{r}_i \cdot \mathbf{q}} \rho(\mathbf{r}_i, \omega) = \rho^0(\mathbf{q}, \omega) + \Delta\rho(\mathbf{q}, \omega)\,. \tag{2.3a}$$

Under the assumption of elastic scattering from defects,

$$\begin{aligned}\Delta\rho(\mathbf{q},\omega) &= -\,\pi^{-1}\,\mathrm{Im}\;\sum_{\mathbf{k}}\Delta G(\mathbf{k},\mathbf{k}+\mathbf{q},\omega)\\ &= -\,\pi^{-1}\,\mathrm{Im}\;\sum_{\mathbf{k}}G^0(\mathbf{k},\omega)T(\mathbf{k},\mathbf{k}+\mathbf{q})G^0(\mathbf{k}+\mathbf{q},\omega)\,,\end{aligned} \tag{2.3b}$$

where $G^0(\mathbf{k},\mathbf{k}',\omega) = \delta_{\mathbf{k},\mathbf{k}'}G^0(\mathbf{k},\omega)$ is the Green function in the basis of surface momentum (eigen)states. A detailed derivation of Eq. 2.3 from Eq. 2.2 is given in Chapter 3.

In Fourier transform STS (FT-STS) the power spectrum of such LDOS modulation measurements is calculated. Examining Eq. 2.3, we see that this can be interpreted physically in terms of (elastic) scattering between iso-energetic states across the Brillouin zone of the underlying host. By analyzing the variation with energy and the geometry of features in the quasiparticle interference (QPI), as measured by FT-STS, it is therefore possible in principle to map the constant energy contours (CECs) of the host at particular scanning energies, and hence the dispersion of electronic states.

Employed in this fashion, FT-STS is a complementary technique to ARPES, a single-particle technique widely used to probe the momentum-resolved spectral function of materials [131, 199]. $I(\mathbf{k},\omega)$, the intensity of photoelectrons emitted at a given momentum and for a specific incident photon energy $E_{\mathrm{ph}} = \omega + E_{\mathrm{KE}} + \phi$, is proportional to the spectral function

$$I(\mathbf{k},\omega) \sim f(\omega)\times -\pi^{-1}\mathrm{Im}\;G(\mathbf{k},\omega+\mathrm{i}0^+) \quad \text{for} \quad \omega<0\,, \tag{2.4}$$

where $f(\omega)$ is the Fermi function, E_{KE} the emitted photoelectron kinetic energy, ϕ the work function, and ω the binding energy of the displaced electron [46]. In direct comparison with ARPES, FT-STS offers two key potential advantages: enhanced energetic and momentum-space resolution of FT-STS measurements, and the ability to map states below *and* above the Fermi level. However, the QPI is an intrinsically two-particle phenomenon, and as already indicated is an information-rich measurement, depending intimately on both the host electronic structure and that of the scattering centre(s). As a result, significant care must be taken in the interpretation of FT-STS measurements in terms of simplistic models, in order to avoid misconstruction of observed results.

2.2 Interpreting FT-STS measurements: QPI and joint density of states

We have introduced FT-STS as a powerful experimental technique to investigate the (surface) band structure of materials and the distribution of, and nature of scattering from, defects/impurities. However, the two-particle nature of the QPI process necessitates careful theoretical work to provide reasonable predictions and/or interpretations, even for qualitative features observed in FT-STS [77].

Early investigations using FT-STS approached the problem phenomenologically, rationalizing the observed features in QPI intensity in terms of the "transition rate" (via Fermi's golden rule) of scattering between points on the CEC at a given energy [78, 183],

$$|\Delta\rho(\mathbf{q},\omega)| \sim \sum_{\mathbf{k}} |T(\mathbf{k},\mathbf{k}+\mathbf{q})|\rho^0(\mathbf{k},\omega)\rho^0(\mathbf{k}+\mathbf{q},\omega)\,. \tag{2.5}$$

We assume that the scattering giving rise to QPI is local in space and s-wave in nature, such that the t-matrix is independent of momentum, $T(\mathbf{k},\mathbf{k}+\mathbf{q}) = T$. The QPI is therefore related directly to the joint density of states (JDOS),

$$\Delta\rho(\mathbf{q},\omega) \sim |T|J(\mathbf{q},\omega)\,,$$

where, $J(\mathbf{q},\omega)$ is simply the autocorrelation of the Im $G^0(\mathbf{k},\omega)$, (2.6)

$$J(\mathbf{q},\omega) = \sum_{\mathbf{k}} \text{Im } G^0(\mathbf{k},\omega)\text{Im } G^0(\mathbf{k}+\mathbf{q},\omega)\,,$$

noting that $\rho^0(\mathbf{k},\omega) = -\pi^{-1}\text{Im } G^0(\mathbf{k},\omega + \text{i}0^+)$. Simplifying further within this definition, *specific* pairs of points in k-space with large JDOS are therefore expected to dominate the (Brillouin zone summed) JDOS [78, 204], leading to the assignment of high-intensity features in the QPI as resulting from these individual scattering events. Such rationale has proven at least partially successful in interpreting experimental FT-STS results, for example Refs. 78, 183 and 184.

By comparison, Eq. 2.3, defining of QPI from a microscopic perspective, becomes

$$\Delta\rho(\mathbf{q},\omega) = -\pi^{-1}\text{Im } T\Lambda(\mathbf{q},\omega), \quad \text{with} \quad \Lambda(\mathbf{q},\omega) = \sum_{\mathbf{k}} G^0(\mathbf{k},\omega)G^0(\mathbf{k}+\mathbf{q},\omega)\,, \tag{2.7}$$

under the assumption of local, s-wave scattering, and therefore

$$\begin{aligned} -\pi\Delta\rho(\mathbf{q},\omega) =& \text{Re } T \left(\sum_{\mathbf{k}} \text{Re } G^0(\mathbf{k},\omega)\text{Im } G^0(\mathbf{k}+\mathbf{q},\omega) \right. \\ & \left. + \sum_{\mathbf{k}} \text{Im } G^0(\mathbf{k},\omega)\text{Re } G^0(\mathbf{k}+\mathbf{q},\omega) \right) \\ & + \text{Im } T \left(\sum_{\mathbf{k}} \text{Re } G^0(\mathbf{k},\omega)\text{Re } G^0(\mathbf{k}+\mathbf{q},\omega) \right. \\ & \left. - \sum_{\mathbf{k}} \text{Im } G^0(\mathbf{k},\omega)\text{Im } G^0(\mathbf{k}+\mathbf{q},\omega) \right). \end{aligned} \tag{2.8}$$

Comparing Eq. 2.6 with Eq. 2.8, it is clear that the phenomenological JDOS calculation, while superficially similar to the full QPI calculation, has no direct correspondence. The QPI depends on the *complex* response function $\Lambda(\mathbf{q},\omega)$ and complex scattering t-matrix T, while the JDOS approximates the experimentally-measured FT-STS in terms of the product of two *real* quantities, the JDOS $J(\mathbf{q},\omega)$ and the magnitude of the scattering t-matrix, $|T|$. Eq. 2.8 demonstrates clearly how the scattering phase shift, $\arg(T)$, directly impacts on the QPI as observed by FT-STS. In the case of magnetic impurities considered in Chapters 3 and 4, a dynamic t-matrix, varying in both magnitude and phase, arises due to electronic correlations on the impurity site, affecting the resultant QPI. The incompleteness of the JDOS interpretation leads in some cases to the absence of features in the QPI as predicted by the JDOS, termed "QPI extinction" [199]. Such "extinctions", which are the result of destructive interference between different scattering contributions in the terms of Eq. 2.8, can have a profound impact upon theoretical predictions of QPI signatures expected in experiment; for example, the absence of (JDOS-predicted) features in the QPI due to intra-Fermi-arc scattering in Weyl semi metals, demonstrated in Ref. 140.

Despite the deficiency of the JDOS approximation, the simplicity of the theoretical framework and directness of the approach compared to the full treatment of the QPI allows the interpretation of the QPI as directly mapping features of CECs in the host band structure, as we demonstrate in Sec. 2.2.1. We seek, therefore, both to understand the features in the JDOS and to develop a deeper understanding of the commonality between the JDOS and the QPI. In particular, we develop careful arguments about when the JDOS may share common features with the QPI measured by STS, and under what requirements for the physical system, beyond the previously discussed restrictions on the form of the scattering t-matrix.

2.2.1 Generalized joint density of states

Comparison of Eqs. 2.6 and 2.8 has shown that the relationship between the QPI and the JDOS is at best qualitative, even in the simple case of local, s-wave scattering due to impurities – differing, for example, in the effect of the scattering phase shift on each. To make more rigorous the connection between the two quantities, further approximation must be made. In the case of a purely imaginary t-matrix, corresponding to resonant scattering from a single bound state, Eq. 2.7 simplifies to $\Delta\rho(\mathbf{q},\omega) \sim |T|\text{Re }\Lambda(\mathbf{q},\omega)$, while a purely real t-matrix, corresponding to weak scattering (in the Born limit) of magnitude v_0, leads to $\Delta\rho(\mathbf{q},\omega) \sim v_0 \,\text{Im }\Lambda(\mathbf{q},\omega)$.

We introduce the "generalized JDOS" (GJDOS),

$$R(\mathbf{q},\omega) = \sum_{\mathbf{k}} \text{Im } G^0(\mathbf{k},\omega) \times G^0(\mathbf{k}+\mathbf{q},\omega)\,, \tag{2.9}$$

the real and imaginary parts of which are related to the QPI in the weak and bound-state scattering limits (respectively) presented above. In the bound-state-scattering case, the QPI is given by

$$\Delta\rho(\mathbf{q},\omega) \sim |T| \left(\sum_{\mathbf{k}} \text{Re } G^0(\mathbf{k},\omega)\ \text{Re } G^0(\mathbf{k}+\mathbf{q},\omega) - \text{Im } R(\mathbf{q},\omega) \right)\,, \tag{2.10a}$$

i.e. $J(\mathbf{q},\omega) \equiv \text{Im } R(\mathbf{q},\omega)$, while in the weak-scattering case, under the condition of centrosymmetric $G^0(\mathbf{k},\omega)$,

$$\Delta\rho(\mathbf{q},\omega) \sim 2|T|\ \text{Re } R(\mathbf{q},\omega)\,, \tag{2.10b}$$

such that $\text{Im }\Lambda(\mathbf{q},\omega) = 2\,\text{Re } R(\mathbf{q},\omega)$.

In order to illustrate clearly the basic framework within which the GJDOS (and QPI) should be interpreted in the first instance, we consider a minimal model for the host material, described by a single, non-interacting 2D band of conduction electrons with a generic dispersion, $\epsilon_{\mathbf{k}}$, such that $G^0(\mathbf{k},z) = (z-\epsilon_{\mathbf{k}})^{-1}$. States of momentum $\mathbf{k} = (k_x, k_y)$ are thus well-defined quasiparticles of a particular energy and with infinite lifetime. The GJDOS is thus

$$\begin{aligned} R(\mathbf{q},\omega) &= -\,\pi^{-1} \int_{1\text{BZ}} \frac{d^2\mathbf{k}}{\Omega_{BZ}} \delta(\omega-\epsilon_{\mathbf{k}}) G^0(\mathbf{k}+\mathbf{q},\omega) \\ &= -\,(\pi\Omega_{BZ})^{-1} \int_{c_{\mathbf{k}}} \frac{dk}{|\boldsymbol{\nabla}\epsilon_{\mathbf{k}}|} \left(\text{P}\left(\frac{1}{\omega-\epsilon_{\mathbf{k}+\mathbf{q}}}\right) - \text{i}\pi^{-1}\delta(\omega-\epsilon_{\mathbf{k}+\mathbf{q}}) \right)\,, \end{aligned} \tag{2.11}$$

where $c_{\mathbf{k}}$ is the CEC at energy ω, defined by $\omega - \epsilon_{\mathbf{k}} = 0$, along which the line integral is performed. It is convenient to parametrize $c_{\mathbf{k}}$ (whose length is $L_{c_{\mathbf{k}}}$) such that $\mathbf{k}(s) = (k_x(s), k_y(s))$, where $k_{x,y}(s)$ are regular functions and $s \in [0, 1)$,

$$R(\mathbf{q}, \omega) = -\frac{L_{c_{\mathbf{k}}}}{\pi \Omega_{BZ}} \int_0^1 \frac{ds}{|\boldsymbol{\nabla} \epsilon_{\mathbf{k}(s)}|} \left(\mathrm{P}\left(\frac{1}{\omega - \epsilon_{\mathbf{k}(s)+\mathbf{q}}} \right) - \mathrm{i}\pi^{-1} \delta(\omega - \epsilon_{\mathbf{k}(s)+\mathbf{q}}) \right) . \tag{2.12}$$

The CEC $c_{\mathbf{k}}$ may consist of a single, continuous curve, or be defined in terms of several disconnected sections; the parametrization of $c_{\mathbf{k}}$ is *piecewise* in this case, but the following analysis is not affected.

Only points, $\mathbf{k}_0$, which lie on both the CEC $c_{\mathbf{k}}$ and $c_{\mathbf{k}+\mathbf{q}}$ contribute to Im $R(\mathbf{q}, \omega)$, simultaneously satisfying

$$\omega - \epsilon_{\mathbf{k}_0} = 0 \quad \text{and} \quad \omega - \epsilon_{\mathbf{k}_0+\mathbf{q}} = 0 \, . \tag{2.13}$$

In order to evaluate the contribution to Im $R(\mathbf{q}, \omega)$ of each point $\mathbf{k}_0$, the function $\epsilon_{\mathbf{k}+\mathbf{q}}$ must be expanded along the CEC $c_{\mathbf{k}}$ around $\mathbf{k}_0 = \mathbf{k}(s_0)$. Expanding to second order in s, the curve parameter,

$$\epsilon_{\mathbf{k}(s)+\mathbf{q}} = \epsilon_{\mathbf{k}(s_0)+\mathbf{q}} + \left(\frac{d\epsilon_{\mathbf{k}(s)+\mathbf{q}}}{ds} \right)_{s=s_0} (s - s_0) + \left(\frac{d^2 \epsilon_{\mathbf{k}(s)+\mathbf{q}}}{ds^2} \right)_{s=s_0} \frac{(s - s_0)^2}{2!} + \dots \, , \tag{2.14}$$

where

$$d\epsilon_{\mathbf{k}} = \boldsymbol{\nabla} \epsilon_{\mathbf{k}} \cdot d\mathbf{k} + \frac{1}{2!} d\mathbf{k}^{\mathrm{T}} (\boldsymbol{\nabla} \boldsymbol{\nabla}^{\mathrm{T}} \epsilon_{\mathbf{k}}) d\mathbf{k} + \dots \tag{2.15a}$$

and

$$d\mathbf{k} = \hat{T}(s) ds + \frac{1}{2!} \kappa(s) \hat{N}(s) ds^2 + \dots \, , \tag{2.15b}$$

where $\hat{T}(s)$, $\hat{N}(s)$ and $\kappa(s)$ are the tangent and normal vectors to and the curvature of $c_{\mathbf{k}}$ at $\mathbf{k}(s)$ respectively. It follows therefore that

$$\frac{d\epsilon_{\mathbf{k}(s)+\mathbf{q}}}{ds} = \boldsymbol{\nabla} \epsilon_{\mathbf{k}(s)+\mathbf{q}} \cdot \hat{T}(s) \, , \tag{2.16a}$$

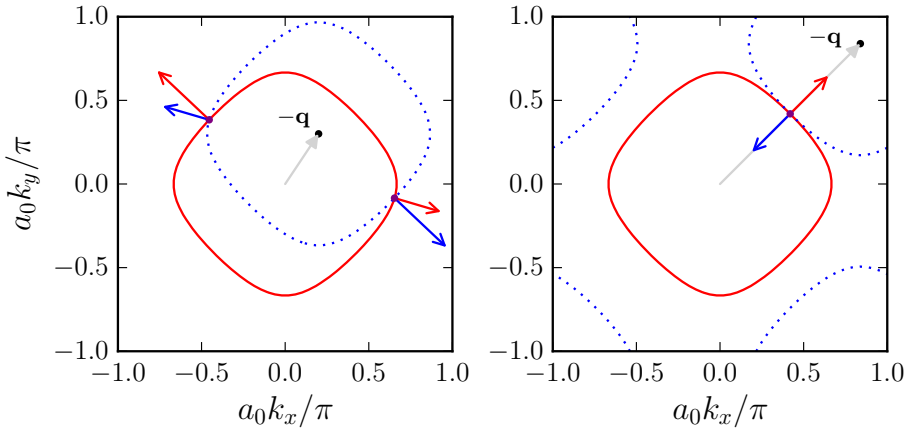

Fig. 2.2 Illustration of JDOS calculation for the single-site 2D square lattice tight-binding model considered in detail in Chapter 3, $\epsilon_{\mathbf{k}} = -2t\big(\cos(a_0k_x) + \cos(a_0k_y)\big)$, at $\omega = -t$. Intersections of CECs $c_{\mathbf{k}}$ and $c_{\mathbf{k+q}}$ defined by $\epsilon_{\mathbf{k}}$ and $\epsilon_{\mathbf{k+q}}$ for a given $\mathbf{q}$ are found and the vector product of the two group velocities $\boldsymbol{\nabla}\epsilon_{\mathbf{k}}$ on each CEC are evaluated. *Left,* $-a_0\mathbf{q}/\pi = (0.2, 0.3)$: $c_{\mathbf{k}}$ and $c_{\mathbf{k+q}}$ cross at two intersection points with non-collinear group velocities, giving a finite JDOS. *Right,* $-a_0\mathbf{q}/\pi \sim (0.8, 0.8)$: $c_{\mathbf{k}}$ and $c_{\mathbf{k+q}}$ touch at a single intersection point such that group velocities are antiparallel and JDOS diverges.

and

$$\frac{d^2\epsilon_{\mathbf{k}(s)+\mathbf{q}}}{ds^2} = \kappa(s)\boldsymbol{\nabla}\epsilon_{\mathbf{k}(s)+\mathbf{q}} \cdot \hat{N}(s) + \hat{T}(s)^{\mathrm{T}}(\boldsymbol{\nabla}\boldsymbol{\nabla}^{\mathrm{T}}\epsilon_{\mathbf{k}(s)+\mathbf{q}})\hat{T}(s)\,. \tag{2.16b}$$

The imaginary part of the integrand in Eq. 2.12 therefore becomes

$$\delta(\omega - \epsilon_{\mathbf{k}(s)+\mathbf{q}}) = -\sum_{\mathbf{k}_0}\left(\frac{1}{|\boldsymbol{\nabla}\epsilon_{\mathbf{k}(s)+\mathbf{q}} \cdot \hat{T}(s)|}\right)_{s=s_0} \delta(s - s_0)\,; \tag{2.17}$$

$\hat{T}_{\mathbf{k}(s_0)}$ is perpendicular to $\boldsymbol{\nabla}\epsilon_{\mathbf{k}(s_0)}$ by definition, so that

$$\text{Im } R(\mathbf{q}, \omega) = -\frac{L_{c_{\mathbf{k}}}}{\pi^2\Omega_{BZ}}\sum_{\mathbf{k}_0}\frac{1}{|\boldsymbol{\nabla}\epsilon_{\mathbf{k}_0} \times \boldsymbol{\nabla}\epsilon_{\mathbf{k}_0+\mathbf{q}}|}\,. \tag{2.18}$$

For an ideal 2D system, therefore, contributions to the JDOS (Im $R(\mathbf{q}, \omega)$) are given from the cross product of the group velocity at pairs of points in $\mathbf{k}$-space separated by $\mathbf{q}$ which both satisfy $\omega - \epsilon_{\mathbf{k}} = 0$ – or, equivalently, the intersection points of the CECs $c_{\mathbf{k}}$ and $c_{\mathbf{k+q}}$, as illustrated in Fig. 2.2 (left panel). Such a contribution is clearly

divergent when $\mathbf{k}_0$ or $\mathbf{k}_0 + \mathbf{q}$ lies on a critical point ($|\boldsymbol{\nabla}\epsilon_{\mathbf{k}}| = 0$), accompanied by a van Hove singularity; however, there is also a divergence if the two group velocities are collinear, such that

$$|\boldsymbol{\nabla}\epsilon_{\mathbf{k}} \times \boldsymbol{\nabla}\epsilon_{\mathbf{k}+\mathbf{q}}| = 0\,. \tag{2.19}$$

This is realized at specific points ($\mathbf{q}_{\text{crit}}$) where $c_{\mathbf{k}}$ and $c_{\mathbf{k}+\mathbf{q}}$ touch (rather than crossing) at one or more points in $\mathbf{k}$-space, equivalent to $\boldsymbol{\nabla}\epsilon_{\mathbf{k}_0+\mathbf{q}} \cdot \hat{T}_{\mathbf{k}_0} = 0$ in Eq. 2.16a. Consequently the expansion in $\epsilon_{\mathbf{k}+\mathbf{q}}$ along the CEC $c_{\mathbf{k}}$ around $\mathbf{k}_0$ must be carried out to second order for such points in order to determine the asymptotic form of $J(\mathbf{q}, \omega)$ as $\mathbf{q} \to \mathbf{q}_{\text{crit}}$.

For a centrosymmetric system, $\epsilon_{\mathbf{k}} = \epsilon_{-\mathbf{k}}$, the group velocity is necessarily antisymmetric with respect to inversion – and thus antiparallel for pairs of points $\mathbf{k}$ and $-\mathbf{k}$. Points on $c_{\mathbf{k}}$ related by inversion therefore satisfy Eq. 2.19, and the JDOS diverges at $\mathbf{q} = 2\mathbf{k}$ for all points on the CEC. The JDOS, therefore, directly maps the CEC at a given energy as lines of divergence in $\mathbf{k}$-space, in close analogy to ARPES (which measures the momentum-resolved spectral function directly).

Interpreting the QPI directly in terms of the JDOS has lead to the widespread use of QPI in mapping the fermiology and dispersion of unusual or novel materials, first in the cuprate superconductors [78, 55], but also in pnictides [215], topological insulators (TIs) [168], and semi-metals [183, 184]. However, obvious problems remain with this simplistic interpretation. The most pathological point in $\mathbf{q}$-space is $\mathbf{q} = \mathbf{0}$, at which *all* points on the CECs $c_{\mathbf{k}}$ and $c_{\mathbf{k}+\mathbf{q}}$ touch; the JDOS diverges strongly here as a result, irrespective of the detailed electronic structure of the host. However, considering instead the response function $\Lambda(\mathbf{q}, \omega)$ which governs the QPI, it is simple to show that

$$\Lambda(\mathbf{0}, \omega) = \sum_{\mathbf{k}} \left(\frac{1}{\omega + \mathrm{i}0^+ - \epsilon_{\mathbf{k}}} \right)^2 = \frac{\partial}{\partial \omega} G^0(\mathbf{r}, \mathbf{r}, \omega)\,, \tag{2.20}$$

such that the QPI only diverges at $\mathbf{q} = \mathbf{0}$ if the derivative of the local Green function of the host diverges, i.e. at a van Hove singularity. The question naturally arises: does $\Lambda(\mathbf{q}, \omega)$, and hence the QPI, share any lines of divergence with the JDOS, and if so, can the extinction of QPI [199] (the absence of high intensity features despite such features in the JDOS, discussed above) for some values of $\mathbf{q}$ be predicted?

Before continuing, we highlight another important implication of this inconsistency between JDOS and QPI. The QPI may be related to Re $R(\mathbf{q}, \omega)$, for example in the limiting weak-scattering case in Eq. 2.10b, and does not diverge at $\mathbf{q} = \mathbf{0}$ in the absence of a van Hove singularity. However, we have demonstrated that the JDOS Im $R(\mathbf{q}, \omega)$

must diverge at $\mathbf{q} = \mathbf{0}$: it might then be expected that the real and imaginary parts of the GJDOS would diverge at common points in $\mathbf{k}$-space. This apparent contradiction is resolved by noting that the definition of $R(\mathbf{q}, \omega)$ in Eq. 2.9 involves Im $G^0(\mathbf{k}, \omega)$, which is not an analytic function of ω or $\mathbf{k}$, and thus $R(\mathbf{q}, \omega)$ is itself non-analytic. By contrast, $\Lambda(\mathbf{q}, \omega)$ depends only on analytic functions (full, complex Green functions), and thus is an analytic function of ω; Re $\Lambda(\mathbf{q}, \omega)$ and Im $\Lambda(\mathbf{q}, \omega)$ are thus related by the familiar Kramers-Kronig relation, and therefore diverge along common curves in $\mathbf{q}$-space. As

$$\text{Re } \Lambda(\mathbf{q}, \omega) = \sum_{\mathbf{k}} \text{Re } G^0(\mathbf{k}, \omega) \text{Re } G^0(\mathbf{k} + \mathbf{q}, \omega) + \text{Im } R(\mathbf{q}, \omega) \,, \tag{2.21}$$

we conclude that the autocorrelation of Re $G^0(\mathbf{k}, \omega)$ exactly cancels divergences in the JDOS for some $\mathbf{q} = \mathbf{0}$, and potentially other $\mathbf{q}_{\text{crit}}$.

In order to determine the conditions under which divergences in the JDOS are not reproduced in the QPI, we consider Re $R(\mathbf{q}, \omega)$ at the point where CECs $c_{\mathbf{k}}$ and $c_{\mathbf{k}+\mathbf{q}}$ touch. This corresponds to the first derivative of $\epsilon_{\mathbf{k}+\mathbf{q}}$ along $c_{\mathbf{k}}$ vanishing at $\mathbf{k}_0$, such that

$$\omega - \epsilon_{\mathbf{k}_0+\mathbf{q}} = -\left(\left(\frac{d^2 \epsilon_{\mathbf{k}(s)+\mathbf{q}}}{ds^2} \right)_{s=s_0} \frac{(s - s_0)^2}{2!} + \dots \right) , \tag{2.22}$$

with the second derivative of $\epsilon_{\mathbf{k}+\mathbf{q}}$ given by Eq. 2.16b, so that

$$\text{Re } R(\mathbf{q}, \omega) = \frac{L_{c_{\mathbf{k}}}}{\pi \Omega_{BZ}} \int_0^1 \frac{ds}{|\boldsymbol{\nabla} \epsilon_{\mathbf{k}(s)}|} \text{P} \left(\left[\left(\frac{d^2 \epsilon_{\mathbf{k}(s)+\mathbf{q}}}{ds^2} \right)_{s=s_0} (s - s_0)^2 + \dots \right]^{-1} \right) . \tag{2.23}$$

Clearly if the second derivative is non-zero, the principal value integral, and thus Re $R(\mathbf{q}, \omega)$, will diverge; if the second derivative also vanishes at $\mathbf{k}_0$, then the PV integral around $\mathbf{k}_0$ takes the form

$$I_{\text{PV}} \sim \frac{1}{|\boldsymbol{\nabla} \epsilon_{\mathbf{k}(s_0)}|} \int_{s_0 - \delta s}^{s_0 + \delta s} ds \, \text{P} \left(\frac{1}{s - s_0} \right)^3 \times \left(\frac{d^3 \epsilon_{\mathbf{k}(s)+\mathbf{q}}}{ds^3} \right)_{s=s_0} , \tag{2.24}$$

which vanishes, and so Re $R(\mathbf{q}, \omega)$ remains finite (provided the third derivative of $\epsilon_{\mathbf{k}(s)+\mathbf{q}}$ does not vanish at s_0).

Consulting Eq. 2.16b, we note that the tangent and normal vectors to $c_{\mathbf{k}}$ are necessarily (respectively) perpendicular to and collinear with $\boldsymbol{\nabla} \epsilon_{\mathbf{k}+\mathbf{q}}$ at $\mathbf{k}_0$, and it

therefore follows that

$$\left(\frac{d^2\epsilon_{\mathbf{k}(s)+\mathbf{q}}}{ds^2}\right)_{s=s_0} = |\boldsymbol{\nabla}\epsilon_{\mathbf{k}_0+\mathbf{q}}|\Big(\kappa(s_0)\frac{\boldsymbol{\nabla}\epsilon_{\mathbf{k}_0}\cdot\boldsymbol{\nabla}\epsilon_{\mathbf{k}_0+\mathbf{q}}}{|\boldsymbol{\nabla}\epsilon_{\mathbf{k}_0}\cdot\boldsymbol{\nabla}\epsilon_{\mathbf{k}_0+\mathbf{q}}|}+\kappa(s_q)\Big)\,. \tag{2.25}$$

The second derivative vanishes if the orientations of $\boldsymbol{\nabla}\epsilon_{\mathbf{k}_0}$ and $\boldsymbol{\nabla}\epsilon_{\mathbf{k}_0+\mathbf{q}}$ are parallel, and the curvatures are equal $\kappa(s_0)=\kappa(s_q)$. As a result, Re $R(\mathbf{q},\omega)$ is not divergent at values of $\mathbf{q}$ for points on the CEC satisfying these criteria, while Eq. 2.19 shows that the JDOS, Im $R(\mathbf{q},\omega)$, *does* diverge at these points. This rather subtle result is relevant only to the $\mathbf{q}=\mathbf{0}$ point for simple, single-band systems, but becomes particularly significant for more complicated, multi-band hosts, for example the transition metal oxide Sr_2RuO_4 considered in Chapter 5. The QPI in multi-band systems is considered in more detail in Section 2.3.1.

Having developed a general approach to interpreting the QPI in simple 2D systems, and carefully examined the relationship with the JDOS, we now illustrate these concepts by investigating the QPI and JDOS in the simple example of a 2D electron gas host with a single, local scattering centre.

2.2.2 QPI & JDOS for the 2D electron gas

In the previous section, the GJDOS $R(\mathbf{q},\omega)$ resulting from a single local scatterer in a 2D system was analyzed, with a focus on finding the positions of divergences in both the real and imaginary parts of $R(\mathbf{q},\omega)$. We now illustrate our findings by considering the QPI and JDOS for the 2D free electron gas (2DEG), the simplest generic model for a host conduction band in 2D, and the de-facto model for electronic surface bands in bulk metallic systems, for example the Cu(111) surface [42, 180]. Furthermore, the QPI for the 2DEG, calculated via $\Lambda(\mathbf{q},\omega)$ defined in Eq. 2.7, may be found in closed analytic form via direct integration, as demonstrated in Ref. 34. Results for $R(\mathbf{q},\omega)$ from the more general approach detailed in Sec. 2.2.1, applicable more widely, may therefore be corroborated with exact solutions for this simplest possible case study.

For a 2DEG with a chemical potential μ and effective mass m,

$$G^0(\mathbf{k},\omega)=\frac{1}{\omega+\mathrm{i}0^+-\epsilon_{\mathbf{k}}} \quad \text{where} \quad \epsilon_{\mathbf{k}}=\frac{|\mathbf{k}|^2}{2m}-\mu\,, \tag{2.26}$$

so that CECs, defined by $\omega-\epsilon_{\mathbf{k}}=0$ are simply circles of radius $\sqrt{2m(\omega+\mu)}$, and $k_\mathrm{F}=\sqrt{2m\mu}$ defines the Fermi surface. Following Ref. 34, $\Lambda(\mathbf{q},\omega)$ is calculated by

expressing the requisite Green functions in the canonical conjugate (real-space) basis,

$$\Lambda(\mathbf{q},\omega) = \sum_{\mathbf{k}} G^0(\mathbf{k},\omega)G^0(\mathbf{k}+\mathbf{q},\omega) = \int d^2\mathbf{r}\, \mathrm{e}^{\mathrm{i}\mathbf{q}\cdot\mathbf{r}} G^0(\mathbf{r},\mathbf{0},\omega)G^0(\mathbf{0},\mathbf{r},\omega)\,. \tag{2.27}$$

Eq. 2.27 can be directly evaluated using the exact expression for the Green function in real space,

$$G^0(\mathbf{0},\mathbf{r},\omega) = \int \frac{d^2\mathbf{k}}{(2\pi)^2} \frac{\mathrm{e}^{\mathrm{i}\mathbf{k}\cdot\mathbf{r}}}{\omega + \mathrm{i}0^+ - \epsilon_{\mathbf{k}}} = -\mathrm{i}\frac{m}{2} H_0^{(1)}\Big(k(\omega)|\mathbf{r}|\Big)\,, \tag{2.28}$$

where $H_0^{(1)}$ is the zeroth order Hankel function of the first kind and

$$k(\omega) = k_{\mathrm{F}}\sqrt{1+\frac{\omega}{\mu}}\,. \tag{2.29}$$

Carrying out the angular and radial integrals in Eq. 2.27, Eq. 2.27 evaluates to [34]

$$\mathrm{Re}\ \Lambda(\mathbf{q},\omega) = \begin{cases} \frac{2m^2}{\pi|\mathbf{q}|\sqrt{|\mathbf{q}|^2-4k(\omega)^2}} \ln\left(\frac{\sqrt{|\mathbf{q}|^2-4k(\omega)^2}+k(\omega)}{\sqrt{|\mathbf{q}|^2-4k(\omega)^2}-k(\omega)}\right) & |\mathbf{q}| > 2k(\omega) \\ -\frac{2m^2}{\pi|\mathbf{q}|\sqrt{4k(\omega)^2-|\mathbf{q}|^2}} \arctan\left(\frac{|\mathbf{q}|}{\sqrt{4k(\omega)^2-|\mathbf{q}|^2}}\right) & |\mathbf{q}| < 2k(\omega) \end{cases}, \tag{2.30a}$$

and

$$\mathrm{Im}\ \Lambda(\mathbf{q},\omega) = \frac{2m^2}{\pi|\mathbf{q}|\sqrt{|\mathbf{q}|^2-4k(\omega)^2}} \quad |\mathbf{q}| > 2k(\omega)\,. \tag{2.30b}$$

By contrast, the calculation of the GJDOS is much more transparent; considering $\mathbf{q} = (q,0)$, the two CECs $c_{\mathbf{k}}$ and $c_{\mathbf{k}+\mathbf{q}}$, both of length $2\pi k(\omega)$, intersect at $\mathbf{k}_0 = (-q/2, \pm\sqrt{k(\omega)^2-(q/2)^2})$, giving the imaginary part of the GJDOS,

$$\begin{aligned} \mathrm{Im}\ R(\mathbf{q},\omega) =& \frac{2\pi k(\omega)}{4\pi^4} \frac{2}{|\mathbf{q}|\sqrt{4k(\omega)^2-|\mathbf{q}|^2}} \\ =& \frac{1}{2k(\omega)\pi^3} \frac{1}{(|\mathbf{q}|/2k(\omega))\sqrt{1-(|\mathbf{q}|/2k(\omega))^2}}\,. \end{aligned} \tag{2.31a}$$

Similarly, the real part of the GJDOS is given by Eq. 2.12 as

$$\begin{aligned}\text{Re } R(\mathbf{q},\omega) =& \frac{\pi k(\omega)}{4\pi^2(k(\omega)/k_\text{F})^2}\int_0^1 \frac{ds}{k(\omega)/m}\frac{1}{|\mathbf{q}|/k(\omega)}\text{P}\left(\frac{1}{(|\mathbf{q}|/k(\omega))+\cos(2\pi s)}\right)\\ =& \frac{m^2}{4k(\omega)^2\pi}\frac{1}{(|\mathbf{q}|/2k(\omega))\sqrt{(|\mathbf{q}|/2k(\omega))^2-1}} \quad |\mathbf{q}|>2k(\omega)\,,\end{aligned} \tag{2.31b}$$

and Re $R(\mathbf{q},\omega)=0$ for $|\mathbf{q}|<2k(\omega)$, following straightforward contour integration, in agreement with Eq. 2.30b with 2Re $R(\mathbf{q},\omega)=$ Im $\Lambda(\mathbf{q},\omega)$. From Eqs. 2.30 and 2.31 it is clear that $\Lambda(\mathbf{q},\omega)$ (and hence $R(\mathbf{q},\omega)$) can be written as a universal function of $|\mathbf{q}|$ rescaled in terms of $k(\omega)$, the radius of the CEC at scanning energy, ω, defined in Eq. 2.29. Despite the relationship between Im $R(\mathbf{q},\omega)$ and Re $\Lambda(\mathbf{q},\omega)$, given by Eq. 2.21, comparison of Eqs. 2.30a and 2.31a yields no simple analytic form for the autocorrelation of the real part of $G^0(\mathbf{k},\omega)$, the difference between the two quantities, and there is no direct quantitative connection between the JDOS, Im $R(\mathbf{q},\omega)$, and the QPI, determined by $\Lambda(\mathbf{q},\omega)$.

The results for $R(\mathbf{q},\omega)$, plotted in Fig. 2.3, clearly demonstrate the discrepancy between the features in the real and imaginary parts of the GJDOS, which differ in the presence of a strongly divergent feature at $|\mathbf{q}|=0$, where the JDOS, Im $R(\mathbf{q},\omega)\sim|\mathbf{q}|^{-1}$, as given by Eq. 2.31. This difference is due to the non-analyticity of the GJDOS $R(\mathbf{q},\omega)$, as discussed in Sec. 2.2.1; the divergence is also absent in Re $\Lambda(\mathbf{q},\omega)$, implying a divergence in the other component as defined in Eq. 2.21 with equal magnitude and opposite sign cancelling that of Im $R(\mathbf{q},\omega)$. Both Re $R(\mathbf{q},\omega)$ and Im $R(\mathbf{q},\omega)$ diverge at $|\mathbf{q}|_\text{crit}=2k(\omega)$, with the functional form Im $R(\mathbf{q},\omega)\sim-|\mathbf{q}-\mathbf{q}_\text{crit}|^{-1/2}$, from above and below respectively; Re $\Lambda(\mathbf{q},\omega)$ is controlled by Im $R(\mathbf{q},\omega)$ at this point, and thus diverges also.

These results illustrate clearly the lack of predictive power of the JDOS in interpreting the QPI; divergent features in JDOS may be present or absent in the QPI, and further work is needed to give more reliable insight, even in the simplest limiting cases (the weak scattering and bound-state scattering cases discussed in Sec. 2.2.1).

Despite this lack of direct correspondence between the QPI and the JDOS, the interpretation of the QPI in terms of scattering between points on a CEC at a given scanning energy is still largely valid, and the presence of strong (divergent) features at $|\mathbf{q}|=2k(\omega)$ in the $\Lambda(\mathbf{q},\omega)$ (and hence the QPI) seen in Fig. 2.3 allows the dispersion of the host material to be mapped in a similar way to ARPES measurements. By recording the position of the divergence, and thus $k(\omega)$, as a function of scanning

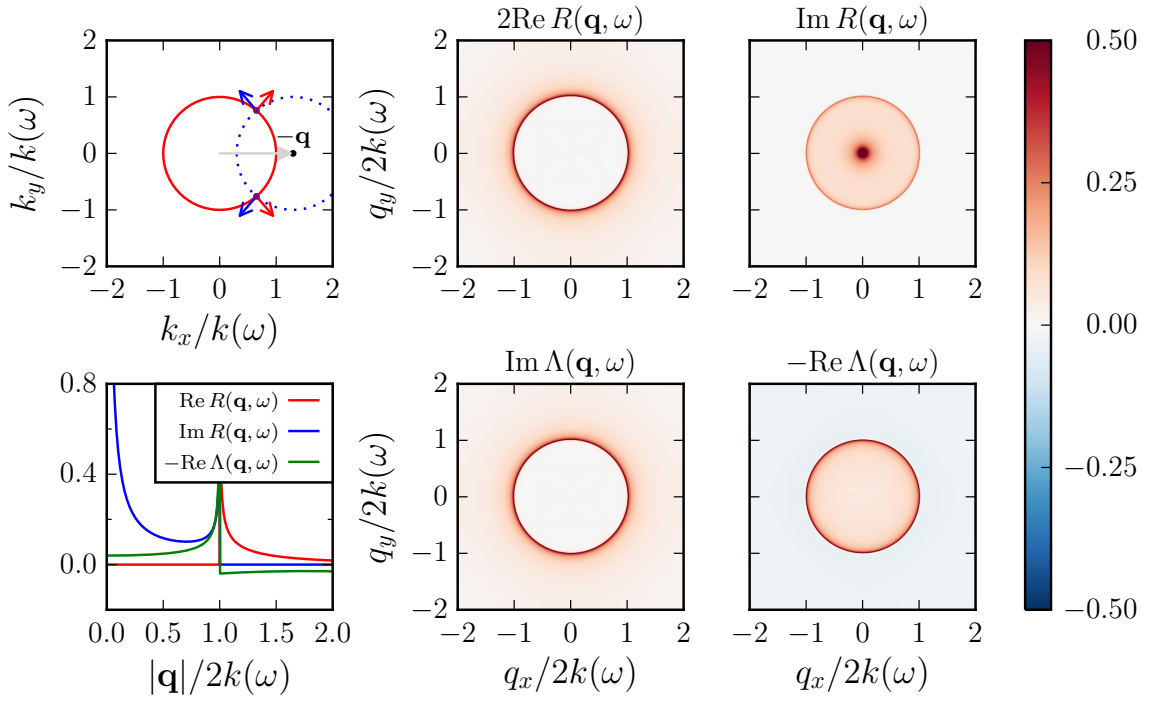

Fig. 2.3 Plots of real and imaginary parts of $R(\mathbf{q},\omega)$ and $\Lambda(\mathbf{q},\omega)$ for the 2DEG, which are universal when rescaled in terms of $k(\omega)$, the radius of the CEC at scanning energy ω. *Upper, left to right:* Visualization of the protocol for calculation of $R(\mathbf{q},\omega)$, with the resultant Re $R(\mathbf{q},\omega)$ and Im $R(\mathbf{q},\omega)$ scaled to match the appropriate part of $\Lambda(\mathbf{q},\omega)$. *Lower, left to right:* Cuts through the real and imaginary parts of $R(\mathbf{q},\omega)$, Re $\Lambda(\mathbf{q},\omega)$ (NB. Im $\Lambda(\mathbf{q},\omega) = 2\mathrm{Re}\,R(\mathbf{q},\omega)$), with colourmaps of Re $\Lambda(\mathbf{q},\omega)$ and Im $\Lambda(\mathbf{q},\omega)$. The divergence at $|\mathbf{q}| = 0$ seen in Im $R(\mathbf{q},\omega)$ is absent in the full Re $\Lambda(\mathbf{q},\omega)$.

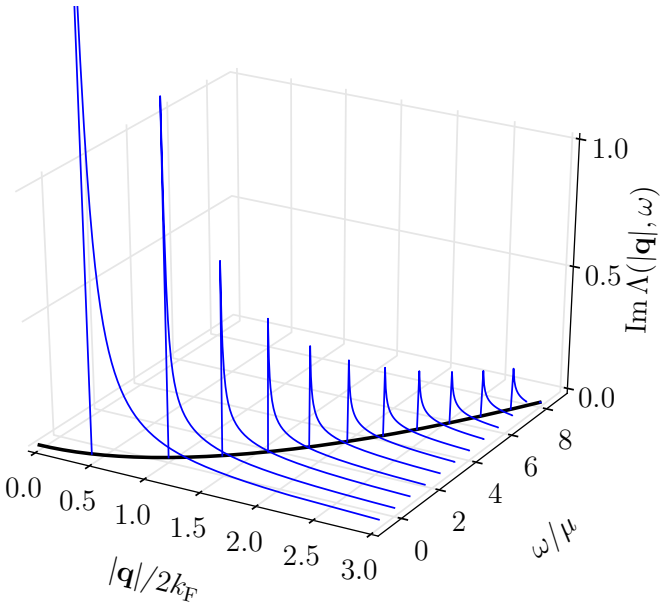

Fig. 2.4 Plot of Im $\Lambda(\mathbf{q},\omega)$ as a function of momentum $|\mathbf{q}|/k_\mathrm{F}$ and energy ω/μ for the 2DEG, showing the position of the divergence (at $|\mathbf{q}| = 2k(\omega)$) which maps out the dispersion of $k(\omega) = \sqrt{2m\omega}$, represented by the black curve.

energy, the Fermi velocity and (effective) electron mass of the host material 2DEG may be determined, as depicted in Fig. 2.4. In weakly-interacting systems such as Cu(111) for which such a 2DEG-like surface band exists, this approach provides an accurate measure, due to the high energy and momentum-space resolution possible via FT-STS, for the effective mass m and the volume enclosed by the Fermi surface.

In more complicated materials, for which the quasiparticle mass may be strongly (and dynamically) renormalized due to electron-electron interactions, or the surface quasiparticles are unusual (for example TIs, unconventional superconductors and (Weyl) semi-metals), FT-STS measurements are still valuable in providing this accurate information about the quasiparticle dispersion.

However, the wealth of information contained in the QPI due to coherent scattering and interference processes offers deeper insights into the physics of the system, potentially providing information on correlations in both the host material [180, 217] and scattering centres [48, 138]; the properties of emergent quasiparticles, for example due to spin-orbit coupling in TIs [219, 120]; and the mechanisms responsible for superconducting pairing in unconventional SCs such as the cuprates [78], pnictides [10, 77] and ruthenates [53]. In the following chapters we study the QPI in several such systems, investigating the way in which electronic correlations are manifest therein, and what

more information may be gained from a more complete study of experimental QPI measurements.

2.3 QPI in realistic systems

In order to model accurately more complex systems (for which experimental FT-STS measurements may be particularly valuable), several important complicating factors have to be considered in addition to the basic theoretical formulation of the QPI given thus far. Care must be taken to give consideration to these effects in order to model accurately the QPI, and thus provide interpretation for experimental measurements. We conclude this chapter with an outline of some key effects which can arise in realistic materials, and profoundly influence the calculated QPI for the systems under study in the remainder of this thesis. These factors are of great importance when calculating the QPI for comparison with experimental results. In Chapter 5, we investigate the QPI in the binary transition metal oxide Sr_2RuO_4, a multi-band system with a complicated surface electronic structure and strong electronic correlations. The considerations made in this section are of particular importance in this case, for which we compare theoretical calculations with experimental FT-STS measurements carried out by collaborators and detailed in Ref. 206.

2.3.1 Multi-band systems

Interesting electronic systems are often so due to orbital degrees of freedom and their mutual interactions and interplay with spin degrees of freedom; multi-band systems arise, and calculations for the QPI must take account of this orbital texture. Additionally, the real-space structure of the unit cell can give rise to multiple bands, and must also be incorporated. The effect on theoretical calculations of the QPI is twofold: not only must the additional structure of the host material be included, but the details of the scattering of conduction electrons must be considered. Such multi-band scattering effects may be particularly significant for the QPI, with small changes in the microscopic detail causing marked changes in the topology and intensity.

Considering the modulations of the LDOS for a generic multi-orbital unit cell, we generalize Eq. 2.2 to

$$\rho(\mathbf{r},\omega) = -\pi^{-1}\,\mathrm{Tr}\;\;\mathrm{Im}\left[\mathbf{G}^0 + \mathbf{G}^0\mathbf{T}\mathbf{G}^0\right](\mathbf{r},\mathbf{r},\omega+\mathrm{i}0^+)\,, \tag{2.32}$$

where $\mathbf{G}^0$ is the (unperturbed) Green function *matrix* for the unit cell. The QPI (as defined in the single-orbital case by Eq. 2.3) is

$$\Delta\rho(\mathbf{q},\omega) = -\pi^{-1}\,\mathrm{Im}\sum_{\mathbf{k}}\mathrm{Tr}\;\;\mathbf{G}^0(\mathbf{k},\omega)\mathbf{T}(\mathbf{k},\mathbf{k}+\mathbf{q})\mathbf{G}^0(\mathbf{k}+\mathbf{q},\omega)\,. \tag{2.33}$$

The evaluation of the LDOS, and hence QPI, involves a trace over the orbital degrees of freedom at a given position $\mathbf{r}$, as the STM measurement of the LDOS is not (controllably) orbitally selective. While spin polarized STM measurements are possible [38, 24], typical STS measurements are not spin-selective and thus the trace in Eq. 2.33 includes spin.

In the case of a single-site unit cell, coupling between spin and/or orbital degrees of freedom generates off-diagonal elements in $\mathbf{G}^0$, and thus the simple picture of the QPI in terms of scattering between points on a CEC is insufficient. We write the Green function matrix in terms of the dyadic decomposition

$$\mathbf{G}^0(\mathbf{k},\omega) = \sum_n G^0_n(\mathbf{k},\omega)\vec{u}_{n,\mathbf{k}}\vec{u}^\dagger_{n,\mathbf{k}}\,, \tag{2.34}$$

where n is the band index, $\vec{u}_{n,\mathbf{k}}$ the corresponding eigenvector of $\mathbf{G}^0(\mathbf{k},\omega)$, and $G^0_n(\mathbf{k},\omega) = (\omega + \mathrm{i}0^+ - \epsilon_{n,\mathbf{k}})^{-1}$ is the electronic Green function of band n (with dispersion $\epsilon_{n,\mathbf{k}}$). Eq. 2.33 is therefore expressed in terms of the (diagonal) band-space Green functions as

$$\Delta\rho(\mathbf{q},\omega) = \sum_{n,m}\left(-\pi^{-1}\,\mathrm{Im}\sum_{\mathbf{k}} G^0_n(\mathbf{k},\omega)T_{nm}(\mathbf{k},\mathbf{k}+\mathbf{q})G^0_m(\mathbf{k}+\mathbf{q},\omega)\right)\,, \tag{2.35a}$$

where the t-matrix is

$$T_{nm}(\mathbf{k},\mathbf{k}+\mathbf{q}) = \mathrm{Tr}\;\;\vec{u}_{n,\mathbf{k}}\vec{u}^\dagger_{n,\mathbf{k}}\mathbf{T}(\mathbf{k},\mathbf{k}+\mathbf{q})\vec{u}_{m,\mathbf{k}+\mathbf{q}}\vec{u}^\dagger_{m,\mathbf{k}+\mathbf{q}}\,. \tag{2.35b}$$

Eq. 2.35 restores the notion of scattering between points on well-defined CECs, summing over such scattering events between each pair of bands (n and m). However the resultant scattering t-matrix for the multi-band systems is momentum-dependent, even for a local scatterer $\mathbf{T}(\mathbf{k},\mathbf{k}+\mathbf{q}) = \mathbf{T}$, due to the momentum dependence of the unitary transformation between band and orbital space (whose columns are $\vec{u}_{n,\mathbf{k}}$).

From Eq. 2.35b the structure of the scattering t-matrix in orbital(/spin) space is clearly essential, even for a local scattering defect. For the weak potential scatterer discussed in Section 2.2 it is reasonable to assume that $\mathbf{T} = v_0\mathbf{I}$, i.e. diagonal in orbital

space. The t-matrix in band space $T_{nm}(\mathbf{k}, \mathbf{k}+\mathbf{q})$ is therefore maximal between states in momentum-space with common orbital composition. In Section 2.2 we demonstrated that dominant (divergent) features in the QPI are observed at points in $\mathbf{q}$-space where the CECs $c_{\mathbf{k}}$ and $c_{\mathbf{k}+\mathbf{q}}$ touch at $\mathbf{k}_0$, such that the group velocities are anti-parallel. By analogy, the QPI in multi-band systems is expected to be dominated by divergences at points in $\mathbf{q}$-space for which $c_{n,\mathbf{k}}$ and $c_{m,\mathbf{k}+\mathbf{q}}$ (CECs for the n and m bands) touch at a point, $\mathbf{k}_0$, *and* the overlap of orbital character between the two bands at this point is maximized. With $u^i_{n,\mathbf{k}}$ the coefficient of orbital i in band n at $\mathbf{k}$, full calculation of Eq. 2.35b for a diagonal scatterer in fact yields

$$T_{nm}(\mathbf{k}, \mathbf{k}+\mathbf{q}) = v_0 \sum_{i,j} u^i_{n,\mathbf{k}} \left(u^j_{n,\mathbf{k}}\right)^* u^j_{m,\mathbf{k}+\mathbf{q}} \left(u^i_{m,\mathbf{k}+\mathbf{q}}\right)^* . \tag{2.36}$$

Under the assumption that one orbital contribution is dominant for a particular band state at a given $\mathbf{k}$, Eq. 2.36 reduces to

$$T_{nm}(\mathbf{k}, \mathbf{k}+\mathbf{q}) \sim v_0 \sum_{i} |u^i_{n,\mathbf{k}}|^2 |u^i_{m,\mathbf{k}+\mathbf{q}}|^2 , \tag{2.37}$$

which is the form that one would expect based on qualitative arguments about maximizing the overlap of orbital character between the two bands.

This treatment of orbital-diagonal scattering applies equally in systems with unusual spin texture (which is typically due to strong spin-orbit coupling [143, 168]). The non-trivial topology of 3D strong TIs generates a 2D metal at the surface, with an effective surface theory of massless Dirac fermions in which spin and momentum are locked together – and as such, back-scattering ($\mathbf{k} \to -\mathbf{k}$) is forbidden without a spin flip. Setting the scattering matrix to be diagonal in spin space, Eq. 2.37 corresponds to a formal generalization of the so-called "spin-dependent scattering probability" (SSP) [168], which heuristically takes the spin texture into account in the framework of the JDOS (discussed in Section 2.2). Of course, scattering in different channels, for which the t-matrix is *not* diagonal in orbital/spin space, gives rise to different QPI signatures [66]. Such off-diagonal terms may arise when considering scattering due to defects in the effective tight binding model of a more complicated multi-orbital host material.

Eqs. 2.35 and 2.36 indicate that the simple arguments made for the single-band case in Section 2.2, demonstrating the presence of divergences in the QPI at scattering vectors relating a specific pair of points on a given CEC for which the group velocities are anti-parallel, can also be extended to the multi-band case. By analogy to the single-band case, we can consider a generalization of the host response function $\Lambda(\mathbf{q}, \omega)$

to

$$\Lambda_{nm}(\mathbf{q},\omega) = \sum_{\mathbf{k}} G_n^0(\mathbf{k},\omega) G_m^0(\mathbf{k}+\mathbf{q},\omega) \tag{2.38}$$

between bands n and m, which is equivalent to the QPI due to scattering between bands n and m if the structure of the t-matrix (Eq. 2.36) is neglected. Whether or not these divergent contributions to $\Lambda_{nm}(\mathbf{q},\omega)$ also result in divergences in the QPI depends on the magnitude and phase of the t-matrix $T_{nm}(\mathbf{k},\mathbf{k}+\mathbf{q})$ between specific pairs of points. Thus the presence (or absence) of divergent features in the QPI can be rationalized in terms of scattering between specific pairs of points in $\mathbf{k}$-space for the multi-band case, as for a single band, with the additional consideration of the specific scattering t-matrix element between any pair of points (which varies in a complicated way across the Brillouin zone).

Another important aspect of the investigation of the GJDOS and QPI in Section 2.2 is that divergent features in the QPI are only expected between points on the CEC (separated by $\mathbf{q}$) where the group velocities are anti-parallel, while the JDOS (commonly used as an approximation to interpret the QPI) also diverges at points where the group velocities are parallel. The corollary of this finding in multi-band systems is that the form of the QPI due to inter-band scattering depends strongly on whether the bands are particle-like or hole-like in nature. Systems involving both particle- and hole-like bands include the Fe-based unconventional superconductors, in which the proposed $s_{\pm}$-wave pairing mechanism is thought to involve spin fluctuations at $\mathbf{q}$ vectors connecting the particle- and hole-like bands [190, 76, 77]. FT-STS is a key tool to further understand and attempt to confirm the underlying mechanism of pairing [215, 156, 214, 10]. In Chapter 5 we investigate the QPI in a different multi-band system, the layered transition metal oxide Sr_2RuO_4. Here the interplay of spin and orbital degrees of freedom, and the presence of strong electronic interactions, generates an unconventional superconducting state, believed to be spin-triplet with p-wave order parameter, with a critical temperature of $T_c \sim 1.5$K. The electronic structure of Sr_2RuO_4 is well-described by a multi-orbital tight binding model on the 2D square lattice, giving rise to both particle-like and hole-like bands; as in the Fe-based superconductor case, spin fluctuations are thought to play a key role in the pairing mechanism. The formalism established here for the QPI in multi-band 2D systems is used to understand and interpret the QPI for Sr_2RuO_4 in Chapter 5.

Multiple bands also arise in systems where the unit cell consists of multiple sites at distinct positions in space, rather than multiple orbitals on a single site. Graphene,

represented by a single-orbital tight binding model on the 2D honeycomb lattice, is one such system, consisting two interpenetrating triangular sublattices. In Chapter 3 we consider the QPI for the honeycomb lattice, detailing the effect of this sublattice structure on the QPI in Section 3.2.

2.3.2 Material-specific & surface effects

FT-STS is a fundamentally 2D technique, which is explicitly surface-sensitive. Bulk states of the host material may contribute to surface LDOS and thus be measured via STS, but only via the projection of these states at the surface. Many of the systems investigated using FT-STS are therefore either formally 2D (for example graphene [220] or the surface states of 3D TIs [168]) or are layered materials giving rise to pseudo-2D electronic structure (for example the cuprate and pnictide superconductors [78, 214], as well as the triplet superconductor Sr_2RuO_4 studied in Chapter 5 of this thesis [206]). While FT-STS is an appropriate technique to apply to such pseudo-2D materials, care must be taken to investigate the possible surface reconstruction effects which may distort the measured electronic structure in comparison with the bulk pseudo-2D electronic structure of such layered materials. The effect of coupling to bulk electronic states of the host material must also be considered.

At the simplest level, coupling of pseudo-2D electronic states to the bulk results in surface states of momentum $\mathbf{k} = (k_x, k_y)$ no longer being eigenstates (and thus perfectly defined quasiparticles of infinite lifetime). Instead the quasiparticles are dephazed, resulting in a finite lifetime and uncertainty in the energy. For weak coupling between bulk and surface, such that the surface quasiparticle lifetime is long, the structure of the QPI is largely the same as the pure 2D case, with sharp features broadened or smeared out in both momentum- and energy-space due to lifetime effects. As the strength of surface-bulk coupling is increased, surface quasiparticles become less well defined, with shorter lifetime and thus a finite, increasing bandwidth of surface states. The limit in which the measured LDOS is simply the projection of a bulk band at the surface is investigated in Section 3.2 in terms of the (100) surface of the 3D cubic tight binding model; the QPI is found to change dramatically on increasing the surface-bulk coupling, going from the 2D square to (100) surface 3D cubic lattices.

Care is taken to ensure the STM tip fashioned in experiment is "atomically sharp" (terminating in a single atom), allowing STS measurements of the LDOS in real space to be carried out with sub-unit-cell resolution. By contrast, theoretical calculations are carried out on lattice models [106], yielding (implicitly) *lattice* Green functions in real space (or their Fourier components). STM measurements naturally probe

the continuum LDOS, and thus the continuum (spatial) Green functions of the host. Expanding in terms of an appropriate Wannier basis, with $W(\mathbf{r}-\mathbf{r}_i)$ the Wannier function at position $\mathbf{r}$ due to lattice point $\mathbf{r}_i$,

$$G(\mathbf{r},\mathbf{r}',\omega) = \sum_{i,j} W(\mathbf{r}-\mathbf{r}_i)W^*(\mathbf{r}'-\mathbf{r}_j)G(\mathbf{r}_i,\mathbf{r}_j,\omega)\,, \tag{2.39}$$

where $G^0(\mathbf{r}_i,\mathbf{r}_j,\omega)$ are the lattice Green functions between lattice point i and j [106, 45]. These continuum Green functions $G^0(\mathbf{r},\mathbf{r}',\omega)$ are then used in the calculation of the LDOS (Eq. 2.2), and thus the QPI. Eq. 2.39 has the form of a 2D convolution in real space; the observed QPI (c.f. Eq. 2.3) is therefore

$$\Delta\rho(\mathbf{q},\omega) = -\pi^{-1}\,\mathrm{Im}\,\sum_{\mathbf{k}} W(\mathbf{k})\Delta G(\mathbf{k},\mathbf{k}+\mathbf{q},\omega)W^*(\mathbf{k}+\mathbf{q})\,, \tag{2.40}$$

where $W(\mathbf{k}) = \int d^2r\ \mathrm{e}^{\mathrm{i}\mathbf{k}\cdot\mathbf{r}}W(\mathbf{r})$.

The QPI is typically calculated in terms of the lattice Green functions (the lattice QPI), with no consideration given to the possible effect of the spatial distribution of local orbitals of the host surface. Recent work has begun to address this issue [106, 45], but such considerations are still not widespread in the literature. In Chapter 3 we explore the effect of calculating the QPI in a representative Wannier basis (the Wannier-basis QPI) for a single impurity, and in Chapter 5 when carrying out detailed QPI calculations for the transition metal oxide Sr_2RuO_4 in order to simulate experimental results.

Moreover, surface-specific features in the electronic structure must also be included in order to calculate the QPI in realistic systems, as we show in Chapter 5 for Sr_2RuO_4, which has a layered physical structure resulting in a pseudo-2D electronic structure. As noted here, QPI and FT-STS studies have largely been restricted to true 2D systems or those with pseudo-2D electronic structure, and the effect of coupling between surface and bulk states is typically neglected. In Chapter 3 we also investigate the QPI for the (100) surface 3D cubic lattice, a system in which the coupling between surface and bulk states is strong, and demonstrate that coupling to the bulk has a profound impact on the resultant QPI.

2.3.3 Electronic correlations

Insight into the nature of electronic correlations in the system under study is a key objective of FT-STS measurements. Interactions between the conduction electrons of

the host give rise to a generically dynamic, momentum-dependent self-energy for the conduction electrons, altering the host Green functions via the Dyson equation,

$$G(\mathbf{k}, z) = \left(G^0(\mathbf{k}, z)^{-1} - \Sigma(\mathbf{k}, z)\right)^{-1} . \tag{2.41}$$

Exact treatment of these interactions is impossible in all but the simplest theoretical models, and thus effective non-interacting or mean-field solutions are often employed to understand the physical content. For strongly-correlated bulk materials, the numerical method of choice is dynamical mean field theory (DMFT) [62, 104]; however, the central approximation of DMFT is to neglect non-local interactions, such that the self-energy, while dynamic, is momentum-independent. While such a treatment becomes exact in the limit of infinite dimensions, using DMFT to accurately describe the physics of low-dimensional systems (e.g. the 2D systems studied here) is a formidable, ongoing challenge [165, 105, 104], and beyond the scope of this thesis.

Despite the difficulty of full theoretical treatment, QPI calculations and experimental FT-STS offer insight into the nature of electronic correlations in such interacting systems. In Chapter 5 we calculate the QPI for one such strongly correlated material, Sr_2RuO_4, using an effective mean-field description for the electronic structure. The comparison of these QPI results with the experimentally measured FT-STS yields information about the failure of the mean-field approach and thus the effect of interactions in the system. Perhaps the most common application of FT-STS to date has been in systems displaying unconventional superconductivity, in particular the cuprate and pnictide high-T_c superconductors [78, 79, 55, 214, 215, 156]. Here the superconducting pairing is driven by electronic interactions, rather than the conventional phonon-mediated mechanism. These unusual pairing mechanisms give rise to characteristic features, for example an anisotropic superconducting order parameter, which may be probed via FT-STS. Sr_2RuO_4, studied in Chapter 5 is one such unconventional superconductor, for which the QPI offers great potential insight.

As well as the interactions between conduction electrons in the host, the QPI is strongly influenced by the nature of the scattering from defects and impurities [48]. In the case of impurities with internal degrees of freedom, for example *magnetic* impurities [74], local interactions on the impurity site have a profound effect on the scattering of (free) host conduction electrons and thus the QPI, via the magnitude and phase of the scattering t-matrix. Systems of magnetic impurities, represented by quantum impurity problems, are often amenable to exact treatment, for example via numerical renormalization group calculations [211, 29]. The QPI due to a single magnetic impurity is the focus of Chapter 3, in which we demonstrate that characteristic signatures of

electronic interactions arise in the QPI. In the case of multiple magnetic impurities, considered in Chapter 4, additional scattering channels arise due to inter-impurity correlations, in addition to the increased complexity due to the interference between scattering from spatially distributed impurities.

2.4 Conclusion

In this chapter we have introduced the QPI, which arises due to scattering of electronic surface states of a (bulk) host material from defects and impurities. The interference of incoming and outgoing electron waves results in modulations in the (electronic) LDOS of the surface around these scattering centres, the spatial distribution of which is measurable via STS as the conductance between STM tip and sample surface. The QPI, related closely to the Fourier transform of these spatial LDOS modulations, is therefore a two-particle quantity which reflects both the nature of the electronic states of the host material and the type and distribution of defects or scattering centres in the material. The conventional approach has been to interpret FT-STS measurements of the QPI in terms of overly simplistic models, employing arguments based on Fermi's golden rule to assign QPI features to specific, individual scattering processes, and thus provide information on the electronic structure of the host material. We have carefully examined the validity of such simple approaches, and sought to develop a more rigorous framework within which the QPI (and FT-STS measurements) may be understood, illustrating our approach for the simple case study of the 2D electron gas.

We have shown that the QPI necessarily involves the interference of many scattering processes, rather than a single, characteristic event, and that the relative phase of these contributions is crucial in the resulting QPI. Moreover, the nature of the scattering centre(s), entering via the scattering t-matrix, was also shown to be of great importance in the qualitative appearance of features in the QPI. In experiment it is very challenging to control the distribution and type of defects or impurities in a sample; as a result, detailed knowledge of the scattering t-matrix is often unavailable. A distribution of impurities in real space results in interference between scattering contributions to the QPI, and is typically of little general value (in the case of random distribution). As a result, the absolute value of the QPI (the power spectrum of surface LDOS modulations) is the meaningful experimental quantity of interest with phase information lost in the resultant FT-STS measurements.

We have provided a basic physical understanding of the QPI as far as possible, and examined the effect of several additional complicating factors that are experimentally

and theoretically relevant, and will be explored more fully in the following chapters of this thesis.

Chapter 3

Quasiparticle interference from magnetic impurities

In Chapter 2 we presented scanning tunnelling spectroscopy (STS) as a direct experimental probe of the local density of electronic states (LDOS) at a particular scanning energy and temperature, related to the differential conductance between STM tip and surface [192, 52]. Moreover, the atomic sharpness of the STM tip allows the LDOS in the vicinity of features such as adsorbed impurities to be mapped in real space [128, 129] by rastering the tip across the surface, as represented schematically in Figure 3.1. Such impurities break translational symmetry at the surface, causing scattering of conduction electrons and modulations in the LDOS that depend strongly on both the electronic structure of the underlying sample "host" and the properties and distribution of impurities.

Fourier transform STS (FT-STS) – in which such LDOS modulations are analyzed in momentum space – thus provides a wealth of information on the nature of the impurity-host and (host-mediated) inter-impurity correlations. We have shown that these FT-STS measurements may be interpreted in terms of the quasiparticle interference (QPI) between the states of the "clean" host (defined in the absence of impurities) [204, 34, 131], a complex response function characterizing both the host and scattering centres (impurities). In this chapter we investigate the QPI due to individual magnetic impurities [14, 74] adsorbed on a range of representative non-magnetic host surfaces, contrasting with the case of a simple scalar impurity or point defect. We demonstrate how the electronic correlations present for magnetic impurities markedly affect the QPI, showing, for example, a large intensity enhancement due to the conventional Kondo effect [74] for a metallic host, and universality at low temperatures and scanning energies.

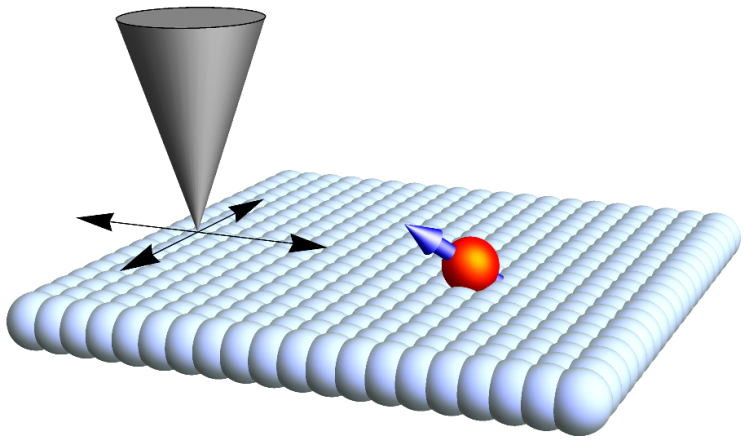

Fig. 3.1 Schematic FT-STS setup: a spatial map of surface LDOS modulations due to electronic scattering from magnetic adatom impurities is extracted from differential conductance measurements as an STM tip is rastered over the surface.

In Chapter 2 we carried out a careful analysis of the relationship between the joint density of states (JDOS), commonly used to interpret FT-STS measurements [135, 184], and the full QPI. We demonstrated that the JDOS approach was insufficient to capture interference effects observed in FT-STS fully, even in the simplest cases. In the magnetic impurity case this failure is profound, as we demonstrate in this chapter; the complex, dynamical nature of the scattering from magnetic impurities, arising due to the effects of electronic correlations on the impurity site, must be fully accounted for in order to accurately calculate the QPI [48]. In this chapter we calculate exactly the QPI due to magnetic adatoms on metallic surfaces, drawing comparison with the case of non-magnetic, "scalar" impurities (s-wave potential scatterers in the weak-scattering Born limit [34]). We examine the qualitative failure of the JDOS approach to capture the dynamic and thermal variation of the QPI in particular, and also investigate qualitatively a number of relevant experimental factors affecting the interpretation of FT-STS measurements in terms of the "true" QPI, calculated theoretically.

Systems of magnetic atoms embedded on non-magnetic surfaces provide realizations of quantum impurity models [74] which are amenable to detailed experimental study and manipulation with STM techniques [118, 191, 128, 129, 130]. Such systems are promising candidates as a basis for nanoscale computational, memory storage and spintronic devices [73, 98], for which the manipulation and control of spin degrees of freedom, and therefore an understanding of the effect resulting from coupling these local correlated degrees of freedom to free bulk states, is essential. They are also

of fundamental interest in their own right, due to the subtle interplay of strongly correlated local spin and orbital degrees of freedom coupled to a conduction electron bath.

Magnetic impurities can be spectroscopically probed *directly* when the STM tip is positioned over an impurity. A narrow resonance in the tunnelling conductance is commonly observed around the Fermi energy in these local STS measurements [118, 191, 128, 129], arising from the formation of a many-body Kondo singlet state (a "Kondo resonance") where the impurity local moment is screened dynamically by surrounding host conduction electrons. For STS studies of Co adatoms on noble metal surfaces, typical Kondo temperatures of $T_{\rm K} \sim 50 - 100$K are extracted from the half-width at half-maximum of the spectral Kondo resonance [202]. The single-orbital Anderson impurity model [14] has been successfully used to rationalize such local STS measurements [176, 195, 223]. It is adopted here as a qualitatively accurate description of a generic, low-spin magnetic adatom, and treated using the numerical renormalization group (NRG) [29]. In other cases, for example high-spin Mn or Fe adatoms, generalized impurity models must be employed to capture the full orbital structure of the adatom and the host material [39, 69, 80]. These calculations are quite specific to the particular system under consideration [61], with the qualitative outcome depending sensitively on the detailed form of the multi-orbital impurity model and the coupling to the host. As a consequence it is difficult to draw general insight from specific calculations on these systems, and thus we adopt a single-orbital impurity model for magnetic impurities throughout.

We discuss the general formulation of QPI due to any number or type of impurities embedded on the surface of tight-binding hosts in Section 3.2, highlighting the differences between the 3D cubic lattice with a (100) surface, the 2D square lattice, and the 2D honeycomb lattice. These simple but representative hosts reproduce a range of possible material realizations: the LDOS for each features distinct behaviour close to the Fermi level, with flat, divergent and vanishing LDOS for the three lattices respectively. Each host lattice gives rise to qualitatively different impurity physics, with, for example, the single-impurity Kondo temperature significantly enhanced (suppressed) by increased (depleted) density of states around the Fermi level [65, 143, 144, 139, 31].

The QPI due to single magnetic and scalar impurities for each host is considered in Section 3.3, drawing attention to the qualitative differences in QPI arising from the different types of scattering centre and host. The rich *dynamical* properties of the QPI are studied in detail for systems containing a magnetic impurity in Section 3.4; we emphasize that this strong energy-dependence cannot be reproduced in systems con-

taining only scalar impurities or structural defects. Indeed, strong electron correlations are shown to produce characteristic signatures in QPI: in metallic systems, the QPI exhibits universality in terms of rescaled scanning energy and temperature due to the Kondo effect, while non-trivial local moment physics is observed in the 2D honeycomb case [65, 56, 30, 143, 122].

Section 3.5 examines the interpretation of experimentally-measurable FT-STS. By simulating the experimental protocol, we investigate the possible deviation of FT-STS measurements from calculated QPI due to the finite size of the LDOS plaquette measurements in real-space. While the LDOS and thus QPI is calculated on the lattice of the underlying host, STS measurements of LDOS are made in real (continuous) space – we also explore, therefore, the effect of different choices of Wannier basis, as discussed in Section 2.3.2. We conclude the chapter by critically examining the relationship between the JDOS and the QPI for the case of a magnetic impurity, in the spirit of Section 2.2, demonstrating the failure of the JDOS to capture important features in the QPI (and hence FT-STS measurements).

3.1 Host systems & impurity problem

3.1.1 Model

We consider a host material with impurities deposited on the surface, which scatter the quasiparticles of the clean host. Initially we consider the general problem of N magnetic surface adatoms, formulating the QPI generally for any type, number and distribution of adatoms.

The clean host is taken to be non-interacting and of tight-binding form, given in its real-space basis by

$$\mathcal{H}_{\text{host}} = \epsilon_0 \sum_{i,\sigma} c^\dagger_{\mathbf{r}_i\sigma} c_{\mathbf{r}_i\sigma} - t \sum_{\langle ij\rangle,\sigma} (c^\dagger_{\mathbf{r}_i\sigma} c_{\mathbf{r}_j\sigma} + \text{H.c.}) \,, \tag{3.1}$$

where $c^\dagger_{\mathbf{r}_i\sigma}$ creates an electron of spin $\sigma = \uparrow/\downarrow$ in the Wannier orbital localized at site $\mathbf{r}_i$; and $\langle ij\rangle$ denotes a sum over nearest-neighbor sites, coupled by a tunnel matrix element t. Here we consider the half-filled host, $\epsilon_0 = 0$.

Specifically, we focus on the simple 2D square lattice, the 3D cubic lattice with a (100) surface, and the 2D honeycomb lattice. The 3D cubic lattice in particular is representative of a wide class of regular metallic systems, with a constant (finite) electronic density of states at low energies. By contrast, the 2D square lattice features

a van Hove singularity with a logarithmically diverging density of states around the Fermi level [144, 124]. The honeycomb lattice, describing graphene within the simplest non-interacting tight-binding approximation, is notable because it is a bipartite lattice with a vanishing (pseudogapped) density of states at low energies [37, 56]. Although simplified, these host systems exemplify a number of distinctive features relevant to real materials, and each induces qualitatively different impurity physics (Section 3.3).

The full model, including N impurities, is given by

$$\mathcal{H} = \mathcal{H}_{\text{host}} + \sum_{\alpha=1}^{N} \mathcal{H}_{\text{imp},\alpha} \ . \tag{3.2}$$

In the simplest case, the local potential at site $\mathbf{r}_\alpha$ is modified by impurity α, breaking translational invariance and causing additional electronic scattering. These static defects, referred to as potential scattering (or scalar) impurities, are described by

$$\mathcal{H}^{\text{ps}}_{\text{imp},\alpha} = v_0 \sum_{\sigma} c^\dagger_{\mathbf{r}_\alpha\sigma} c_{\mathbf{r}_\alpha\sigma} \ . \tag{3.3}$$

This simple model, while often appropriate to describe point defects in materials, does not faithfully capture the physics of many adsorbed impurity adatoms — in particular magnetic impurities, which are *dynamic* objects with internal degrees of freedom and strong local Coulomb interactions. In this chapter we focus primarily on these adsorbed *magnetic* impurities [74], described in terms of correlated quantum levels,

$$\begin{aligned} \mathcal{H}^{\text{AIM}}_{\text{imp},\alpha} = \sum_{\sigma} \epsilon_d d^\dagger_{\alpha\sigma} d_{\alpha\sigma} + U d^\dagger_{\alpha\uparrow} d_{\alpha\uparrow} d^\dagger_{\alpha\downarrow} d_{\alpha\downarrow} \\ + V \sum_{\sigma} \left(d^\dagger_{\alpha\sigma} c_{\mathbf{r}_\alpha\sigma} + \text{H.c.} \right) \ , \end{aligned} \tag{3.4}$$

where $d^\dagger_{\alpha\sigma}$ creates a spin-σ electron on impurity α, which is coupled to host site $\mathbf{r}_\alpha$ by tunnelling matrix element V. For simplicity we consider explicitly the particle-hole symmetric case $\epsilon_d = -U/2$. Before continuing, we emphasize that true magnetic impurities preserve SU(2) spin symmetry and time-reversal symmetry. The term "magnetic impurity" is commonly used in the QPI literature for a static local moment [78, 204, 7], corresponding to a single site with a local magnetic field (and thus non-zero magnetization). Such an impurity breaks spin and time-reversal symmetry, and is completely distinct from the quantum impurity models considered in this thesis.

3.1.2 Impurity dynamics

Single-particle dynamics of correlated impurities embedded in a non-interacting host are described generically by the Green function matrix $[\mathbf{G}_d(z=\omega+\mathrm{i}0^+)]_{\alpha,\beta} \equiv G_d^{\alpha\beta}(\omega) = \langle\langle d_{\alpha\sigma}; d^\dagger_{\beta\sigma}\rangle\rangle_\omega$, with $\langle\langle \hat{A}; \hat{B}\rangle\rangle_\omega = \mathcal{F}_t[-\mathrm{i}\theta(t)\langle\{\hat{A}(t), \hat{B}(0)\}\rangle]$ the Fourier transform of the retarded correlator; $\omega = \omega + \mathrm{i}0^+$ is implicit in all appropriate quantities henceforth, unless otherwise noted. The matrix Dyson equation for the impurity Green functions is

$$[\mathbf{G}_d(\omega)]^{-1} = [\mathbf{g}_d(\omega)]^{-1} - \mathbf{\Sigma}(\omega) \ . \tag{3.5}$$

The non-interacting (but host-coupled) impurity propagators are given by

$$[\mathbf{g}_d(\omega)]^{-1} = (\omega + \mathrm{i}0^+ - \epsilon_d)\mathbf{I} - \mathbf{\Gamma}(\omega) \ , \tag{3.6}$$

in terms of the hybridization matrix $\mathbf{\Gamma}(\omega)$ with elements $[\mathbf{\Gamma}(\omega)]_{\alpha,\beta} = V^2 G^0(\mathbf{r}_\alpha, \mathbf{r}_\beta, \omega)$; where $G^0(\mathbf{r}_\alpha, \mathbf{r}_\beta, \omega) = \langle\langle c_{\mathbf{r}_\alpha\sigma}; c^\dagger_{\mathbf{r}_\beta\sigma}\rangle\rangle^0_\omega$ is the (retarded) propagator between sites $\mathbf{r}_\alpha$ and $\mathbf{r}_\beta$ of the clean host (in the absence of impurities), and $\mathbf{r}_\alpha$ and $\mathbf{r}_\beta$ are the host sites to which impurities α and β are coupled. The self-energy matrix $\mathbf{\Sigma}(\omega)$ contains all the nontrivial information due to electronic interactions, which give rise to many-body effects such as the Kondo effect and RKKY interaction, investigated later in this chapter and in Chapter 4.

In this chapter we employ NRG to solve the underlying quantum impurity problem [29, 211, 108, 109]. In the spirit of Ref. 28, equations of motion can be used to obtain an expression for the self-energy matrix,

$$\mathbf{\Sigma}(\omega) = [\mathbf{G}_d(\omega)]^{-1}\mathbf{F}_d(\omega) \ , \tag{3.7}$$

where $[\mathbf{F}_d(\omega)]_{\alpha,\beta} = U\langle\langle d_{\alpha\sigma}; d^\dagger_{\beta\sigma} d^\dagger_{\beta\bar{\sigma}} d_{\beta\bar{\sigma}}\rangle\rangle_\omega$. Both $\mathbf{G}_d(\omega)$ and $\mathbf{F}_d(\omega)$ are calculated directly in NRG using the full density matrix approach [210, 159] within the complete Anders-Schiller basis [12].

In the case of a single impurity, the Dyson equation, Eq. 3.5, reduces to $G_d^{11}(\omega) = (\omega + \mathrm{i}0^+ - \epsilon_d - \Gamma(\omega) - \Sigma_{11}(\omega))^{-1}$, with the hybridization $\Gamma(\omega) = V^2 G^0(\mathbf{r}_1, \mathbf{r}_1, \omega)$ related simply to the clean host LDOS (itself independent of position due to translational invariance). In NRG a discretized version of the conduction electron Hamiltonian is formulated, and mapped onto a semi-infinite 1D chain with the impurity located at one end [29]. Discretizing the energy scale logarithmically leads to the "Wilson chain" representation in which hopping matrix elements decrease exponentially down the chain [211, 29]. The renormalization group (RG) scheme involves iterative diagonalization,

starting at the impurity and working down the Wilson chain, discarding high-energy states at each step [29].

3.1.3 Host dynamics

The full dynamics of the host, in the presence of impurities, is embodied in the lattice Green functions $G(\mathbf{r}_i, \mathbf{r}_j, \omega)$ connecting arbitrary host sites $\mathbf{r}_i$ and $\mathbf{r}_j$. They can be related exactly to the above impurity Green functions by equations of motion [224]:

$$G(\mathbf{r}_i, \mathbf{r}_j, \omega) - G^0(\mathbf{r}_i, \mathbf{r}_j, \omega) = \sum_{\alpha,\beta} G^0(\mathbf{r}_i, \mathbf{r}_\alpha, \omega) T_{\alpha\beta}(\omega) G^0(\mathbf{r}_\beta, \mathbf{r}_j, \omega) \ , \tag{3.8}$$

where the sum runs over impurities α and β, and $T_{\alpha\beta}(\omega)$ is the real-space t-matrix and G^0 denotes the Green function for the clean system, in the absence of impurities (with ^{0} used analogously for other quantities). For magnetic impurities described by $\mathcal{H}_{\text{imp}}^{\text{AIM}}$ in Eq. 3.4, the t-matrix takes the form

$$T_{\alpha\beta}^{\text{mag}}(\omega) = V^2 G_d^{\alpha\beta}(\omega) \ , \tag{3.9}$$

requiring as such a knowledge of the full impurity Green functions from Eq. 3.5. By contrast, the t-matrix for potential scattering impurities, described by $\mathcal{H}_{\text{imp}}^{\text{ps}}$ in Eq. 3.3, can be obtained simply in closed form,

$$T_{\alpha\beta}^{\text{ps}}(\omega) = v[\mathbf{I} - v\mathbf{G}^0(\omega)]_{\alpha\beta}^{-1} \ , \tag{3.10}$$

where the elements $[\mathbf{G}^0(\omega)]_{\alpha\beta} \equiv G^0(\mathbf{r}_\alpha, \mathbf{r}_\beta, \omega)$ are clean host Green functions connecting pairs of impurity sites.

For the clean host, Eq. 3.1 can also be written as

$$\mathcal{H}_{\text{host}} = \sum_{\mathbf{k},\sigma} \epsilon_{\mathbf{k}} c_{\mathbf{k}\sigma}^\dagger c_{\mathbf{k}\sigma} \tag{3.11}$$

with $\epsilon_{\mathbf{k}}$ the dispersion ($\mathbf{k}$ labels the Bloch state momentum). The t-matrix equation (Eq. 3.8) can also be transformed into the momentum-space basis,

$$\Delta G(\mathbf{k}, \mathbf{k}', \omega) = G^0(\mathbf{k}, \omega) T(\mathbf{k}, \mathbf{k}', \omega) G^0(\mathbf{k}', \omega) \ , \tag{3.12}$$

where $\Delta G(\mathbf{k},\mathbf{k}',\omega) = G(\mathbf{k},\mathbf{k}',\omega) - G^0(\mathbf{k},\omega)\delta_{\mathbf{k},\mathbf{k}'}$ and $G^0(\mathbf{k},\omega) = (\omega + \mathrm{i}0^+ - \epsilon_{\mathbf{k}})^{-1}$. All quasiparticle scattering induced by the impurities is now contained in

$$T(\mathbf{k},\mathbf{k}',\omega) = \frac{1}{\Omega_{BZ}} \sum_{\alpha,\beta} \mathrm{e}^{\mathrm{i}(\mathbf{k}'\cdot\mathbf{r}_\beta - \mathbf{k}\cdot\mathbf{r}_\alpha)} \times T_{\alpha\beta}(\omega) \ , \tag{3.13}$$

where Ω_{BZ} is the volume of the first Brillouin zone (1BZ).

3.2 QPI

As discussed in Chapter 2, the differential conductance $dI(\mathbf{r},V)/dV$ between STM tip and surface for a particular bias V is proportional to the LDOS, $\rho(\mathbf{r},\omega = \mathrm{e}V)$, of the sample at (surface) position $\mathbf{r}$ at sufficiently low temperature and bias [192, 52]. STS thus measures the energy-resolved electronic structure of the sample at a particular point in real space.

The QPI is the Fourier transform of a real-space *surface* LDOS map $\rho(\mathbf{r}_i,\omega)$, obtained at given scanning energy ω, and measured by STS over an $L \times L$ sample region

$$\rho(\mathbf{q},\omega) = \sum_{i\in(L\times L)} \mathrm{e}^{-\mathrm{i}\mathbf{q}\cdot\mathbf{r}_i} \rho(\mathbf{r}_i,\omega) \ . \tag{3.14}$$

In 2D systems such as graphene, or effective 2D layered systems such as the cuprates, STS thus probes directly and in full the desired electronic structure of the underlying host. In 3D systems, by contrast, the lattice probed by STS corresponds to the crystallographic surface lattice, and the density of states measured that of the surface atomic layer; the STS measurement is thus the projection at the surface of bulk electronic structure and spatial modulations in the LDOS due to impurities. This effect is addressed in Section 3.2.2.

As discussed in Chapter 2, the FT-STS technique has primarily been employed to investigate the electronic structure of materials, mapping Fermi surfaces and the dispersion of constant energy contours with scanning energy [160, 161, 184]. This provides complementary information to angularly-resolved photoemission spectroscopy (ARPES) [131, 135, 199], with the advantages of being able to probe both conduction *and* valence states, and offering enhanced energetic and momentum resolution. FT-STS has proven of particular value in the study of layered materials such as cuprates and pnictides [78, 79, 55, 214, 215, 156] as well as topological insulators [168, 219], graphene [27, 220] and heavy-fermion materials [193, 217]. However, much of the analysis

of experimental evidence relies on crude, phenomenological models for the QPI. In Chapter 2 we demonstrated the potential pitfalls of overly simplistic interpretation of FT-STS measurements in these terms, showing that such models have limited predictive power, even for qualitative features in the QPI. In some cases (for example weak, disorder-induced scattering in cuprates [78]), the local defects giving rise to scattering and hence the QPI may be reasonably approximated as scalar impurities in the Born limit [34]. However, this simplification has been shown to be insufficient or misleading in many cases (particularly for systems involving multiple bands), even for scalar impurities [193, 217]; for magnetic adatoms, the full interacting impurity model must be considered.

A strong signal is observed in experiment at $\mathbf{q} = \mathbf{0}$, and is also expected at $\mathbf{q} = \sum_i n_i \mathbf{A}_i$ where $\mathbf{A}_i$ are the reciprocal lattice vectors of the surface lattice (and n_i any integer). This signal is extensive in the plaquette size L^2, with contributions from the LDOS of the clean host sampled at each site, corresponding to trivial Bragg scattering. This simply provides an underlying background signal to the two-particle interference processes of interest; in Chapter 2 we demonstrated that enhanced scattering at Bragg momenta, present in the JDOS, is not seen in the QPI due to the interference of scattering paths. The QPI, the impurity contribution to the measured FT-STS, is then obtained by subtracting the result for the clean system without impurities,

$$\Delta\rho(\mathbf{q},\omega) = \sum_{i\in(L\times L)} \mathrm{e}^{-\mathrm{i}\mathbf{q}\cdot\mathbf{r}_i}\Delta\rho(\mathbf{r}_i,\omega) \tag{3.15}$$

where $\Delta\rho = \rho - \rho^0$ (with ρ^0 for the clean host). Since $\rho^0(\mathbf{q},\omega) \propto \delta_{\mathbf{q},\mathbf{0}}$, $\Delta\rho(\mathbf{q},\omega)$ scales with the number of impurities. The normalized QPI power spectrum, $|\Delta\rho(\mathbf{q},\omega)/N|^2 \propto |\Delta\rho(\mathbf{q},\omega)/L^2|^2$, is intensive, independent of the number of impurities or sample region size (for a given impurity number density).

We now give a general formulation for calculating the QPI due to scattering from single or multiple impurities, applying equally to the case of (static) potential scattering defects or magnetic (dynamic, interacting) impurities.

3.2.1 Real-space formulation

Following the experimental protocol, the QPI can be calculated by discrete Fourier transform of the LDOS within an $L \times L$ region of the host surface, using Eq. 3.15. The LDOS at site $\mathbf{r}_i$ in the presence of impurities is related to the local host Green

function, $\rho(\mathbf{r}_i,\omega) = -\pi^{-1}\text{Im}\ G(\mathbf{r}_i,\mathbf{r}_i,\omega)$, such that from Eq. 3.8,

$$\Delta\rho(\mathbf{r}_i,\omega) = -\pi^{-1}\text{Im}\ \sum_{\alpha,\beta} G^0(\mathbf{r}_i,\mathbf{r}_\alpha,\omega)T_{\alpha\beta}(\omega)G^0(\mathbf{r}_\beta,\mathbf{r}_i,\omega) \tag{3.16}$$

in terms of the full scattering t-matrix and non-local host Green functions of the clean host. The virtue of Eq. 3.16 is that it is entirely general, and can in principle be used for any lattice with any number or type of impurities. Although the LDOS is sampled over a finite region in experiment, the host system is of course in the thermodynamic limit.

The accurate calculation of lattice Green functions $G^0(\mathbf{r}_i,\mathbf{r}_j,\omega)$ is itself a subtle and well-studied problem [198, 97, 67, 43]. Exact diagonalization of finite-sized lattices or discrete Fourier transforms can yield poor approximations to Green functions of the desired (semi-)infinite systems, especially in the vicinity of van Hove singularities [18]. The single-site tight binding models considered here admit exact solutions for local and near non-local lattice Green functions for periodic boundary conditions in the thermodynamic limit, from which recursive relations can be used, in principle, to generate all non-local functions [97, 147, 146]. However, these techniques are numerically unstable for large site separations $|\mathbf{r}_i - \mathbf{r}_j|$ as shown in detail in Ref. 18, and the treatment of semi-infinite systems, such as the 3D cubic (100) surface, is not possible. The "Recursion Method" [162] provides a general and powerful methodology for calculating lattice Green functions via continued fraction expansions of the resolvent matrix (inverse Green function) [71, 72, 51], but converged solutions can be computationally demanding, particularly in the region of singularities and for non-local lattice Green functions [18, 19]. Specific methodologies have also been developed to treat semi-infinite systems, for example based on iterative calculation of transfer matrices [172] and via "Bond cutting" methods, treating the surface as a perturbation on the infinite bulk structure [164]. However, no method provides a robust, numerically inexpensive way to calculate far non-local lattice Green functions (between lattice points separated by tens or hundreds of sites) as a full function of frequency. Consequently, calculation of all $N \times L^2$ non-local Green functions required in order to directly calculate the LDOS modulations for a system of N impurities in an $L \times L$ region via Eq. 3.16, and thus simulate the experimental procedure, is a major challenge.

In Appendix A we develop instead a novel technique for fast and accurate numerical calculation of free Green functions on hypercubic-type lattices, which we employ in Section 3.5.1 to simulate the FT-STS procedure. The method involves successive convolutions of simpler 1D Green functions which are known exactly in closed form;

moreover, the convolution itself can be performed efficiently using fast Fourier transform, as detailed in Appendix A.

3.2.2 Scattering state formulation

The "true" QPI containing all scattering information is obtained by taking the thermodynamic limit of plaquette size, $L \to \infty$. Translational symmetry implies a basis of states with well defined momentum parallel to the surface over the first *surface* Brillouin zone (1SBZ). The local Green function for a surface lattice site is expressed in terms of this basis by 2D Fourier transformation,

$$G(\mathbf{r}_i, \mathbf{r}_i, \omega) = \iint_{1\text{SBZ}} \frac{d^2\mathbf{k}_\parallel d^2\mathbf{k}'_\parallel}{\Omega_{BZ}} \, \mathrm{e}^{-\mathrm{i}\mathbf{r}_i\cdot(\mathbf{k}'_\parallel - \mathbf{k}_\parallel)} \times G(\mathbf{k}_\parallel, \mathbf{k}'_\parallel, \omega) \; , \tag{3.17}$$

with Ω_{BZ} now the volume of the 1SBZ. Writing $\Delta\rho(\mathbf{r}_i, \omega) = -\pi^{-1}\mathrm{Im}\ \Delta G(\mathbf{r}_i, \mathbf{r}_i, \omega)$, Eq. 3.15 takes the form,

$$\Delta\rho(\mathbf{q}, \omega) = -\pi^{-1} \sum_i \mathrm{e}^{-\mathrm{i}\mathbf{q}\cdot\mathbf{r}_i} \mathrm{Im} \iint_{1\text{SBZ}} \frac{d^2\mathbf{k}_\parallel d^2\mathbf{k}'_\parallel}{\Omega_{BZ}} \, \mathrm{e}^{-\mathrm{i}\mathbf{r}_i\cdot(\mathbf{k}'_\parallel - \mathbf{k}_\parallel)} \Delta G(\mathbf{k}_\parallel, \mathbf{k}'_\parallel, \omega) \; , \tag{3.18}$$

where $\Delta G(\mathbf{k}_\parallel, \mathbf{k}'_\parallel, \omega) = G(\mathbf{k}_\parallel, \mathbf{k}'_\parallel, \omega) - G^0(\mathbf{k}_\parallel, \mathbf{k}'_\parallel, \omega)$. Permuting the Fourier sum and taking the imaginary part in Eq. 3.18,

$$\Delta\rho(\mathbf{q}, \omega) = -\frac{1}{2\pi\mathrm{i}} \left[Q(\mathbf{q}, \omega) - Q(-\mathbf{q}, \omega)^* \right] \; , \tag{3.19}$$

where

$$Q(\mathbf{q}, \omega) = \int_{1\text{SBZ}} d^2\mathbf{k}_\parallel \; \Delta G(\mathbf{k}_\parallel, \mathbf{k}_\parallel + \mathbf{q}, \omega) \tag{3.20a}$$

$$\equiv \sum_{\alpha,\beta} T_{\alpha\beta}(\omega) \times \Lambda_{\alpha\beta}(\mathbf{q}, \omega) \; . \tag{3.20b}$$

As highlighted by Eq. 3.20b, the QPI factorizes into a momentum-independent scattering amplitude $T_{\alpha\beta}(\omega)$ (Eqs. 3.9 or 3.10), and a host response function $\Lambda_{\alpha\beta}(\mathbf{q}, \omega)$ which depends only on the host lattice and the spatial location of impurities, but not the type of impurity (and thus details of the scattering). The explicit form of this host function must be determined separately for each lattice, as considered below.

2D square lattice

We consider first the 2D square lattice, where the QPI calculation is conceptually simplest. As the system is itself two-dimensional, the surface-momentum basis is simply the diagonal representation, $\mathbf{k} = \mathbf{k}_\parallel$. The QPI thus follows from Eqs. 3.20a, 3.12 and 3.13, and is indeed of form Eq. 3.20b with

$$\Lambda_{\alpha\beta}(\mathbf{q},\omega) = \int_{1\mathrm{SBZ}} \frac{d^2\mathbf{k}}{\Omega_{BZ}}\, G^0(\mathbf{k},\omega)G^0(\mathbf{k}+\mathbf{q},\omega)\mathrm{e}^{\mathrm{i}[\mathbf{k}\cdot\mathbf{r}_\alpha - (\mathbf{k}+\mathbf{q})\cdot\mathbf{r}_\beta]} \; . \tag{3.21}$$

The free momentum-space Green functions are themselves given by $G^0(\mathbf{k},\omega) = (\omega + \mathrm{i}0^+ - \epsilon_\mathbf{k})^{-1}$, with 2D square lattice dispersion (and lattice constant a_0)

$$\epsilon_\mathbf{k} = -2t\left(\cos(\mathrm{a}_0\mathrm{k}_x) + \cos(\mathrm{a}_0\mathrm{k}_y)\right) \; ; \tag{3.22}$$

in terms of the lattice hopping matrix element t appearing in Eq. 3.1, giving a half-bandwidth of $4t$. For numerical calculations, poles in $G^0(\mathbf{k},\omega)$ are broadened using complex frequency, $\omega + \mathrm{i}0^+ \to \omega + \mathrm{i}\eta$ with finite η, as is conventional. For the QPI colour plots, we use $\eta/t = 10^{-3}$, while for Brillouin zone cuts we use $\eta/t = 10^{-4}$ for improved accuracy near divergences.

$\Lambda_{\alpha\beta}(\mathbf{q},\omega)$ can be computed efficiently by using the convolution theorem to do the Brillouin zone integration:

$$\mathcal{F}_\mathbf{k}[\Lambda_{\alpha\beta}(\mathbf{q},\omega)] = \mathcal{F}_\mathbf{k}[G^0(\mathbf{k},\omega)\mathrm{e}^{\mathrm{i}\mathbf{k}\cdot\mathbf{r}_\alpha}] \times \mathcal{F}_\mathbf{k}[G^0(\mathbf{k},\omega)\mathrm{e}^{-\mathrm{i}\mathbf{k}\cdot\mathbf{r}_\beta}]$$

where $\mathcal{F}_\mathbf{k}$ denotes the 2D fast Fourier transform.

3D cubic lattice with (100) surface

3D host lattices are more subtle, due to the surface-sensitive nature of the STM measurement. As only the surface LDOS is probed, the QPI amounts to a partial trace over the t-matrix equation Eq. 3.12, in contrast to the full trace for the 2D square lattice, given by Eq. 3.21. The QPI must thus be evaluated in a basis that preserves the layer index, the surface momentum basis of Eq. 3.17, rather than the (fully) diagonal basis of Eq. 3.12. $\Delta G(\mathbf{k}_\parallel, \mathbf{k}_\parallel + \mathbf{q}, \omega)$ in Eq. 3.20 thus involves propagators between states with surface momentum $\mathbf{k}_\parallel$ and $\mathbf{k}_\parallel + \mathbf{q}$. The 2D transform of $G(\mathbf{r}_i, \mathbf{r}_i, \omega)$, Eq. 3.17, leads to a diagonal representation in each 2D plane in isolation – but surface states labelled by $\mathbf{k}_\parallel$ remain coupled to the bulk (and thus to each other). In general, $\Delta G(\mathbf{k}_\parallel, \mathbf{k}_\parallel + \mathbf{q}, \omega)$

does not therefore take the form of Eq. 3.12, but rather

$$\Delta G(\mathbf{k}_\parallel, \mathbf{k}'_\parallel, \omega) = \iint_{1\text{SBZ}} \frac{d^2\mathbf{k}''_\parallel d^2\mathbf{k}'''_\parallel}{\Omega_{BZ}} \, \tilde{G}^0(\mathbf{k}_\parallel, \mathbf{k}''_\parallel, \omega) T(\mathbf{k}''_\parallel, \mathbf{k}'''_\parallel, \omega) \tilde{G}^0(\mathbf{k}'''_\parallel, \mathbf{k}'_\parallel, \omega) \ , \tag{3.23}$$

where $\tilde{G}^0(\mathbf{k}_\parallel, \mathbf{k}''_\parallel, \omega)$ is a complex through-bulk propagator. Calculation of the QPI thus in general requires the full integrals over intermediate scattering pathways. Alternatively, Eq. 3.23 may be formulated in terms of a semi-infinite system of principal layers, each of which consists of one or more atomic layers of the lattice, and thus potentially a multi-site unit cell for the principal layer. Translational invariance parallel to the surface guarantees that the in-plane momentum $\mathbf{k}_\parallel$ is well-defined in the diagonal basis of this principal layer description, but the surface LDOS measured via STS will amount to a partial trace over only the topmost atomic layer within the surface principal layer – an equivalent problem to the intermediate scattering pathways of Eq. 3.23.

In the case of hypercubic-type lattices, a significant simplification arises because the surface principal layer consists only of a single layer of the cleaved lattice, and thus the basis of $\mathbf{k}_\parallel$-states of the surface atomic layer is in fact diagonal. As such a surface momentum t-matrix equation with the same structure as Eq. 3.12 still applies, albeit with modified host surface Green functions. The result for the 3D cubic lattice (100) surface is simply,

$$\Delta G(\mathbf{k}_\parallel, \mathbf{k}'_\parallel, \omega) = G^0_{\text{surf}}(\mathbf{k}_\parallel, \omega) T(\mathbf{k}_\parallel, \mathbf{k}'_\parallel, \omega) G^0_{\text{surf}}(\mathbf{k}'_\parallel, \omega) \ , \tag{3.24}$$

where the t-matrix is still given by Eq. 3.13, but

$$G^0_{\text{surf}}(\mathbf{k}_\parallel, \omega) = f\left(\frac{\omega - \epsilon_{\mathbf{k}_\parallel}}{2t}\right) \quad \text{where} \quad tf(\tilde{\omega}) = \tilde{\omega} - \begin{cases} \text{sgn}(\tilde{\omega})\sqrt{\tilde{\omega}^2 - 1} & |\tilde{\omega}| > 1 \\ \text{i}\sqrt{1 - \tilde{\omega}^2} & |\tilde{\omega}| \leq 1 \end{cases} , \tag{3.25}$$

with $\epsilon_{\mathbf{k}_\parallel}$ the 2D square lattice dispersion, Eq. 3.22. This broadens the pole in $G^0(\mathbf{k}, \omega)$ arising for the pure 2D system, to an ellipse of width $2t$ centred on $\omega = \epsilon_{\mathbf{k}_\parallel}$ in $G^0_{\text{surf}}(\mathbf{k}_\parallel, \omega)$ for the 3D system; the effect of coupling to the bulk is to dephase the surface quasiparticles, giving them a finite lifetime. It follows that the structure of the host function $\Lambda_{\alpha\beta}(\mathbf{q}, \omega)$ is the same as in the 2D square case, Eq. 3.21, with $G^0_{\text{surf}}(\mathbf{k}_\parallel, \omega)$ in place of $G^0(\mathbf{k}, \omega)$. In Section 3.3 we calculate the true 3D cubic QPI via Eqs. 3.19, 3.20 and 3.21, using the exact expression for the bulk-coupled surface Green functions, Eq. 3.25.

For more complex systems where such a prescription is not available, the bulk dephazing of pure 2D surface states could be approximated by using $G^0(\mathbf{k}_\parallel, \omega) = (\omega + \mathrm{i}\tau^{-1} - \epsilon_{\mathbf{k}_\parallel})^{-1}$, such that the surface states are well defined and $\tau \gg 0$. Simple poles in the surface momentum Green functions are thereby broadened by τ^{-1}, where τ is the quasiparticle lifetime.

Honeycomb lattice

The 2D honeycomb lattice is more complicated due to the bipartite structure consisting of two interlocking triangular sublattices. The unit cell thus contains two sites, A and B, and thus two orbitals giving rise to two electronic bands [37]. Eq. 3.1 may be written compactly in terms of the basis state vector of A and B sites for each unit cell, $\vec{\psi}^\dagger_{\mathbf{r}_i,\sigma} = \left(c^\dagger_{A,\mathbf{r}_i,\sigma}, c^\dagger_{B,\mathbf{r}_i,\sigma}\right)$, with 2×2 intra-cell and inter-cell Hamiltonian matrices, diagonalized by Fourier transform,

$$\vec{\psi}_{\mathbf{r}_i,\sigma} = \int_{1\mathrm{BZ}} \frac{d^2\mathbf{k}}{\Omega^{1/2}_{BZ}} \, \mathrm{e}^{-\mathrm{i}\mathbf{r}_i\cdot\mathbf{k}} \, \vec{\psi}_{\mathbf{k},\sigma} \, . \tag{3.26}$$

This leads to

$$\mathcal{H}_{\mathrm{host}} = \sum_{\mathbf{k},\sigma} \vec{\psi}^\dagger_{\mathbf{k},\sigma} \mathbf{H}(\mathbf{k}) \vec{\psi}_{\mathbf{k},\sigma} \quad \text{where} \quad \mathbf{H}(\mathbf{k}) = \begin{pmatrix} \epsilon_0 & -t(\mathbf{k}) \\ -t(\mathbf{k})^* & \epsilon_0 \end{pmatrix} , \tag{3.27}$$

and

$$t(\mathbf{k}) = t\mathrm{e}^{-\mathrm{i}\mathbf{k}\cdot\boldsymbol{\tau}} \left(1 + \mathrm{e}^{\mathrm{i}\mathbf{k}\cdot\mathbf{a}_1} + \mathrm{e}^{\mathrm{i}\mathbf{k}\cdot\mathbf{a}_2}\right) \tag{3.28}$$

in terms of the triangular lattice vectors $\mathbf{a}_1$ and $\mathbf{a}_2$ and the inter-sublattice vector $\boldsymbol{\tau} = \mathbf{r}^A_i - \mathbf{r}^B_i$ (where $\mathbf{r}^\gamma_i$ is the position in real space of the $\gamma = A/B$ site of the i-th unit cell). Henceforth ϵ_0 (the site energy) is set to 0 for half-filling.

Generalizing Eq. 3.16 to take account of this sublattice structure gives the LDOS modulation at site $\gamma = A/B$ of the i-th unit cell as

$$\Delta\rho(\mathbf{r}^\gamma_i, \omega) = -\pi^{-1}\mathrm{Im} \sum_{\alpha,\beta} \left[\mathbf{G}^0(\mathbf{r}_i, \mathbf{r}_\alpha, \omega)\mathbf{T}_{\alpha\beta}(\omega)\mathbf{G}^0(\mathbf{r}_\beta, \mathbf{r}_i, \omega)\right]_{\gamma\gamma} , \tag{3.29}$$

where $\mathbf{T}_{\alpha\beta}(\omega)$ is the 2×2 scattering t-matrix between the (A and B) sites of unit cells $\mathbf{r}_\alpha$ and $\mathbf{r}_\beta$ to which impurities α and β couple (respectively). Here we consider impurities coupling only to a single sublattice site ($\gamma_{\alpha,\beta}$ is either A or B), such that only one element of $\mathbf{T}_{\alpha\beta}(\omega)$ is non-zero, $\mathbf{T}_{\alpha\beta}(\omega) = T_{\alpha\beta}(\omega)\mathbf{C}_{\alpha\beta}$ where $[\mathbf{C}_{\alpha\beta}]_{ij} = \delta_{i,\gamma_\alpha}\delta_{j,\gamma_\beta}$ is the connectivity matrix of impurities α and β. Consequently the QPI contains

contributions from each sublattice,

$$\Delta\rho_\gamma(\mathbf{q},\omega) = -\pi^{-1}\sum_i \mathrm{e}^{-\mathrm{i}\mathbf{q}\cdot\mathbf{r}_i^\gamma}\Delta\rho(\mathbf{r}_i^\gamma,\omega) \tag{3.30}$$

with the real-space sum over i spanning unit cells, and $\mathbf{r}_i^\gamma$ the position in real space of site γ; as $\mathbf{r}_i^B = \mathbf{r}_i^A + \boldsymbol{\tau}$ there is a phase factor between the two contributions of $\mathrm{e}^{-\mathrm{i}\mathbf{q}\cdot\tau}$.

Using Eq. 3.26 to expand $\Delta\rho(\mathbf{r}_i^\gamma,\omega)$ in momentum space, $\Delta\rho_\gamma(\mathbf{q},\omega)$ takes the same form as Eq. 3.18,

$$\Delta\rho_\gamma(\mathbf{q},\omega) = -\pi^{-1}\sum_i \mathrm{e}^{-\mathrm{i}\mathbf{q}\cdot\mathbf{r}_i^\gamma}\mathrm{Im}\iint_{1\mathrm{BZ}}\frac{d^2\mathbf{k}d^2\mathbf{k}'}{\Omega_{BZ}}\,\mathrm{e}^{-\mathrm{i}\mathbf{r}_i\cdot(\mathbf{k}'-\mathbf{k})}\left[\Delta\mathbf{G}(\mathbf{k},\mathbf{k}',\omega)\right]_{\gamma\gamma}\,. \tag{3.31}$$

In the (multi-orbital) unit cell basis, the t-matrix equation (analogous to Eq. 3.12) is then calculated in terms of the matrix Green functions $\mathbf{G}(\mathbf{k},\omega) = ((\omega+\mathrm{i}0^+)\mathbf{I}-\mathbf{H}(\mathbf{k}))^{-1}$, giving

$$\Delta\mathbf{G}(\mathbf{k},\mathbf{k}',\omega) = \mathbf{G}^0(\mathbf{k},\omega)\mathbf{T}(\mathbf{k},\mathbf{k}',\omega)\mathbf{G}^0(\mathbf{k}',\omega)\,, \tag{3.32}$$

with

$$\mathbf{T}(\mathbf{k},\mathbf{k}',\omega) = \sum_{\alpha,\beta}\frac{\mathbf{T}_{\alpha\beta}(\omega)}{\Omega_{BZ}}\,\mathrm{e}^{-\mathrm{i}\mathbf{r}_i\cdot(\mathbf{k}'-\mathbf{k})}\,. \tag{3.33}$$

Equivalently, as outlined in Section 2.3.1, $\Delta\mathbf{G}(\mathbf{k},\mathbf{k}',\omega)$ is expressed in terms of the (diagonal) $+/-$ bands,

$$\Delta\mathbf{G}(\mathbf{k},\mathbf{k}',\omega) = \sum_{p,p'=+,-} G_p^0(\mathbf{k},\omega)\,\vec{u}_{p,\mathbf{k}}\vec{u}_{p,\mathbf{k}}^{\,\dagger}\mathbf{T}(\mathbf{k},\mathbf{k}',\omega)\vec{u}_{p',\mathbf{k}}\vec{u}_{p',\mathbf{k}}^{\,\dagger}\,G_{p'}^0(\mathbf{k}',\omega)\,, \tag{3.34}$$

such that $G_p^0(\mathbf{k},\omega) = (\omega+\mathrm{i}0^+-\epsilon_{p,\mathbf{k}})^{-1}$ and $\vec{u}_{p,\mathbf{k}}^{\,\dagger} = (\mathrm{e}^{\mathrm{i}\phi(\mathbf{k})/2},\, p\,\mathrm{e}^{-\mathrm{i}\phi(\mathbf{k})/2})/\sqrt{2}$, with

$$\epsilon_{\pm,\mathbf{k}} = \pm\,|t(\mathbf{k})| \tag{3.35a}$$

$$\phi(\mathbf{k}) = \arg\ t(\mathbf{k})\,. \tag{3.35b}$$

At low energies, $\omega \ll t$, this description reduces to two inequivalent Dirac cones centred at $\mathrm{K} = 2\pi/3\mathrm{a}_0(1,+1/\sqrt{3})$ and $\mathrm{K}' = 2\pi/3\mathrm{a}_0(1,-1/\sqrt{3})$, such that

$$\epsilon_{\mathbf{k}}^{\pm} = \pm v_\mathrm{F}|\mathbf{k}-\mathbf{k}_\mathrm{K}| \quad \text{where} \quad v_\mathrm{F} = \frac{\sqrt{3}}{2}\mathrm{a}_0 t\,. \tag{3.36}$$

The QPI contribution then follows as,

$$\Delta\rho_\gamma(\mathbf{q},\omega) = -\frac{1}{2\pi \mathrm{i}}\left[Q_\gamma(\mathbf{q},\omega) - Q_\gamma(-\mathbf{q},\omega)^*\right] \tag{3.37}$$

where

$$Q_\gamma(\mathbf{q},\omega) = \sum_{\alpha,\beta} T_{\alpha\beta}(\omega) \times \Lambda^\gamma_{\alpha\beta}(\mathbf{q},\omega). \tag{3.38}$$

Eqs. 3.37 and 3.38 are thus analogues of Eqs. 3.19 and 3.20, with

$$\Lambda^\gamma_{\alpha\beta}(\mathbf{q},\omega) = \int_{1\mathrm{BZ}} \frac{d^2\mathbf{k}}{\Omega_{BZ}}\, \mathrm{e}^{\mathrm{i}(\mathbf{k}\cdot\mathbf{r}_\alpha - (\mathbf{k}+\mathbf{q})\cdot\mathbf{r}_\beta)} \times \left(\sum_{p,p'=+,-} \left[\vec{u}_{p,\mathbf{k}}\vec{u}^{\,\dagger}_{p,\mathbf{k}}\mathbf{C}_{\alpha\beta}\vec{u}_{p',\mathbf{k}}\vec{u}^{\,\dagger}_{p',\mathbf{k}}\right]_{\gamma\gamma} G^0_p(\mathbf{k},\omega)\; G^0_{p'}(\mathbf{k}',\omega)\right). \tag{3.39}$$

We stress that both the inter-band scattering and the momentum-dependent phase factors appearing in Eq. 3.39 are important, and affect the full QPI qualitatively. In particular, we note that inter-band scattering contributions to the QPI are relevant despite the fact that Im $G^0_+(\mathbf{k},\omega)$Im $G^0_-(\mathbf{k},\omega) = 0$ follows from the sign-definite dispersion for each band, given by Eq. 3.35a.

3.3 Single impurity QPI: magnetic & scalar impurities

The generalized problem involving N magnetic impurities, spatially separated and coupled to conduction electrons of the host lattice, is naturally highly rich and complex, and is the subject of Chapter 4. In this chapter we focus on the QPI due to a single magnetic or scalar impurity, in order to understand the essential features of the QPI. Moreover, the interpretation of experimental FT-STS measurements is typically in terms of a single scattering centre – the simplest form for the scattering t-matrix in Eqs. 3.16 and 3.20 [34, 102]. In this case the QPI is given by Eq. 3.20b (with $\alpha = \beta = 1$, dropped hereafter),

$$Q(\mathbf{q},\omega) = T(\omega)\Lambda(\mathbf{q},\omega)\ , \tag{3.40}$$

with $T(\omega)$ the single-impurity t-matrix and explicit forms for the host functions $\Lambda(\mathbf{q},\omega)$, to be given in Secs. 3.3.2-3.3.4.

As explained in Chapter 2, the impurity is often taken to be a static potential defect in the weak-scattering Born limit [34]. The t-matrix is then pure real and energy-independent,

$$T^{\mathrm{ps}}(\omega) \simeq v_0 \,, \tag{3.41}$$

with v_0 the potential scattering strength (see Eq. 3.3). Eq. 3.41 is the leading-order approximation to the exact t-matrix given by Eq. 3.10, holding provided $|v_0 G^0(\mathbf{r}_\alpha, \mathbf{r}_\alpha, \omega)| \ll 1$. We emphasize however that this approximation is *not* valid for stronger scattering potentials, or even for weak scattering potentials at scanning energies ω in the vicinity of divergences in the host density of states (arising for example at $\omega = 0$ in the 2D square lattice); in such cases, higher-order terms in the Born series, involving powers of $G^0(\mathbf{r}_\alpha, \mathbf{r}_\alpha, \omega)$, cannot be neglected. In particular we emphasize that the *phase* of the scattering t-matrix depends non-trivially on both the strength of the potential scatterer *and* the magnitude and phase of $G^0(\mathbf{r}_\alpha, \mathbf{r}_\alpha, \omega)$. As discussed in Chapter 2, a strong scattering potential (for example from a bound state) gives rise to a purely imaginary t-matrix, and qualitatively affects the resultant QPI. The higher-order, multiple-scattering terms in the Born series may also introduce an energy-dependence to t-matrix, which is typically weak except in the very close vicinity of van Hove points. In this chapter we employ Eq. 3.41 to describe the potential scatterer, as the simplest "zeroth-order" approximation that may be made for generic, unspecified scattering, typically assumed for a weak perturbation [34, 102, 131]. However, we note that when comparing QPI calculations to experimental FT-STS measurements, the specific nature of the impurity scattering must be considered even for the potential scattering case, as in Chapter 5.

In the special case of a single impurity on a centrosymmetric surface, $Q(\mathbf{q}, \omega) = Q(-\mathbf{q}, \omega)$, so (from Eq. 3.19) $\Delta\rho(\mathbf{q}, \omega) = -\pi^{-1}\mathrm{Im}\, Q(\mathbf{q}, \omega)$. For a scalar impurity in the Born limit, the QPI is therefore given (as in Chapter 2) by

$$\Delta\rho(\mathbf{q}, \omega) \overset{\text{scalar}}{=} -\pi^{-1}\, v_0 \Lambda''(\mathbf{q}, \omega) \,, \tag{3.42}$$

where $\Lambda(\mathbf{q}, \omega) = \Lambda'(\mathbf{q}, \omega) + \mathrm{i}\Lambda''(\mathbf{q}, \omega)$. The QPI scanning-energy dependence for the case of a scalar impurity is thus solely due to $\Lambda''(\mathbf{q}, \omega)$.

For magnetic impurities by contrast, electron correlations give rise to nontrivial dynamics. From Eq. 3.9,

$$T^{\mathrm{mag}}(\omega) = V^2 G_d(\omega) \tag{3.43}$$

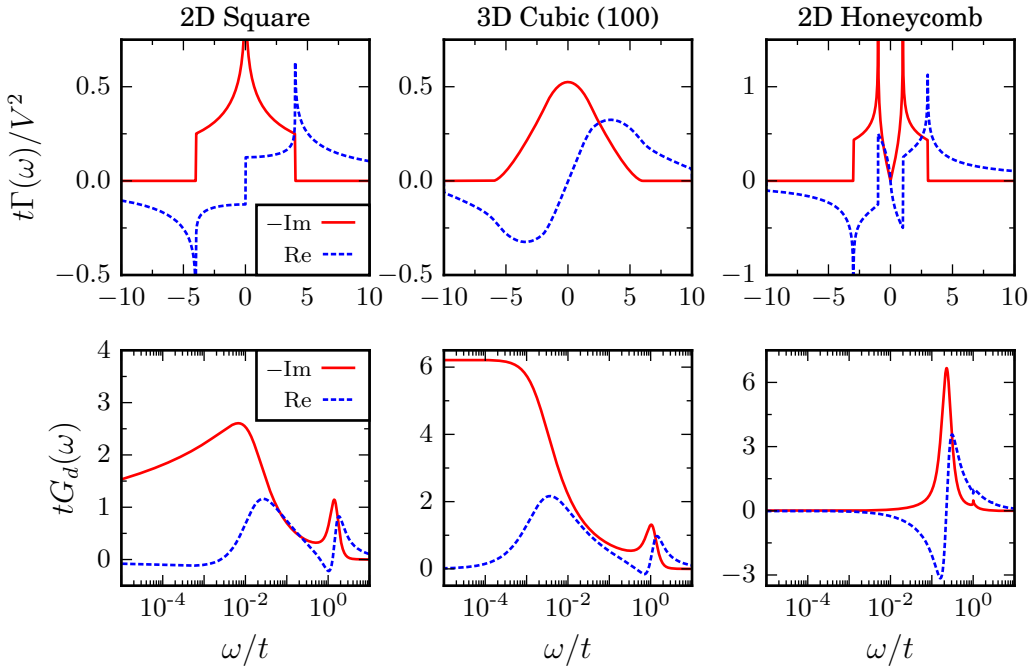

Fig. 3.2 *Upper:* Impurity-host hybridization functions, plotted as $t\Gamma(\omega)/V^2$ for each lattice. *Lower:* Dynamics of a single magnetic impurity on various lattices at $T = 0$, plotted as $-\text{Im}\ tG_d(\omega)$ (solid lines) and $\text{Re}\ tG_d(\omega)$ (dashed) vs ω/t, calculated via NRG. Impurity parameters: $U = 1.95t$ and $V = 0.555t$ for 2D square and 3D cubic lattices; $U = 0.704t$ and $V = 0.493t$ for 2D honeycomb lattice.

in terms of the impurity Green function $G_d(\omega)$; the QPI follows from Eqs. 3.19 and 3.40. The QPI for a single magnetic impurity on a centrosymmetric surface is therefore,

$$\Delta\rho(\mathbf{q},\omega) \overset{\text{mag}}{=} -\frac{V^2}{\pi}\Big[\text{Re}\ G_d(\omega)\Lambda''(\mathbf{q},\omega) + \text{Im}\ G_d(\omega)\Lambda'(\mathbf{q},\omega)\Big]\ , \tag{3.44}$$

with contributions from both real and imaginary parts of $\Lambda(\mathbf{q},\omega)$, and weights that depend on the impurity Green function at energy ω. As discussed below, the Kondo effect produces a scattering enhancement at low temperatures and scanning energies, causing a crossover in the QPI from being dominated by $\Lambda''(\mathbf{q},\omega)$ at high energies (similar to that of a scalar impurity) to being dominated by $\Lambda'(\mathbf{q},\omega)$ at low energies. For simplicity we begin by considering the low-temperature limit, $T \lesssim T_\text{K}$, for which the impurity dynamics (and thus conduction electron scattering and QPI) are essentially those at $T = 0$.

3.3.1 Effect of host on impurity dynamics

For a magnetic impurity, the QPI depends on both the host function $\Lambda(\mathbf{q},\omega)$ and the impurity Green function $G_d(\omega)$ – which itself depends on the host. Specifically, the impurity problem is controlled by the hybridization function $\Gamma(\omega)$, related to the clean host density of states, $\rho_0(\omega)$, by $-\text{Im}\,\Gamma(\omega) = \pi V^2 \rho_0(\omega)$. The Kondo physics is sensitive to the behaviour of $\rho_0(\omega)$ near the Fermi level ($\omega = 0$) [65, 143, 144, 139, 122], given for the three lattices under investigation as

$$\rho_0(\omega) \overset{|\omega|\ll t}{\sim} \begin{cases} \frac{\log(16t/|\omega|)}{2\pi^2 t} & : \text{2D square} \\ \frac{1}{6t} - \frac{\omega^2}{6\sqrt{2}\pi^2 t^3} & : \text{3D cubic, (100) surface} \\ \frac{|\omega|}{\sqrt{3}\pi t^2} & : \text{honeycomb .} \end{cases} \tag{3.45}$$

These lattices exemplify three paradigms, with densities of states that are diverging, flat, or pseudogapped at low-energy. Real and imaginary parts of $t\Gamma(\omega)/V^2$ are plotted as a function of ω/t for each of the three lattices in the upper panels of Figure 3.2.

The density of states for metallic systems is typically flat at low energies. This gives rise to an exponentially-small Kondo scale [74] $T_\text{K}/t \sim \exp[-\pi U/8V^2\rho_0(0)]$, and low-energy Fermi liquid behaviour [74]

$$\text{Im}\Gamma(\omega) \times \text{Im}G_d(\omega) \overset{|\omega|\ll T_\text{K}}{\sim} 1 - \alpha_\omega(\omega/T_\text{K})^2 + \ldots\,, \tag{3.46}$$

with Fermi level spectral pinning, $-\pi V^2\rho_0(0)\text{Im}\; G_d(0) = 1$ (from the definition of Im $\Gamma(\omega)$ given earlier in the section). This is shown for a magnetic impurity on the (100) surface of a 3D cubic lattice in Figure 3.2 (centre panel), where the imaginary and real parts of $tG_d(\omega)$ are plotted vs ω/t. We have chosen representative impurity parameters $U = 1.95t$ and $V = 0.56t$, yielding $T_\text{K} \approx 5\times10^{-3}t$, where T_K is defined throughout as the half-width at half-maximum of the Kondo resonance Im $\Gamma(\omega = T_\text{K}) \times$ Im $G_\text{d}(\omega = T_\text{K}) = \frac{1}{2}$Im $\Gamma(0) \times$ Im $G_\text{d}(0)$. With the host bandwidth $12t = 11$eV (such that $U = 1.79$eV and $V = 0.51$eV) we obtain $T_\text{K} \approx 57$K, consistent with established results for Co atoms on a Cu surface [195, 119, 202]. As seen from Figure 3.2 (centre), the Kondo effect results in a large imaginary part $-t\text{Im}\; G_d(\omega) \sim 6t^2/(\pi V^2) \simeq 6.2$ for low energies $|\omega| \ll T_\text{K}$. We emphasize that the Kondo temperatures adopted here, representative of experimentally measured values, are quite large; the low-temperature limit $T \lesssim T_\text{K}$, which we consider in the first instance, therefore corresponds to relatively high temperatures which are easily accessible in experiment.

For the 2D square lattice, the low-energy divergence in the host density of states results in an enhanced Kondo temperature [144, 139]. In any Kondo-screened phase, the pinning condition from Eq. 3.46 still holds [63, 122], implying that,

$$-\text{Im } G_d(\omega) \overset{|\omega|\to 0}{\sim} \frac{2\pi t}{V^2}\Big[\ln(16t/|\omega|)\Big]^{-1} , \tag{3.47}$$

which decays logarithmically at low energies. As confirmed in the left panel of Figure 3.2, the impurity spectrum $-\text{Im } tG_d(\omega)$ therefore shows a maximum at $|\omega| \sim T_\text{K}$. With the same parameters as the 3D cubic system, we now obtain a much higher $T_\text{K} \approx 584\text{K}$.

Finally, in the honeycomb lattice (for which the density of states is pseudogapped) the Kondo effect is suppressed due to the depleted density of states near the Fermi level, and the local moment phase is stable for any U/V^2 at particle-hole symmetry [65, 56]. The impurity spectrum then takes the low-energy form

$$-\text{Im } G_d(\omega) \overset{|\omega|\to 0}{\sim} \alpha'|\omega| \tag{3.48}$$

(with α' a constant). This decay of $G_d(\omega)$ is demonstrated in the right panel of Figure 3.2. With $t = 2.84\text{eV}$, the honeycomb lattice models the π/π^* bands of graphene [167]; we use $U = 0.704t$ and $V = 0.493t$ as realistic impurity parameters obtained from ab-initio calculations for Co atoms on graphene [208]. We now turn to the QPI due to a single magnetic or scalar impurity in turn for these three lattices in turn.

3.3.2 2D square lattice

The QPI is obtained from Eq. 3.42 and 3.44 for scalar and magnetic impurities respectively, with $\Lambda(\mathbf{q},\omega)$ for a single impurity given from Eq. 3.21 (with $\mathbf{r}_\alpha = \mathbf{r}_\beta = \mathbf{0}$),

$$\Lambda(\mathbf{q},\omega) = \int_{1\text{SBZ}} \frac{d^2\mathbf{k}}{\Omega_{BZ}}\, G^0(\mathbf{k},\omega)G^0(\mathbf{k}+\mathbf{q},\omega) . \tag{3.49}$$

Figure 3.3 shows the absolute value of the QPI $|\Delta\rho(\mathbf{q})|$ as a colour map in $\mathbf{q}$-space (upper panels), comparing the scalar impurity (left) with the magnetic impurity (right), at a fixed scanning energy $\omega \simeq T_\text{K}$, using the same parameters as Figure 3.2. The lower panel shows a cut across the Brillouin zone of $\Delta\rho(\mathbf{q})/\Delta\rho_\text{tot}$, where $\Delta\rho_\text{tot} \equiv \Delta\rho_\text{tot}(\omega) = \int_{1\text{BZ}} d^2\mathbf{q}|\Delta\rho(\mathbf{q},\omega)|$ is the total scattering amplitude at energy ω. For a single impurity, the topology in $\mathbf{q}$-space, on which we now focus, is completely determined by the host function $\Lambda(\mathbf{q},\omega)$ (see Eqs. 3.42 and 3.44), as we argued in Chapter 2.

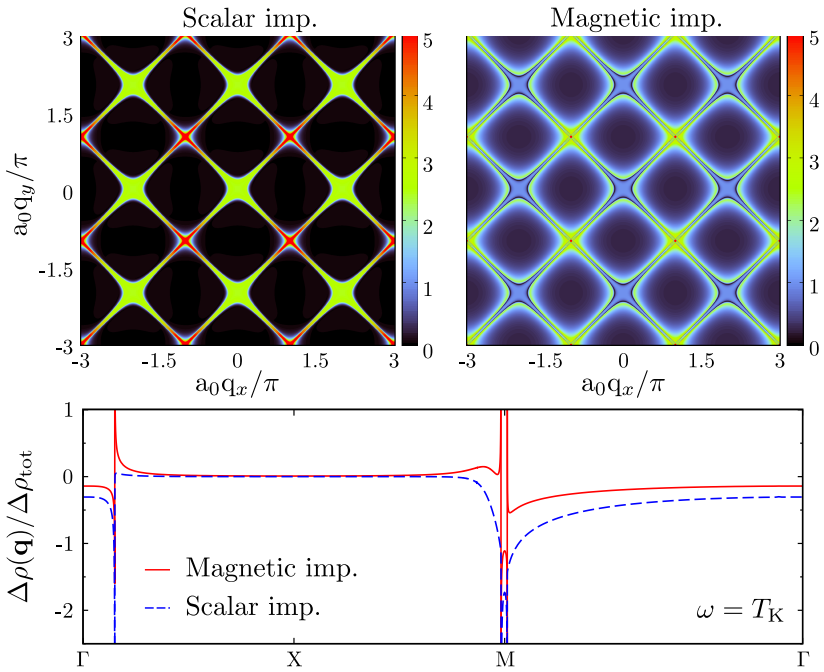

Fig. 3.3 QPI for a single impurity on the 2D square lattice at scanning energy $\omega = 0.055t$. Upper panels compare the QPI colourmaps $|\Delta\rho(\mathbf{q})|$ for scalar (left) and magnetic (right) impurities; lower panel shows a Brillouin zone cut along the path $\Gamma \to \mathrm{X} \to \mathrm{M} \to \Gamma$, plotted as $\Delta\rho(\mathbf{q})/\Delta\rho_{\rm tot}$ for $\omega = 5 \times 10^{-2}t$. Symmetry points defined as $\mathbf{q}_\Gamma = \mathbf{0}$, $\mathbf{q}_\mathrm{X} = \mathbf{A}_1$, $\mathbf{q}_\mathrm{M} = \mathbf{A}_1 + \mathbf{A}_2$ in terms of reciprocal lattice vectors $\mathbf{A}_1 = 2\pi/\mathrm{a}_0(1,0)$, $\mathbf{A}_2 = 2\pi/\mathrm{a}_0(0,1)$. Magnetic impurity parameters as given in Figure 3.2 such that the scanning energy $\omega = T_\mathrm{K}$, and $v = 0.5t$ for the scalar impurity.

In Section 2.2 of that chapter, we found that both real and imaginary parts of $\Lambda(\mathbf{q},\omega)$ were divergent along (the same) specific envelope(s) in $\mathbf{q}$-space, corresponding to $\mathbf{q}$ vectors that join points on the constant energy contour (CEC) for a given scanning energy (ω) at which the group velocities $\boldsymbol{\nabla}\epsilon_\mathbf{k}$ and $\boldsymbol{\nabla}\epsilon_{\mathbf{k}+\mathbf{q}}$ are antiparallel. The dispersion of electronic states defined in Eq. 3.22, $\epsilon_\mathbf{k}$, is inversion-symmetric, and thus the group velocities are antisymmetric with respect to inversion. Lines of divergence are thus expected in both real and imaginary parts of $\Lambda(\mathbf{q},\omega)$, and hence the QPI, at $\mathbf{q}^*(\omega) = 2\mathbf{k}_{c(\omega)}$, where $\mathbf{k}_{c(\omega)}$ lies on the CEC c at energy ω; divergences are also expected at $\mathbf{q}$ points related to $\mathbf{q}^*$ by translations of the reciprocal lattice, $\mathbf{q}^* + n\mathbf{A}_i$ (where $n\mathbf{A}_i$ is any multiple of a reciprocal lattice vector). Furthermore, results from the case study of $\Lambda(\mathbf{q},\omega)$ for the 2D electron gas in Section 2.2.2 suggest that the real and imaginary parts of $\Lambda(\mathbf{q},\omega)$ should diverge as $|\mathbf{q}-\mathbf{q}^*|^{-1/2}$ as the line is approached from one side of the envelope and be finite when approached from the other, with the real and imaginary parts diverging from opposite sides. Figure 3.3 clearly demonstrates

the commonality of the divergent lines between the magnetic and scalar impurity QPI, leading to similar **q**-space topology for both colour plots. However, there are marked differences between the two cases in the magnitudes of the QPI response away from the lines of divergence, and the behaviour on approaching these lines.

From Eq. 3.22, the CEC $\mathbf{k}_{c(\omega)}$ for the 2D square lattice at scanning energy ω is described by,

$$\cos\left(\mathrm{a}_0\left(k_{c(\omega)}\right)_x\right)+\cos\left(\mathrm{a}_0\left(k_{c(\omega)}\right)_y\right)+(\omega/2t)=0\,, \tag{3.50}$$

in agreement with the QPI for both scalar and magnetic impurities in Figure 3.3. Around the Γ symmetry point, Eq. 3.50 reduces approximately to a rectangular hyperbola,

$$\left(q_x^*\right)^2-\left(q_y^*\right)^2 \overset{|\omega|\ll t}{\sim} \pm\, a_\Gamma(\omega)^2 \tag{3.51}$$

with the dispersive properties controlled by $a_\Gamma(\omega)$; around the M point, the intense features in the QPI *appear* to be similar in form, despite the fact that the divergent lines are in fact given by straight line segments,

$$(\mathrm{a}_0 q_y^*-\pi)\pm(\mathrm{a}_0 q_x^*-\pi) \overset{|\omega|\ll t}{\sim} \pm\, a_{\mathrm{M}}(\omega)\,. \tag{3.52}$$

This discrepancy illustrates that care must be taken when interpreting features in the experimentally-measured QPI as divergences in $\Lambda(\mathbf{q},\omega)$, as regions of high (but finite) intensity may distort the perceived topology of the true divergences.

In **q**-space, $\Lambda''(\mathbf{q},\omega)$ is found to approach the divergence envelope as

$$\Lambda''(\mathbf{q},\omega) \overset{\mathbf{q}\to\mathbf{q}^*}{\sim} \left|\mathbf{q}-\mathbf{q}^*\right|^{-1/2} \tag{3.53}$$

when approaching a point $\mathbf{q}^*$ from the Γ or M points. The region enclosed by these divergences is therefore characterized by high QPI scattering intensity — see Figure 3.3 for the scalar impurity. $\Lambda''(\mathbf{q},\omega)$ does not however diverge on approaching from X, and remains comparatively small in its vicinity. In fact, $\Lambda''(\mathbf{q},\omega)$ is *odd* in ω due to the exact symmetry $\Lambda(\mathbf{q},\omega)=\Lambda(\mathbf{q},-\omega)^*$. The scalar impurity QPI $\Delta\rho(\mathbf{q},\omega)\sim\omega$ thus vanishes at low energies away from the lines of divergence.

The situation is rather different for the magnetic impurity because both real and imaginary parts of $\Lambda(\mathbf{q},\omega)$ are important (Eq. 3.44). Because $\Lambda'(\mathbf{q},\omega)$ is even in ω, residual QPI intensity around the X symmetry point persists even at low energies, due to finite $\Lambda'(\mathbf{q},\omega=0)=b'_{\mathbf{q}}$. $\Lambda'(\mathbf{q},\omega)$ also diverges algebraically (as Eq. 3.53) on

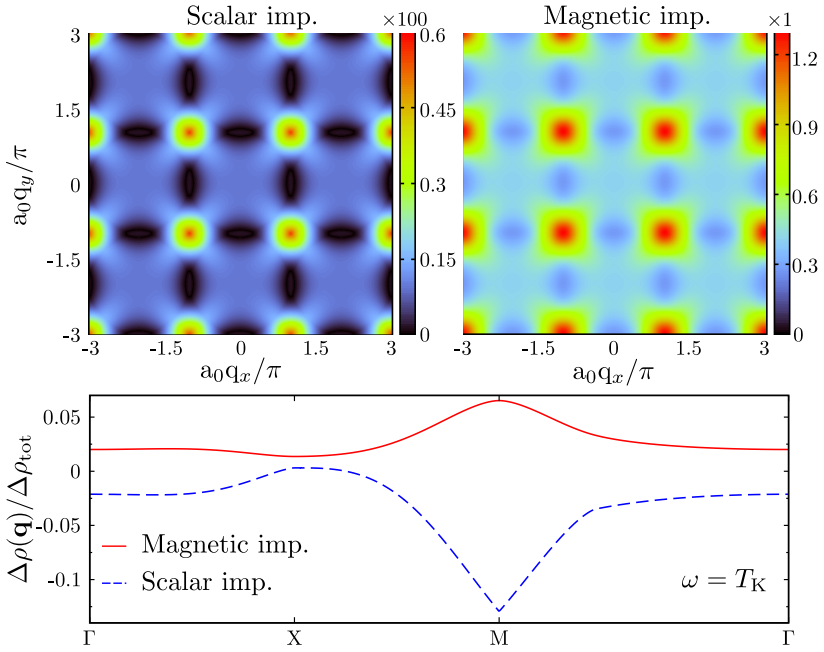

Fig. 3.4 QPI for an impurity on the (100) surface of a 3D cubic lattice for scanning energy $\omega = 5 \times 10^{-3}t$. As in Figure 3.3, upper panels compare the QPI colourmaps $|\Delta\rho(\mathbf{q})|$ for scalar (left) and magnetic (right) impurities, while lower panel shows a Brillouin zone cut along the path $\Gamma \to \mathrm{X} \to \mathrm{M} \to \Gamma$, plotted as $\Delta\rho(\mathbf{q})/\Delta\rho_{\rm tot}$. Magnetic impurity parameters as given in Figure 3.2 such that the scanning energy $\omega = T_{\rm K}$, and $v = 0.5t$ for the scalar impurity.

approaching the singular lines from X (it does not diverge in the vicinity of Γ or M). As such, the QPI scattering intensity is enhanced around X for magnetic impurities.

Further, as shown in the lower panel of Figure 3.3, the *sign* of $\Delta\rho(\mathbf{q},\omega)$ can be reversed by the contribution from the second term in Eq. 3.44. This is a hallmark of scattering from magnetic impurities, where Im $G_d(\omega) < 0$ can become large due to the Kondo effect (see Figure 3.2). This leads to additional structure in the measurable $|\Delta\rho(\mathbf{q})|$, not found in QPI for scalar impurities.

3.3.3 3D cubic lattice with (100) surface

The (100) surface of the 3D cubic lattice is again a square lattice, but surface states are dephased by coupling to the bulk. This leads to the t-matrix Eq. 3.24 for a single impurity, and

$$\Lambda(\mathbf{q},\omega) = \int_{\rm 1SBZ} \frac{d^2\mathbf{k}_\parallel}{\Omega_{BZ}}\, G^0_{\rm surf}(\mathbf{k}_\parallel,\omega) G^0_{\rm surf}(\mathbf{k}_\parallel + \mathbf{q},\omega) \tag{3.54}$$

with scattering vectors $\mathbf{q} \equiv \mathbf{q}_\parallel$ confined to the 2D surface (and $G^0_{\rm surf}(\mathbf{k}_\parallel, \omega)$ given by Eq. 3.25).

The dephazing due to the bulk broadens the features of $G^0_{\rm surf}(\mathbf{k}_\parallel, \omega)$ for the surface band compared to the sharply-defined features of $G^0(\mathbf{k}, \omega)$ for the bulk band of the 2D square lattice, giving rise to very different QPI responses – despite the two bands sharing the same dispersion relation, Eq. 3.22, and thus CECs. The simple picture of the QPI in terms of scattering between well-defined quasiparticle states lying on a given CEC [78, 204] is no longer valid, and the ability of the QPI to map the CEC as discussed in Chapter 2 and Section 3.3.2 is lost. The resulting QPI, shown in Figure 3.4, does not contain the divergences arising in the 2D square lattice — but remnants of this singular structure appear in broadened regions of enhanced scattering intensity around the M symmetry point in the cubic lattice. The global four-fold symmetry of the QPI evolves locally into a continuous rotational symmetry around this point, with $\Lambda(\mathbf{q}, \omega) \equiv \Lambda(|\mathbf{q} - \mathbf{q}_{\rm M}|, \omega)$ for $|\omega| \ll t$. Further, the QPI for the scalar impurity (which only depends on $\Lambda''(\mathbf{q}, \omega)$) is distinctly conical, with

$$\Lambda''(\mathbf{q}, \omega) \overset{\mathbf{q}\to\mathbf{q}_{\rm M}}{\sim} a''_{\rm M}(\omega) + b''_{\rm M}(\omega)\,|\mathbf{q} - \mathbf{q}_{\rm M}| + \mathcal{O}\,|\mathbf{q} - \mathbf{q}_{\rm M}|^2 \ , \tag{3.55}$$

as determined from numerical calculations. By contrast the QPI for a magnetic impurity is found to be controlled by the quadratic term (see Figure 3.4) since

$$\Lambda'(\mathbf{q}, \omega) \overset{\mathbf{q}\to\mathbf{q}_{\rm M}}{\sim} a'_{\rm M}(\omega) + c'_{\rm M}(\omega)\,|\mathbf{q} - \mathbf{q}_{\rm M}|^2 + \mathcal{O}\,|\mathbf{q} - \mathbf{q}_{\rm M}|^4 \ . \tag{3.56}$$

A striking feature of the QPI for the 3D cubic lattices is the difference in *intensity* between scalar and magnetic impurities (note the rescaled colour range in Figure 3.4). There are two distinct reasons for this. First, $\Lambda''(\mathbf{q}, \omega)$ is odd in ω, whence $\Lambda''(\mathbf{q}, \omega) \sim \omega$ at low energies $|\omega| \ll t$. For the scalar impurity, Eq. 3.42 implies that the QPI, $\Delta\rho(\mathbf{q}, \omega) \sim \omega$, is therefore also small. By contrast, the QPI for a magnetic impurity (Eq. 3.44) has a contribution from $\Lambda'(\mathbf{q}, \omega)$, which remains finite as $\omega \to 0$.

Second, in the case of magnetic impurities, the Kondo effect produces a spectral resonance in Im $G_d(\omega)$ of width $T_{\rm K}$ that does not decay at low energies (cf. Eq. 3.47 and Figure 3.2). In consequence, the QPI is considerably more intense at low energies for magnetic impurities than scalar impurities in standard flat-band metallic systems.

3.3.4 2D honeycomb lattice

The 2D honeycomb lattice, modelling the π and π^* bands in graphene within a nearest-neighbor tight-binding picture [167], generates additional structure in the QPI due to the bipartite nature of the lattice and the low-energy pseudogapped density of states given by Eq. 3.45 [208, 207, 184].

A single impurity coupled to a single honeycomb site (on sublattice $\gamma_\alpha = A$ or B) breaks sublattice symmetry, and thus inversion symmetry for the system. The single-impurity QPI is therefore obtained from Eq. 3.19 and Eq. 3.40, with $\Lambda(\mathbf{q},\omega)$ comprising contributions from both sublattices,

$$\Lambda(\mathbf{q},\omega) = \sum_{\gamma} \Lambda^{\gamma}_{\alpha\alpha}(\mathbf{q},\omega) \; . \tag{3.57}$$

$\Lambda^{\gamma}_{\alpha\alpha}(\mathbf{q},\omega)$ itself is given by Eq. 3.39, and depends on the phase ϕ defined in Eq. 3.35b. This phase has a marked qualitative effect on the resulting QPI, and cannot be neglected. For centrosymmetric lattices, the QPI is periodic across the first Brillouin zone because $\Lambda(\mathbf{q}+n\mathbf{A}_i,\omega) = \Lambda(\mathbf{q},\omega)$ with integer n for any reciprocal lattice vector $\mathbf{A}_i$. But in the honeycomb lattice

$$\Lambda(\mathbf{q}+3n\mathbf{A}_i,\omega) = \Lambda(\mathbf{q},\omega) \; , \tag{3.58}$$

arising because $\phi(\mathbf{k}+n\mathbf{A}_i) = \phi(\mathbf{k}) + \exp[2n\pi\mathrm{i}/3]$. This property follows from Eqs. 3.28 and 3.35b, noting that $\boldsymbol{\tau} = \frac{1}{3}[\mathbf{a}_1+\mathbf{a}_2]$ in terms of the real-space lattice vectors, and $\mathbf{a}_i \cdot \mathbf{A}_j = 2\pi\delta_{ij}$ as usual. As such, the period of the QPI is enlarged to include the third Brillouin zone.

Figure 3.5 plots the QPI due to scalar and magnetic impurities respectively at a scanning energy $\omega = 0.3t$. The Dirac cone electronic structure at low energies $\omega \ll t$ (Eq. 3.36) gives rise to circular features around the Γ/Γ_2 points (located at $\mathbf{q}_\Gamma = \mathbf{0}$ and $\mathbf{q}_{\Gamma_2} = \mathbf{A}_1$ respectively) characteristic of intra-valley ("on-cone") scattering. As a consequence of the enlarged periodicity of the phase ϕ, the QPI features are distinct around the Γ and Γ_2 points, despite arising from the same intra-valley scattering processes, because $\Lambda(\mathbf{q}_{\Gamma_2},\omega) = \Lambda(\mathbf{q}_\Gamma,\omega) \times \exp[-\pi\mathrm{i}/3]$. At low energies $|\omega| \ll t$, these points are surrounded by lines of divergence in $\Lambda(\mathbf{q},\omega)$ at $\mathbf{q} = \mathbf{q}^*$,

$$|\mathbf{q}-\mathbf{q}^*| = d_\Gamma(\omega) \; , \tag{3.59}$$

dispersing *linearly* as $d_{\Gamma/\Gamma_2}(\omega) = 2|\omega|/v_\mathrm{F}$, due to the effective Dirac cone structure at low energies given by Eq. 3.36 (where v_F is the Fermi velocity). For the scalar impurity at low energies $|\omega| \ll t$, both points are surrounded by flat regions of high scattering

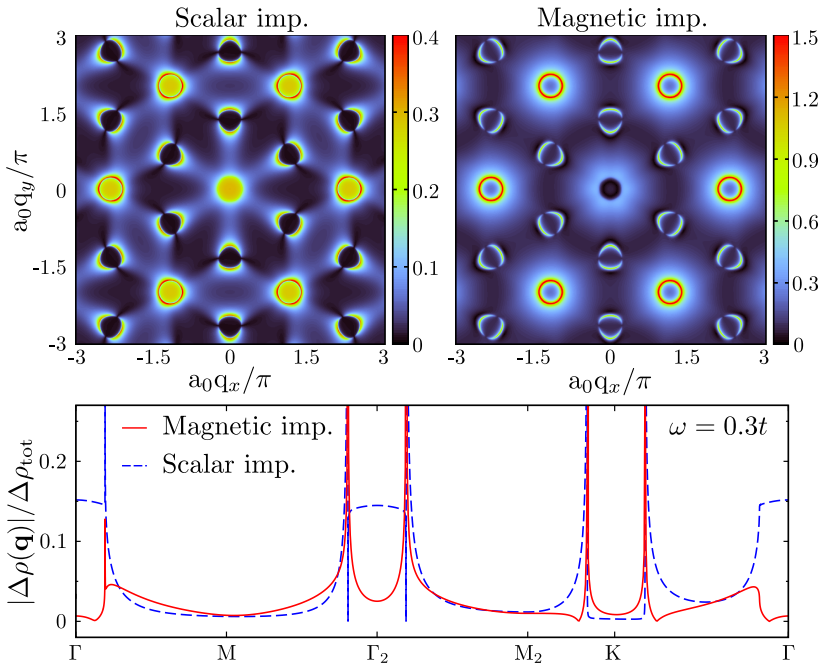

Fig. 3.5 QPI for a single impurity on the honeycomb lattice for scanning energy $\omega = 0.3t$. As in Figure 3.3 the upper panels compare the QPI colourmaps $|\Delta\rho(\mathbf{q})|$ for scalar (left) and magnetic (right) impurities, while lower panel shows a Brillouin zone cut of the QPI plotted as $|\Delta\rho(\mathbf{q})|/\Delta\rho_{\rm tot}$ along the path $\Gamma \to \mathrm{M} \to \Gamma_2 \to \mathrm{M}_2 \to \mathrm{K} \to \Gamma$, where $\mathbf{q}_\Gamma = \mathbf{0}$, $\mathbf{q}_\mathrm{M} = \frac{1}{2}\mathbf{A}_1$, $\mathbf{q}_{\Gamma_2} = \mathbf{A}_1$, $\mathbf{q}_{\mathrm{M}_2} = \mathbf{A}_1 + \frac{1}{2}\mathbf{A}_2$, $\mathbf{q}_\mathrm{K} = \frac{2}{3}\mathbf{A}_1 + \frac{1}{3}\mathbf{A}_2$, in terms of reciprocal lattice vectors $\mathbf{A}_{1,2} = 2\pi/\mathrm{a}_0(\frac{1}{\sqrt{3}}, \pm 1)$. Magnetic impurity parameters as given in Figure 3.2, and $v = 0.5t$ for the scalar impurity.

intensity,

$$|\Delta\rho(\mathbf{q},\omega)| \overset{|\mathbf{q}|\lesssim|\mathbf{q}^*|}{\sim} b_\Gamma \,, \tag{3.60}$$

with $b_\Gamma = b_{\Gamma_2}$ independent of scanning energy ω. However, the local environment of the Γ and Γ_2 points is different. The immediate vicinity of the Γ_2 point possesses a continuous rotational symmetry, with divergences in the QPI along the entire singular line $\mathbf{q} = \mathbf{q}^*$,

$$\Lambda(\mathbf{q},\omega) \overset{\mathbf{q}\to\mathbf{q}^*}{\sim} \ln^2\left|\mathrm{a}_0\left(\mathbf{q}-\mathbf{q}^*\right)\right| . \tag{3.61}$$

The form of these divergences is different to the conventional (inverse square root) algebraic form for the divergences, found in Chapter 2 for the 2D electron gas and for the 2D square lattice in Section 3.3.2, likely due to the more complex nature of the quasiparticles on each Dirac cone [37]. By contrast, a lower six-fold symmetry is found around the Γ point as $\omega \to 0$ due to divergent *points* arising only when $\mathbf{q}^*$ is perpendicular to $\mathbf{A}_1$, $\mathbf{A}_2$ and $(\mathbf{A}_1 + \mathbf{A}_2)$.

Complex features in the QPI also appear in the vicinity of the K symmetry points due to inter-valley ("off-cone") scattering, and are again enclosed by singular lines, denoted $\mathbf{q}^*$. These features possess only reflection symmetry about the line $(\mathbf{q}_\Gamma - \mathbf{q}_\mathrm{K})$, the continuous rotational symmetry being lifted by the underlying phase texture (itself arising because the impurity couples to a single sublattice). The line of divergence along $\mathbf{q}^*$ is intersected by a perpendicular nodal line at pinch-points where $(\mathbf{q}^* - \mathbf{q}_\mathrm{K}) \cdot (\mathbf{q}_\Gamma - \mathbf{q}_\mathrm{K}) = 0$. For the scalar impurity, scattering is forbidden within the region around the K point enclosed by the singular lines. These features are seen clearly in the QPI map and cuts for the scalar impurity presented in Figure 3.5. At higher scanning energies, trigonal warping sets in, giving rise to a local three-fold point symmetry around $\mathbf{q}_\mathrm{K}$.

For the magnetic impurity, the relative weight of $\Lambda'(\mathbf{q}, \omega)$ and $\Lambda''(\mathbf{q}, \omega)$ in the QPI depends on the complex t-matrix, $T(\omega)$, which evolves with scanning energy ω (see Figure 3.2). Importantly, this can lead to distinctive features in the measurable QPI, $|\Delta\rho(\mathbf{q}, \omega)|$. Accidental cancellation of terms in Eq. 3.19 can produce characteristic "dark spots" of suppressed scattering in the QPI. An example is shown Figure 3.5, where $|\Delta\rho(\mathbf{q}, \omega)| \simeq 0$ for $|\mathbf{q}| < |\mathbf{q}^*|$ in the vicinity of the Γ point. In contrast to the scalar impurity case (Eq. 3.60), the QPI in general depends on ω and varies with $\mathbf{q}$ in the vicinity of the Γ and Γ_2 points when magnetic impurities are present. Indeed, magnetic impurities also induce scattering near the K point.

3.4 Characteristic Kondo physics in the QPI

3.4.1 Scanning-energy dependence

We turn now to dynamical features of the QPI for the three lattices, comparing scalar and magnetic impurities. Numerically-exact results that exemplify the key physics are presented in Figure 3.6

For scalar impurities, the scanning-energy dependence of the QPI is due entirely to the ω-dependence of $\Lambda(\mathbf{q}, \omega)$, which characterizes the clean host lattice. The real part of this function is plotted as a colour map in the centre column panels of Figure 3.6 (the real and imaginary parts are related by Hilbert transformation).

For magnetic impurities, QPI dynamics result from both $\Lambda(\mathbf{q}, \omega)$ and the impurity Green function $G_d(\omega)$, whose spectrum is plotted in the left column panels of Figure 3.6 (see also Figure 3.2 and Eqs. 3.46–3.48 for the detailed low-energy behaviour). The

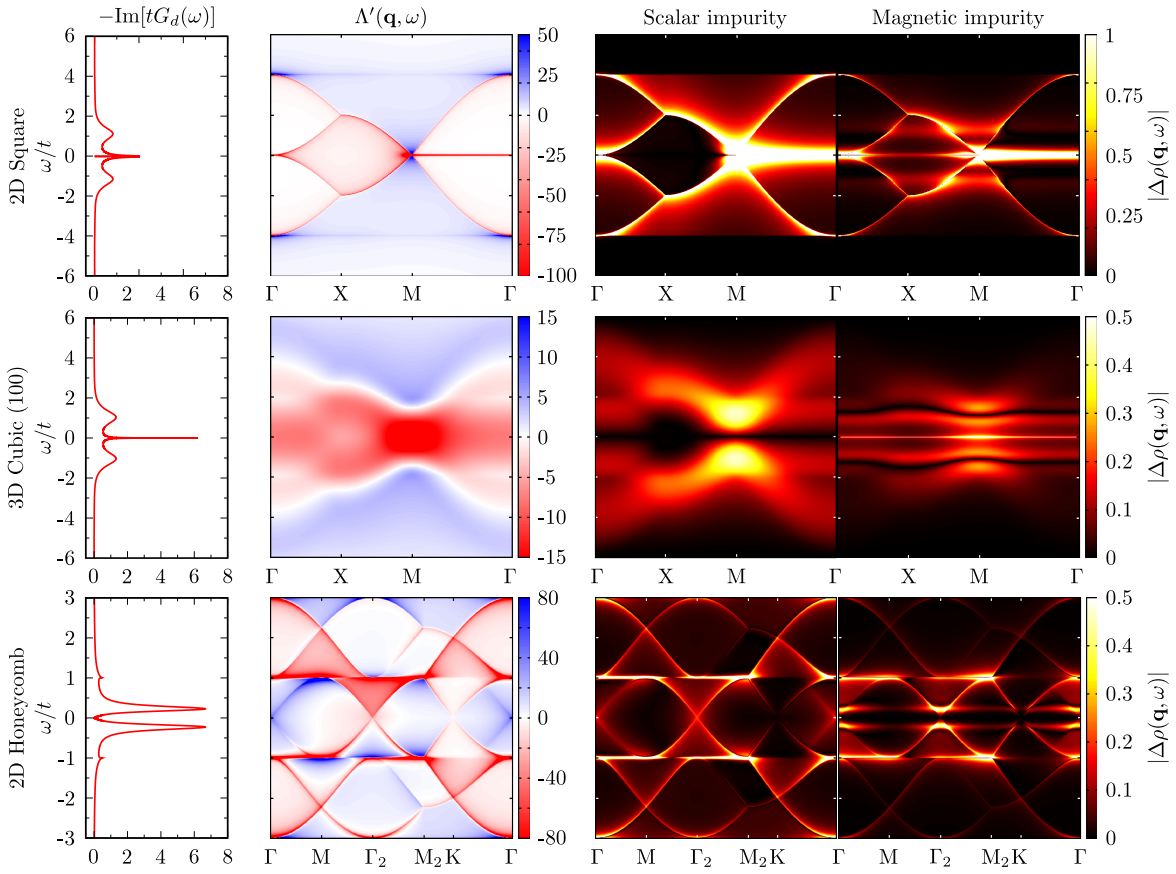

Fig. 3.6 QPI dynamics for a single impurity on various lattices: 2D square, 3D cubic (100) surface, honeycomb (top, middle, and bottom row panels respectively). Right column panels: colour plots of the QPI $|\Delta\rho(\mathbf{q},\omega)|$ across a Brillouin zone cut as a function of scanning energy ω/t, comparing scalar and magnetic impurities. Centre column panels show a colour plot of the host function $\Lambda'(\mathbf{q},\omega)$ over the same $\mathbf{q}$-cut and energies. Left column panels show the spectral function for a magnetic impurity, $-\mathrm{Im}[tG_d(\omega)]$ vs ω/t, calculated via NRG at $T = 0$. Magnetic impurity parameters as in Figure 3.2. Scalar impurity $v = 0.15t$.

nontrivial scanning-energy dependence of the QPI reflects the rich structure of the underlying quantum impurity problem.

For the 2D square lattice, divergences in $\Lambda(\mathbf{q},\omega)$, described by Eqs. 3.51 and 3.52, give rise to lines of intense scattering in the QPI. The dispersive properties of these features are controlled at low energies $|\omega| \ll t$ by $a_\Gamma(\omega)$ and $a_\mathrm{M}(\omega)$, which are related by continuity at the edge of the Brillouin zone through $a_\mathrm{M}(\omega) = a_\Gamma(\omega)^2/(2\pi)$. We find linear dispersion of the divergent features around the M symmetry point, implying

$$a_\mathrm{M}(\omega) \sim |\omega| \qquad ; \qquad a_\Gamma(\omega) \sim |\omega|^{1/2} \,, \tag{3.62}$$

as confirmed directly in the upper panels of Figure 3.6.

As $\omega \to 0$, the divergences are confined to the line $q_x^* = q_y^*$ connecting Γ and M symmetry points, so that

$$\Lambda(q_x = q_y, \omega) \overset{|\omega|\ll t}{\sim} a_\mathbf{q}\delta(\omega) + b_\mathbf{q}|\omega| + \mathrm{i}c_\mathbf{q}\frac{1}{\omega} + \ldots \,, \tag{3.63}$$

with the non-analytic nature of $\Lambda(q_x = q_y, 0)$ due to the presence of the van Hove point in the 2D square lattice at $\omega = 0$. The QPI itself thus diverges along this line with the universal asymptotic form,

$$|\Delta\rho(q_x = q_y, \omega)| \overset{|\omega|\to 0}{\sim} \begin{cases} \left|\frac{1}{\omega}\right| & : \text{ scalar} \\ \frac{1}{|\omega|\ln^2(16t/|\omega|)} & : \text{ mag.} \,, \end{cases} \tag{3.64}$$

where $\mathrm{Re}\, G_d(\omega \to 0) \sim [\ln(16t/|\omega|)]^{-2}$ is used in the case of the magnetic impurity (obtained by Hilbert transform of Eq. 3.47). The divergence is thus sharper along the M-Γ line for magnetic impurities, as evident in Figure 3.6.

Away from this divergent line (for instance along the cut $\Gamma \to X \to M$ in Figure 3.6), the QPI is characterized by vanishing scattering intensity at low scanning energies due to

$$\Lambda(q_x \neq q_y, \omega) \overset{|\omega|\to 0}{\sim} \tilde{a}_\mathbf{q} + \tilde{b}_\mathbf{q}|\omega| + \mathrm{i}\tilde{c}_\mathbf{q}\omega\ln|\omega/t| + \ldots \,, \tag{3.65}$$

giving rise to the asymptotic behaviour of the QPI,

$$|\Delta\rho(q_x \neq q_y, \omega)| \overset{|\omega|\to 0}{\sim} \begin{cases} \omega\ln|\omega/t| & : \text{ scalar} \\ \frac{1}{\ln(16t/|\omega|)} & : \text{ mag.} \end{cases} \tag{3.66}$$

As a result, the QPI intensity for the magnetic impurity decays much more slowly than that of the scalar impurity as the scanning energy is reduced in the vicinity of the X symmetry point – see Figure 3.6.

At higher scanning energies $|\omega| \sim U/2$, the "Hubbard satellites" in the spectral function of the magnetic impurity, arising due to valence fluctuations on the impurity site [74], give rise to enhanced scattering near the M and X points. These features are not of course present in the scalar impurity QPI, and are as such one signature of strong electron correlations in magnetic impurities.

For the 3D cubic lattice the dynamics are rather different, for two reasons: the host function $\Lambda(\mathbf{q}, \omega)$ does not contain divergences, and the magnetic impurity Green function does not vanish at low energies because the host density of states is essentially flat for $|\omega| \ll t$.

For a scalar impurity on the cubic (100) surface, the QPI intensity vanishes everywhere at low energies $|\omega| \to 0$ because $\Lambda''(\mathbf{q}, \omega) = -\Lambda''(\mathbf{q}, -\omega)$ is odd in ω — see centre row panels of Figure 3.6. By contrast, the Kondo effect gives rise to enhanced scattering at temperatures and energies $\ll T_{\mathrm{K}}$; this gives rise to a large finite QPI intensity for $\omega \ll T_{\mathrm{K}}$. This is the typical behaviour expected for magnetic impurities in standard metallic systems.

Finally, we consider QPI dynamics on the the honeycomb lattice. In the case of the scalar impurity, the region of intense intra-valley scattering around Γ and Γ_2 described by Eq. 3.60 disperses linearly at low energies according to Eq. 3.59, with $d_\Gamma(\omega) \sim \omega$. As $\omega \to 0$, the only divergent points are at $\mathbf{q}^* = \mathbf{q}_\Gamma$ and $\mathbf{q}_{\Gamma_2}$. At $\mathbf{q} = \mathbf{q}_{\mathrm{K}}$, the QPI $\Delta\rho(\mathbf{q}_{\mathrm{K}}, \omega) = 0$ is identically zero for any $|\omega| < t$. These features are shown in the lower panels of Figure 3.6.

The QPI for the magnetic impurity near these points shows intense scattering at energies $|\omega| \sim U/2$, corresponding to the Hubbard satellites in the impurity spectral function due to charge fluctuations. At lower energies, however, $G_d(\omega)$ vanishes linearly according to Eq. 3.48 due to the host LDOS which also vanishes linearly at low energies. Importantly, the Kondo effect is suppressed at particle-hole symmetry, and the local moment phase is always stable for any interaction strength [65, 56]. Electron correlations give rise to the nontrivial spin-flip scattering typical of such degenerate non-Fermi liquid phases [65, 122]. As a result the QPI for the magnetic impurity

vanishes everywhere at low energies, according to

$$|\Delta\rho(\mathbf{q},\omega)| \overset{|\omega|\to 0}{\sim} \begin{cases} |\omega| \ln^3 \left|\omega/t\right| & : \ \mathbf{q} = \mathbf{q}_{\Gamma_{(2)}} \\ 0 & : \ \mathbf{q} = \mathbf{q}_{\mathrm{K}} \\ |\omega| \ln \left|\omega/t\right| & : \ \text{elsewhere} \, . \end{cases} \tag{3.67}$$

3.4.2 Universality

We focus now on a single magnetic impurity on the (100) surface of a 3D cubic lattice – the case most relevant to standard metallic systems where the host density of states becomes essentially flat at low energies, $\omega \ll t$, as indicated by Eq. 3.45. At energy scales significantly below the hopping matrix element t, the physics of the system is essential that of a flat conduction band in the (infinitely) wide-band limit [74]. The Kondo effect is operative in such systems [74], with a spectral resonance setting in on temperature/energy scales $\sim T_{\mathrm{K}}$ as depicted in the centre panel of Figure 3.2. This resonance embodies enhanced spin-flip scattering, which screens the impurity local moment dynamically. Importantly, all physical properties depend only on the single emergent scale T_{K} at low temperatures/energies, reflecting the *universal* RG flow between local moment and strong coupling fixed points [74].

At sufficiently low temperatures $T \ll T_{\mathrm{K}}$, the impurity Green function $G_d(\omega)$ is a universal function of ω/T_{K} on all energy scales $|\omega| \ll \min(t, V^2/U)$ — not only for $|\omega| \ll T_{\mathrm{K}}$ where strong coupling Fermi liquid behaviour Eq. 3.46 holds, but also for $|\omega| \gg T_{\mathrm{K}}$ where local moment physics dominates the dynamics. In that case, the impurity spectral function takes the asymptotic form [64],

$$-\mathrm{Im}\ G_d(\omega) \overset{|\omega|\gg T_{\mathrm{K}}}{\sim} \frac{1}{1 + a \ln^2 |b\omega/T_{\mathrm{K}}|} \, , \tag{3.68}$$

with $a, b = \mathcal{O}(1)$ constants. This behaviour for $T_{\mathrm{K}} \ll |\omega| \ll \min(t, V^2/U)$ is universal because the hybridization function Im $\Gamma(\omega)$ is essentially constant for $|\omega| \ll \min(t, V^2/U)$ on the cubic lattice (and Re $\Gamma(\omega) \sim \omega$).

Similarly, the real part of the host function $\Lambda'(\mathbf{q},\omega)$ becomes constant on energy scales $|\omega| \ll t$, while $\Lambda'(\mathbf{q},\omega) \sim \omega$. In the scaling limit $T_{\mathrm{K}} \to 0$, Im $G_d(\omega)$ thus controls the energy-dependence of the QPI in the universal regime (see Eq. 3.44). In practice, non-universal contributions are negligible for finite $T_{\mathrm{K}} \ll \min(t, V^2/U)$.

In consequence, the entire QPI develops a universal scanning-energy dependence at low energies and temperatures. This means that magnetic impurities with different interaction strengths U and couplings V on different metallic substrates give the

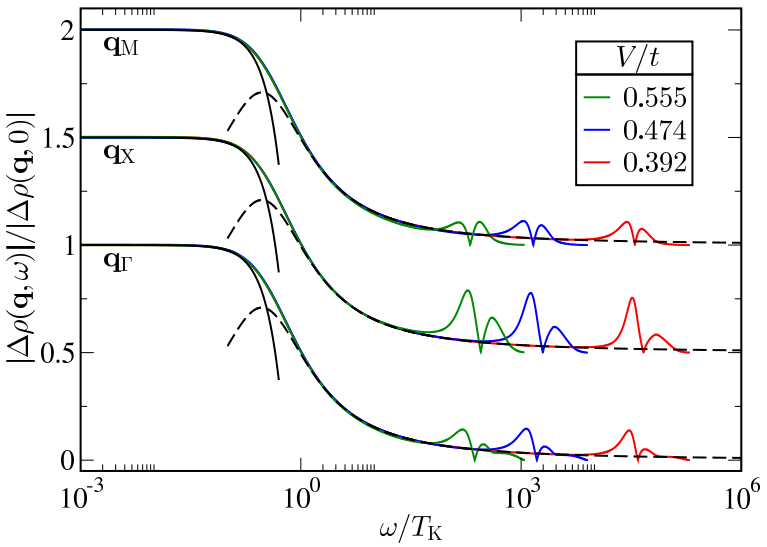

Fig. 3.7 QPI $|\Delta\rho(\mathbf{q},\omega)|/|\Delta\rho(\mathbf{q},0)|$ vs ω/T_K for a magnetic impurity on the 3D cubic (100) surface for scattering vectors $\mathbf{q} = \mathbf{q}_\Gamma$, $\mathbf{q}_\mathrm{X}$ and $\mathbf{q}_\mathrm{M}$ (vertically offset by 0.5 for clarity), plotted for a range of impurity parameters: $V/t = 0.555$, 0.474, 0.392 with fixed $U = 1.95t$, corresponding to $T_\mathrm{K}/t = 5 \times 10^{-3}$, 7×10^{-4} and 3×10^{-5}. Eq. 3.46 (solid line) and Eq. 3.68 (dashed) describe $|\omega| \ll T_\mathrm{K}$ and $\gg T_\mathrm{K}$ asymptotes.

same normalized low-temperature/energy QPI $|\Delta\rho(\mathbf{q},\omega)|/|\Delta\rho(\mathbf{q},0)|$ when plotted vs rescaled scanning-energy ω/T_K, for any scattering vector $\mathbf{q}$. Rescaled experimental QPI data for different systems should thus collapse onto a part of this universal curve, providing the unambiguous signature of scattering from magnetic impurities. This scaling collapse is demonstrated for the 3D cubic lattice in Figure 3.7. Departure from universality is governed by the onset of ω-dependence in $\Lambda(\mathbf{q},\omega)$, which is distinct for each $\mathbf{q}$; for the experimentally relevant parameters used, this is found to occur at $|\omega| \gtrsim 20T_\mathrm{K} \simeq 0.1t$.

3.4.3 Thermal effects

So far we have considered $T = 0$, appropriate in practice when $T \lesssim T_\mathrm{K} \ll t$, such that temperature is the smallest energy scale in the problem. This regime is of most relevance, as typical STM experiments are conducted at ~ 5K [202]; however, studies at higher T may also be performed [148], allowing the change in QPI upon increasing temperature through T_K and beyond to be investigated.

Non-interacting conduction electrons and uncorrelated impurities (such as the scalar impurity) in practice have effectively T-independent electronic structure, and thus QPI. By contrast, electronic correlations of the magnetic adatom exhibit a strong

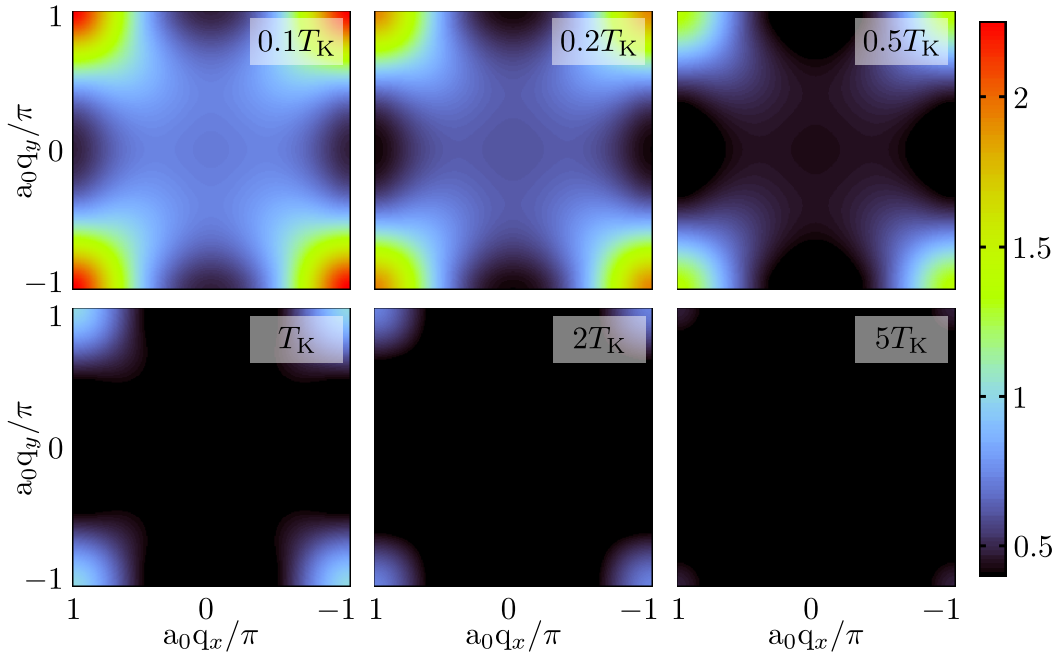

Fig. 3.8 Simulated experimental FT-STS measurements $|\Delta\rho_{\text{meas}}(\mathbf{q}, \omega = 0.1T_K)|$ for a single magnetic impurity (parameters as in Figure 3.2, such that $T_K = 5 \times 10^{-3}t$) at fixed scanning energy, plotted across the 1BZ for a series of temperatures, $T/T_K = 0.1$, 0.2, 0.5, 1, 2 and 5.

T-dependence, entering the t-matrix via the impurity Green function. As T is increased in metallic systems, the Kondo singlet is broken, destroying the Kondo resonance on the scale $T \gtrsim T_K$ and resulting in local-moment physics [74]. This results in a quite dramatic change in the t-matrix, and hence QPI, on increasing T through T_K.

In addition to this interaction-driven T-dependence, the local tunnelling current measured in STS is weakly T-dependent due to thermal excitation of conduction electrons; at finite-T, the differential conductance is given by

$$\frac{dI}{dV}(\mathbf{r}_i, \omega = eV, T) \propto \int_{-\infty}^{\infty} d\varepsilon\ \rho(\mathbf{r}_i, \varepsilon, T) f'(\omega - \varepsilon, T), \tag{3.69}$$

where $f'(\omega - \varepsilon, T) = \frac{d}{d\omega} f(\omega - \varepsilon, T)$ and $f(x, T) = [1 + \exp(x/T)]^{-1}$ is the Fermi function. Eq. 3.69 represents the convolution of the LDOS (T-dependent only for the magnetic impurity) with a broadening kernel, controlled by T. The QPI measured via FT-STS, $\Delta\rho_{\text{meas}}(\mathbf{q}, \omega, T)$, is then related to the "true" QPI by:

$$\Delta\rho_{\text{meas}}(\mathbf{q}, \omega, T) = \int_{-\infty}^{\infty} d\varepsilon\ \Delta\rho(\mathbf{q}, \varepsilon, T) f'(\omega - \varepsilon, T) \tag{3.70}$$

Figure 3.8 shows the thermal evolution of the QPI for an impurity embedded on the 3D cubic (100) surface. For the magnetic impurity, the magnitude of the QPI decreases substantially as T increases through $T_{\rm K}$, and the Kondo resonance is suppressed. By contrast the QPI for a scalar impurity has a much simpler T-dependence (entering only via the thermal broadening, Eq. 3.70), with essentially no T-dependence for $T \ll t$, as depicted by the dashed line in Figure 3.9. The strong T-dependence of QPI is a characteristic signature of Kondo physics in systems with magnetic impurities.

The asymptotic low-T expansion of the impurity Green function at particle-hole symmetry and $\omega = 0$ (applicable in the regime $\omega \ll T \ll T_{\rm K}$) is a universal function of the Kondo temperature [74],

$$\mathrm{Im}\Gamma(\omega = 0) \times \mathrm{Im}\, G_d(\omega = 0, T) \overset{T \ll T_{\rm K}}{\sim} 1 - \alpha_T (T/T_{\rm K})^2 + \ldots \tag{3.71}$$

This leads to a close correspondence between the ω- and T-dependence of the QPI (via the impurity Green function, comparing Eqs. 3.46 and 3.71), as seen by comparison of the upper and lower panels in Figure 3.9.

As such we expect to observe universal scaling in the T-dependence of the QPI for the magnetic impurity, analogous to that of the ω-dependence. The comparison of the pure QPI and the thermally broadened FT-STS signal in the inset of Figure 3.9 (inset) demonstrates this universal behaviour, which is unaffected by the thermal broadening of the STM-measured conductance Eq. 3.70 (up to a trivial scale factor).

3.5 Interpretation of FT-STS

3.5.1 Finite-size effects

In experiment, the surface LDOS $\Delta\rho(\mathbf{r}_i, \omega)$ is measured over an $L \times L$ plaquette using STM [78], with the QPI obtained from Eq. 3.15. The $\mathbf{q}$-space resolution of the resulting QPI naturally depends on the real-space sample size. The "true" QPI is recovered as $L \to \infty$, obtained theoretically by the t-matrix approach.

We now consider explicitly the effects of finite sample size, by simulating the experimental protocol. The LDOS for these surface sites is calculated exactly using Eq. 3.16, with the non-local free Green functions obtained using the convolution method described in the appendix.

Figure 3.10 shows a Brillouin zone cut through the QPI for a magnetic impurity on the cubic lattice (100) surface, computed in the $L \to \infty$ limit using the t-matrix approach (solid line). This true QPI is compared with results for the same system

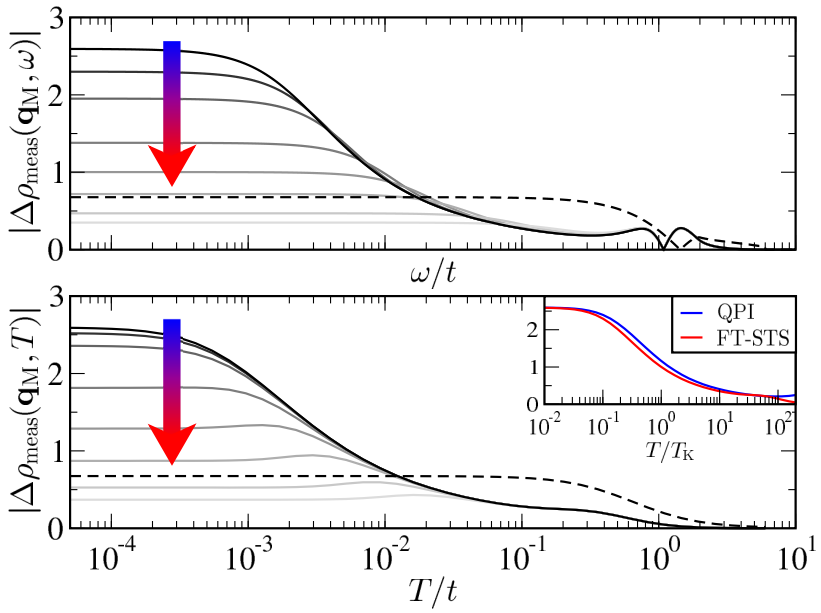

Fig. 3.9 QPI $|\Delta\rho_{\rm meas}(\mathbf{q}_{\rm M})|$ for a single magnetic impurity (parameters given in Figure 3.2, such that $T_{\rm K} = 5\times10^{-3}t$) at the point $\mathbf{q}_{\rm M} = (\pi,\pi)$ in the 1BZ, shown as a function of ω (T) at a series of different T (ω) in the upper (lower) panel; such that $T/T_{\rm K}$ ($\omega/T_{\rm K}$) = $0.01, 0.1, 0.2, 0.5, 1, 2, 5, 10$. Increasing T from low to high is denoted by the arrow. The QPI due to a scalar impurity is also plotted (dashed line) for comparison.
Lower panel inset: measured FT-STS (red) and the "true" QPI (blue), as a function of $T/T_{\rm K}$, showing very similar universal behaviour in each case (up to a scale factor due to thermal broadening).

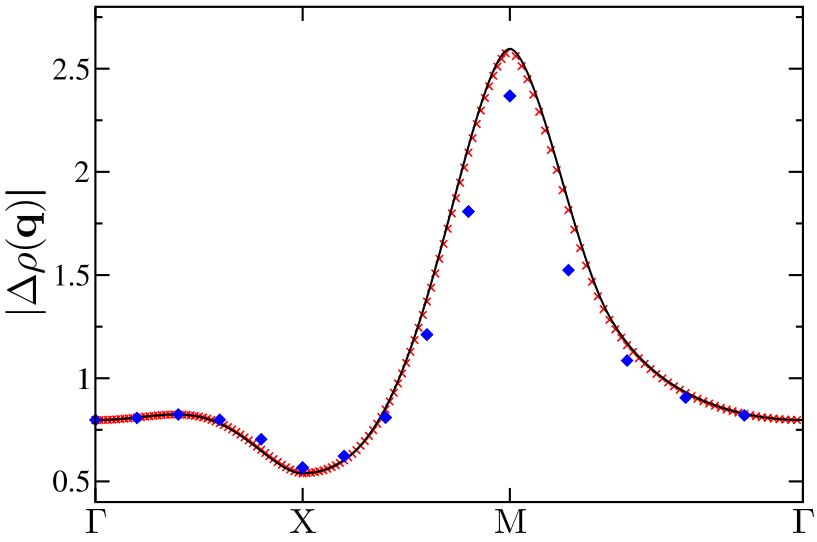

Fig. 3.10 Brillouin zone cut of $|\Delta\rho(\mathbf{q},\omega)|$ for a magnetic impurity on the 3D cubic (100) surface at $\omega = 10^{-4}t$. Exact QPI (line) calculated via the t-matrix approach (Eq. 3.44), compared with the direct real-space approach (Eq. 3.15), sampling an $L \times L$ surface plaquette with $L = 100$ (cross points) and $L = 10$ (diamond points). Impurity parameters as in Figure 3.2.

restricting to an $L \times L$ surface sample, with $L = 100$ (crosses) and $L = 10$ (diamonds). The true QPI is very well-approximated when $L = 100$ is used (corresponding to a plaquette of side length $\sim 10^2$ Å, as typical in experiment [78]). The $\mathbf{q}$-space resolution is also sufficient to capture accurately all features. Indeed, even for an extremely small sample region $L = 10$, the accuracy is surprisingly good- although the discretization is severe.

Reassuringly, the experimental protocol reproduces accurately the true QPI. A large sample size is however still needed to resolve sharp $\mathbf{q}$-space features; in 2D systems, the characteristic sharp cusps in the QPI in Figs 3.3 and 3.5 would require very large LDOS samples in real space.

3.5.2 JDOS interpretation

In Chapter 2 we considered the frequently-used interpretation of the QPI in terms of the joint density of states (JDOS), for example in Refs. 78, 183, 184. Based on simple phenomenological arguments [184] it is argued that the amplitude of impurity-induced scattering from $\mathbf{k}$ to $\mathbf{k}'$ at energy ω is dependent on the product of the densities of quasiparticle states at $\mathbf{k}$ and $\mathbf{k}' = \mathbf{k} + \mathbf{q}$, i.e. the *joint* density of states between the two points. Moreover it is proposed that the QPI may be dominated by individual

contributions between specific pairs of points in **k**-space both with high densities of states, giving rise to the assignment of particular features in the QPI $|\Delta\rho(\mathbf{q},\omega)|$ in terms of these characteristic vectors. This allows the inference of the electronic structure of the clean host material, in particular the fermiology and dispersion of electronic bands. Formalizing this phenomenological approach, the JDOS is defined as

$$J(\mathbf{q},\omega) = \int_{1\mathrm{BZ}} \frac{d^2\mathbf{k}}{\Omega_{BZ}} \,\mathrm{Im}\; G^0(\mathbf{k},\omega)\,\mathrm{Im}\; G^0(\mathbf{k}+\mathbf{q},\omega)\,, \tag{3.72}$$

where $\rho^0(\mathbf{k},\omega) = \pi^{-1}\mathrm{Im}\; G^0(\mathbf{k},\omega)$ is the spectral density of (surface) states at scanning energy ω. In the case of 2D or pseudo-2D systems, for which the surface quasiparticle lifetime is long, the JDOS is related to scattering between particular pairs of points on a constant energy contour (CEC) in **k**-space, as shown in Chapter 2. $J(\mathbf{q},\omega)$ defined via Eq. 3.72 may also be calculated for 3D systems in which surface states couple to the bulk, for example the 3D cubic (100) surface investigated in Section 3.3.3 and elsewhere in this chapter – although the simple picture of scattering between points lying on a CEC is lost due to dephazing of surface quasiparticles by coupling to the bulk, as discussed in Section 3.3.3.

The relative success of the JDOS approach in some cases, demonstrated in Ref. 204, for example, and the simplicity of the JDOS picture has motivated efforts to connect rigorously the QPI and JDOS. Notably, the perturbative approach employed in Ref. 183 attempts the link by assuming a constant scattering amplitude and phase along the constant energy contour. However, a faithful description of interfering scattering processes typically requires relative phase information; and the JDOS simply lacks information about overlap matrix elements between states in the impurity-coupled system. In consequence, the QPI may be small even when the JDOS is large (as may be verified explicitly). The JDOS picture then fails to capture the basic physics of the scattering – as is known, for example, in graphene [184], in topological insulators [66, 120] and Weyl semi-metals [140].

In Chapter 2, we undertook a careful analysis of the relationship between JDOS and QPI, establishing the approximations and fundamental limitations of the former in predicting the latter, and demonstrating that no quantitative link between the two quantities exists in any case. It was shown that the JDOS is most closely related to the QPI for a simple scalar impurity on a centrosymmetric lattice, for which the two quantities are the imaginary and real parts (respectively) of a generalized joint density

of states (GJDOS), a complex response function defined as

$$R(\mathbf{q},\omega) = \int\limits_{1\mathrm{BZ}} \frac{d^2\mathbf{k}}{\Omega_{BZ}}\ \mathrm{Im}\ G^0(\mathbf{k},\omega)\ G^0(\mathbf{k}+\mathbf{q},\omega)\,. \tag{3.73}$$

From Eqs. 3.42 and 3.49 (or Eq. 3.54), the QPI in this case can be written as $\Delta\rho(\mathbf{q},\omega) = v_0 \mathrm{Im}\ \Lambda(\mathbf{q},\omega)$, such that

$$\Delta\rho(\mathbf{q},\omega) = 2v_0 \int\limits_{1\mathrm{BZ}} \frac{d^2\mathbf{k}}{\Omega_{BZ}}\ \mathrm{Im}\ G^0(\mathbf{k},\omega)\mathrm{Re}\ G^0(\mathbf{k}+\mathbf{q},\omega)\ , \tag{3.74}$$

where we have exploited periodicity across the 1SBZ, i.e. $\mathrm{Im}\ \Lambda(\mathbf{q},\omega) = 2\mathrm{Re}\ R(\mathbf{q},\omega)$, while $J(\mathbf{q},\omega) = \mathrm{Im}\ R(\mathbf{q},\omega)$. Despite the QPI and JDOS being related to the real and imaginary parts of $R(\mathbf{q},\omega)$, we emphasize that they are *not* Hilbert conjugates as $R(\mathbf{q},\omega)$ is not an analytic function. In Chapter 2 we demonstrated that (divergent) features in the JDOS were not necessarily reproduced in the QPI.

Nevertheless, the JDOS interpretation of the QPI may be qualitatively correct for dilute scalar impurities on centrosymmetric lattices, because the underlying **q**-space topology of singular lines is similar for $\mathrm{Re}\ R(\mathbf{q},\omega)$ and $\mathrm{Im}\ R(\mathbf{q},\omega)$. In Section 2.2.1 we established, for 2D systems, the singular lines along which (and points at which) the JDOS diverges. Moreover, criteria for these lines to be present also in the QPI were established. By way of illustration, the left panels of Figure 3.11 compare the JDOS (lower panel) to the QPI (upper panel) for the 2D square lattice. The structure of both quantities is qualitatively similar, displaying common envelopes traced by lines of divergence in **q**-space. However, the detailed behaviour of the JDOS differs substantially from that of the QPI: extra structure is evident around the Γ ($\mathrm{a}_0\mathbf{q} = (0,0)$) point *inside* the envelope of divergence, while the intensity of the JDOS *outside* the divergent envelope is significantly larger than that of the QPI, and the functional form as the divergent envelope is approached from M ($\mathrm{a}_0\mathbf{q} = (\pi,0)$) is also different. The middle panels of Figure 3.11 plot the JDOS and QPI for the 3D cubic lattice (100) surface (respectively); in this case the JDOS fails completely to capture the **q**-space structure and intensity of the QPI, even displaying a different periodicity. This is due to the failure of the simple picture of scattering quasiparticles on a CEC: in the 3D cubic (100) surface case, there are substantially more scattering contributions, which interfere in a non-trivial manner to give the QPI. The JDOS neglects the *interference* of such scattering terms, in effect simply summing the magnitudes of such scattering

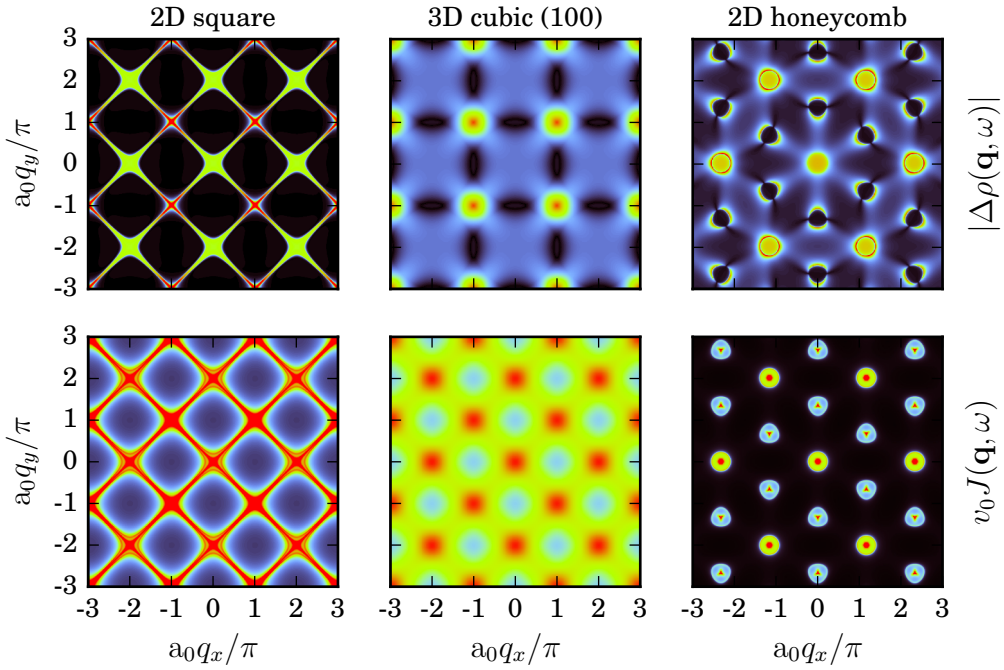

Fig. 3.11 Comparison of QPI, $|\Delta\rho(\mathbf{q},\omega)|$ (upper panels), with the JDOS (lower panels), plotted as $v_0 J(\mathbf{q},\omega)$, for the 2D square (left), 3D cubic (100) surface (middle) and 2D honeycomb (right) lattices for scanning energy ω and Born impurity scattering potential v as in Figs. 3.3, 3.4 and 3.5 respectively. Colour maps are scaled to highlight relevant features as the relative intensities of the JDOS and QPI are somewhat arbitrary, given the (at best) qualitative link between the two quantities.

amplitudes across the Brillouin zone, and thus naturally fails to accurately represent the QPI.

The above connection via Eq. 3.73 does *not* hold in the case of non-centrosymmetric lattices, or lattices with multiple sites or orbitals, for which Eq. 3.74 is inapplicable. The QPI, $\Delta\rho(\mathbf{q},\omega)$, must instead be calculated via the general procedure given in Section 3.2.2 in the case of the 2D honeycomb lattice, involving in that case an additional momentum dependence of the scattering t-matrix and phase factors resulting from the real-space sublattice structure (Eqs. 3.37–3.39). This explains the failure of the JDOS interpretation in the case of impurities in graphene, discussed Section 3.3.4 [184]. The JDOS for such a multi-band system is defined heuristically in band space as

$$J_{nm}(\mathbf{q},\omega) = \int_{1\mathrm{BZ}} \frac{d^2\mathbf{k}}{\Omega_{BZ}} \,\mathrm{Im}\, G^0_n(\mathbf{k},\omega)\,\mathrm{Im}\, G^0_m(\mathbf{k}+\mathbf{q},\omega)\,, \tag{3.75}$$

such that intra- and inter-band scattering ($n = m$ and $n \neq m$ respectively) are both permitted, and the momentum dependence of the t-matrix, arising even in the local s-wave scattering case due to inter-orbital coupling in the host Hamiltonian, is neglected. In the case of the honeycomb lattice, the sign-definite dispersion for each band (Eq. 3.35a) means that $\mathrm{Im}\, G^0_{+(-)}(\mathbf{k},\omega) = 0$ and thus $J_{++(--)}(\mathbf{q},\omega) = 0$ for $\omega < (>)0$, while $J_{+-}(\mathbf{q},\omega) = 0$ for all ω. We emphasize that, by contrast, the full QPI, calculated via Eqs. 3.37–3.39, includes (potentially non-zero) contributions due to inter-band scattering of the form $\sim \mathrm{Re}\, G^0_-(\mathbf{k},\omega)\,\mathrm{Re}\, G^0_+(\mathbf{k}+\mathbf{q},\omega)$. The right panels of Figure 3.11 plot the QPI (upper panel) and JDOS (lower panel) for the honeycomb lattice. As in the 2D square lattice case discussed above, the JDOS predicts the approximate topology of the QPI in $\mathbf{q}$ space, but fails to capture detailed information about both the magnitude inside and outside the envelopes of divergence, and the functional form on approaching the divergent lines from either side. The lack of phase information contained in the JDOS renders the Γ and Γ_2 points ($\mathrm{a}_0\mathbf{q} = (0,0)$ and $2\pi(1/\sqrt{3},1)$) equivalent, in contrast to the QPI (as discussed in Section 3.3.4). Most significantly, the features around K ($\mathrm{a}_0\mathbf{q} = 2\pi(1/\sqrt{3},1/3)$), which result from inter-valley scattering (see Section 3.3.4 for details), differ substantially in the QPI and JDOS. The distinctive "pinch point" structure, in which the intensity of the QPI around the divergent envelope has nodes along the line perpendicular to $\Gamma \to \mathrm{K}$ is completely absent in the JDOS; these features reflect the orbital texture of the scattered quasiparticles, which is lost in the JDOS.

Finally, we emphasize that the presence of magnetic impurities renders the JDOS an even less accurate predictor for the QPI. This is because the t-matrix is a complex

dynamical object: the real and imaginary parts of the host response function $\Lambda(\mathbf{q},\omega)$, defined by Eq. 3.20b both contribute to the QPI, with the sign and magnitude of each contribution depending on the magnitude and phase of the t-matrix. The resulting interference between different contributions to the QPI is thus dependent on phase information that is simply not contained in the JDOS.

3.5.3 Wannier basis expansion of the QPI

In Section 2.3 we considered several complicating factors that may arise in an experimental setting when measuring the QPI via FT-STS. The STM tip measures the LDOS in (continuous) real space, while theoretical calculations are typically carried out on (tight binding) lattice models of the underlying host, in which information about atomic wavefunctions is "integrated out" (encoded solely in the form of the hopping matrix elements). Moreover the STM tip is atomically sharp, providing sub-unit-cell spatial resolution and thus able to probe oscillations in the LDOS with momenta outside of the first Brillouin zone. In order to correctly account for the true spatial structure of the LDOS, the lattice LDOS must be expanded in an appropriate Wannier basis, as discussed in Section 2.3.2. The simplest, albeit somewhat crude, approximation is to neglect the Wannier expansion coefficients, formally equivalent to setting $W(\mathbf{r}-\mathbf{r}_i)=\delta(\mathbf{r}-\mathbf{r}_i)$, assuming that STS directly probes the lattice Green functions of the host system. We have adopted this convention implicitly thus far in this chapter (as is conventional in theoretical calculations of the QPI – see, for example Refs. 34, 204, 102).

From Section 2.3.2, we expand the lattice Green functions in the (local) Wannier basis of each site,

$$G(\mathbf{r},\mathbf{r}',\omega)=\sum_{i,j}W(\mathbf{r}-\mathbf{r}_i)W^*(\mathbf{r}'-\mathbf{r}_j)G(\mathbf{r}_i,\mathbf{r}_j,\omega)\,, \tag{3.76}$$

giving the QPI calculated in the Wannier basis

$$\Delta\rho(\mathbf{q},\omega)=-\pi^{-1}\,\mathrm{Im}\;\sum_{\mathbf{k}}W(\mathbf{k})\Delta G(\mathbf{k},\mathbf{k}+\mathbf{q},\omega)W^*(\mathbf{k}+\mathbf{q})\,, \tag{3.77}$$

where $W(\mathbf{k})=\int d^2r\;\mathrm{e}^{\mathrm{i}\mathbf{k}\cdot\mathbf{r}}W(\mathbf{r})$ [106, 45]. For a host material consisting of s-like atomic orbitals, Wannier functions of Gaussian form are plausible, $W(\mathbf{r})=N_{\mathbf{r}}\mathrm{e}^{-|\mathbf{r}|^2/2\mathrm{a}^2}$, where the ratio a/a_0 controls the extension of the Wannier orbital within the unit cell (with normalization constant $N_{\mathbf{r}}$). The Fourier transform gives $W(\mathbf{k})=N_{\mathbf{k}}\mathrm{e}^{-|\mathrm{a}_0\mathbf{k}|^2(\mathrm{a}/\mathrm{a}_0)^2/2}$, and so the consideration of the full continuum representation of the Green functions

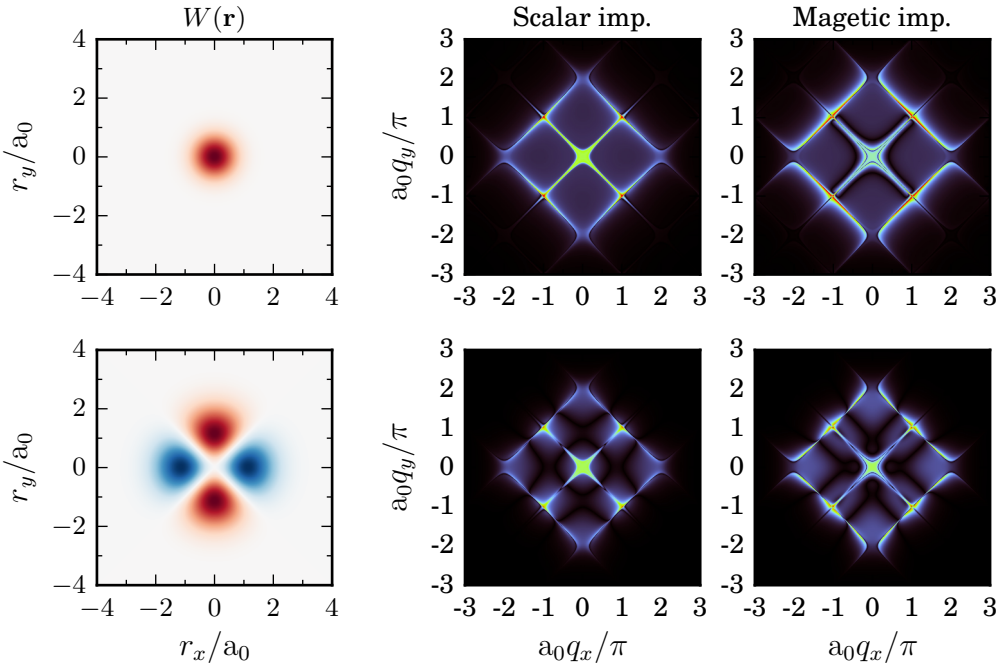

Fig. 3.12 QPI, $|\Delta\rho(\mathbf{q},\omega)|$, calculated in the Wannier basis (of *s*-wave and *d*-wave orbital symmetries for upper and lower panels respectively), with the left panels plotting the local Wannier function $W(\mathbf{r})$, given by Eqs. 3.78 and 3.79, for each case. $W(\mathbf{r})$ is red(blue) for positive(negative) phase.

in the Wannier basis is to impose a smooth, isotropic cutoff in the momentum-space components of the LDOS modulation pattern, controlled by $(\mathrm{a}_0/\mathrm{a})$, limiting the resolution of experimental FT-STS measurements in **q**-space. By contrast, the simple approximation that the FT-STS probes the lattice QPI directly results in a signal that is *periodic* in momentum space, as seen in Section 3.3. Experimentally observed FT-STS measurements, for example Refs 78 and 206, typically extends out to approximately twice the first Brillouin zone, consistent with the concept of a momentum-space cutoff in the scattering information that may be measured by the STM tip.

For a metallic system, the radial extension of the surface Wannier orbitals is expected to be a significant fraction of the lattice constant, $\mathrm{a}/\mathrm{a}_0 \sim 0.5$. The upper panels of Figure 3.12 plot the QPI due to a scalar (middle panel) and magnetic impurity (right panel), calculated in the Wannier basis of *s*-like local orbitals in real space $W(\mathbf{r})$

such that

$$W(\mathbf{r}) = N^s_{\mathbf{r}}\, \mathrm{e}^{-(r_x^2+r_y^2)/(2a^2)} \tag{3.78}$$

for $\mathrm{a} = 0.5\mathrm{a}_0$ (depicted in the left panel). By comparison, the QPI response plotted in Figure 3.3 is recovered for $\mathrm{a} \lesssim 0.1\mathrm{a}_0$. The QPI in the first Brillouin zone is qualitatively similar to that plotted in Figure 3.3, calculated directly from the lattice LDOS, but the cutoff-effect of the evaluation in the Wannier basis is clear beyond the first Brillouin zone. Moreover, the intensity of the QPI in certain regions is significantly altered: for example, outside the envelope of divergent lines described in Section 3.3.2, the QPI due to a scalar impurity has almost zero intensity for the lattice QPI (Figure 3.3 left panel), while there is residual intensity in the Wannier-basis QPI (Figure 3.12 left panel). This is due to destructive interference of higher-momentum components in the lattice case, while the Wannier-basis QPI has incomplete cancellation of intensity at these scattering vectors due to the imposed cut-off in momentum space.

Isotropic, *s*-like Wannier orbitals are an appropriate basis for simple metallic systems, but in many of the materials studied via FT-STS the relevant conduction electron bands are derived from atomic orbitals of higher angular momentum and multi-site unit cells. As such Wannier bases consisting of higher angular harmonics (of *p*-, *d*- or even *f*-wave symmetry) must also be considered. By way of illustration, we consider the case of a *d*-wave symmetric Wannier basis, chosen to reproduce the symmetry of the Cu $3d_{x^2-y^2}$ orbital, from which the active band in the cuprate high-T_c superconductor $Bi_2Sr_2CaCu_2O_8$ [106, 45]. In the lower panels of Figure 3.12 we plot the QPI for scalar (middle panel) and magnetic impurities (right panel), calculated in a Wannier basis of *d*-wave symmetry,

$$W(\mathbf{r}) = N^d_{\mathbf{r}} \left(r_x^2 - r_y^2\right) \mathrm{e}^{-(r_x^2+r_y^2)/(2a^2)}\,, \tag{3.79}$$

with $\mathrm{a} = 0.8\mathrm{a}_0$, depicted in the left panel of Figure 3.12. The nodal structure of the Wannier orbital in real space is reflected in additional **q**-space structure in the QPI in comparison to the simple *s*-wave case for both scalar and magnetic impurities, which depends on the spatial extent of the Wannier orbitals. While the symmetry of the Wannier basis has a significant impact on the QPI, the exact form of the Wannier orbital is found to have a much smaller effect.

Given the substantive effect that the choice of Wannier basis can have on the resultant QPI, an accurate representation is needed in order to accurately match to (or predict) experimental FT-STS measurements. In order to achieve quantitative

accuracy, more advanced electronic structure calculations are necessary in order to predict the detailed form of the relevant Wannier orbitals [106]. However, insight can be gained easily via appropriate phenomenological forms for the spatial wavefunctions of appropriate symmetry and radial extent. In Chapter 5 we investigate the QPI in Sr_2RuO_4, a complex transition metal oxide in which the choice of Wannier basis is expected to be relevant, using similar wavefunctions to calculate the Wannier-basis QPI.

3.6 Conclusion

In this chapter, we have studied theoretically the use of quasiparticle interference (QPI), measured in FT-STS experiments, as a probe of magnetic adatoms on surfaces. Following a general detailed formulation of the QPI due to an arbitrary distribution of impurities, we turned explicitly to single-impurities adsorbed on a range of host surfaces, taken to be non-interacting electronic systems. The (100) surface of a 3D simple cubic lattice, 2D honeycomb and 2D square lattices are considered, in which the Fermi-level densities of states respectively embody standard metallic behaviour, pseudogap behaviour, and a divergence due to a Van Hove singularity. In all cases, the single-impurity QPI factorizes into a local scattering t-matrix, and a host response function $\Lambda(\mathbf{q}, \omega)$ at scanning energy $\omega = eV$.

The scattering t-matrix for a magnetic impurity is simply related to the impurity Green function – itself dependent on the host lattice – and thus the rich dynamics due to electronic correlations are manifest in the QPI. The (single) quantum impurity system is solved exactly using NRG for each host [29], providing numerically exact impurity Green functions at a range of energies and temperatures. Despite the local, momentum-independent nature of these correlations, the $\mathbf{q}$-space structure of the QPI is found to be qualitatively different from that of a simple scalar impurity due to non-trivial phase shifts associated with scattering from magnetic impurities, which reflect, for example, the Kondo effect [74].

The host response function $\Lambda(\mathbf{q}, \omega)$ is also non-trivial, despite being a property of the free, non-interacting host system. It displays significant structure in $\mathbf{q}$-space, symptomatic of the symmetry and dimensionality of the host. However, its energy-dependence becomes featureless for $|\omega| \ll t$ (with t the inter-site lattice hopping). By contrast, the Kondo physics due to a magnetic impurity is controlled by an emergent scale $T_K \ll t$, and so scattering becomes strongly energy-dependent at low energies. As a consequence, the QPI exhibits *universal* scaling in terms of ω/T_K and T/T_K — a

characteristic hallmark for systems containing magnetic impurities. Conversely, the QPI for systems containing scalar impurities has no energy or temperature dependence on scales $\ll t$.

Having considered the "true" QPI of the underlying host lattice due to both scalar and magnetic impurities, we considered the consequences of several complicating practical factors for experimental FT-STS measurements and their interpretation. The effect of the finite size of measured LDOS maps in real space was considered, and it was found that measurements over a reassuringly small plaquette gave good quantitative agreement with the theoretical QPI (corresponding to the infinite-plaquette limit). The commonly-used interpretation of the QPI measured via FT-STS in terms of the JDOS, explored in Chapter 2 was critically examined for the case of the three representative lattices studied here, and the clear failure of the JDOS to reproduce qualitative features present in the QPI demonstrated. In particular, the JDOS failed severely in the cases of the 3D cubic (100) surface and 2D honeycomb lattices, due (respectively) to the neglect of interference between multiple scattering processes and the underlying orbital texture (multi-band nature) of the host material. We concluded by investigating the effect of including spatial information about the local orbital basis of the host material, calculating the QPI in a model basis of Wannier functions in order to simulate the FT-STS measured via the true LDOS modulations in (continuous) real space. The Wannier-basis QPI was compared to the lattice QPI which is typically calculated in theoretical investigations of the QPI [34, 102, 106], and it was found that the symmetry and radial extent of the local Wannier basis has a significant qualitative impact on the theoretical FT-STS prediction. Consequently, detailed, quantitative comparison between theory and experiment necessitates a careful consideration of the spatial structure of the orbitals probed via STM.

Thus far we have considered local correlation effects only in the form of electron interactions arising for isolated magnetic impurities. In Chapter 4 we turn to the more complex case of multiple, mutually-interacting magnetic impurities embedded in non-interacting host materials, and the resultant QPI. Such systems will display an even wider array of impurity physics, due to the competition of local and non-local (RKKY-type) interactions between impurities. These interactions have a significant impact on the QPI for randomly distributed impurities at experimentally relevant number densities. FT-STS also offers the ability to investigate the effect of interactions between the conduction electrons of the host material, of particular interest for systems in which unusual many-body states are manifest, such as unconventional superconductors. In Chapter 5 we consider the QPI in one such material, Sr_2RuO_4, of interest as an

unconventional superconductor consisting of spin-1 Cooper pairs, for which QPI may provide insights into the nature of the superconducting state and pairing mechanism [174, 206]. Electronic correlations in the normal state are investigated via comparison of theoretical calculations with experimental measurements, and predictions for the QPI in the superconducting state are also made in anticipation of future experimental work.

Chapter 4

Multiple magnetic impurities on surfaces: scattering & QPI

In Chapter 3 we investigated in detail the QPI resulting from a single magnetic impurity, demonstrating the rich *dynamical* structure of the QPI in this case, in comparison with the standard Born scatterer. Described in terms of a single interacting quantum level, such a magnetic impurity can host a free local moment at high energies/temperatures, which is then screened in metallic systems by conduction electrons through the Kondo effect [74, 211, 108] below a characteristic scale $T_{\rm K}^{\rm 1imp}$. The enhanced spin-flip scattering responsible for the Kondo effect at low energies leads to a characteristic impurity spectral resonance [74, 64, 159, 210] observable in STS [118, 191, 128, 129, 202]. Interacting quantum impurities give rise to non-trivial many-body effects which manifest in the induced real-space LDOS modulations from a single magnetic impurity. This produces a characteristic QPI signal, which acquires a universal temperature and scanning-energy dependence at low energies due to universality of the Kondo resonance in terms of $\omega/T_{\rm K}^{\rm 1imp}$ and $T/T_{\rm K}^{\rm 1imp}$ as discussed in Chapter 3.

The dynamics of the QPI therefore provides information on both the phase and magnitude of the scattering t-matrix due to such impurities [143, 48]. The numerical renormalization group (NRG) [211, 108, 29] was employed as the theoretical method of choice for treating a single quantum impurity: it provides access to numerically-exact dynamical impurity quantities on essentially any temperature/energy scale [159, 210, 12]. Solution of the local impurity problem then allows other real-space quantities [136] to be calculated, as well as the QPI, as detailed generally in Chapter 3.

However, real systems contain many impurities: the real-space surface region of a host material probed by STS to obtain QPI could include $N \gtrsim 10 - 100$ impurities, depending on sampling size and impurity density. For potential scatterers of arbitrary

strength the physics remains rather trivial, and the exact scattering t-matrix can be obtained via a summation of an infinite series of intra- and inter-impurity scattering terms [138, 140]. In the case of weak potential scattering, the form of the t-matrix is particularly simple; however the impact on the QPI is significant as discussed in Section 4.4.1. By contrast, systems containing many *magnetic* impurities embody subtle interplays between Kondo physics, effective through-host RKKY interactions, and disorder in the impurity distribution. A full solution in closed form to the scattering problem in such systems is naturally impossible; instead, we seek to develop physically motivated approximations, as described below. These two scenarios (weak potential scattering impurities and magnetic impurities) and the validity of an independent impurity picture are studied in Section 4.4 of this chapter.

We specify a model in Section 4.1 that takes into account explicitly the surface of a 3D metallic host onto which multiple magnetic impurities are deposited, thereby allowing calculation of surface LDOS maps and QPI. Realistic parameters are chosen, yielding single-impurity Kondo temperatures in the range $T_{\mathrm{K}}^{\mathrm{1imp}} \sim 0.1 - 100\mathrm{K}$ relevant to experiment. Electronic and quasiparticle scattering in this system is described in terms of the t-matrix, itself controlled by impurity dynamical quantities. The theoretical prescription for calculating QPI for a many-impurity system in terms of the impurity Green functions is given in Section 4.3, including the effect of surface quasiparticle dephazing by the host bulk.

Solving such a model with N interacting quantum impurities is a formidable challenge because in general it involves N coupled screening channels. Generalization of NRG to deal with two spatially-separated impurities already represents a very significant increase in computational complexity, although accurate results for dynamical quantities are now possible, as discussed in Section 4.2. Our approach to the many-impurity problem in this chapter begins with a detailed analysis of the two-impurity model, known as the Alexander Anderson model (AAM), solved using NRG. The two impurities interact indirectly via an effective RKKY interaction mediated by the host conduction electrons. In the past, the AAM has been approximated via simpler two-impurity models such as the two-impurity Kondo model and two-impurity Anderson models, which feature two impurities, each coupled to their own respective conduction bands, with a direct coupling between them to approximate the host-mediated interaction (see Refs. 87 and 90, for example). In Section 4.2 we treat the *full* AAM explicitly via NRG, which allows the local impurity-host and the non-local inter-impurity interactions to be treated non-perturbatively and on the same footing, rather than resorting to effective models. Moreover, we demonstrate the rich phenomenology of the AAM that

arises due to the dynamic nature of the inter-impurity interaction, which is not fully captured by approximate models. While the qualitative physics of the AAM is broadly similar to that of the effective models referenced above, the more complicated nature of the inter-impurity interaction leads to a significantly more subtle interplay between local (impurity-host) and non-local (inter-impurity) interactions, and some departures from the oversimplified picture given by studies of the reduced, effective models. For experimentally relevant impurity parameters, we find that inter-impurity interactions are important when the impurities are separated by a few lattice sites, giving rise to a rich range of correlated electron physics with distinctive QPI signatures.

A key finding of this chapter is that the impurities behave essentially independently for surprisingly small inter-impurity separation. This has implications for the onset of the "dilute limit" in many-impurity systems. In this case, local quantities are in essence blind to the multi-impurity nature of the system – but the QPI is still affected by a (trivial) impurity structure factor. Calculations for the two-impurity system allow identification of the minimum impurity separation required for the onset of this dilute limit for experimentally relevant parameters, facilitating a description in terms of independent impurities. A "dilute cluster" limit is also identified in systems with higher impurity density, where inter-impurity interactions are only important within independent clusters. We calculate the QPI due to two and many impurities, and explore the consequences of the independent impurity/cluster paradigm. Intra-cluster interactions are found to be important for capturing local spectroscopic details, but to have a weak overall effect on QPI due to low cluster occurrence at typical experimental impurity densities. Our results provide a framework to investigate the effects of disorder due to interacting impurities at experimentally relevant surface coverages.

4.1 Model for multiple magnetic impurities

We consider $N > 1$ magnetic impurities deposited on the surface of a metallic host system. The full Hamiltonian is given by

$$\mathcal{H} = \mathcal{H}_{\text{host}} + \sum_{\alpha=1}^{N} \mathcal{H}_{\text{imp},\alpha} \ . \tag{4.1}$$

The host is taken here to be an infinite 3D cubic tight binding lattice, cleaved to reveal the (100) surface, as studied for the single-impurity case in Chapter 3:

$$\mathcal{H}_{\text{host}} = -t\sum_{z=0}^{\infty}\Big(\sum_{\langle ij\rangle,\sigma}(c^{\dagger}_{(\mathbf{r}_i,z)\sigma}c_{(\mathbf{r}_j,z)\sigma}+\text{H.c.})+\sum_{i,\sigma}(c^{\dagger}_{(\mathbf{r}_i,z)\sigma}c_{(\mathbf{r}_i,(z+1))\sigma}+\text{H.c.})\Big), \qquad (4.2)$$

where $c^{\dagger}_{\mathbf{r}_i z\sigma}$ creates an electron of spin $\sigma =\uparrow/\downarrow$ in the single Wannier orbital localized at site $\mathbf{r}_i$ of layer z (with $z = 0$ denoting the surface), and $\langle ij\rangle$ denotes the sum over nearest-neighbour sites of a 2D square lattice layer. The resulting LDOS on the translationally-invariant surface is finite and flat at low energies, so although we focus on this specific host realization, the real-space physics is rather generic and typical of metallic 3D systems. More complicated materials can always be cast in the layered form of Eq. 4.2 by generalizing to a matrix structure.

As in Chapter 3, we treat the surface explicitly to allow study of the QPI, which is necessarily obtained through surface measurement in FT-STS experiments. We note that coupling the surface layer to the semi-infinite bulk is required to capture the important effects of surface quasiparticle dephazing. Properties of the clean host are characterized by its real-space Green functions, here calculated exactly using the convolution method introduced in Ref. 48, and discussed in detail in Appendix A.

Each magnetic impurity α is described in terms of a single interacting quantum level, tunnel-coupled to a surface ($z = 0$) host site at position $\mathbf{r}_\alpha$,

$$\mathcal{H}_{\text{imp},\alpha} = \sum_{\sigma}\left(\epsilon_d+\frac{U}{2}d^{\dagger}_{\alpha\bar{\sigma}}d_{\alpha\bar{\sigma}}\right)d^{\dagger}_{\alpha\sigma}d_{\alpha\sigma}+V\left(d^{\dagger}_{\alpha\sigma}c_{(\mathbf{r}_\alpha,0)\sigma}+\text{H.c.}\right), \qquad (4.3)$$

where $d^{\dagger}_{\alpha\sigma}$ creates a spin-σ electron on impurity level α. Importantly, such an Anderson impurity has internal spin and charge dynamics due to the local electronic interactions. This is in contrast to a static "magnetic" impurity caricatured by an inhomogeneous magnetic field that breaks underlying time-reversal and spin SU(2) symmetry (and is non-interacting). This chapter aims to present the general formulation of the scattering problem in a system of multiple interacting impurities embedded in a metallic host as simply as possible, and the resultant QPI, using the single-level Anderson impurity as an illustrative case. The generalization of Eq. 4.3 to multi-orbital magnetic impurities is therefore not considered in this chapter (the formal aspects of the scattering problem being largely unchanged).

The generalized quantum impurity problem involving N magnetic impurities, spatially separated and coupled to conduction electrons of the host lattice, is distinctly nontrivial and exhibits a rich range of correlated electron physics. The $N = 1$ model,

comprising a single magnetic impurity, is studied in detail in Chapter 3. Even this simplest case already exhibits strong, non-trivial dynamical effects due to interactions, such as the Kondo effect [74, 39, 69].

In the case of multiple impurities, richer physical behaviour arises due to an effective RKKY interaction which couples impurities indirectly [169, 96, 216, 92, 49]. The RKKY interaction is mediated via the host lattice and therefore depends on the specific impurity distribution in real-space. There is an interplay between local correlations, which lead to independently Kondo screened impurities, and non-local, inter-impurity correlations that result in the formation of entangled clusters themselves screened collectively in a multi-stage process. Impurities can also "screen themselves" by forming inter-impurity singlet states when the effective RKKY interaction is strongly antiferromagnetic.

As has already been highlighted, full treatment of the N-impurity model is a formidable theoretical and computational challenge even for $N = 2$, due to the irreducible two-channel nature of the problem [138]. Consonantly, the problem becomes prohibitively difficult to treat exactly for three or more impurities; this limitation is not only practical (computational), but moreover the treatment of $N \geq 3$ systems via NRG is formally restricted to particular, high-symmetry cases, as is discussed in Section 4.4. Recent technical advances in the field, as detailed in Ref. 187, raise the possibility of treating the three-impurity model exactly within the restraints of these symmetry requirements.

Despite the intractability of the general many-impurity model, much of the essential physics of the many-impurity system is present in the two-impurity model, which contains both local Kondo-type interactions between impurities and the host, and non-local RKKY interactions between the two impurities. As such, the study of this model provides qualitative insights into the many-impurity case, as well as being of interest in its own right. Before investigating the manifestation of the many-impurity effects in the context of QPI due to magnetic adatoms on surfaces, we first investigate the real-space two-impurity Anderson model (known as the Alexander Anderson model [8], given by Eqs. 4.1 and 4.3 with $N = 2$) generally.

4.2 The Alexander Anderson model

The Alexander Anderson model (AAM), given by Eqs. 4.1 and 4.3 with $N = 2$,

$$\mathcal{H}_{AA} = \mathcal{H}_{\text{host}} + \sum_{\alpha=1,2}\sum_{\sigma}\left(\epsilon_d + \frac{U}{2}d^{\dagger}_{\alpha\bar{\sigma}}d_{\alpha\bar{\sigma}}\right)d^{\dagger}_{\alpha\sigma}d_{\alpha\sigma} + V\left(d^{\dagger}_{\alpha\sigma}c_{(\mathbf{r}_\alpha,0)\sigma} + \text{H.c.}\right), \qquad (4.4)$$

consists of two spatially-separated Andersonian impurity sites coupled to a common free-electron conduction band via a local ($s-$wave) hybridization. The model was first proposed in 1964 [8] as a minimal model to investigate the mutual interaction of interacting impurities coupled indirectly via a mediating conduction band. It is thought that a detailed understanding of the physics of the AAM, would provide significant insight into many-impurity systems and correlated lattice models, for example the periodic Anderson model. Despite this, and the large body of work on the single-impurity Anderson model (see Ref. 74 for an overview), limited progress has been made for the AAM due to the significantly increased complexity over the single-impurity Anderson model already alluded to in this chapter. Here we consider the AAM in the context of magnetic adatoms on surfaces, treating the model exactly via NRG. Such calculations have only recently become possible due to increased computational power and technical advances [187], as we explain in Section 4.2.1. While the AAM is explored in the case of magnetic adatoms herein, we note the wider context of these results in the understanding of more complicated models such as the periodic Anderson model.

The two-impurity problem is the simplest to capture the competition between Kondo physics and inter-impurity interactions [87, 90]: a leading-order perturbative treatment generates the host-mediated RKKY interaction, coupling impurities by indirect exchange [169, 96, 216, 87, 112]. The magnitude and sign of the RKKY interaction depends sensitively on the dimensionality and geometry of the host [1], and on the impurity separation vector $\mathbf{R} = (\mathbf{r}_2 - \mathbf{r}_1)$ [11].

Two spatially-separated Anderson impurities are often modelled by a two-impurity Kondo model (2IKM) [87, 90], describing two exchange-coupled spin-$\frac{1}{2}$ impurities each coupled to its own independent conduction electron channel. The physics of this model is immensely rich: Kondo-screened and inter-impurity singlet phases arise, separated by a non-Fermi liquid quantum critical point (QCP) [91, 4, 5, 142]. The characteristics of this QCP are those of the two-channel Kondo (2CK) type [142], named for the two-channel Kondo model in which a single spin-$\frac{1}{2}$ impurity is coupled to two independent conduction channels. Competition between Kondo-screening of the

impurity by each channel gives rise to frustration when the strength of the coupling is the same to both channels, resulting in a non-Fermi liquid 2CK QCP [142].

However, the 2IKM is oversimplified because the two conduction electron channels are not strictly independent in a true real-space system, both being constructed from states of the same electronic host [11]. This is reflected by finite off-diagonal elements of the hybridization matrix, $\mathbf{\Gamma}(\omega)$ in Eq. 4.8. Since $\Gamma_{12}(\omega) = V^2 G^0_{\mathrm{surf}}(\mathbf{r}_1, \mathbf{r}_2, \omega)$ involves the conduction electron propagator between sites on the surface of the host ($\mathbf{r}_1 \neq \mathbf{r}_2$) to which the impurities couple, the two-impurity problem evidently features inter-channel charge transfer processes. These processes have an effect on the renormalization group (RG) flow upon decreasing the energy scale towards the ground sate (they are "RG relevant") – simple perturbations that break the same symmetries can be incorporated directly into the 2IKM, and are known to destabilize the critical point [5]. In such cases, continuous crossovers between regimes of a common Fermi liquid phase arise ubiquitously at low temperatures and energies [179, 141].

The AAM does not therefore support a quantum phase transition. Instead, there is a crossover as a function of impurity separation or impurity-host coupling, with the Kondo regime evolving continuously into an RKKY-dominated regime [182, 33, 157, 222]. This crossover is also known from a simpler variant of the two-impurity Anderson model, in which a hopping t' directly tunnel-couples impurities which are themselves coupled to independent conduction electron channels [170, 171, 92, 89]. In that case, the RKKY interaction is generated to second-order in the tunnel-couplings, while the inter-channel charge transfer arises to third-order [89]. Due to this difference in the orders of the RKKY and inter-channel charge transfer terms, the parameters of the model may be tuned to suppress the latter. As such, despite the lack of a phase transition, upon tuning of the parameters, the RG flow of the model can pass arbitrarily close to the QCP before eventually flowing to a Fermi liquid ground state; critical physics characteristic of the QCP is thus observed on finite energy/temperature scales [89]. NRG, which allows essentially exact calculation of both static and dynamic properties of the system on any temperature or energy scale, is thus invaluable for investigations of such models: approaches focusing on solely the ground-state properties of the system may fail to capture such manifestations of critical physics at intermediate RG flow (finite temperatures/energies).

Returning to the full AAM, it is important to emphasize that inter-channel charge transfer processes cannot simply be neglected: finite $G^0_{\mathrm{surf}}(\mathbf{r}_1, \mathbf{r}_2, \omega)$ is the common origin of both the RKKY interaction itself and the relevant perturbations destroying 2IKM criticality. This commonality makes it unclear if and how the relevant system

parameters, namely the impurity-host interaction strength and the inter-impurity separation (and hence inter-impurity interaction strength), may be tuned in order to access critical physics in the spirit of the tunnel-coupled 2IAM variant discussed above [89]. Furthermore, the *dynamical* nature of $G^0_{\text{surf}}(\mathbf{r}_1, \mathbf{r}_2, \omega)$, resulting from through-lattice electronic propagation, produces nontrivial RG flow. Physical regimes of the real-space model might therefore be inaccessible within the tunnel-coupled 2IAM (where $G^0_{\text{surf}}(\mathbf{r}_1, \mathbf{r}_2, \omega)$ is effectively replaced by an independently tunable real constant hopping t'), or in the 2IKM (where it is neglected altogether).

Clearly if one is interested in the physics of the AAM one must study the full model directly, treating both (local) intra-impurity correlations and (non-local) inter-impurity correlations on an equal basis. As already indicated, such a treatment within NRG has only recently become possible [137, 187]; in order to carry out NRG, the model must first be recast in an appropriate form, as described below.

4.2.1 Numerical Renormalization Group

The NRG procedure for a single-channel quantum impurity model involves formulation in terms of a small, interacting Hamiltonian coupled to a band of free conduction electrons, written in Wilson chain form as a single channel of conduction electrons [211, 108, 109, 29]. The zero-orbital of the semi-finite Wilson chain then corresponds to the effective local orbital (which may be one or more sites of the host lattice) to which the impurity system couples. By contrast, the AAM is a fundamentally two-channel model, despite consisting physically of only one band of conduction electrons, due to the spatial separation of the impurities: the two impurities couple to different sites. Furthermore, the local orbitals to which the impurities couple define the zero-orbitals of two Wilson chains that are not orthogonal to each other at every site down the chain (see Figure 4.1 lower panel), forming a ladder. This results in hopping terms between orbitals of the two Wilson chains, disrupting the familiar exponential decay of couplings between successive sites down the Wilson chains. This exponential decay is essential in generating the separation of energy scales between NRG iterations, which gives the procedure its RG character [211]. This is necessary in order that the truncation of the high-energy sector of the Hilbert space at each step, required to prevent an exponential increase in the size of the Hilbert space from iteration to iteration, may be carried out [29].

Consequently a diagonal basis for the two Wilson chains must be found, rendering the problem amenable to NRG; as we describe below, this is achieved by taking even and odd combinations of the two local orbitals to which the impurities couple, and using

these as the zero-orbitals of two new Wilson chains. Each iteration therefore involves coupling two orbitals, one of each chain, onto the truncated system composed of the interacting Hamiltonian plus a section of the Wilson chains (before diagonalization and truncation of high energy states, as per the conventional NRG procedure [29]). This results in a significant increase in computational complexity over a single channel problem, unless the transformation to a basis in which the two Wilson chains are orthogonal renders the system as two completely independent subsystems (discussed below).

Of central interest, and calculable within NRG [159, 210], are the impurity single-particle dynamics – described generically by elements of the retarded Green function matrix

$$[\mathbf{G}_d(\omega)]_{\alpha,\beta} \equiv G_d^{\alpha\beta}(\omega) = \langle\langle d_{\alpha\sigma}; d^\dagger_{\beta\sigma}\rangle\rangle_\omega, \tag{4.5}$$

where

$$\langle\langle \hat{A}\,; \hat{B}\rangle\rangle_\omega = \mathcal{F}_t\left[-i\theta(t)\langle\{\hat{A}(t), \hat{B}(0)\}\rangle\right] \tag{4.6}$$

is the Fourier transform of the retarded real-time correlator. The propagator $G_d^{\alpha\beta}(\omega)$ therefore contains information on the energy-dependent scattering of electrons between impurities α and β, which manifests in the QPI (as discussed in Section 4.3), as well as providing insight into the state of the impurities themselves.

For a many-impurity system, such Green functions are obtained from a matrix Dyson equation,

$$[\mathbf{G}_d(\omega)]^{-1} = [\mathbf{g}_d(\omega)]^{-1} - \mathbf{\Sigma}(\omega), \tag{4.7}$$

where the non-interacting (but host-coupled) impurity Green functions are given by

$$[\mathbf{g}_d(\omega)]^{-1} = (\omega + \mathrm{i}0^+ - \epsilon_d)\mathbf{I} - \mathbf{\Gamma}(\omega), \tag{4.8}$$

in terms of the hybridization matrix $\mathbf{\Gamma}(\omega)$ with elements $[\mathbf{\Gamma}(\omega)]_{\alpha,\beta} = V^2 G^0_{\mathrm{surf}}(\mathbf{r}_\alpha, \mathbf{r}_\beta, \omega)$. This hybridization matrix describes the coupling to the two (non-orthogonal) Wilson chains, described above. In general, $G^0_{zz'}(\mathbf{r}_\alpha, \mathbf{r}_\beta, \omega) = \langle\langle c_{(\mathbf{r}_\alpha,z)\sigma}; c^\dagger_{(\mathbf{r}_\beta,z')\sigma}\rangle\rangle^0_\omega$ is the propagator between site $\mathbf{r}_\alpha$ of layer z and $\mathbf{r}_\beta$ of layer z' in the clean host (without impurities). As we consider explicitly the surface here, we denote $G_{\mathrm{surf}}(\mathbf{r}, \mathbf{r}', \omega) \equiv G_{00}(\mathbf{r}, \mathbf{r}', \omega)$ throughout. The positions $\mathbf{r}_\alpha$ and $\mathbf{r}_\beta$ denote the host surface sites (or effective orbitals) to which the impurities α and β are coupled.

The self-energy matrix $\mathbf{\Sigma}(\omega)$ contains all effects due to electronic interactions, which give rise to the nontrivial physics in the system. Furthermore, impurity self-energies can be calculated accurately within NRG through the identity,

$$\mathbf{\Sigma}(\omega) = [\mathbf{G}_d(\omega)]^{-1}\mathbf{F}_d(\omega) \ , \tag{4.9}$$

where $[\mathbf{F}_d(\omega)]_{\alpha,\beta} = U\langle\langle d_{\alpha\sigma}; d^\dagger_{\beta\sigma}d^\dagger_{\beta\bar{\sigma}}d_{\beta\bar{\sigma}}\rangle\rangle_\omega$ (a matrix generalization to many impurities of the result originally given for the single-impurity Anderson model [28]). Both $\mathbf{G}_d(\omega)$ and $\mathbf{F}_d(\omega)$ are calculated directly in NRG using the full density matrix approach [159, 210] within the complete Anders-Schiller basis [12]. Impurity Green functions then follow from the matrix Dyson equation, Eq. 4.7.

As indicated above, a transformation that diagonalizes the hybridization matrix (corresponding to the orthogonalization of the two Wilson chains) is required in order to cast the model in a form amenable to treatment with NRG. For the AAM, the translational invariance of the host surface implies that the transformation can be achieved for all ω by a single canonical transformation of operators to an even/odd orbital basis, as illustrated schematically in Fig. 4.1. This yields $G_d^{e/o}(\omega) = (\omega + \mathrm{i}0^+ - \epsilon_d - \Gamma_{e/o}(\omega) - \Sigma_{e/o})^{-1}$, in terms of even/odd quantities $\mathcal{O}_{e/o} = \mathcal{O}_{11} \pm \mathcal{O}_{12}$ (noting that $\mathcal{O}_{11} = \mathcal{O}_{22}$ and $\mathcal{O}_{12} = \mathcal{O}_{21}$ due to the symmetry between the two impurities).

On the level of the Hamiltonian, this transformation corresponds to taking even and odd combinations of the impurity and host fermionic operators around the mirror plane between the two impurities [87, 90]. The explicit form of the resultant even and odd conduction channels in terms of the basis of states of the conduction band is generally complex (detailed in Ref. 222 and 112). However, we emphasize that this complicated transformation of operators is exactly equivalent in this case to the (much cleaner) formulation presented above, in which the energy-dependent hybridization matrix $\mathbf{\Gamma}(\omega)$ is rendered in diagonal form by taking even and odd combinations of $\Gamma_{11}(\omega)$ and $\Gamma_{12}(\omega)$. This can be seen by considering the even/odd combinations of the fermionic operators corresponding to the local orbitals to which each impurity couples,

$$c_{e/o\,\sigma} = \frac{1}{\sqrt{2}}\left(c_{\mathbf{r}_1\sigma} \pm c_{\mathbf{r}_2\sigma}\right) \ , \tag{4.10}$$

which leads directly to $\langle\!\langle c_{e/o\,\sigma}; c^\dagger_{e/o\,\sigma}\rangle\!\rangle^0 = \langle\!\langle c_{1\sigma}; c^\dagger_{1\sigma}\rangle\!\rangle^0 \pm \langle\!\langle c_{1\sigma}; c^\dagger_{2\sigma}\rangle\!\rangle^0$, so that $\Gamma_{e/o}(\omega) = \Gamma_{11}(\omega) \pm \Gamma_{12}(\omega)$.

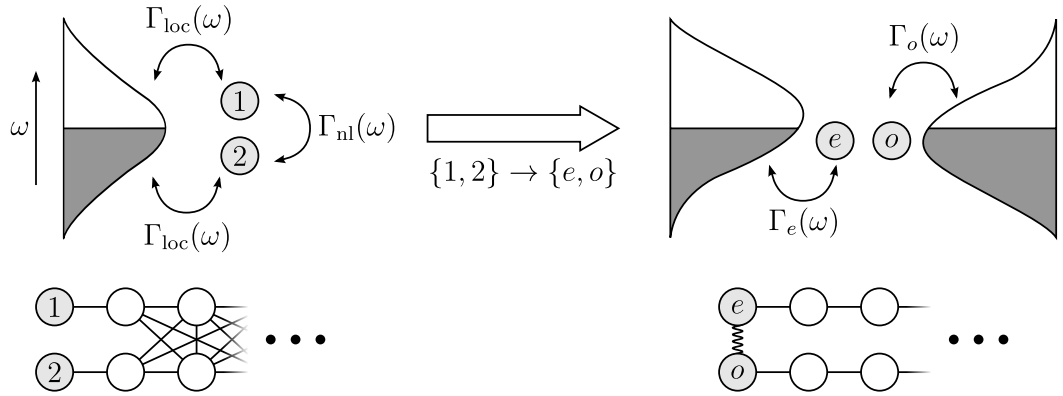

Fig. 4.1 Schematic representation for the transformation of the AAM into the even/odd basis, amenable to treatment via NRG. The AAM, consisting of two impurity sites coupled to a common conduction electron band via hybridization functions $\Gamma_{\rm loc}(\omega)$, and therefore indirectly coupled to each other via $\Gamma_{\rm nl}(\omega)$, is transformed by taking even/odd combinations into an effective 2IAM in which each impurity (even/odd) couples solely to its respective channel. Note the difference in the energy dependence of the even and odd conduction bands, given by $\Gamma_{\rm nl}(\omega)$. Below, the same transformation is represented in terms of the two Wilson chains, showing the orthogonalization of the two chains defined by the zero-orbitals to which each (real) impurity couples. The transformation scrambles the (local) interaction term, so that even and odd impurities are coupled by two-electron hopping terms as denoted by sinuated line (see Eqs. 4.11 and 4.12).

Considering the impurity Hamiltonian given in Eq. 4.4, the transformation given by Eq. 4.10 and $d_{e/o\,\sigma} = 2^{-1/2}(d_{1\sigma} \pm d_{2\sigma})$ gives,

$$\mathcal{H}_{AA} = \mathcal{H}_{\text{host}} + \sum_{p=e,o} \sum_{\sigma} \epsilon_d d^{\dagger}_{p\sigma} d_{p\sigma} + V \left(d^{\dagger}_{p\sigma} c_{p\sigma} + \text{H.c.} \right) + \mathcal{H}_{\text{int}} \tag{4.11}$$

where

$$\begin{aligned} \mathcal{H}_{\text{int}} =& \frac{U}{2} \left(d^{\dagger}_{e\uparrow} d_{e\uparrow} + d^{\dagger}_{o\uparrow} d_{o\uparrow} \right) \left(d^{\dagger}_{e\downarrow} d_{e\downarrow} + d^{\dagger}_{o\downarrow} d_{o\downarrow} \right) \\ &+ \frac{U}{2} \left(d^{\dagger}_{e\uparrow} d_{o\uparrow} + d^{\dagger}_{o\uparrow} d_{e\uparrow} \right) \left(d^{\dagger}_{e\downarrow} d_{o\downarrow} + d^{\dagger}_{o\downarrow} d_{e\downarrow} \right). \end{aligned} \tag{4.12}$$

The on-site Hubbard interaction of the form $\sim d^{\dagger}_{p\,\sigma} d_{p\,\sigma} d^{\dagger}_{p\,\bar{\sigma}} d_{p\,\bar{\sigma}}$, where $\sigma = -\bar{\sigma} = \uparrow / \downarrow$ is present in the even/odd basis, as it is in Eq. 4.4 for the $\{1, 2\}$ basis of impurity states. However $\mathcal{H}_{\text{int}}$ in the even/odd basis has additional terms which couple the even and odd impurities. Terms of the form $\sim d^{\dagger}_{p\,\sigma} d_{p\,\sigma} d^{\dagger}_{p'\,\bar{\sigma}} d_{p'\,\bar{\sigma}}$ act as an inter-site repulsion of opposite spins between the two impurity sites, while other terms $\sim -d^{\dagger}_{p\,\sigma} d^{\dagger}_{p\,\bar{\sigma}} d_{p'\,\sigma} d_{p'\,\bar{\sigma}}$ hop a pair of fermions from one site to the other.

In the non-interacting system ($U = 0$) where $\Sigma_{e/o} = 0$, the even and odd channels are strictly independent: the even(odd) impurity combination couples only to the even(odd) host combination. The calculation then reduces to two independent one-channel calculations. However, the even/odd transformation scrambles the interaction term, generating cross terms in Eq. 4.12 which couple the even and odd channels for $U \neq 0$ – thereby requiring an irreducible two-channel NRG calculation. We emphasize that this coupling due to interactions is not in the form of a simple, single-particle hopping between even and odd impurity sites, but instead a two-particle, non-local interaction involving the transfer of a *pair* of electrons, and thus conserving the electron "parity" (states of even(odd) numbers of electrons do not couple to states of odd(even) numbers of electrons). As a result, the (single-particle) self-energy is diagonal in the even/odd basis, despite the coupling of the two channels, in the same way that the on-site interaction for a single impurity model couples the up and down spin channels without causing spin flipping.

The original information about the real-space separation of the impurities is encoded in the *difference* between the dynamical quantities $\Gamma_e(\omega)$ and $\Gamma_o(\omega)$. As noted in Refs 5 and 11, the full energy dependence of these functions is required to capture the true real-space physics of the problem. The explicit transformation of real-space conduction electron operators to an even/odd basis (as described in Ref. 112) can be highly complicated, depending on the host lattice and inter-impurity separation vector. We

note however that this is not required, since the transformation can be performed on the level of the continuous, energy-dependent hybridization functions.

The two-impurity NRG calculation then involves a logarithmic discretization [211, 108, 29] of even/odd hybridization functions $\Gamma_{e/o}(\omega)$. A discretized version of the full model is then formulated in terms of even and odd impurity combinations, coupled to the end of even and odd Wilson chains. The model is then diagonalized iteratively, starting from a subsystem comprising the impurities themselves, and then building up the chains by successively coupling on even and odd Wilson chain orbitals. The couplings down each Wilson chain decrease exponentially due to the logarithmic discretization, and so high-energy states can be safely discarded at each NRG step to avoid exponential Hilbert space growth. The physics of the problem is revealed on progressively lower energies/temperatures as the Wilson chains grow in length – this is the essential RG character of the quantum impurity problem.

As already emphasized, the computational complexity of real-space two-impurity (necessarily two-channel) problems is significantly greater than that of single-impurity problems [137, 145], which involve only a single effective conduction electron channel – although accurate results are now possible. On the addition of a new pair of (even and odd) Wilson chain orbitals, the the growth of the intermediate Hilbert space is exponentially larger for two channels than in the single-channel case ($4^2 = 16\times$ growth vs. $4^1 = 4\times$ growth) before truncation and retention of the low-energy sector. Moreover, the low-energy sector of the Hilbert space to be retained must be larger to avoid truncation errors, and therefore minimize the discarded weight of the density matrix at each step. In addition, the truncation and retention of the low-energy sector of this intermediate Hilbert space at each step requires particular care for the AAM (in comparison to other two-channel problems such as the conventional 2IKM and 2IAM). This is because, as noted above, the dynamic inter-impurity coupling is encoded solely in the difference in energy dependence of the even and odd channel hybridization functions; these differences must be captured in the logarithmically discretized form of the Hamiltonian used in NRG in order to reproduce the physics of the full (continuous) model faithfully.

In all NRG calculations for the AAM presented in this thesis we adopt a discretization parameter $\Lambda = 2$, retaining $N_K = 10,000 - 15,000$ states at each step of the iterative process; these parameters have been found to give good convergence with variation of Λ, as well as minimizing the discarded weight of the density matrix at each iteration. By comparison, a conventional single-channel NRG calculation with a featureless (or "flat") hybridization function may require only $N_K = 1,000$ retained

states for converged results, while $N_K = 8,000$ states may suffice for an analogous two-channel calculation with featureless hybridization functions. Further improvements in accuracy may be achieved by employing the interleaved NRG methodology of Refs. 145 and 187, which helps to mitigate the significant increase in computational difficulty in two-channel calculations. The interleaved approach is limited in some cases for which there is channel symmetry, as such symmetries are broken artificially in the course of the calculation. However, the AAM formulated in the even/odd basis is necessarily channel-asymmetric: the non-trivial inter-impurity physics is encoded in the difference between the even and odd hybridization functions.

4.2.2 Impurity parameters for magnetic adatoms on metallic surfaces

Before studying the general physics of the AAM in detail, it is useful to consider what range of model parameters are appropriate for the magnetic adatom system for which the QPI is being investigated. As detailed in Chapter 3, the Kondo physics of a single magnetic impurity is sensitive to the underlying model parameters and host material through its LDOS [74, 48], related to the hybridization $\Gamma(\omega)$. However, the RG flow and associated universality is controlled by an emergent energy scale $T_{\rm K}^{\rm 1imp}$ – the single-impurity Kondo temperature. In the Kondo limit [74], $T_{\rm K}^{\rm 1imp}$ is determined by the interaction strength U/Γ_0, where $\Gamma_0 = \pi V^2 \rho_0$ and $\rho_0 = 1/6t$ is the Fermi level surface LDOS of the 3D cubic lattice.

In real systems, experimentally-measured Kondo temperatures are known to vary widely, even for a given impurity type and host material [191]. This is principally due to differences in the hybridization Γ_0, which is sensitive to details of the impurity's local environment. Guided by this, in this chapter we use realistic, fixed values of the conduction electron bandwidth, $12t = 11$ eV, and impurity interaction strength $U = 3t = 2.75$ eV (taken from Refs. 185, 195, 119 for Co impurities on Au). For convenience, we consider particle-hole symmetry, $\epsilon_d = -U/2$, such that the impurity is singly-occupied. Appropriate choice of V then gives rise to a realistic spread of single-impurity Kondo temperatures, as summarized in Table 4.1.

We note that U/Γ_0 in the range 12–16 yields Kondo temperatures consistent with classic studies of Co atoms on a Cu or Au surface [130, 101, 202, 191, 185, 195, 119]; while a passivating layer of Cu_2N between surface impurities and bulk reduces the hybridization to yield $T_{\rm K}^{\rm 1imp} \approx 2$K [155, 223]. Indeed, $U/\Gamma_0 = 24$–28 is more appropriate for Fe in Au, where $T_{\rm K}^{\rm 1imp} \approx 0.3$K [212]. In the investigations of the QPI detailed below,

U/Γ_0	$T_{\mathrm{K}}^{\mathrm{1imp}}$
12	85K
16	15K
20	3K
24	0.5K
28	0.1K

Table 4.1 Kondo temperatures T_{K} for a single impurity on the 3D cubic lattice surface, with bandwidth $12t = 11$ eV and $U = 2.75$ eV. T_{K} is calculated as the half-width at half-maximum of the Kondo spectral resonance at $T = 0$ using NRG.

we use these impurity parameters in the context of many-impurity systems, where different emergent energy scales and physics naturally arise.

4.2.3 Overview of the AAM

The transformation of the AAM Hamiltonian to the even/odd basis, given by Eqs. 4.11 and 4.12 and represented schematically in Figure 4.1, yields a model consisting of even and odd impurities coupled to even and odd baths of conduction electrons with differing energetic dispersions (given by $\Gamma_{e/o}(\omega)$). The on-site interaction terms of Eq. 4.4 are scrambled by the even/odd transformation, giving rise to two-electron interaction terms which couple the even and odd impurities. Both the energy dependence of the even/odd hybridization functions *and* the complicated interaction term are necessary in order to describe inter-impurity physics of the model. However, the AAM is qualitatively similar to simpler 2IAM/2IKM variants in which two (correlated single level or spin-$\frac{1}{2}$) impurities are coupled in series between two conduction electron channels of constant dispersion, $\Gamma_{L/R}(\omega) = \Gamma_0$, with a parametrized effective (tunnelling or exchange) coupling between the impurities. Motivated by this fact, and the relative difficulty of studying the full AAM, such reduced models have been widely studied in the literature in order to understand the general physics of the full AAM (see, for example, Refs. 87, 90, 1, 5).

As already alluded to, investigations of these simplified models capture the basic phenomenology of the AAM, allowing the qualitative features of the model to be understood. In the case of an antiferromagnetic effective RKKY interaction between impurities, the competition between local impurity-host interactions and indirect (host-mediated) inter-impurity coupling gives rise to the independently Kondo screened (IKS) and inter-impurity singlet (IIS) Fermi-liquid regimes, separated by a continuous

crossover [33, 5]. The absence of a quantum phase transition and critical point (QCP) between the IKS and IIS regimes [5] is examined in detail in Section 4.2.6. In the case of a sufficiently large ferromagnetic effective RKKY interaction, the impurities may form an entangled spin-1 object which is itself screened in a multi-stage process – the so-called spin-1 Kondo screened (S1KS) regime [154].

Thus, the interplay between single-impurity Kondo physics and the effective host-mediated interaction between two magnetic impurities, is expected to give rise to a rich range of physics. However, the relationship of the relevant energy scales governing these two interactions to the bare parameters of the Hamiltonian, namely the energy scales U, V and t, and the inter-impurity separation, $\mathbf{R}$, is nontrivial. From the bare scales entering the problem, two emergent scales arise: the single-impurity Kondo temperature $T_{\mathrm{K}}^{\mathrm{1imp}}$ and the effective inter-impurity RKKY exchange coupling, J_{RKKY}. The relative size of these scales, and the sign of J_{RKKY}, controls the underlying RG flow and low-energy physics [87, 90].

NRG calculations of the full AAM, for example presented in Figure 4.3, uphold this picture of the general physics. We consider the AAM Hamiltonian, with a generic metallic host conduction electron band modelled by the 3D cubic (100) surface tight binding model. This allows T_{K} and J_{RKKY} to be extracted for given impurity parameters and inter-impurity separation vector $\mathbf{R}$. However there remains no detailed understanding of the the relationship between the parameters of the AAM and the emergent energy scales controlling the physics, nor a consistent basis for mapping these parameters onto those of a reduced, toy model, such as the serially-coupled 2IAM or 2IKM. It is therefore also instructive to obtain simple perturbative estimates for comparison – although such treatments cannot capture the inherently non-perturbative nature of both the RKKY and Kondo scales.

In order to estimate T_{K}, a third-order perturbative scaling treatment is carried out in the spirit Anderson's "Poor Man's scaling" approach [15]. This is essentially a modified (one-loop) RG calculation in which the (high energy) states of the conduction band are successively integrated out by perturbatively treating excitations due to the coupling of impurity and host involving these high-energy states, yielding renormalized model parameters. The action of this RG operation is to increase the strength of the effective coupling between impurity and conduction band while decreasing the effective bandwidth; the Kondo scale is then identified as a scale-invariant quantity in the RG procedure which relates the effect coupling and bandwidth at any point along the RG flow [15]. Given the perturbative nature of this (specific) approach, the result can only be expected to agree well with the true Kondo scale below some cutoff in the interaction

strength, beyond which the perturbative treatment breaks down. For a single impurity on the cubic lattice surface at particle-hole symmetry, such a calculation yields [74]

$$T_{\mathrm{K}}^{\mathrm{1imp}} = at\,\sqrt{\frac{\Gamma_0}{U}}\exp\left(-\frac{\pi}{8}\times\frac{U}{\Gamma_0}\right)\,, \tag{4.13}$$

where $\Gamma_0 = \pi V^2/6t$, as in Section 4.2.2. The estimates compare well with exact (non-perturbative) results in Table 4.1 using $a \approx 3$, indicating that the perturbative treatment is reasonably reliable in this parameter range.

A similar scaling treatment of the RKKY coupling, in comparison, is much more involved. Such calculations have been carried out for simplified two-impurity models [88, 107], but not the full AAM, for two central reasons. In the AAM, the processes responsible for the RKKY coupling are of fourth order in the impurity-host coupling, significantly increasing the difficulty of the scaling calculation. Moreover, the crucial dependence of the RKKY interaction on the functional form of the impurity-host hybridization with energy must also be accounted for. As a consequence, no unanimous conclusions have been reached about an approximate functional form for the expected emergent RKKY interaction scale [88, 107, 54], nor a detailed understanding of the competition between the (non-perturbative) RKKY and Kondo scales.

We do not attempt such a perturbative scaling treatment here, employing instead a (simpler) approach of treating the impurity-host coupling as a static coupling, calculated perturbatively. We calculate $J_{\mathrm{RKKY}}^{\mathrm{PT}}$, the static effective RKKY coupling constant in the low-energy effective model for the AAM (at particle-hole symmetry) of two spin-$\frac{1}{2}$ impurities embedded in the host. The impurity-host exchange coupling J in this case is given by the well-known (second order) Schrieffer Wolff projection [178], $J = 8V^2/U$. $J_{\mathrm{RKKY}}^{\mathrm{PT}}$ is then calculated as the leading (second-)order perturbation in this exchange coupling [112],

$$J_{\mathrm{RKKY}}^{\mathrm{PT}} = \left(\frac{48t}{\pi^2}\times\frac{\Gamma_0}{U}\right)^2 \int_{-6t}^{0} d\epsilon \int_{0}^{6t} d\epsilon'\,\mathrm{P}\left(\frac{\mathrm{Im}\;G_{\mathrm{surf}}^{0}(\mathbf{R},\epsilon)\,\mathrm{Im}\;G_{\mathrm{surf}}^{0}(\mathbf{R},\epsilon')}{\epsilon'-\epsilon}\right)\,, \tag{4.14}$$

where P denotes the principal value, and $G_{\mathrm{surf}}^{0}(\mathbf{R},\epsilon) \equiv G_{\mathrm{surf}}^{0}(\mathbf{r}_1,\mathbf{r}_2,\epsilon)$ are free host Green functions connecting surface impurity sites $\mathbf{r}_1$ and $\mathbf{r}_2$.

We emphasize that the comparison between these two scales, $T_{\mathrm{K}}^{\mathrm{1imp}}$ and $J_{\mathrm{RKKY}}^{\mathrm{PT}}$, can only be qualitative; while $T_{\mathrm{K}}^{\mathrm{1imp}}$ is an emergent scale generated by a perturbative RG procedure, $J_{\mathrm{RKKY}}^{\mathrm{PT}}$ is a bare parameter in a low-energy effective model of the AAM. This is reflected in the functional forms of Eqs. 4.13 and 4.14: $T_{\mathrm{K}}^{\mathrm{1imp}}$ depends exponentially on the bare parameters of the AAM, while $J_{\mathrm{RKKY}}^{\mathrm{PT}}$ depends algebraically

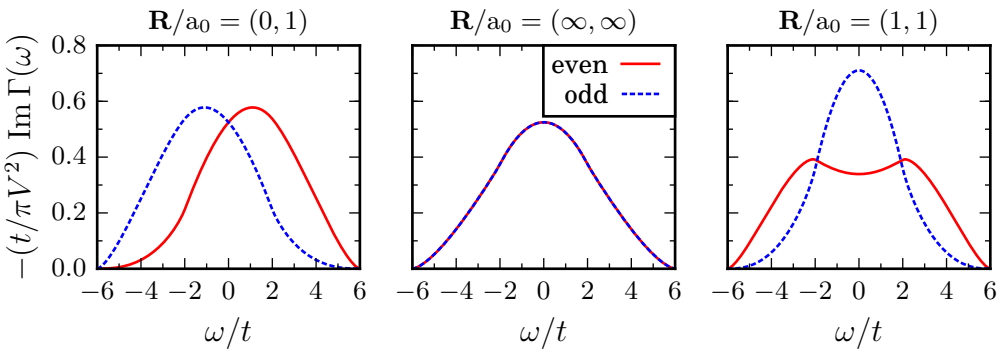

Fig. 4.2 Imaginary parts of the even and odd hybridization functions $-(t/V^2)\mathrm{Im}\,\Gamma_{e/o}(\omega)$ for two impurities on the 3D cubic (100) surface at separations $\mathbf{R}/a_0 = (1,0), (\infty,\infty)$ and $(1,1)$, giving rise to the inter-impurity singlet (IIS), independently Kondo screened (IKS) and and spin-1 Kondo screened (S1KS) regimes respectively.

on the same parameters, despite both scales deriving from the same fundamental interaction. Nevertheless, these analytical estimates serve as a useful guide, inform both our choice and understanding of the relevant parameter regimes of the AAM, as well as a providing framework within which to interpret numerical results. Moreover, such estimates are widely used in the literature when discussing the phenomenology of the competition between (independent) Kondo screening and cooperative, inter-impurity effects in systems of many impurities, for example in Ref. 49. A comparison of the true RKKY scale obtained by exact numerical calculations with the analytical approximation given by Eq. 4.14, is therefore instructive – see Section 4.2.4.

Physical quantities, such as impurity dynamics and thermodynamics, provide detailed information about the underlying physics and screening mechanisms. Figure 4.3 plots NRG results for the (local) impurity spectral function $\Gamma_0 \mathrm{Im}\, G_d^{11}(\omega)$ and the impurity contribution to the system entropy $S_{\mathrm{imp}}(T)/k_{\mathrm{B}}$, as functions of energy and temperature respectively, for each of the three regimes outlined above, exemplified by systems for which $U/\Gamma_0 = 28$ and $\mathbf{R}/a_0 = (1,0)$, $(1,1)$ and (∞,∞) for the inter-impurity singlet, spin-1 Kondo screened and individually Kondo screened cases respectively. The imaginary part of the respective even and odd channel hybridization functions $-\mathrm{Im}\,\Gamma_{e/o}(\omega)$ for these three cases are plotted in Figure 4.2.

Considering the spectral function, a Hubbard satellite peak arises in all cases at high energies $|\omega| \sim U/2$, corresponding to impurity charge fluctuations [74]. For $|\omega| \ll U$, the impurities become essentially singly-occupied and magnetic moments form. Similarly, the projection out of doubly-occupied and vacant states as T is decreased results in a reduction of the impurity entropy *per impurity* from $\ln(4)$ to

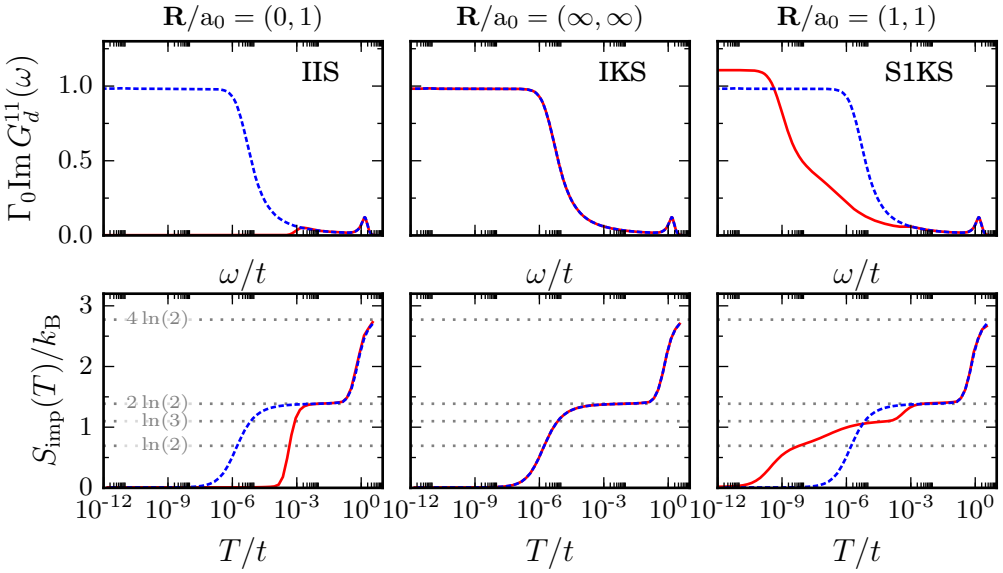

Fig. 4.3 Representative impurity spectra $\Gamma_0 \mathrm{Im}\, G_d^{11}(\omega)$ (upper panels) and impurity contribution to the entropy $S_{\mathrm{imp}}(T)$ (lower panels) calculated via NRG for the three regimes of the AAM, consisting of two equivalent magnetic impurities on the 3D cubic (100) surface with $U/\Gamma_0 = 28$ (see Table 4.1). *Left – Right:* $\mathbf{R}/a_0 = (1,0)$ (IIS regime), $\mathbf{R}/a_0 = (\infty,\infty)$ (IKS regime) and $\mathbf{R}/a_0 = (1,1)$ (S1KS regime). Solid (red) lines represent the AAM result, while dashed (blue) lines represent the single-impurity result for the same parameters.

ln(2) on the same scale. Although the impurities are coupled by the effective RKKY interaction, at energies or temperatures $\gg |J_{\rm RKKY}|$, the impurities behave essentially independently. Corrections to this local moment fixed point then control the physics; when $\max(|J_{\rm RKKY}|, T_{\rm K}^{\rm 1imp} \ll |\omega| \ll U$, incipient RG flow for each impurity towards a Kondo-screened strong-coupling state produces the classic inverse logarithmic spectral behaviour detailed in Ref. 64,

$$-\Gamma_0 \mathrm{Im}\ G_d^{11}(\omega) \sim \frac{1}{1 + b \ln^2 |c\ \omega / T_K^{\rm 1imp}|}\ , \tag{4.15}$$

with b, c constants of $\mathcal{O}(1)$.

At large inter-impurity separations, we expect the mutual interaction to be weaker, and thus one expects $T_{\rm K}^{\rm 1imp} \gg |J_{\rm RKKY}|$ for a given U/Γ_0 as $|\mathbf{R}| \to \infty$. Each impurity is then individually Kondo-screened essentially independently of the other below the single-channel scale $T_{\rm K}^{\rm 1imp}$, thereby quenching their magnetic moments and rendering the RKKY exchange interaction inoperative – the independently Kondo screened (IKS) regime. This screening is accompanied by a reduction in the impurity contribution of the entropy from $S_{\rm imp}/k_{\rm B} = 2\ln(2)$ to 0 on the same scale, $T_{\rm K}$. The low-energy behaviour of the impurity spectral function has the characteristic Fermi liquid asymptotics [74],

$$-\Gamma_0 \mathrm{Im}\ G_d^{11}(\omega) \ \overset{|\omega| \ll T_{\rm K}}{\sim}\ p - q \left(\frac{\omega}{T_{\rm K}}\right)^2\ , \tag{4.16}$$

where $T_{\rm K} \equiv T_{\rm K}^{\rm 1imp}$ and $q = \mathrm{O}(1)$. The pinning condition p, considered in detail in Appendix B, is somewhat more complex in the case of two impurities than the single-impurity case, where $p = 1$ at particle-hole symmetry is given simply by the Friedel sum rule [74, 110]. In the independent-impurity limit ($|\mathbf{R}| \to \infty$)

By contrast, at small inter-impurity separations (for example $\mathbf{R}/\mathrm{a}_0 = (1,0)$, $(1,1)$ in Figure 4.3), $|J_{\rm RKKY}| \gg T_{\rm K}^{\rm 1imp}$ and RKKY physics dominates, causing the impurities to bind together in either singlet or triplet configurations for negative/antiferromagnetic (AFM) or positive/ferromagnetic (FM) $J_{\rm RKKY}$ respectively. In both scenarios, the single-impurity RG flow is cut off on the scale of $J_{\rm RKKY}$, and single-impurity Kondo physics is disrupted. In the case of an AFM $J_{\rm RKKY}$, represented in Figure 4.3 by $\mathbf{R}/\mathrm{a}_0 = (1,0)$, this results in an impurity spectrum $\mathrm{Im}\ G_d^{11} \simeq 0$ for $|\omega| \ll |J_{\rm RKKY}|$. Confirming this physical picture, the impurity contribution to entropy is quenched from $S_{\rm imp}/k_{\rm B} = 2\ln(2)$ to 0 on the same scale, with the functional form of the crossover from local-moment to singlet state differing from that of Kondo screening. The effective RKKY coupling in this case can thus be extracted from these crossovers

as $|J_{\mathrm{RKKY}}|/t \approx 10^{-3}$. Clearly the inter-impurity singlet state formed has markedly different properties from the (individual) Kondo singlet states of the independently Kondo screened regime described above. Moreover, we note that the inter-impurity singlet state remains entangled with the host, which mediates the indirect exchange coupling (in contrast to the situation in the 2IKM with direct exchange, where the singlet decouples).

In the case of a FM RKKY interaction, represented in Figure 4.3 by $\mathbf{R}/\mathrm{a}_0 = (1, 1)$, the impurities form a triplet configuration below a temperature scale of J_{RKKY} with an associated impurity entropy $S_{\mathrm{imp}} = \ln(3)$. This non-local, spin-1 object couples to both the even and odd conduction channels, and as such is exactly Kondo screened, as described in Ref. 154. The Kondo screening of the inter-impurity triplet is distinctly two-stage in this case, with two energy scales, $T_{\mathrm{K}}^{\mathrm{inter}}/t \approx 10^{-7}$ and $T_{\mathrm{K}}^{S=1} \approx 10^{-10}t$, due to the inequivalence between the even and odd channel hybridization functions. We note particularly the strong suppression in magnitude of the spin-1 Kondo scale $T_{\mathrm{K}}^{S=1}$ in comparison to the corresponding single-impurity Kondo scale $T_{\mathrm{K}}^{\mathrm{1imp}}$ [177, 151]. On energy scales $T_{\mathrm{K}}^{\mathrm{inter}} \ll |\omega| \ll |J_{\mathrm{RKKY}}|$, spin-1 local moment physics naturally arises, with spectral behaviour again that of Eq. 4.15, but with the characteristic scale $T_{\mathrm{K}}^{\mathrm{1imp}}$ replaced by $T_{\mathrm{K}}^{\mathrm{inter}}$. Analogously, for a sufficient separation between $T_{\mathrm{K}}^{\mathrm{inter}}$ and $T_{\mathrm{K}}^{S=1}$, spin-$\frac{1}{2}$ local moment physics and accompanying spectral behaviour is observed with a characteristic scale $T_{\mathrm{K}}^{S=1}$. In fact, for sufficiently separated $|J_{\mathrm{RKKY}}|$, $T_{\mathrm{K}}^{\mathrm{inter}}$ and $T_{\mathrm{K}}^{S=1}$, universal lineshapes are obtained as a function of $|\omega|/T_{\mathrm{K}}^{S=1}$ and $T/T_{\mathrm{K}}^{S=1}$ for all $|\omega|$ and $T \ll |J_{\mathrm{RKKY}}|$. In particular, the lowest-energy behaviour is again characteristic of flow to a Fermi liquid ground state, with a fully quenched entropy, $S_{\mathrm{imp}}(0) = 0$. The low-energy behaviour of the impurity spectrum has the characteristic Fermi liquid asymptotics of Eq. 4.16, but with $T_{\mathrm{K}} \equiv T_{\mathrm{K}}^{S=1}$, the spin-1 Kondo scale. The Fermi level pinning condition p in the S1KS regime has a different form than the independently Kondo screened and inter-impurity singlet (AFM J_{RKKY}) regimes, as detailed in Appendix B – again, the single-impurity value $p = 1$ is recovered in the limit $|\mathbf{R}| \to \infty$.

4.2.4 Effect of impurity separation

The inter-impurity separation $\mathbf{R} = \mathbf{r}_2 - \mathbf{r}_1$ is encoded via the hybridization matrix, $\mathbf{\Gamma}(\omega)$, whose elements are given by $[\mathbf{\Gamma}(\omega)]_{\alpha\beta} = V^2 G^0_{\mathrm{surf}}(\mathbf{r}_\alpha, \mathbf{r}_\beta, \omega)$. Specifically, the off-diagonal elements of the hybridization matrix are given by $[\mathbf{\Gamma}(\omega)]_{12(21)} = V^2 G^0_{\mathrm{surf}}(\mathbf{R}, \omega)$.

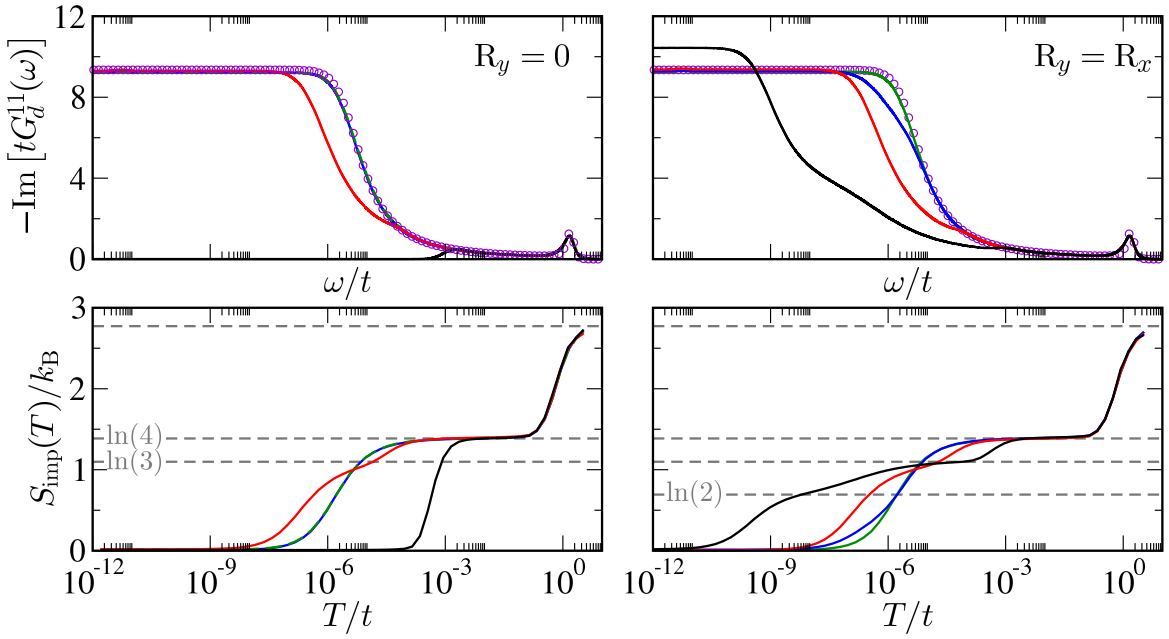

Fig. 4.4 Two equivalent magnetic impurities on the 3D cubic (100) surface with $U/\Gamma_0 = 28$ (see Table 4.1). NRG results for the local impurity spectrum $-\mathrm{Im}[tG_d^{11}(\omega)]$ vs ω/t at $T = 0$ (upper panels) and the temperature-dependence of the impurity contribution to entropy $S_{\mathrm{imp}}(T)$ vs T/t for the same systems (lower panels). Inter-impurity vector $\mathbf{R}$, with $\mathrm{R}_y = 0$ (left panels) and $\mathrm{R}_y = \mathrm{R}_x$ (right), where $\mathrm{R}_x/\mathrm{a}_0 = 1, 2, 3, 4$ for black, red, blue and green lines. Circle points plot the single-impurity result.

Transformation to the even/odd basis yields a diagonal hybridization matrix, for which

$$\Gamma_{e/o}(\omega) = V^2 \left(G^0_{\text{surf}}(\mathbf{0}, \omega) \pm G^0_{\text{surf}}(\mathbf{R}, \omega) \right). \tag{4.17}$$

At large inter-impurity lattice separations, we expect that the lattice Green function $G^0_{\text{surf}}(\mathbf{R}, \omega)$ decays to zero, rendering the even and odd channel hybridization functions equivalent. Similarly, the effective RKKY coupling $J^{\text{PT}}_{\text{RKKY}}$ predicted by Eq. 4.14 also goes to zero for large $\mathbf{R}$ – the two impurities are effectively independent, and therefore in the IKS regime described above. It is found that $J^{\text{PT}}_{\text{RKKY}}$ decays faster than $|\mathbf{R}|^{-3}$ as separation is increased, in contrast to the textbook results for the 2D and 3D electron gas (for which $J^{\text{PT}}_{\text{RKKY}} \sim |\mathbf{R}|^{-d}$, where d is the dimensionality [74]).

As inter-impurity separation is decreased, the expected RKKY coupling increases until the emergent scale $|J_{\text{RKKY}}|$ increases above that of $T_{\text{K}}^{\text{1imp}}$, at which point the system crosses over into the inter-impurity singlet or spin-1 Kondo screened regime, depending on the sign of J_{RKKY}. The centrosymmetry of the 3D cubic (100) host lattice enforces particle-hole symmetry requirements on the lattice Green functions; specifically, the parity of the Manhattan distance $d_{\text{M}}(\mathbf{R}) = \text{R}_x + \text{R}_y$ determines the parity of the lattice Green function with respect to frequency, ω,

$$G^0_{\text{surf}}(\mathbf{R}, -\omega) = (-1)^{(d_{\text{M}}(\mathbf{R})+1)} G^0_{\text{surf}}(\mathbf{R}, \omega)^* , \tag{4.18}$$

as seen in Figure 4.2. As a result of this well-defined parity due to centrosymmetry and thus particle-hole symmetry of the host lattice, the effective RKKY interaction $J^{\text{PT}}_{\text{RKKY}}$ calculated via Eq. 4.14 is sign-definite with respect to the Manhattan distance $d_{\text{M}}(\mathbf{R})$. Even Manhattan distances give rise to ferromagnetic (FM) coupling $J^{\text{PT}}_{\text{RKKY}} > 0$, while odd Manhattan distances give antiferromagnetic (AFM) coupling $J^{\text{PT}}_{\text{RKKY}} < 0$. The well-defined parity of the lattice Green function with respect to frequency, and the resultant regularity in the effective RKKY interaction, holds only for simple lattices such as the monatomic hypercubic tight binding lattice; for a more complicated, generic host, the sign of the RKKY interaction must be determined by evaluation of Eq. 4.14.

Table 4.2 shows the perturbative estimate for the RKKY coupling, as obtained from numerical evaluation of Eq. 4.14 for various inter-impurity separations. For separations with $\text{R}_y = 0$, there is a clear alternation between antiferromagnetic and ferromagnetic coupling, while for $\text{R}_y = \text{R}_x$, only ferromagnetic coupling arises, as expected on parity grounds. The rapid decay of $J^{\text{PT}}_{\text{RKKY}}$ with increasing separation $|\mathbf{R}|$ is also clearly seen (even for small separations) from this simple calculation. The variation in the true, emergent RKKY coupling scale, J_{RKKY}, and its interplay with Kondo physics,

	$(J^{\rm PT}_{\rm RKKY}/t)\times(U/\Gamma_0)^2$	
R_x	$\mathrm{R}_y=0$	$\mathrm{R}_y=\mathrm{R}_x$
1	$+4.5\times10^{-2}$	-2.5×10^{-2}
2	-2.5×10^{-3}	-2.0×10^{-3}
3	$+1.0\times10^{-4}$	-2.9×10^{-5}
4	-2.5×10^{-6}	-3.2×10^{-5}

Table 4.2 Perturbative estimate of the RKKY coupling from Eq. 4.14, given as $(J^{\rm PT}_{\rm RKKY}/t)\times(U/\Gamma_0)^2$ between impurities on the 3D cubic lattice (100) surface, for inter-impurity separations $\mathbf{R}=(\mathrm{R}_x,\mathrm{R}_y)$ as per Fig. 4.4.

must however be extracted from the full NRG solution for the two-impurity model, which takes into account both the dynamical nature of the inter-impurity coupling and renormalization effects.

Figure 4.4 plots the local impurity spectral function and impurity contribution to the entropy for a series of separations along the lines $\mathrm{R}_y=0$ and $\mathrm{R}_y=\mathrm{R}_x$ for two identical impurities with $U/\Gamma_0=28$, for which $T_{\rm K}^{\rm 1imp}/t=5\times10^{-6}$. Along the line $\mathrm{R}_y=0$, the alternation of the sign of $J_{\rm RKKY}$ with Manhattan distance is seen for $\mathrm{R}_x/\mathrm{a}_0=1$ to 2, for which inter-impurity singlet and spin-1 Kondo screened physics, respectively, are seen. In comparison to the perturbative predictions of $J^{\rm PT}_{\rm RKKY}$ in Table 4.2, the observed values of the emergent scale $J_{\rm RKKY}/t\simeq-10^{-3}$ and $+5\times10^{-5}$ for $\mathrm{R}_x/\mathrm{a}_0=1$ and 2 respectively. However the rapidly decaying strength of the RKKY interaction predicted by Table 4.2 sees the RKKY interaction cut off by the local Kondo screening scale $T_{\rm K}^{\rm 1imp}$, so that independently Kondo screened physics is seen for $\mathrm{R}_x/\mathrm{a}_0\geq3$. Along $\mathrm{R}_y=\mathrm{R}_x$, the sign of $J_{\rm RKKY}$ is positive for all separations, as expected from $J^{\rm PT}_{\rm RKKY}$ (and the parity of the Manhattan distance). The values of $J_{\rm RKKY}$ extracted from NRG calculations for $\mathrm{R}_x/\mathrm{a}_0=1,2$ and 3 are $J_{\rm RKKY}/t\simeq+5\times10^{-4},+5\times10^{-5}$ and $+8\times10^{-6}$; for $\mathrm{R}_x/\mathrm{a}_0\geq4$, the inter-impurity interaction is again cut off by the local Kondo screening scale $T_{\rm K}^{\rm 1imp}$.

The local impurity properties are strongly affected when their separation is on the order of a few lattice sites. Importantly, however, the impurities are found to behave essentially independently for rather small separations, $|\mathbf{R}|\gtrsim4\sqrt{2}\mathrm{a}_0$. This is in accord with recent theoretical work [11], as well as experimental observation [130, 101, 191, 155, 202], where systems with small average impurity separation appear to be described in terms of the independent impurity paradigm. From a real-space perspective this might seem puzzling. A so-called "Kondo cloud" of conduction electrons surrounds each

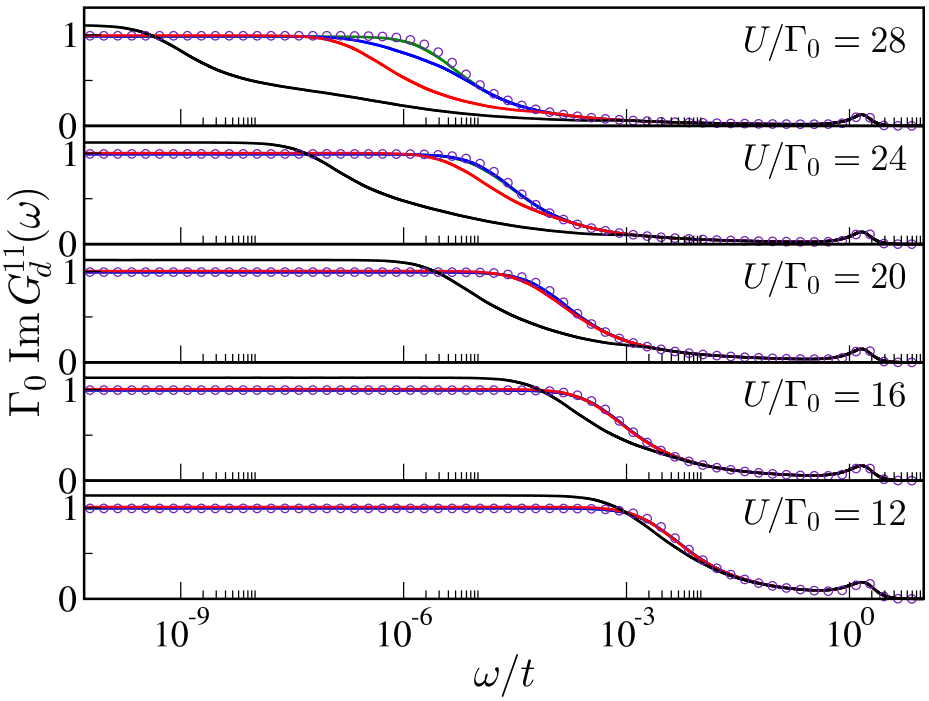

Fig. 4.5 Evolution of impurity spectra $-t\mathrm{Im}\,G_d^{11}(\omega)$ with decreasing U/Γ_0, obtained by NRG. Plotted at $T = 0$ vs ω/t for $\mathrm{R}_x/\mathrm{a}_0 = \mathrm{R}_y/\mathrm{a}_0 = 1, 2, 3, 4$ as the black, red, blue and green lines. Circle points plot the corresponding single-impurity results.

impurity and is responsible for screening its magnetic moment. This screening cloud is typically large, characterized [3, 136, 32] by a length scale $\xi_{\mathrm{K}}^{1\mathrm{imp}} \sim \hbar v_F/k_B T_{\mathrm{K}}^{1\mathrm{imp}}$ (with v_F the Fermi velocity). Our results show that such Kondo clouds can be substantially interpenetrating, even though the screening itself remains independent – a real-space region containing $\sim 10^{23}$ conduction electrons can support $\sim 10^{23}$ orthogonal collective states capable of screening impurities independently [136].

4.2.5 Effect of impurity hybridization strength

As noted in Section 4.2.2, the impurity-host hybridization (and hence single-impurity Kondo temperature) can vary widely in real systems. Here we examine how the physics described in the previous subsection evolves with U/Γ_0.

In Figure 4.5, we consider again the local impurity spectrum $-\mathrm{Im}[tG_d^{11}(\omega)]$ at $T = 0$ with impurity separation $\mathrm{R}_x = \mathrm{R}_y = 1, 2, 3, 4a_0$, for the range of U/Γ_0 given in Table 4.1 (keeping $U = 3t$ fixed). With increasing hybridization Γ_0 (and hence increasing $T_{\mathrm{K}}^{1\mathrm{imp}}$), we find that independent Kondo physics becomes relatively more important, overwhelming the effects of inter-impurity interactions at progressively

smaller impurity separations (c.f. Eqs. 4.13 and 4.14). For $U/\Gamma_0 = 12$, the impurities behave essentially independently already when separated by $\mathbf{R} = (2, 2)$. The interplay between Kondo and RKKY physics is naturally more pronounced for larger U/Γ_0 where the single-impurity Kondo scale $T_{\mathrm{K}}^{\mathrm{1imp}}$ is smaller.

4.2.6 Observation of critical physics in the AAM

In Section 4.2.3 we began an overview of the physics of the AAM, based on the qualitative picture established by investigations of simpler, related models; this was largely upheld by exact NRG calculations for the full AAM. For an AFM effective RKKY coupling, it was confirmed that the relative strengths of the inter-impurity RKKY and impurity-host local Kondo screening interactions controlled the formation of either an inter-impurity singlet (IIS) state or two independently Kondo-screened (IKS) impurity singlet states. The simplest two-impurity, two-channel models qualitatively capturing this competition are the classic two-impurity Kondo and two-impurity Anderson models (2IKM and 2IAM respectively), in which two impurities, each coupled to a single channel of conduction electrons via a constant hybridization function, are arranged in series, with a direct (static) inter-impurity exchange or tunnel coupling. In comparison to the full AAM in the even/odd impurity basis, given by Eqs. 4.11 and 4.12, these models differ in the form of the interaction term (which is more complex in the even/odd basis AAM) and the lack of energetic structure in the two hybridization functions. While calculations for the full AAM support the qualitative picture of these simpler models, we have demonstrated in previous sections that the correspondence between the parameters of the full and simplified models may be non-trivial in the absence of a rigorous, controlled mapping onto a reduced version of the full AAM. An important question, then, is whether or not a given feature of the simplified 2IKM or 2IAM models is observable in the full AAM and, if so, for what physical parameters.

One feature of particular interest in the 2IKM is the presence of a quantum phase transition (QPT) between two Fermi-liquid phases characterized by independently Kondo screened and inter-impurity singlet states respectively, with a quantum critical point (QCP) at zero temperature [91]. This QCP has been shown to be non-Fermi liquid in character [4, 57], and maps to the well-known two-channel Kondo (2CK) fixed point [58, 142, 5] originally observed in the two-channel Kondo model (consisting of a single spin-$\frac{1}{2}$ impurity coupled to two conduction electron channels). When the parameters are tuned such that the inter-impurity coupling and the impurity-bath (Kondo) coupling are frustrated, the Kondo scale, T_{K}, controls the RG flow to an unstable fixed point associated with the QCP, with a characteristic impurity entropy of

$\frac{1}{2}\ln(2)$ [4, 57], exemplifying the non-Fermi liquid nature of the ground state. However, detailed analysis of has shown that the QCP is destabilized by inter-channel charge transfer processes [142], giving rise to a second energy scale, T^*, controlling the RG flow away from the unstable fixed point and to a stable Fermi-liquid fixed point. Including such charge-transfer terms directly in the 2IKM gives rise instead to a continuous crossover at low temperature/energy between the two Fermi liquid regimes (independently Kondo screened and inter-impurity singlet), as described in Ref. 141.

Analogously, the (tunnel-coupled) 2IAM has been shown not to possess a QPT, due to inter-channel charge transfer [170, 171, 89]. In Ref. 89 a perturbative treatment, eliminating excitations from the manifold of singly-occupied impurity states in the spirit of the Schrieffer-Wolff transformation [178], demonstrated that the low-energy effective model for the tunnel-coupled 2IAM was a 2IKM with just such an inter-channel charge transfer term, arising as an inevitable consequence of inter-impurity coupling. There is no set of parameters for the 2IAM in which charge transfer may be suppressed without decoupling the impurities. However, the functional dependence in the relative strengths of the inter-channel charge transfer and inter-impurity interaction terms on the bare parameters of the model differ. As a result, these parameters may be tuned to minimize the effect of the charge transfer relative to the inter-impurity coupling and Kondo screening, the competition of which is required for the critical physics of the 2IKM. As a result, the two relevant energy scales, T_{K} and T^* may be tuned such that $T_{\mathrm{K}} \ll T^*$ [89], allowing critical physics to be observed over a finite energy(temperature) range in the 2IAM , $T^* < \omega(T) < T_{\mathrm{K}}$, with the characteristic impurity entropy of $\frac{1}{2}\ln(2)$ and a local impurity spectral function pinned at $-\Gamma_0 \mathrm{Im}\, G_d^{11}(\omega) = 0.5$ (approached as $\sqrt{\omega}$ for $T^* < \omega < T_{\mathrm{K}}$ for the channel-asymmetric case of the 2IAM and the 2IKM with additional charge transfer terms [89, 142]).

The qualitative relationship between the full AAM and these simpler variants raises the intriguing possibility of observing quantum critical physics and non-Fermi liquid behaviour in the relatively conventional (and realizable) setting of the AAM. However, a perturbative treatment similar to that of Ref. 89 in the case of the 2IAM is not practical for the full AAM due to the increased complexity of the model, as discussed in Section 4.2.3. As a consequence, a simple approximate functional dependence of the inter-channel charge transfer term, as well as the effective RKKY interaction is not available. It is expected, however, that such charge transfer terms naturally arise within the AAM due to finite, through-lattice inter-impurity coupling – which also gives rise to the RKKY term. Furthermore, symmetry analysis of the 2CK QCP in simpler two-impurity models [5, 170, 171] demonstrated that the critical point is only stable in

the presence of particle-hole symmetry in *both* conduction electron channels, such that $\mathrm{Im}\,\Gamma_{e/o}(-\omega) = \mathrm{Im}\,\Gamma_{e/o}(+\omega)$. As demonstrated in Section 4.2.4, however, the AFM effective RKKY interaction is only generated when the Manhattan distance is odd, giving a different particle-hole symmetry between the conduction electron channels, $\mathrm{Im}\,\Gamma_{e/o}(-\omega) = \mathrm{Im}\,\Gamma_{o/e}(+\omega)$, and thus the (pristine) QCP cannot be realized in the AAM.

Nevertheless, the possibility remains (in principle) that the symmetry-breaking terms destabilizing the QCP are sufficiently small that critical physics is observable over some intermediate energy/temperature range. As detailed in Section 4.2.4 and 4.2.5, the separation distance over which the effective RKKY interaction remains significant is rather short for physically realistic parameters, with the inter-impurity interaction competing with independent Kondo screening only over the range of a few lattice sites. As indicated by Eq. 4.13, a larger interaction strength U results in a smaller T_{K}, so that the competition between local Kondo screening and inter-impurity (RKKY) singlet formation (between T_{K} and J_{RKKY}) occurs for smaller J_{RKKY} – and thus for larger impurity separations. However, the observation of critical physics is predicated on frustration between Kondo screening and RKKY singlet formation, necessitating extreme fine tuning in the two energy scales. In the simplified cases of the 2IKM and 2IAM, the control of both scales is (relatively) straightforward, and thus tuning to the critical point is readily achieved. However, the highly non-trivial dependence of the inter-impurity coupling J_{RKKY} on the bare parameters of the AAM makes this a much more challenging prospect – and the subject of ongoing investigations.

4.3 QPI due to two magnetic impurities

Having carefully considered the fundamental physics of the AAM, we consider the effect of the inter-impurity physics discussed here on the QPI due to two impurities, entering via the impurity single-particle dynamics. By studying first the two-impurity QPI, we hope to gain insight into the more complicated and realistic many-impurity case. In Chapter 3 we demonstrated that the QPI is highly sensitive to the details of the defects or impurities and the (local) scattering that generates modulations in the LDOS. In Chapter 2, we gave the qualitative interpretation of the QPI in terms of the joint density of states, JDOS, derived from simple Fermi golden rule arguments, which neglects the details of the scattering. This interpretation thus fails to capture the local, single-impurity physics encoded in the QPI for magnetic impurities, necessitating a more advanced treatment via the formalism developed in Section 3.2. Here we extend

this formalism to consider two magnetic impurities embedded on the surface of the 3D cubic (100) host, and investigate the resultant QPI due to inter- and intra-impurity correlations.

As discussed in Chapter 2, the QPI is obtained via FT-STS from the LDOS map $\rho(\mathbf{r}_i, \omega)$ at scanning energy ω and temperature T [160, 161, 184]. Modulations in the LDOS are measured in real-space over a sample region of size $L \times L$,

$$\rho(\mathbf{q}, \omega) = \sum_{i \in (L \times L)} \mathrm{e}^{-\mathrm{i}\mathbf{q}\cdot\mathbf{r}_i} \rho(\mathbf{r}_i, \omega) \ , \tag{4.19}$$

where $\rho(\mathbf{r}_i, \omega) = -\pi^{-1}\mathrm{Im}\, G_{\mathrm{surf}}(\mathbf{r}_i, \mathbf{r}_i, \omega)$ is the LDOS of the host surface at position $\mathbf{r}_i$. The full surface Green functions $G_{\mathrm{surf}}(\mathbf{r}_i, \mathbf{r}_j, \omega)$ describe electronic propagation between sites of the host surface in the presence of impurities. The contribution to the full Green function due to scattering from all impurities is given in terms of the surface Green functions of the clean (impurity-free) host in real-space via a t-matrix equation,

$$G_{\mathrm{surf}}(\mathbf{r}_i, \mathbf{r}_j, \omega) = G^0_{surf}(\mathbf{r}_i, \mathbf{r}_j, \omega) + \sum_{\alpha,\beta} G^0_{\mathrm{surf}}(\mathbf{r}_i, \mathbf{r}_\alpha, \omega) T_{\alpha\beta}(\omega) G^0_{\mathrm{surf}}(\mathbf{r}_\beta, \mathbf{r}_j, \omega), \tag{4.20}$$

where the sum runs over impurity sites α and β; and the t-matrix is given explicitly in terms of the impurity Green functions by

$$T_{\alpha\beta}(\omega) = V^2 G_d^{\alpha\beta}(\omega). \tag{4.21}$$

We emphasize that the effect of inter-impurity correlations are manifest in both the diagonal and off-diagonal elements of the impurity Green function matrix (and hence the t-matrix), despite the diagonal elements being related to *local* impurity Green functions. While off-diagonal elements of the t-matrix represent scattering channels that arise uniquely due to interactions, the absence of these inter-impurity terms does not mean that the impurities are independent: local impurity quantities can be profoundly affected by inter-impurity correlations, as seen in Section 4.2.

The surface sites of the host are of course coupled to those in the bulk, although the STM tip itself probes only the surface. As detailed in Chapter 3, we therefore formulate the scattering problem most effectively in the "surface diagonal" basis, in which the layer index z is preserved, leading to a description of the QPI in terms of surface quasiparticles. This follows from the *partial* diagonalization of $\mathcal{H}_{\mathrm{host}}$ (Eq. 4.2)

by 2D Fourier transformation of layers parallel to the surface,

$$c_{\mathbf{k}_\parallel z\sigma} = \frac{1}{\Omega_{BZ}^{1/2}} \sum_{\mathbf{r}_i} \mathrm{e}^{\mathrm{i}\mathbf{r}_i\cdot\mathbf{k}_\parallel} c_{\mathbf{r}_i z\sigma}, \tag{4.22}$$

where Ω_{BZ} is the volume of the first (surface) Brillouin zone (1SBZ). The host Hamiltonian then reduces to a bundle of decoupled 1D chains,

$$\mathcal{H}_{\text{host}} = \sum_{\mathbf{k}_\parallel,\sigma} \Big(\sum_{z=0}^{\infty} \epsilon_{\mathbf{k}_\parallel}^{\text{2D}} c_{\mathbf{k}_\parallel z\sigma}^\dagger c_{\mathbf{k}_\parallel z\sigma} + (c_{\mathbf{k}_\parallel z\sigma}^\dagger c_{\mathbf{k}_\parallel (z+1)\sigma} + \text{H.c.}) \Big), \tag{4.23}$$

where $\epsilon_{\mathbf{k}_\parallel}^{\text{2D}} = -2t[\cos(\mathrm{a}_0 k_x) + \cos(\mathrm{a}_0 k_y)]$ is the 2D square lattice dispersion, given in terms of surface momentum $\mathbf{k}_\parallel \equiv (k_x, k_y)$, and with lattice constant a_0. As a consequence, $G_z^0(\mathbf{k}_\parallel, \mathbf{k}'_\parallel, \omega) \equiv \langle\langle c_{\mathbf{k}_\parallel z\sigma}; c_{\mathbf{k}'_\parallel z\sigma}^\dagger \rangle\rangle_\omega^0 \propto \delta_{\mathbf{k}_\parallel,\mathbf{k}'_\parallel}$. Surface quasiparticles are however dephazed by the bulk even in the clean host [48], giving rise to a finite surface quasiparticle lifetime, with

$$G_{\text{surf}}^0(\mathbf{k}_\parallel, \omega) = f\left(\frac{\omega - \epsilon_{\mathbf{k}_\parallel}^{\text{2D}}}{2t}\right) \quad \text{where} \quad tf(\tilde{\omega}) = \tilde{\omega} - \begin{cases} \mathrm{sgn}(\tilde{\omega})\sqrt{\tilde{\omega}^2 - 1} & |\tilde{\omega}| > 1 \\ \mathrm{i}\sqrt{1 - \tilde{\omega}^2} & |\tilde{\omega}| \leq 1 \end{cases}. \tag{4.24}$$

Scattering of surface quasiparticles due to impurities is then described by a surface t-matrix equation [48],

$$G_{\text{surf}}(\mathbf{k}_\parallel, \mathbf{k}'_\parallel, \omega) = G_{\text{surf}}^0(\mathbf{k}_\parallel, \omega)\delta_{\mathbf{k}_\parallel,\mathbf{k}'_\parallel} + G_{\text{surf}}^0(\mathbf{k}_\parallel, \omega) T(\mathbf{k}_\parallel, \mathbf{k}'_\parallel, \omega) G_{\text{surf}}^0(\mathbf{k}'_\parallel, \omega)\ , \tag{4.25}$$

with the t-matrix itself given by,

$$T(\mathbf{k}_\parallel, \mathbf{k}'_\parallel, \omega) = \frac{V^2}{\Omega_{BZ}} \sum_{\alpha,\beta} \mathrm{e}^{\mathrm{i}(\mathbf{k}'\cdot\mathbf{r}_\beta - \mathbf{k}\cdot\mathbf{r}_\alpha)} \times G_d^{\alpha\beta}(\omega)\ . \tag{4.26}$$

Following the procedure detailed in Chapter 3 for magnetic impurities on the 3D cubic (100) surface, the QPI may be calculated either in real space, simulating the experimental measurement, or directly in momentum space of the surface band. Taking the sample size $L \to \infty$ in Eq. 4.19 and subtracting the trivial contribution at $\mathbf{q} = \mathbf{0}$ from the clean system, the exact QPI, $\Delta\rho(\mathbf{q}, \omega) = \rho(\mathbf{q}, \omega) - \rho^0(\mathbf{q}, \omega)$ is given by,

$$\Delta\rho(\mathbf{q}, \omega) = -\frac{1}{2\pi\mathrm{i}} \Big(Q(\mathbf{q}, \omega) - Q(-\mathbf{q}, \omega)^* \Big)\ , \tag{4.27}$$

where

$$\begin{aligned} Q(\mathbf{q},\omega) &= \int\limits_{1\mathrm{SBZ}} \frac{d^2\mathbf{k}_\parallel}{\Omega_{BZ}} \left(G_{\mathrm{surf}}(\mathbf{k}_\parallel, \mathbf{k}_\parallel + \mathbf{q}, \omega) - G^0_{\mathrm{surf}}(\mathbf{k}_\parallel, \omega)\delta(\mathbf{q}) \right) \\ &= V^2 \sum_{\alpha,\beta} G_d^{\alpha\beta}(\omega) \times \Lambda_{\alpha\beta}(\mathbf{q},\omega) \end{aligned} \tag{4.28}$$

is given in terms of the full impurity Green functions $G_d^{\alpha\beta}(\omega)$. The quantity $\Lambda_{\alpha\beta}(\mathbf{q},\omega)$ is defined for the clean surface of the host material, and follows from Eqs. 4.25 and 4.26 in terms of the (diagonal) surface quasiparticle Green functions as,

$$\Lambda_{\alpha\beta}(\mathbf{q},\omega) = \int\limits_{1\mathrm{SBZ}} \frac{d^2\mathbf{k}_\parallel}{\Omega_{BZ}} \, G^0_{\mathrm{surf}}(\mathbf{k}_\parallel,\omega) G^0_{\mathrm{surf}}(\mathbf{k}_\parallel + \mathbf{q},\omega) \mathrm{e}^{\mathrm{i}\left(\mathbf{k}_\parallel \cdot \mathbf{r}_\alpha - (\mathbf{k}_\parallel - \mathbf{q})\cdot \mathbf{r}_\beta\right)} \, . \tag{4.29}$$

Eq. 4.29 can be computed as a convolution, taking advantage of the computational efficiency of the fast Fourier transform (FFT) via the convolution theorem.

Scattering from two magnetic impurities produces rich structure in the QPI. Two-impurity QPI differs from the idealized single-impurity limit in three key ways. First, the existence of a real-space vector $\mathbf{R} = \mathbf{r}_2 - \mathbf{r}_1$ connecting impurity positions gives rise to additional complex phase factors in the surface scattering t-matrix, see Eq. 4.26. Only in the single impurity case can these be eliminated by a suitable basis choice. Second, there are both local ($\alpha = \beta$) and non-local ($\alpha \neq \beta$) contributions to the QPI in Eqs. 4.27 and 4.28 due to the matrix structure of the impurity Green functions $\mathbf{G}_d(\omega)$. Third, these Green functions themselves develop rich dynamics due to the interplay between Kondo and effective RKKY physics. As highlighted in Chapter 3, the resulting non-trivial scanning-energy and temperature dependence of the QPI is the hallmark of scattering from quantum impurities Ref. 48.

For a generic system containing two equivalent impurities, the QPI can be decomposed into local and non-local contributions, $\Delta\rho(\mathbf{q},\omega) = \Delta\rho_{\mathrm{loc}}(\mathbf{q},\omega) + \Delta\rho_{\mathrm{nl}}(\mathbf{q},\omega)$. Eqs. 4.26–4.28 imply,

$$\Delta\rho_\gamma(\mathbf{q},\omega) = -\frac{1}{2\pi\mathrm{i}}[Q_\gamma(\mathbf{q},\omega) - Q_\gamma(-\mathbf{q},\omega)^*] \, , \tag{4.30a}$$

$$Q_\gamma(\mathbf{q},\omega) = V^2 G_d^\gamma(\omega) \times \Lambda_\gamma(\mathbf{q},\omega) \, , \tag{4.30b}$$

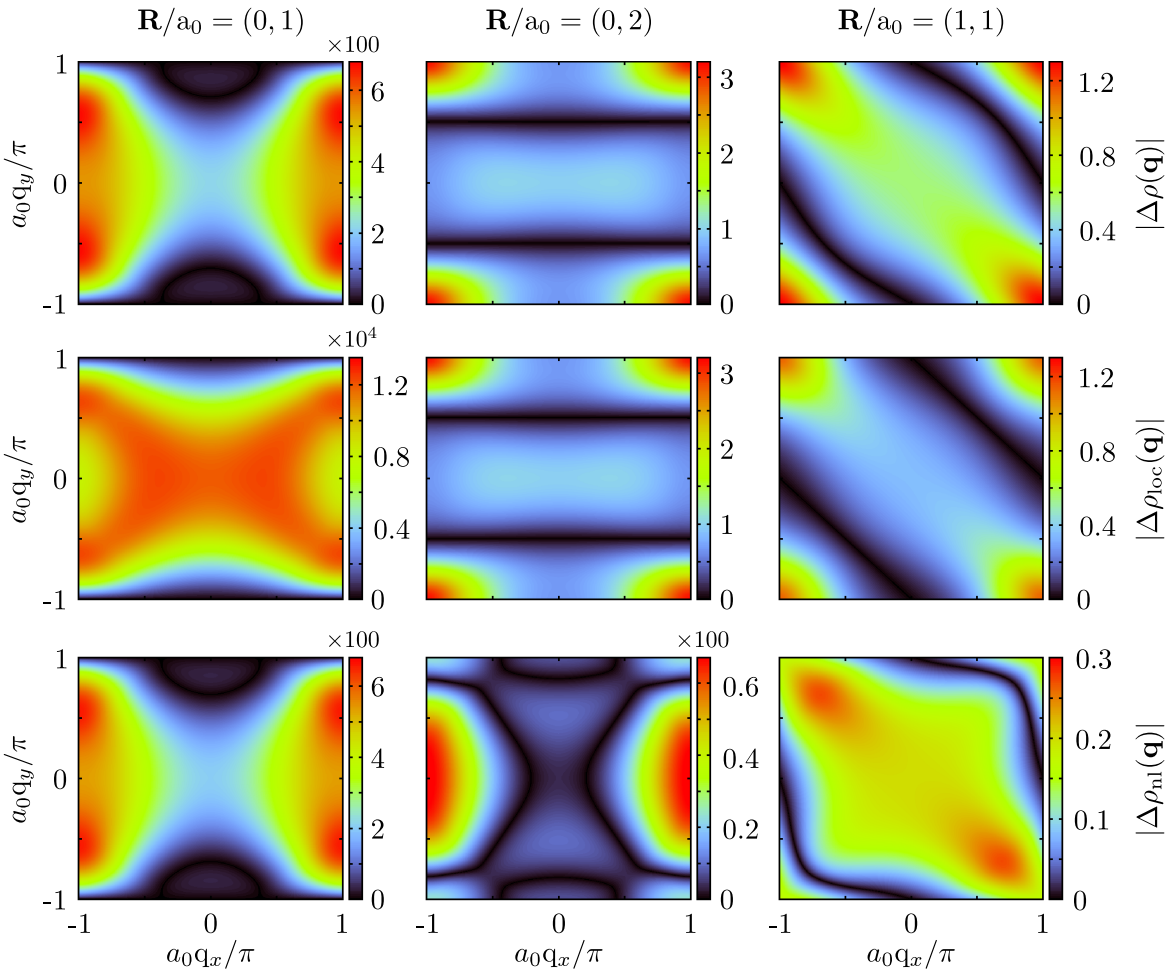

Fig. 4.6 QPI for two equivalent magnetic impurities on the 3D cubic (100) surface, separated by vectors $\mathbf{R}/a_0 = (0,1)$, $(0,2)$ and $(1,1)$, as shown in the left, centre and right column panels, respectively. The full QPI $|\Delta\rho(\mathbf{q},\omega)|$ is shown in the upper row panels, while the local and non-local contributions, obtained from Eqs. 4.30, 4.31, are shown in the centre and lower row panels. Obtained for $U/\Gamma_0 = 28$ as per Figure 4.4, with scanning energy $\omega = 10^{-6}t \equiv 0.1T_{\rm K}^{\rm 1imp}$.

with γ =loc or nl, because $G_d^{\rm loc}(\omega) \equiv G_d^{11}(\omega) = G_d^{22}(\omega)$ and $G_d^{\rm nl}(\omega) \equiv G_d^{12}(\omega) = G_d^{21}(\omega)$ as a result of the equivalence of the two impurities. The host functions are defined as,

$$\Lambda_{\rm loc}(\mathbf{q},\omega) = \cos(\tfrac{1}{2}\mathbf{q}\cdot\mathbf{R}) \times \Lambda(\mathbf{q},\omega)\ , \tag{4.31a}$$

and

$$\Lambda_{\rm nl}(\mathbf{q},\omega) = \int_{\rm 1SBZ} \frac{d^2\mathbf{k}_\parallel}{\Omega_{BZ}}\ \cos(\tfrac{1}{2}\mathbf{q}\cdot\mathbf{R} - \mathbf{k}_\parallel\cdot\mathbf{R}) G_0^0(\mathbf{k}_\parallel,\omega) G_0^0(\mathbf{k}_\parallel+\mathbf{q},\omega)\ , \tag{4.31b}$$

where $\Lambda(\mathbf{q},\omega)$ appearing in Eq. 4.31a is the corresponding single-impurity result [48],

$$\Lambda(\mathbf{q},\omega) = \int_{\rm 1SBZ} \frac{d^2\mathbf{k}_\parallel}{\Omega_{BZ}}\ G_0^0(\mathbf{k}_\parallel,\omega) G_0^0(\mathbf{k}_\parallel+\mathbf{q},\omega)\ . \tag{4.32}$$

Interference between scattering events from each impurity leads to a modulation of the QPI, controlled by the inter-impurity separation vector $\mathbf{R}$. In particular, the local contribution $\Delta\rho_{\rm loc}(\mathbf{q},\omega)$ in Eq. 4.31a carries an overall factor $\cos(\frac{1}{2}\mathbf{q}\cdot\mathbf{R})$ which lowers the symmetry of the QPI, and introduces nodal lines of suppressed scattering when $\mathbf{q}\cdot\mathbf{R} = (2n+1)\pi$. This is demonstrated in the centre row panels of Figure 4.6, where colour plots of $|\Delta\rho_{\rm loc}(\mathbf{q})|$ are presented for $\mathbf{R}/\mathrm{a}_0 = (0,1)$, $(0,2)$ and $(1,1)$ in the left, centre and right columns, respectively (corresponding to the inter-impurity singlet, independently Kondo screened and spin-1 Kondo screened regimes of the AAM discussed in Section 4.2).

By contrast, the relative scattering phase does not appear simply as an overall prefactor to the non-local contribution $\Delta\rho_{\rm nl}(\mathbf{q},\omega)$ in Eq. 4.31b. The nodal structure is therefore more complicated, as shown in the lower row panels of Figure 4.6.

Importantly, the local and non-local contributions to the total QPI $\Delta\rho(\mathbf{q})$, plotted in the upper row columns, are weighted according to the local and non-local Green function elements – see Eq. 4.30. As discussed in Section 4.2.4, the impurity separation has a major effect on the impurity dynamics. For $\mathbf{R}/\mathrm{a}_0 = (0,1)$, the non-local contribution to the QPI dominates at low energies $\omega = 10^{-6}t$, reflecting the strongly antiferromagnetic RKKY interaction that binds the impurities together in a singlet state. This is shown in the left column panels of Figure 4.6 (note the rescaled colour range); the full QPI $\Delta\rho(\mathbf{q})$ therefore resembles closely its non-local contribution, $\Delta\rho_{\rm nl}(\mathbf{q})$.

For $\mathbf{R}/\mathrm{a}_0 = (0,2)$ by contrast, the local contribution dominates (again, note the rescaled colour range for the centre column panels), and the structure of the full QPI $\Delta\rho(\mathbf{q})$ now resembles closely $\Delta\rho_{\rm loc}(\mathbf{q})$. As shown in the right column panels, both local

and non-local effects are important when the impurities are separated by $\mathbf{R}/\mathrm{a}_0 = (1,1)$, due to the fine balance of Kondo and RKKY physics in this system.

When the two impurities are well-separated, each is Kondo-screened essentially independently of the other, as discussed in Section 4.2.4. This is reflected in the vanishing of non-local impurity Green functions $G_d^{12}(\omega) \simeq 0$, and hence the vanishing of the non-local contribution to the QPI, $\Delta\rho_{\mathrm{nl}}(\mathbf{q})$. It was demonstrated in Section 4.2.4 that for parameters in an experimentally relevant range this independent screening is observed from very short separations, $|\mathbf{R}| \gtrsim 4\sqrt{2}\mathrm{a}_0$. On the other hand, the profound impact on the QPI due inter-impurity interactions over short distances for two magnetic magnetic impurities demonstrates that such many-impurity effects must be taken into account when considering the QPI – albeit only for impurities in close proximity. In a typical experimental setting, the full many-impurity case is expected; the control of the distribution of impurities is challenging or impossible, and therefore careful consideration of the effect of inter-impurity interactions is required when calculating the QPI, as we now address.

4.4 Many Impurities

The treatment of models that consist of many magnetic impurities is an inherently formidable task, as discussed in Section 4.2.1, because they involve N interacting sites coupled to many screening channels. In particular, NRG (usually considered the numerical method of choice for quantum impurity problems) cannot traditionally be used for $N > 2$ impurity/channel systems. Recent developments with NRG – which either utilize model symmetries fully [209, 69, 186], or exploit the fine-grained RG description obtained by interleaving different Wilson chains [145, 187] – significantly reduce the computational cost of solving multichannel problems. Although models with $N = 3, 4$ and possibly 5 channels can now be treated with NRG, true *many*-impurity systems remain out of reach.

Furthermore, such real-space problems cannot generally be cast in the required form involving N impurities connected to the end of N *decoupled* Wilson chains. The matrix Dyson equation, Eq. 4.7, can only be diagonalized by a single canonical transformation of operators in special cases where elements of the hybridization matrix possess the symmetry $\Gamma_{ii}(\omega) = \Gamma^{\mathrm{loc}}(\omega)$ and $\Gamma_{i\neq j}(\omega) = \Gamma^{\mathrm{nl}}(\omega)$. Only in this case can one obtain a representation in which $G_d^{\nu}(\omega) = (\omega + \mathrm{i}0^+ - \epsilon_d - \Gamma_{\nu}(\omega) - \Sigma_{\nu})^{-1}$ are independent, as required for treatment with NRG. In general, we expect the distribution of magnetic impurity adatoms on a metallic surface to be disordered for low impurity concentrations.

The system therefore does not fulfill the high-symmetry requirement for decomposition in this way, and therefore be tractable via NRG.

The relatively short range of these inter-impurity interactions in the magnetic adatom system admits the possibility that the many-impurity case may be treated beyond the independent-impurity limit via systematic approximation. Sections 4.2.4 and 4.2.5 revealed that two impurities behave essentially independently when $|\mathbf{R}| > \mathrm{R_{dil}}$, such that the system is in the indepedently Kondo screened regime in which local Kondo screening by the host conduction electrons cuts off the nascent inter-impurity RKKY interaction. Beyond this length scale the physics is simply that of two independently Kondo screened impurities, and as such, impurities with realistic parameters on the prototypical 3D cubic lattice (100) surface can be treated independently for a rather small separation $\mathrm{R_{dil}} \approx 4\sqrt{2}\mathrm{a_0}$. Depending on the specific real-space distribution of impurities, the system could therefore be decomposed into essentially decoupled and hence independent smaller clusters. Indeed, if *all* impurities in a given finite sample region are separated by more than $\mathrm{R_{dil}}$, each impurity can be treated independently. This situation corresponds to the "dilute limit": here an accurate description of the local physics of each impurity is obtained from a model involving a single impurity in the same host.

For given impurity surface coverage, $\phi = N/N_s$ (with N_s the number of surface lattice sites), the average inter-impurity separation $\langle|\mathbf{R}|\rangle \sim \mathrm{a_0}\,\phi^{-1/2}$. But even for low coverage where $\langle|\mathbf{R}|\rangle \gg \mathrm{R_{dil}}$, the sample may occasionally contain groups of a few impurities located close enough that their mutual interactions cannot be neglected. These rare "clusters" may nonetheless still be well-separated from other impurities or clusters, whence independent clusters can be treated separately. At a given coverage, and with a specific impurity distribution, one can then describe accurately the many-impurity system in terms of independent impurities and clusters.

The question then naturally presents itself: what is the typical occurrence of impurity clusters of size N_c at a given impurity coverage? To answer this question, we calculate the configurationally-averaged fraction of impurity clusters as a function of surface coverage (with the impurities distributed at random) via numerical simulation of a large number of random impurity distributions at a given surface coverage, ϕ. Specifically, we take a cluster of size N_c to comprise N_c impurities, each within a cutoff distance $\mathrm{R_{dil}}$ of another impurity of that cluster (but separated from other impurities by more than $\mathrm{R_{dil}}$). Conceptually this is equivalent to factorizing the full multi-impurity system into a set of irreducible impurity clusters; for given coverage, and surface sample size relevant to FT-STS experiments, the average number of clusters

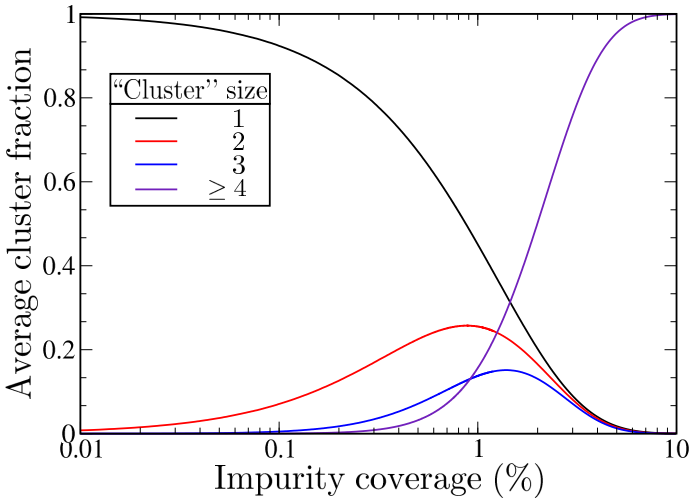

Fig. 4.7 Average fraction of impurity clusters of size $N_c = 1, 2, 3$ and ≥ 4, vs impurity coverage for a random distribution of impurities on a cubic lattice surface. "Clusters" are defined by finding each set of impurities for which no impurity is more than the impurity cutoff distance ($\mathrm{R_{dil}} = 4\sqrt{2}\mathrm{a_0}$) from at least one other impurity in the cluster.

of size $N_c = 2, 3, 4, \ldots$ can then be determined. In Figure 4.7 the variation of the fraction of impurities in a cluster of size N_c with surface coverage is plotted, with $\mathrm{R_{dil}} = 4\sqrt{2}\mathrm{a_0}$ used as the cluster cutoff. We note from Section 4.2.5 that this is a relatively conservative definition of the cluster: a larger $T_{\mathrm{K}}^{\mathrm{1imp}}$ leads to smaller $\mathrm{R_{dil}}$, and hence the earlier onset of the dilute limit.

At a representative impurity coverage of 0.04%, we find that $\sim 96.9\%$ of impurities are independent (a cluster size $N_c = 1$), 3% must be treated as an $N_c = 2$ impurity pair (as described in detail in Section 4.2), and 0.1% are in clusters of $N_c \geq 3$. In a $500\mathrm{a_0} \times 500\mathrm{a_0}$ sample region, 0.04% impurity density corresponds to 100 surface impurities: the surface is already rather crowded, with mean separation $\langle|\mathbf{R}|\rangle \sim 28\mathrm{a_0}$. But even then, there are on average only 3 clusters with $N_c = 2$ in such a sample.

We note that impurity coverage can be controlled through various experimental protocols. For example, the extreme dilute limit of $10^{-6}\%$ impurity coverage can be accessed (see for example Ref. 163), and even specific distributions can be realized by careful manipulation of individual impurities [130, 155]. Doped thin films (such as Cr on Cu in Ref. 68) realize effective 2D systems with impurity densities on the order of $\sim 0.01\%$. Alternatively, evaporation techniques from wires onto surfaces (see for example Ref. 101202) controllably achieve up to $\sim 0.1\%$ impurity density; while dilute alloys are often characterized by an equivalent surface impurity coverage of $0.03 - 0.3\%$ [70, 50, 81].

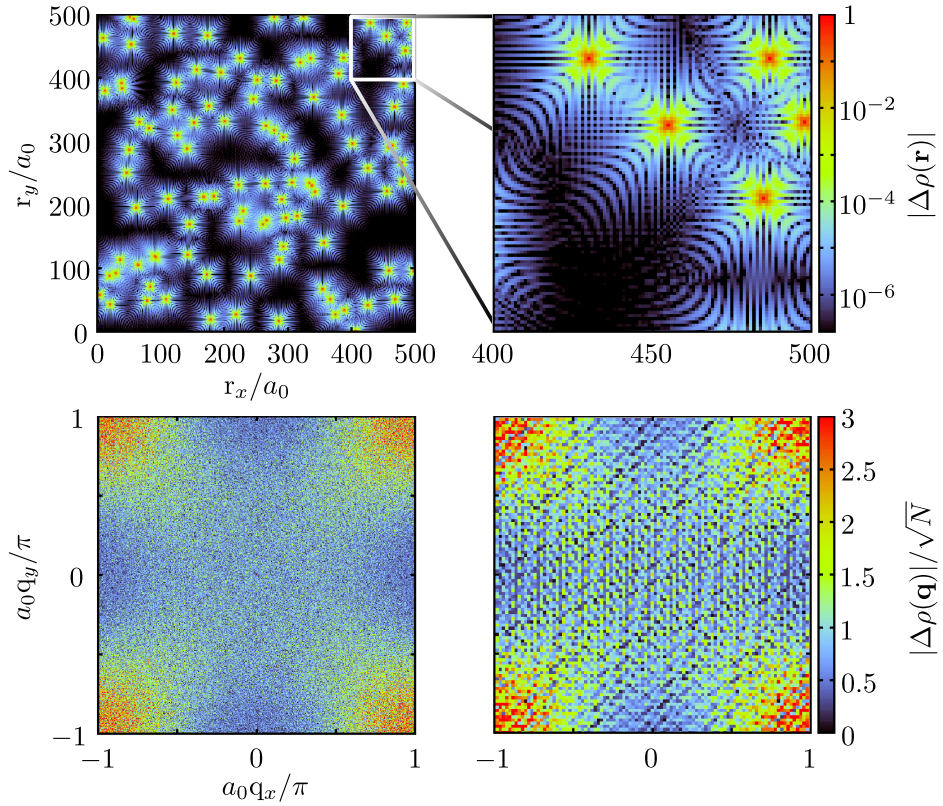

Fig. 4.8 Independent magnetic impurities deposited randomly on a 3D cubic lattice (100) surface. Upper panels: real-space LDOS maps. Lower panels: corresponding QPI. Left panels for $N = 100$ impurities within a $500a_0 \times 500a_0$ sample region, while right panels show a $100a_0 \times 100a_0$ sub-block containing $N = 5$ impurities. Calculated for $U/\Gamma_0 = 28$ and scanning energy $\omega = 10^{-6}t \equiv 0.1T_K^{1imp}$.

The results of Figure 4.7 show that at these experimentally-relevant surface coverages, there is a clear scale separation for cluster occurrence. This suggests a hierarchy of approximation in which the contribution from very rare clusters with size $N_c > N_c^{max}$ is neglected. Interestingly, at the above typical coverages, many-impurity systems are very well described in terms of independent impurities and independent clusters of size $N_c = 2$. Such systems are therefore amenable to treatment with NRG, using only single-impurity results and two-impurity results as in presented in Chapter 3 and Section 4.2.

4.4.1 Independent impurities: dilute limit

Motivated by the above, we first consider a many-impurity system within an independent impurity picture. Specifically, we study the semi-infinite 3D cubic lattice, with $N = 100$

magnetic impurities placed randomly in a $500\mathrm{a}_0 \times 500\mathrm{a}_0$ sample plaquette on the surface (corresponding to 0.04% impurity density).

The independent impurity approximation implies a strictly diagonal hybridization matrix $\mathbf{\Gamma}(\omega) = V^2 G^0(\mathbf{r}_i, \mathbf{r}_i, \omega)\,\mathbf{I}$. Each impurity then behaves identically to a single quantum impurity in the same host: the impurity distribution does not affect the local impurity physics at this level. The off-diagonal elements of the t-matrix vanish as a result, $T_{\alpha\beta}(\omega) \equiv V^2 G_d^{\alpha\beta}(\omega) = \delta_{\alpha\beta} V^2 G_d^{\mathrm{loc}}(\omega)$, so that the QPI comprises only "local" contributions (from the diagonal terms of the t-matrix, in comparison with Eqs. 4.30 and 4.31 for the interacting two-impurity case). Moreover, these local contributions from the diagonal elements of the real-space t-matrix differ from the interacting-impurity case, as the local impurity Green functions are also affected by inter-impurity correlations, as discussed above.

Despite this, the impurity distribution still strongly affects the real-space LDOS map through Eq. 4.20, even for independent impurities, and the resultant QPI thus also depends on the impurity distribution. It is given generally by Eq. 4.27, but with

$$Q(\mathbf{q}, \omega) = T(\mathbf{q}, \omega) \times \Lambda(\mathbf{q}, \omega) \tag{4.33}$$

where $\Lambda(\mathbf{q}, \omega)$ is the single-impurity function Eq. 4.32, compared with the full multi-impurity result, Eq. 4.28. The t-matrix $T(\mathbf{q}, \omega)$ is the therefore the product of a structure factor, $S(\mathbf{q}) = \sum_\alpha \mathrm{e}^{-\mathrm{i}\mathbf{q}\cdot\mathbf{r}_\alpha}$, and the local t-matrix, $T_{\mathrm{loc}}(\omega) = V^2 G_d^{\mathrm{loc}}(\omega)$, reflecting the independent and identical nature of the impurities:

$$T(\mathbf{q}, \omega) = S(\mathbf{q}) \times T_{\mathrm{loc}}(\omega)\,. \tag{4.34}$$

The experimentally-measurable power spectrum of the QPI follows as

$$|\Delta\rho(\mathbf{q}, \omega)|^2 = \Big(\sum_{\alpha,\beta} \cos\left[(\mathbf{r}_\alpha - \mathbf{r}_\beta)\cdot\mathbf{q}\right] \Big) \times |\Delta\rho_{1\mathrm{imp}}(\mathbf{q}, \omega)|^2\,, \tag{4.35}$$

where $\Delta\rho_{1\mathrm{imp}}(\mathbf{q}, \omega) = -\frac{V^2}{\pi}\mathrm{Im}\,\Big(G_d^{\mathrm{loc}}(\omega) \times \Lambda(\mathbf{q}, \omega)\Big)$ is the pristine single-impurity QPI, as given in Chapter 3. As such, the QPI for a many-impurity system in the dilute limit is related simply to the single-impurity QPI, but with an overlaid moiré pattern due to the superposed cosine factors in Eq. 4.35.

This is demonstrated in Figure 4.8, for an $N = 100$ impurity system. The upper left panel shows the full spatial map of the LDOS, which allows the impurity positions to be clearly identified. Despite the comparatively high surface density of 0.04% and the apparent crowding, there are only two $N_c = 2$ impurity clusters in the $500\mathrm{a}_0 \times 500\mathrm{a}_0$

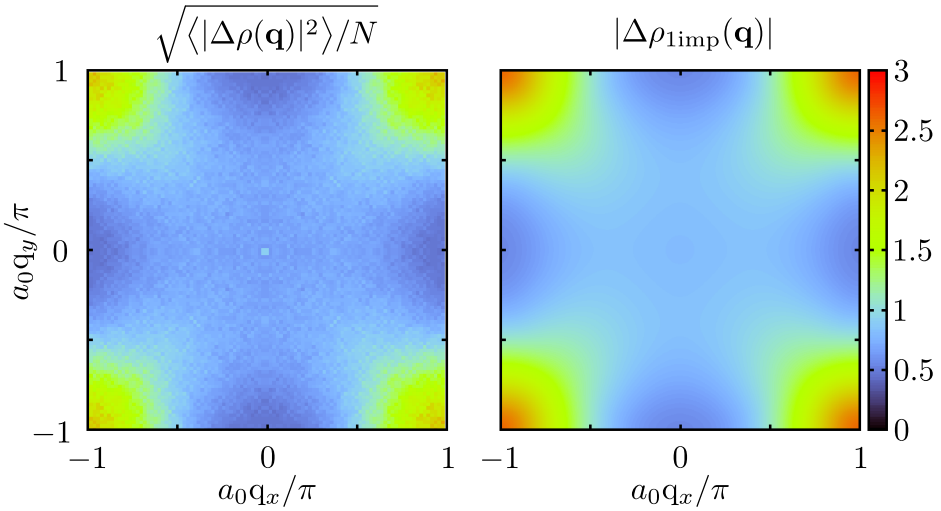

Fig. 4.9 Left panel: block-averaged and symmetrized QPI, obtained by combining $M = 25$ sub-blocks of size $100\mathrm{a}_0 \times 100\mathrm{a}_0$ from the original $500\mathrm{a}_0 \times 500\mathrm{a}_0$ sample shown in the left panels of Figure 4.8. The right panel shows the pristine single-impurity result for comparison.

surface sample (although recall that in this subsection all impurities are treated independently). The upper right panel shows an expanded view of the LDOS for a $100\mathrm{a}_0 \times 100\mathrm{a}_0$ sub-block sample containing $N = 5$ impurities. The corresponding QPI for both samples is shown in the lower panels of Figure 4.8.

Although the basic structure of the pristine single-impurity QPI survives, the many impurity QPI appears noisy due to the impurity disorder. The $\mathbf{q}$-space resolution of the QPI in the lower right panel is naturally more coarse than that in the lower left, because the real-space sample is smaller. The moiré structure of the QPI due to the $N = 5$ impurities is also much more apparent, with well-defined interference fringes characteristic of the underlying impurity separation vectors.

For random independent impurities, the QPI calculated via Eq. 4.35 from an $L \times L$ surface sample in the limit $L \to \infty$ recovers the single-impurity result [34, 102]. Equivalently, the single-impurity QPI can in principle be recovered by averaging the QPI over different disorder realizations, since

$$|\Delta\rho_{1\mathrm{imp}}(\mathbf{q},\omega)|^2 = \frac{\langle|\Delta\rho(\mathbf{q},\omega)|^2\rangle}{N + N^2\delta_{\mathbf{q},\mathbf{0}}}\,, \tag{4.36}$$

where we have used $\langle|S(\mathbf{q})|^2\rangle = N + N^2\delta_{\mathbf{q},\mathbf{0}}$. Such configurational averaging may not however be experimentally feasible, due to the difficulty in controlling surface topography across disparate real-space regions.

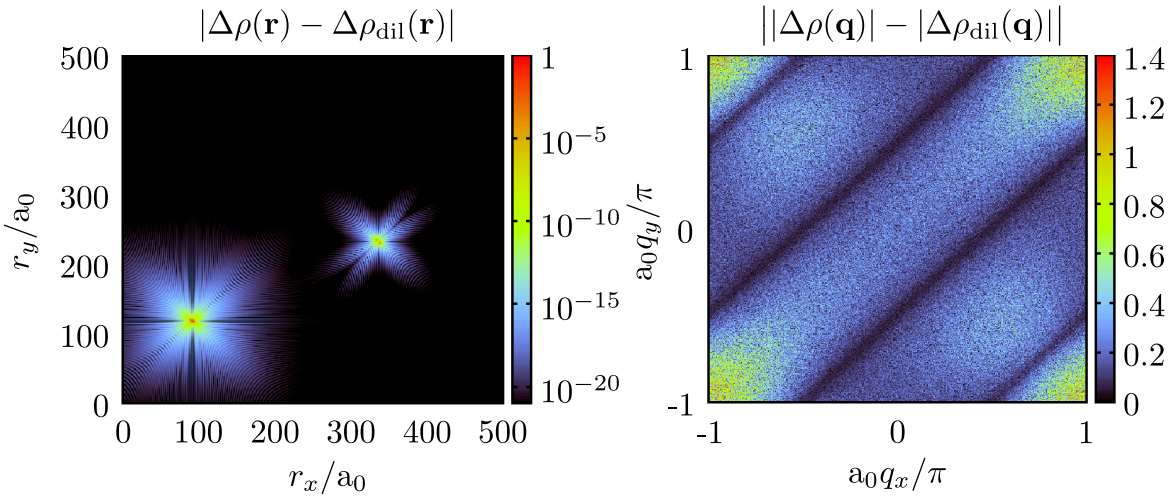

Fig. 4.10 $N = 100$ impurities within a $500\mathrm{a}_0 \times 500\mathrm{a}_0$ surface region of a 3D cubic lattice. Impurity distribution and parameters as in Figure 4.8. Left panel: spatially-resolved LDOS difference $|\Delta\rho(\mathbf{r}) - \Delta\rho_{\rm dil}(\mathbf{r})|$, where $\Delta\rho(\mathbf{r})$ is calculated within the independent cluster approximation (treating inter-impurity interactions in the two $N_c = 2$ clusters exactly), while $\Delta\rho_{\rm dil}(\mathbf{r})$ is calculated assuming the dilute limit within an independent impurity picture. Right panel: corresponding QPI difference $|\Delta\rho(\mathbf{q}) - \Delta\rho_{\rm dil}(\mathbf{q})|$.

Instead, one can consider a single $L \times L$ sample region decomposed into M smaller sub-blocks of size $L_b \times L_b$, as in Figure 4.8. The QPI from each block can be calculated and the results averaged. If the underlying lattice symmetry is known, the QPI pattern can also be symmetrized by averaging over equivalent scattering vectors $\mathbf{q}$, further reducing the effect of configurational noise. This method reduces the effect of impurity disorder in the QPI at the expense of $\mathbf{q}$-space resolution. This protocol was used to obtain the QPI in the left panel of Figure 4.9, averaging over $M = 25$ non-overlapping sub-blocks of $100\mathrm{a}_0 \times 100\mathrm{a}_0$ lattice sites. The result is clearly seen to be quantitatively comparable to the "ideal" single-impurity QPI, shown in the right panel.

4.4.2 Independent clusters: beyond the dilute limit

We now go beyond the dilute limit by taking into account explicitly the contribution from impurity clusters whose mutual interactions are important. These clusters are nevertheless well-separated from other impurities or clusters, and therefore remain independent.

Within this approximation, the hybridization matrix is block-diagonal, with $[\mathbf{\Gamma}(\omega)]_{\alpha\neq\beta}$ taken to be non-zero only for impurities α and β that are both members of the same

cluster. The t-matrix $T_{\alpha\beta}(\omega)$ then has the same block diagonal structure, and the full QPI is as usual computed using Eqs. 4.27 and 4.28.

As a concrete example, we use the same impurity disorder realization as in Figure 4.8, corresponding to $N = 100$ magnetic impurities within a $500\mathrm{a}_0 \times 500\mathrm{a}_0$ region on the 3D cubic lattice surface (the specific distribution can be visualized through the LDOS modulations in the upper left panel). In this representative case there are two $N_c = 2$ clusters, and no larger clusters. The two-impurity clusters are treated independently from the remaining impurities, which are themselves taken to be independent single-impurity problems. Within this framework, the quantum impurity problems are solved using NRG, and the QPI calculated. Since inter-cluster correlations are negligible when clusters are well-separated (as discussed in Section 4.2.4), this independent cluster approximation is essentially exact.

The local impurity physics of the $N_c = 2$ clusters is strongly affected by inter-impurity interactions as examined in detail in Section 4.2. This effect would be observable through spectroscopic local measurements with STM, albeit that the contribution to the overall QPI is expected to be weak because scattering is dominated by the 96% of (effectively independent) impurities in the sample.

The left panel of Figure 4.10 shows the *difference* between the real-space LDOS calculated using the independent cluster method, and the LDOS obtained through the independent impurity approximation of Section 4.4.1. We find that this difference is highly localized to the cluster sites themselves (note the logarithmic colour scale). This confirms that bulk properties are not strongly affected by the contribution from dilute clusters (although an accurate description of *local* quantities does of course require the more sophisticated treatment of intra-cluster interactions).

In the right panel of Figure 4.10 we plot the corresponding difference in the QPI, as calculated using the independent cluster and independent impurity approximations. The change in the QPI is dominated by intra-cluster contributions for an $N_c = 2$ pair with separation vector $\mathbf{R}/\mathrm{a}_0 = (2, 2)$, as seen directly from the modulation of QPI intensity in the Figure (the impurities in the other $N_c = 2$ cluster are separated by $\mathbf{R}/\mathrm{a}_0 = (4, 4)$; intra-cluster interactions are weak in this case, and so its contribution to the overall QPI is small).

Our results indicate that the independent impurity picture, strictly applicable only in the dilute limit, works surprisingly well when the cluster incidence is low. Then the physics of independent quantum impurities dominates the QPI – even for relatively large impurity densities up to 0.1% when sampling a surface region of size $L \times L$, with $L \sim 100\mathrm{a}_0 - 1000\mathrm{a}_0$. To capture inter-impurity interactions, which become important

for local quantities near clusters and for fine details in the QPI, the independent cluster method can be employed.

4.5 Conclusion

In this chapter we have studied systems of multiple magnetic impurities deposited on the surface of a 3D metallic host, the associated scattering of conduction electrons and the resultant signatures in QPI. Scattering from multiple impurities for the surface LDOS and the resultant QPI was considered formally for an arbitrary system of many interacting impurities; however, such systems are impossible to treat exactly, and so an approximate description was sought. From solution of the real-space two-impurity model, we are able to define and identify a dilute impurity limit for many-impurity systems, in which each impurity in practice behaves independently of the others. For realistic parameters, the length scale $\mathrm{R_{dil}}$ for the onset of the dilute limit is found to be strikingly low — the inter-impurity separation need only be a few lattice sites. Overall, the physics is overwhelmingly dominated by independent single-impurity effects for impurity coverages up to $\sim 0.1\%$ when the Kondo temperature is small, $T_{\mathrm{K}} \sim 0.1K$; while for $T_{\mathrm{K}} \sim 100K$, a surface coverage up to $\sim 1\%$ is found to remain dilute. The QPI therefore reflects the pristine single-impurity result, as presented in Chapter 3, modulated only by a trivial structure factor due to the real-space impurity distribution. As such, the temperature and scanning-energy dependence of the QPI are entirely characteristic of the underlying single-impurity Kondo effect.

Going beyond the dilute limit to higher impurity coverage, inter-impurity interactions within impurity clusters must naturally be taken into account. The clusters themselves can nevertheless be well-separated, and therefore behave independently. An "independent cluster" approximation, applying in a dilute (cluster) limit, then yields accurate results for the physics of such many-impurity systems. In order to capture the effect of inter-impurity interactions, in Section 4.2 we considered as a minimal model the case of two magnetic impurities, separated in real space, embedded on the (100) surface of the 3D cubic lattice host. The so-called Alexander Anderson model was demonstrated to involve complicated through-lattice inter-impurity correlations, resulting in a dynamic coupling between the impurities not captured in the simpler reduced models often employed to describe the physics of the multi-impurity case. Indeed, the relative strengths of local impurity-host interactions and non-local inter-impurity interactions was found to depend non-trivially on both the impurity parameters (such

as the interaction strength, U) and the magnitude and orientation of the separation vector between impurities.

The local impurity-host interactions give rise to essentially independent Kondo screening of the two impurities; the inter-impurity interaction, by contrast, results in either the formation of an inter-impurity singlet or a non-local, spin-1 state (then itself screened by interaction with the host conduction electrons) depending on the nature of the effective RKKY interaction (antiferromagnetic or ferromagnetic respectively). The interplay of these effects gives rise to distinctive signatures, as demonstrated by the impurity contribution to the entropy and the local impurity spectral function, both calculated exactly via NRG, presented in Section 4.2. The competition between local antiferromagnetic interactions (responsible for Kondo screening) and an effective antiferromagnetic RKKY interaction between impurities is of particular interest. As discussed in Section 4.2.6, the frustration between these two competing effects may result in signatures of the critical physics at the two-impurity Kondo critical point being observable in the AAM at finite energy scales.

The physics of the Alexander Anderson model is significantly more complicated than that of the simplified, reduced models often invoked to describe it. Despite its simplicity, the model acts as a minimal model for the competition between local and non-local interactions in more complicated magnetic materials. A more complete understanding of the physics is therefore very desirable, and the subject of ongoing work. In particular, calculations of the entanglement between the two impurities, and between the impurities and the host, may shed further light on the nature of the inter-impurity interactions in the system. We also plan to investigate a range of host materials, including those without particle-hole symmetry, to deepen the understanding of how the dynamical nature of the inter-impurity interaction, mediated by the conduction electrons, impacts upon the physics of the system.

An independent cluster picture must of course ultimately fail when impurity coverage is increased towards and above a percolation threshold where the entire system becomes "connected". The physics then involves a subtle interplay between Kondo, RKKY, and disorder effects, and the collective heavy fermion physics of the diluted periodic Anderson lattice. As discussed in this chapter, the treatment of truly many-impurity systems such as these is not possible solely via NRG calculations, and remains a formidable open problem in the field.

Chapter 5

QPI in strontium ruthenate: correlations & superconductivity

The binary transition metal oxide strontium ruthenate forms a range of layered perovskite-like compounds in the Ruddlesden-Popper series, $Sr_{n+1}Ru_nO_{3n+1}$, consisting of n (AB-stacked) 2D layers of vertex-sharing RuO_6 octahedra followed by an intercalating SrO plane. Despite being superficially similar in structure, the family of compounds exhibits a significant range of phenomenology, due to the interplay and interactions between lattice, orbital, charge and spin degrees of freedom (on the partially-filled transition metal site, with the nominal oxidation state Ru^{IV} giving an electronic configuration of $4d^4$). The full perovskite ($n = \infty$) $SrRuO_3$ is a bulk ferromagnet (FM) with $T_C \sim 165$K [123], while the intermediate phase $Sr_3Ru_2O_7$ exhibits an unusual anisotropic metamagnetic state, exhibiting nematic spatial order [115, 116]. The $n = 1$ case, Sr_2RuO_4 is arguably the most interesting member of the family, exhibiting an exotic superconducting (SC) phase with an order parameter (OP) of p-wave symmetry below $T_c \sim 1.5$K [127, 134]. The structure, depicted in Figure 5.1, consists of single RuO_2 planes intercalated between pairs of SrO planes, somewhat analogous to the planar structure of the cuprate unconventional superconductors (consisting of CuO_2 planes). As a consequence of this planar structure, the RuO_2 layers are almost (electronically) isolated in the direction of the c-axis, with a pseudo-2D, multi-band electronic structure, described in Section 5.1.1. The ground state is non-magnetic, but in close proximity to a number of structural and magnetic instabilities, such that several different structural/magnetic phases lie close to the ground state and thus influence the physics at low temperature. The pairing mechanism giving rise to the unusual SC state is still somewhat unclear due to the multi-band nature of the system and the relatively small magnitude of the pairing interaction [127, 197, 53], but is

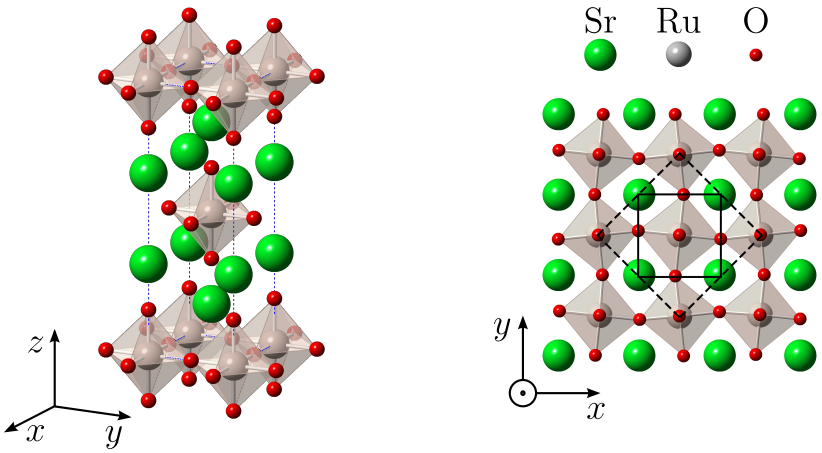

Fig. 5.1 *Left:* Unit cell structure of Sr_2RuO_4, demonstrating the layered nature of the compound, which can be thought of as *AB* stacked 2D layers of vertex sharing RuO_6 octahedra with interstitial Sr, or as RuO_2 planes between two SrO planes. *Right:* Top view of SrO surface following cleave along the (001) lattice plane, showing the reconstructed surface structure, with the undistorted unit cell (solid line) and reconstructed surface unit cell (dashed line).

thought to be closely linked to spin fluctuations in one or more of the bands [181, 134, 95, 203], as discussed in Section 5.1.2.

In Chapter 2 we demonstrated that the QPI may be interpreted loosely in terms of an in-situ scattering experiment, providing information on both the scattered quasiparticles of the host and the scatterer(s). Furthermore it was shown that strong features in the QPI may arise from scattering between particular pairs of conduction electron states in momentum space, and may be used to map the electronic structure of the host material. The dispersion of these features with scanning energy may be mapped by experimentally measuring the QPI (via FT-STS), and thus the dispersion of the corresponding host conduction band states mapped also. Indeed, FT-STS has been employed in this manner to study correlated materials similar to Sr_2RuO_4, such as cuprate and pnictide superconductors [78, 214] and heavy fermion compounds [193].

In order to carry out STM studies on the conduction bands derived primarily from the Ru orbitals, a surface must be revealed that allows electron tunnelling into the RuO_2 layers. Experimental evidence [132] and theoretical calculations [158] indicate that clean cleavage along the (001) plane may be achieved, exposing a surface SrO layer depicted in Figure 5.1. Tunnelling into the RuO_2 layer is then facilitated by orbital overlap via apical oxygen atoms of the surface RuO_6 octahedra. The surface layer of RuO_6 octahedra has been shown to undergo reconstruction [47, 196], with a static rotational distortion of the surface RuO_6 octahedra around the *c*-axis of

approximately 6°, corresponding to the "freezing out" of a (soft) bulk phonon mode [133]. The modified surface electronic structure that results from this distortion is discussed in Section 5.1.1. The planar structure and the ability to cleave cleanly to expose the RuO_2 layers to STM make Sr_2RuO_4 a good candidate for investigation via FT-STS. Local STS has been shown to be a valuable tool to shed light on the electronic structure, providing the (sub-)meV energy resolution necessary to probe the SC state [53]; FT-STS offers the possibility of resolving the momentum-space structure of the SC gap and giving further insight into the pairing mechanism.

FT-STS is therefore expected to provide valuable insight into both the normal and SC state of Sr_2RuO_4 [7, 59]. However, the QPI in this multi-band interacting system is significantly more complicated than the simple, single-band examples considered in Chapters 3 and 4, as discussed previously in Section 2.3. The interference of all possible scattering processes gives rise to the QPI pattern observed via FT-STS: as emphasized in previous chapters, a careful theoretical treatment is therefore required in order to make valid predictions and provide accurate interpretation of experimental FT-STS measurements. Previous theoretical studies [7, 59] have not only employed a simplified model for the electronic structure in the normal and SC state (for example neglecting the effect of spin-orbit coupling (SOC)), but moreover have not considered the effect of these complicating experimentally-relevant factors, which we have shown may have a profound impact on the measured QPI.

The multi-band structure of the host material, and the manner in which the states of the host are scattered by impurities, is of particular importance. In order to investigate these issues, we first detail an effective free tight binding model for the electronic structure in both the normal state and the SC state in Section 5.1, before calculating the QPI arising in the normal state in detail in Section 5.2. We include the effect on the QPI of several complicating factors, considering the strength of scattering from impurities, the spatial anisotropy of the host material orbitals that the STM tip probes and the surface reconstruction detailed above, and compare the calculated QPI to experimental results reproduced from Ref. 206.

In Section 5.3 we present collaborative results in which experimental FT-STS measurements of the QPI are compared to theoretical QPI calculated within the free tight binding description given in Section 5.1: deviations from this effective model provide insight into the electronic correlations in the normal state. We show that the normal state of Sr_2RuO_4 is of interest in its own right, displaying significant interaction effects and a departure from the commonly-held picture of a the weakly-interacting ("good") Fermi liquid [20], which are readily observed in FT-STS measurements. A

detailed understanding of the normal state is essential in order to understand the SC state, particularly in light of the likelihood that the pairing mechanism is driven by interaction effects (specifically spin fluctuations), which persist in the normal state.

Having carefully considered the normal-state QPI, we turn to the SC state in Section 5.4. The SC-state QPI is calculated based on the theoretical models introduced in Section 5.1.2, comparing the results for both candidate SC OPs. We demonstrate that the QPI may be used to distinguish between the two proposed OPs, indirectly providing evidence of the SC pairing mechanism. Experimental efforts to measure the QPI in the SC state are ongoing: the results of Section 5.4 provide predictions for the QPI to be tested by experiment, with specific features indicative of each SC pairing scenario identified.

5.1 Strontium ruthenate electronic structure

In order to calculate the QPI for the normal and SC states of Sr_2RuO_4, a description of the electronic structure of the clean material (in the absence of impurities) in both phases is required. Strong electronic correlations, SOC and the multi-orbital nature of the problem present a significant challenge for ab-initio band structure calculations, as discussed in Section 2.3.3. In order to simulate the QPI, we therefore adopt an effective mean field, tight binding description of the electronic structure in the normal state, retaining the multi-orbital nature and SOC in a minimal model of the Ru t_{2g} orbitals. Reducing the orbital basis from the full atomistic basis of the unit cell to that of the relevant Ru t_{2g} orbitals lowers the complexity of the problem, integrating out unimportant orbital degrees of freedom (for example to bridging O $2p$ orbitals) and replacing these by tight binding hopping matrix elements on a square lattice of (three-orbital) Ru atom sites. This effective quasiparticle tight binding model is parametrized to fit the experimentally-observed electronic structure [218], as detailed in Section 5.1.1. The SC pairing is also treated at mean field level, employing an effective Bogoliubov-de Gennes description with an anisotropic SC gap function, candidates for which are given in Section 5.1.2.

5.1.1 Normal state

The commonly-held picture of the Sr_2RuO_4 normal state is that of a conventional Fermi liquid [20]. A minimal model for the relevant conduction electron bands, derived from the Ru t_{2g} orbitals, is given by an effective three-orbital tight binding model of

electrons hopping on a 2D square lattice. Following Ref. 174 and Refs. 37–41 therein:

$$\mathcal{H}_{\text{host}} = \sum_{s,\mathbf{k}} \psi_s^\dagger(\mathbf{k}) \mathbf{H}_s(\mathbf{k}) \psi_s(\mathbf{k}) \,, \tag{5.1}$$

where $\psi_s(\mathbf{k}) = \left(c_{a,s,\mathbf{k}},\, c_{b,s,\mathbf{k}},\, c_{c,-s,\mathbf{k}}\right)^T$, representing the $4d_{xz}$, $4d_{yz}$ with spin $+s$ and $4d_{xy}$ orbitals with spin $-s$ respectively with $s = +1(-1)$ for up(down) spins. The Hamiltonian kernel in this basis is given by

$$\mathbf{H}_s(\mathbf{k}) = \begin{pmatrix} \epsilon_a(\mathbf{k}) & g(\mathbf{k}) - \mathrm{i}\eta & \mathrm{i}\eta \\ g(\mathbf{k}) + \mathrm{i}\eta & \epsilon_b(\mathbf{k}) & -s\eta \\ -\mathrm{i}\eta & -s\eta & \epsilon_c(\mathbf{k}) \end{pmatrix} , \tag{5.2}$$

with

$$\epsilon_i(\mathbf{k}) = -2t_{i,x}\cos(\mathrm{a}_0 k_x) - 2t_{i,y}\cos(\mathrm{a}_0 k_y) - 4t_{i,xy}\cos(\mathrm{a}_0 k_x)\cos(\mathrm{a}_0 k_y) - \mu_i \,, \tag{5.3a}$$

and

$$g(\mathbf{k}) = -4t_{a,b}\sin(\mathrm{a}_0 k_x)\sin(\mathrm{a}_0 k_y) \,. \tag{5.3b}$$

The spin-orbit coupling (SOC) is controlled by the parameter η, and $g(\mathbf{k})$ represents the inter-orbital hopping between a and b ($4d_{xz}$ and $4d_{yz}$) orbitals. The parameters for this effective free model are chosen to reproduce the shape of the Fermi surfaces (FSs) and the ratio of effective masses for the resultant bands as obtained by experiment [174], such that $(t_{a,x} = t_{b,y},\, t_{a,y} = t_{b,x},\, t_{a,xy} = t_{b,xy},\, t_{c,x} = t_{c,y},\, t_{c,xy},\, t_{ab},\, \mu_a = \mu_b,\, \mu_c,\, \eta) = (1.0, 0.1, 0.0, 0.8, 0.3, 0.01, 1.0, 1.1, 0.1)t$. As noted in Ref. 174, both t_{ab} and η have the effect of producing repulsion between the bands, and as such there is some freedom in their choice. We adopt the value of t_{ab} used therein, which is smaller than calculations without SOC [153, 203], but in agreement with recent fits to ARPES data in which SOC is taken into account [197, 218].

Diagonalization yields three pairs of bands with pseudospin $\sigma = \pm 1$, labelled α, β and γ; the β and γ bands are particle-like in nature, while the α band is hole-like. Throughout we use roman letters to refer to orbital and spin space while greek letters refer to band and pseudospin. Figure 5.2 plots the FSs of these three bands across the first Brillouin zone (1BZ), which agree well with experimental results from ARPES and quantum oscillation studies [127, 126]. The orbital contributions to each band around the FS are depicted in Figure 5.2 via the hue of the plotted spectral

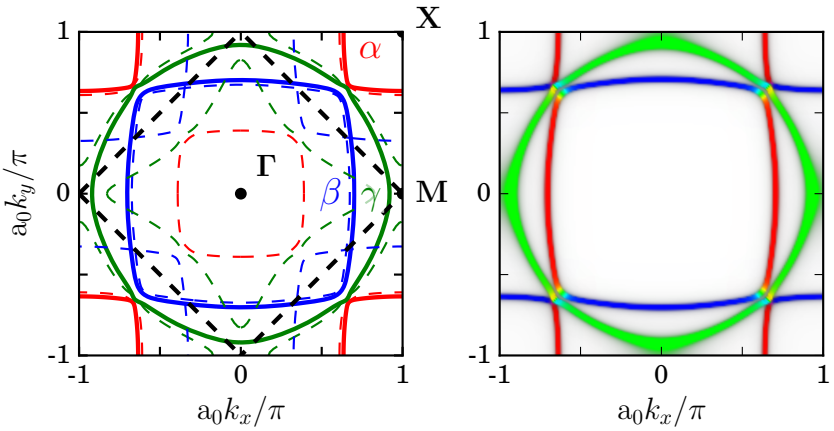

Fig. 5.2 *Left:* Fermi surfaces of the α, β and γ bands of Sr_2RuO_4 (denoted by red, blue and green respectively) across the 1BZ calculated within the three-orbital tight binding model described by Eqs. 5.1 and 5.2. Solid lines represent the bulk bands and 1BZ, while dashed lines represent the surface bands and the reduced 1BZ due to the $\sqrt{2} \times \sqrt{2}$ surface reconstruction, described in the text. *Right:* The spectral function, $-\operatorname{Tr}\operatorname{Im} G^0(\mathbf{k}, \omega + \mathrm{i}0^+)$, for the bulk bands, plotted across the 1BZ, showing the α, β and γ bands in terms of the relative contribution from the a, b and c orbitals (red, blue and green respectively).

function, $-\operatorname{Tr}\operatorname{Im} G^0(\mathbf{k}, \omega)$, with red, blue and green representing the a, b and c orbitals respectively. The α and β bands are seen to be largely derived from the a and b ($4d_{xz}$ and $4d_{yz}$, out-of-plane) orbitals, while the γ band is largely derived from the c ($4d_{xy}$, in-plane) orbital.

In addition to the bulk electronic structure described by Eqs. 5.1 and 5.2, Sr_2RuO_4 is known to undergo a reconstruction of the surface upon cleavage at low temperature [47, 196], resulting in a rotation in the RuO_6 octahedra of $\sim 6°$ and a doubling of the unit cell, as shown in Figure 5.1. This reconstruction results in a down-folding of the α, β and γ bands into the reduced surface Brillouin zone (SBZ), and an accompanying adjustment in the effective strength of electronic correlations and FS topology [196]. In terms of the tight binding model described by Eqs. 5.1 and 5.2, this reconstruction of the surface band FSs is well-described by a simple shift in the chemical potential of each orbital, $\mu_{a/b,\mathrm{surf}} = \mu_{a/b} - 25\mathrm{meV}$ and $\mu_{c,\mathrm{surf}} = \mu_c + 25\mathrm{meV}$, as depicted in Figure 5.2 (c.f. Figure 1 of Ref. 196, in which a detailed treatment of the surface reconstruction via DFT is carried out). The most significant effect of this reconstruction is a change in FS topology of the γ band, which becomes hole-like rather than electron-like (as it is in the bulk). The van Hove point in the γ band due to the critical point at $\mathbf{k}_\mathrm{X} = (\pi, 0)$ (at which $|\boldsymbol{\nabla}\epsilon_{\gamma,\mathbf{k}}| = 0$), which is above the Fermi level for the unreconstructed bulk

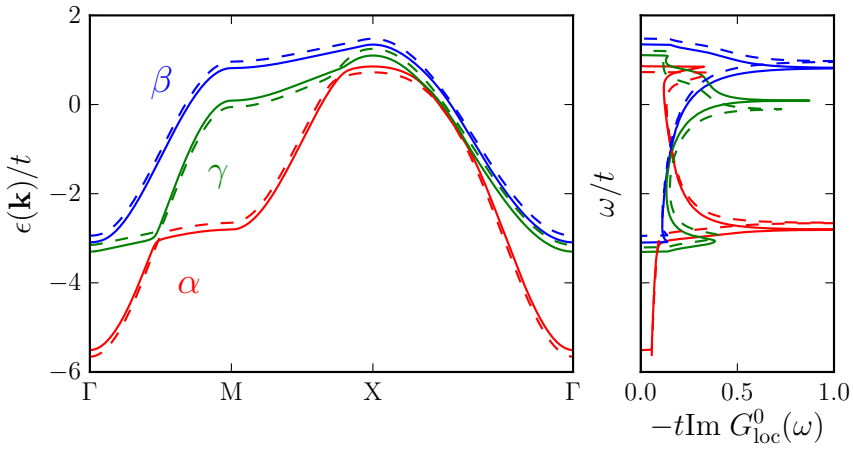

Fig. 5.3 *Left:* Dispersion of the α (red), β (blue) and γ (green) bulk and surface bands (solid and dashed lines respectively) along a cut between the high symmetry points of the 1BZ, $\Gamma \to \mathrm{M} \to \mathrm{X} \to \Gamma$. *Right:* Local density of states for each bulk and surface band.

band, is shifted to below the Fermi level for the surface band, as shown in Figure 5.3. By contrast, the α and β bands are more weakly affected.

The multi-orbital tight binding model presented in this section is used to calculate the normal-state QPI in Section 5.2. As already indicated, the conventional picture of the Sr_2RuO_4 normal state electronic structure is one of a *weakly*-correlated Fermi liquid [20], although recent ARPES measurements have called this into question [82, 85]. In Section 5.2 we present a comparison between the calculated QPI for the effective free-electron model discussed in this section and experimental FT-STS results presented in Ref. 206, clearly demonstrating significant correlation effects indicative of a more complicated, strongly-correlated state.

5.1.2 *p*-wave superconducting state

As introduced in the preamble to this chapter, Sr_2RuO_4 is primarily of interest due to the very unusual nature of the superconducting phase, found below $T_c \sim 1.5$K [127]. Experimental evidence strongly indicates a SC order parameter (OP) of *odd* parity (see Refs. 150, 127 and references therein), in contrast to the even-parity OPs due to both the conventional (*s*-wave) phonon-mediated pairing mechanism of BCS theory and the interaction-driven (*d*-wave) pairing mechanism of the cuprates. This implies the formation of spin-triplet ($S = 1$) Cooper pairs, also demonstrated in experiment [83, 95]: an electronic analogue to the spin-triplet *p*-wave state of paired neutral fermions in superfluid ^{3}He [17, 16]. The exact nature of the odd-parity SC state is still unclear,

but further experimental evidence of time-reversal symmetry breaking from muon spin-relaxation [125] and polar optical Kerr effect measurements [213] strongly suggest a chiral OP [127, 20, 203]. Such a chiral SC state is topologically non-trivial, with non-zero Chern number [175], and may support Majorana zero modes bound in vortices – which could be used for topological quantum information processing [149]. However, the chiral SC state is also expected to support edge currents, which have not been observed despite intense experimental scrutiny [75, 44]: this central contradiction in the phenomenology of the SC phase in Sr_2RuO_4 casts doubt on the chiral nature of the p-wave state, and thus its topological character [94].

One key difficulty in the theoretical understanding of the SC state lies in the subtle interplay of orbital and spin degrees of freedom in the presence of strong electron interactions, necessitating a full treatment of the multi-band system [203, 174]. Particular controversy revolves around the identity of the dominant SC instability, given the three bands arising due to the Ru t_{2g} orbitals. The prevailing assumption of the field has been that the 2D γ band, derived largely from the in-plane $4d_{xy}$ orbital is the active band due to the proximity to the van Hove singularity at +49meV, as supported by strong-coupling functional RG calculations [203]. In such case, the SC pairing is expected to be associated with FM spin fluctuations at small momenta, again due to the van Hove point in the γ band close to the Fermi level, which favours an FM state. However, recent specific heat and STS measurements [53] indicate a similar gap amplitude on all three bands, with a slightly larger gap on the quasi-1D α and β bands. This is in agreement with weak-coupling RG calculations [166, 174], in which the SC instability is comparable on all three bands. It is proposed that the pairing mechanism is driven by incommensurate spin fluctuations at higher momenta, due to nesting of the FSs in the quasi-1D α and β bands [194, 175]. These fluctuations have been found to be antiferromagnetic (AFM) in nature [181, 166].

An explicit theoretical treatment of interactions in the multi-band system, necessary in order to fully describe the SC phase on a microscopic level, is beyond the scope of this thesis. Instead, we treat the SC state via a mean-field description, extending the effective tight binding model of Section 5.1.1 via a static SC pairing term for each band, $\nu = \alpha, \beta, \gamma$,

$$\mathcal{H}_{\mathrm{SC},\nu}(\mathbf{k}) = -\sum_{\sigma,\sigma'} \left[\mathbf{\Delta}_\nu(\mathbf{k})\right]_{\sigma,\sigma'} c^\dagger_{\nu,\sigma} c^\dagger_{\nu,\sigma'} + \left[\mathbf{\Delta}_\nu(\mathbf{k})\right]^*_{\sigma,\sigma'} c_{\nu,\sigma} c_{\nu,\sigma'} \,, \tag{5.4}$$

where the nature of the SC pairing is informed by both theoretical and experimental findings [174, 175, 53, 127]. The anisotropic SC gap function is chosen to have p-wave

symmetry, $\boldsymbol{\Delta}_\nu(-\mathbf{k}) = -\boldsymbol{\Delta}^\nu_{\sigma,\sigma'}(-\mathbf{k})$, in keeping with experimental findings. The full (mean-field) Bogoliubov-de Gennes Hamiltonian may thus be written in Nambu spinor notation as

$$\mathcal{H}_{\text{host,SC}} = \sum_{\mathbf{k}} \Psi^\dagger(\mathbf{k}) \mathbf{H}_{\text{BdG}}(\mathbf{k}) \Psi(\mathbf{k}) \,, \tag{5.5}$$

where

$$\mathbf{H}_{\text{BdG}}(\mathbf{k}) = \begin{pmatrix} \mathbf{H}_{+1}(\mathbf{k}) \oplus \mathbf{H}_{-1}(\mathbf{k}) & -\boldsymbol{\Delta}(\mathbf{k}) \\ -\boldsymbol{\Delta}(\mathbf{k})^* & -\mathbf{H}_{+1}(\mathbf{k}) \oplus \mathbf{H}_{-1}(\mathbf{k}) \end{pmatrix} \tag{5.6}$$

and $\Psi^\dagger(\mathbf{k}) = \big(\psi^\dagger_{+1}(\mathbf{k}),\, \psi^\dagger_{-1}(\mathbf{k}),\, \psi_{+1}(\mathbf{k}),\, \psi_{-1}(\mathbf{k})\big)$.

The spin components of the gap function may be elegantly represented in terms of a complex *vector* OP, $\mathbf{d}_\nu(\mathbf{k}) = (d_{\nu,x}(\mathbf{k}),\, d_{\nu,y}(\mathbf{k}),\, d_{\nu,z}(\mathbf{k}))$, such that $\boldsymbol{\Delta}_\nu(\mathbf{k}) = \mathrm{i}(\mathbf{d}_\nu(\mathbf{k}) \cdot \boldsymbol{\sigma})\sigma_2$ (with $\boldsymbol{\sigma} = (\sigma_1, \sigma_2, \sigma_3)$ the Pauli vector):

$$\boldsymbol{\Delta}_\nu(\mathbf{k}) = \begin{pmatrix} \Delta^\nu_{\uparrow,\uparrow}(\mathbf{k}) & \Delta^\nu_{\uparrow,\downarrow}(\mathbf{k}) \\ \Delta^\nu_{\downarrow,\uparrow}(\mathbf{k}) & \Delta^\nu_{\downarrow,\downarrow}(\mathbf{k}) \end{pmatrix} = \begin{pmatrix} -d_{\nu,x}(\mathbf{k}) + \mathrm{i}d_{\nu,y}(\mathbf{k}) & d_{\nu,z}(\mathbf{k}) \\ d_{\nu,z}(\mathbf{k}) & d_{\nu,x}(\mathbf{k}) + \mathrm{i}d_{\nu,y}(\mathbf{k}) \end{pmatrix} . \tag{5.7}$$

The d vector notation conveniently describes the symmetry of the triplet SC state, the spin and orbital angular momentum of Cooper pairs and the $\mathbf{k}$-space structure of the SC gap in a compact way, as well as having a direct physical interpretation (see Ref. 127 for more details). In this formalism, a singlet SC is represented by $\Delta_{\uparrow,\uparrow} = -\Delta_{\downarrow,\downarrow} = \Delta_s$, or equivalently $d_x = -\Delta_s$. The chiral OP for the triplet SC state of Sr_2RuO_4 is given generally by

$$\mathbf{d}_\nu = \Delta_{\nu,0}(p_x \pm \mathrm{i}p_y)\hat{z} \,, \tag{5.8}$$

where $p_{x(y)}$ represents any function with the same symmetry properties as $\sin(\mathrm{a}_0 k_{x(y)})$ under the operations of the Ru local point group. This chiral p-wave SC state is analogous to the superfluid state of the A-phase of ^{3}He. An alternative helical spin-triplet OP, $\mathbf{d}_\nu = \Delta_{\nu,0}(p_x\hat{x} \pm p_y\hat{y})$, analogous to the B-phase of ^{3}He has also been proposed in order to explain the absence of edge currents [174], but does not break time-reversal symmetry and thus is not considered here.

Numerous attempts have been made to resolve the apparent lack of observed appreciable edge currents with the evidence of time-reversal symmetry breaking indicative of a chiral state [26, 113, 173]. Strong-coupling RG calculations predict a dominant SC gap on the 2D γ band driven by FM spin fluctuations, while the α and β bands

are merely spectators, potentially with sub-dominant SC gaps induced via SOC. This gives rise to the simplest possible "naive" form for the chiral OP, corresponding to nearest-neighbour SC pairing,

$$d^0_{\nu,z}(\mathbf{k}) = \Delta_{\nu,0}\Big(\sin\left(\mathrm{a}_0 k_x\right) + \mathrm{i}\sin\left(\mathrm{a}_0 k_y\right) \Big)\,, \tag{5.9}$$

such that $\Delta_{\gamma,0} \gg \Delta_{\alpha/\beta,0}$. By contrast, weak-coupling RG calculations have indicated a SC pairing mechanism driven by AFM spin fluctuations in the quasi-1D α and β bands caused by FS nesting, giving rise to similar gap sizes on all three bands and SC pairing over a longer range. It was recently argued in Ref. 175, that the absence of edge currents may be reconciled with a chiral OP for a state with a large topological invariant (Chern number), in agreement with RG calculations taking into account both multi-band and SOC effects [174, 175]. A microscopically-plausible ansatz for the SC gap in orbital space ($n \in \{a, b, c\}$, corresponding to the $4d_{xz}, 4d_{yz}$ and $4d_{xy}$ orbitals respectively) was proposed which shows good agreement with the numerical RG result [175],

$$\Delta_{n,\mathrm{RG}}(\mathbf{k}) = \sum_{i=1,2,3} \Delta^x_{n,i} g_i(k_x, k_y) + \mathrm{i}\Delta^y_{n,i} g_i(k_y, k_x)\,, \tag{5.10}$$

with $g_1(k_x, k_y) = \sin(k_x)$, $g_2(k_x, k_y) = \sin(k_x)\cos(k_y)$ and $g_3(k_x, k_y) = \sin(3k_x)$, for $(\Delta^x_{a,1} = \Delta^y_{b,1}, \Delta^x_{a,2} = \Delta^y_{b,2}, \Delta^x_{a,3} = \Delta^y_{b,3}) = (0, 0.2, 1)\Delta$, $\Delta^y_{a,i} = \Delta^x_{b,i} = 0\ \forall\ i$ and $(\Delta^x_{c,1} = \Delta^y_{c,1}, \Delta^x_{c,2} = \Delta^y_{c,2}, \Delta^x_{c,3} = \Delta^y_{c,3}) = (0.18, 0.15, -0.3)\Delta_{\mathrm{RG}}$ where Δ_{RG} sets the SC gap scale in absolute terms. The OP in band space is obtained by applying the transformation that diagonalizes the normal state Hamiltonian in spin/orbital space defined in Eqs. 5.1 and 5.2.

Figure 5.4 depicts the variation of magnitude and phase of the chiral OPs $d^0_z(\mathbf{k})$ and $d^{\mathrm{Fit}}_z(\mathbf{k})$ around the FS for each of the three bands calculated via Eqs. 5.9 and 5.10. While both OPs are valid on symmetry grounds, they display dramatically different physical properties; indeed they represent topologically distinct states, as codified by their respective total Chern number, C, given by the sum of the Chern numbers of the individual bands at the Fermi level C_ν. The Chern number is given by the winding of the phase of $d_{\nu,z}$ around the FS, equivalent to the skyrmion number of the BdG Hamiltonian [201]

$$C_\nu = \frac{1}{4\pi}\int_{\mathrm{FS}} d\mathbf{k}\hat{H}_\nu \cdot \left(\partial_{k_x}\hat{H}_\nu \times \partial_{k_y}\hat{H}_\nu\right)\,, \tag{5.11}$$

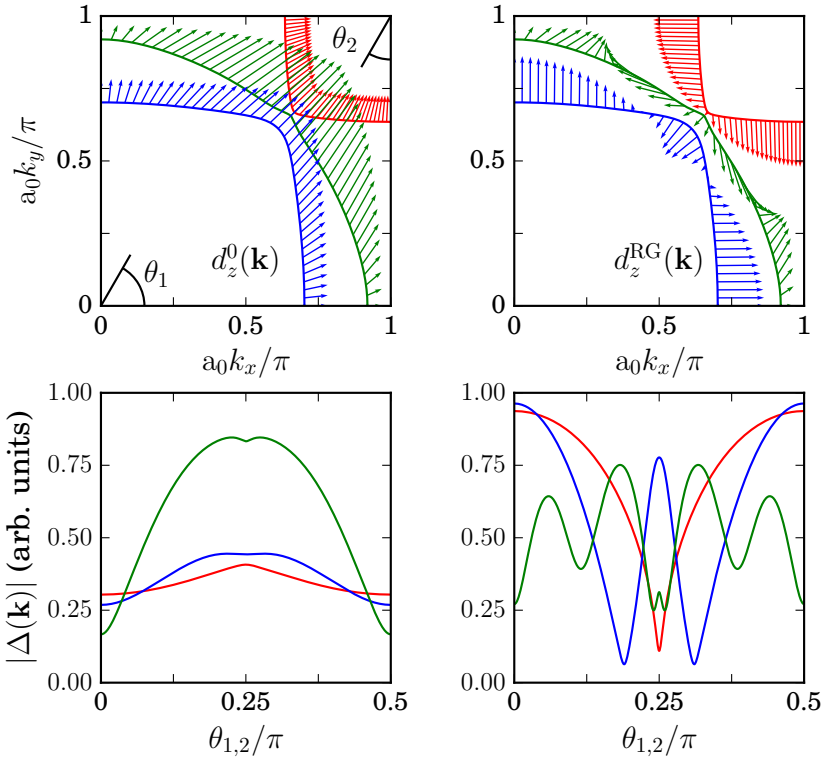

Fig. 5.4 *Upper panels:* Variation of two possible chiral p-wave SC OPs d_z^0 and d_z^{RG}, described by Eqs. 5.9 and 5.10, around the Fermi surface for Sr_2RuO_4. The x and y components of the arrows give the real and imaginary parts of $d_{\nu,z}$ respectively. *Lower panels:* Corresponding variation in the magnitude of the SC gap $|\Delta_\nu(\mathbf{k})| = \sqrt{\mathbf{d}_\nu(\mathbf{k}) \cdot \mathbf{d}_\nu(\mathbf{k})}$ around the FS for each possible chiral OP. The ratio of SC gap magnitudes $\Delta_{\nu,0}$ for the $\nu = \alpha, \beta$ and γ bands is chosen as $1:1:2$ for the simpler chiral OP, d_z^0, reflecting the expectation of dominant SC pairing in the γ band, while the relative gap magnitudes for d_z^{RG} are fit to numerical results from the RG calculations of Ref. 174.

where $\vec{H}_\nu = (\mathrm{Re}\ d_{\nu,z}(\mathbf{k}), -\mathrm{Im}\ d_{\nu,z}(\mathbf{k}), \epsilon_\nu(\mathbf{k}))$ and $\hat{H} = \vec{H}/|\vec{H}|$. Inspecting d_z^0 in Figure 5.4 it is clear that the phase of $d_{\nu,z}^0$ winds once around the FS for all three bands. The winding is anticlockwise for the particle-like β and γ bands, so that $C_{\beta,\gamma} = +1$, and clockwise for the hole-like α band, giving $C_\alpha = -1$; the total Chern number is therefore $C = +1$. The winding of d_z^{Fit} is significantly more complicated: the particle-like β and γ bands exhibit Chern numbers of $C_{\beta,\gamma} = -3$, giving a total Chern number of -7. While it has been shown that edge currents are inevitable in systems with $|C| = 1$, they vanish in systems with higher Chern number $|C| > 1$ (see Ref. 175 and references therein), perhaps reconciling the absence of edge currents with the chiral state suggested by broken time-reversal symmetry.

Direct measurement of the Chern number is not possible; it has also not been possible to measure the phase of the SC OP, although a method for direct determination of the SC gap sign structure via FT-STS has recently been proposed for pnictide SCs [77]. However, in Sr_2RuO_4 the unusual winding of the phase of d_z around the FS is accompanied by significant modulations in the magnitude of the proposed SC gap function, as seen clearly in Figure 5.4. The simple chiral OP d_z^0 results in a dominant SC gap on the γ band with deep minima along the $\Gamma \to \mathrm{M}$ ($(0,0) \to (0, \pi/\mathrm{a}_0)$ direction, with flatter SC gap functions of smaller magnitude on α and β. By contrast, the RG-fit chiral OP d_z^{RG} displays gaps of similar magnitudes on all three bands, with a deep minima in $|\Delta_\alpha^{\mathrm{RG}}|$ along $\Gamma \to \mathrm{X}$ ($(0,0) \to (\pi/\mathrm{a}_0, \pi/\mathrm{a}_0)$), and in $|\Delta_\beta^{\mathrm{RG}}|$ either side of the $\Gamma \to \mathrm{X}$ line, while the $|\Delta_\gamma^{\mathrm{RG}}|$ has a highly oscillatory structure with shallow minima along $\Gamma \to \mathrm{M}$, $\Gamma \to \mathrm{X}$ and between these directions (at $\theta_1 \simeq \pi/4$). These features, while not causally linked to the winding of the phase around the FS, are strongly suggestive of this state of higher Chern number. Due to the relatively small absolute magnitude of the SC gap in Sr_2RuO_4, resulting in a low critical temperature of $T_c \sim 1.5$K, the accurate measurement of such features requires sub-meV energetic resolution and high resolution in momentum space. This is beyond the reach of ARPES, but may be feasibly achieved via FT-STS measurements, which offer the ability to directly probe the anisotropy of Bogoliubov quasiparticles in momentum space, and thus the SC gap structure, as we discuss in Section 5.4.

While the primary interest in Sr_2RuO_4 lies in the unusual SC state at low temperature, an understanding of the normal state is vital to understand the SC state. Moreover, spin fluctuations due to the aforementioned proximity of both AFM (in the pseudo-1D $4d_{xz}$ and $4d_{yz}$ orbitals) and FM (in the 2D $4d_{xy}$ orbital) spin-density-wave-ordered states to the ground state, which are believed to be involved in the SC pairing mechanism, are also observed in the normal state. Consideration of the

QPI (and FT-STS) in the normal state is therefore a necessary prelude to further (direct) investigations of the SC state, as well as providing insights into the underlying correlation effects in Sr_2RuO_4 and thus, indirectly, the SC mechanism. We now turn to the QPI for the normal state, and the comparison with experimental FT-STS results.

5.2 Normal state QPI

As discussed earlier in this chapter, detailed calculations of the QPI are required in order to correctly interpret experimental FT-STS measurements, particularly in a complex multi-band system such as Sr_2RuO_4. A number of relevant complicating effects must be considered, going beyond the simplest idealized calculation, in order to accurately reproduce experimental features such as the strength and type of scattering, and the detailed physical and electronic structure of the host material surface in real space.

In Chapters 2 and 3, the QPI was defined directly in terms of the modulations in the LDOS of the host material. However, FT-STS experiments in fact measure the conductance between STM tip and host material, which is closely related to the LDOS [192, 52]. The multi-orbital electronic structure of Sr_2RuO_4 requires a more careful consideration of the relationship between the measured conductance and the LDOS. The spatial anisotropy of the Ru $4d$ t_{2g} orbitals results in different degrees of overlap with STM tip orbitals, and thus affects the tunnelling current and conductance. In order to accurately account for these effects, we calculate the QPI as the power spectrum of the spatial interference pattern of the conductance, g_c, measured via STM, $P(\mathbf{q},\omega) = |g_c(\mathbf{q},\omega)|^2$. We calculate the interference of scattered conduction electron states, treating the scattering in terms of the full t-matrix within the three-orbital model described by Eqs. 5.1 and 5.2,

$$\Delta\rho_i(\mathbf{q},\omega) = -\pi^{-1}\mathrm{Im}\sum_{s,\mathbf{k}}\left[\mathbf{G}^0_s(\mathbf{k},\omega)\mathbf{T}(\mathbf{k},\mathbf{k}+\mathbf{q})\mathbf{G}^0_s(\mathbf{k}+\mathbf{q},\omega)\right]_{ii}, \tag{5.12}$$

where $\mathbf{G}^0_s(\mathbf{k},\omega) = \left((\omega+\mathrm{i}0^+)\mathbf{I} - \mathbf{H}_s(\mathbf{k})\right)^{-1}$ the unperturbed (retarded) Green function matrix in orbital/spin space (and $\mathbf{H}_s(\mathbf{k})$ defined by Eq. 5.2). For the normal state of Sr_2RuO_4, we calculate the QPI over the 1BZ on a 2048×2048 grid in $\mathbf{k}$-space (a spacing of $a_0(\delta k)/\pi \lesssim 10^{-3}$), employing a broadening parameter, $\delta = 5$meV, such that $\omega + \mathrm{i}0^+ \to \omega + \mathrm{i}\delta$. The conductance is then given by tracing over the contribution from

each orbital,

$$g_c(\mathbf{q},\omega) = g_c^0(\mathbf{q},\omega) + \sum_{i=a,b,c} C_i \Delta\rho_i(\mathbf{q},\omega)\,, \tag{5.13}$$

where the orbital-dependent coefficient C_i reflects the magnitude of the tunnelling matrix element between the tip and orbital i, controlled by the spatial anisotropy of the $4d$ t_{2g} orbitals. Experimental evidence suggests that cleavage of the bulk crystal results in a surface SrO layer [158, 47], as depicted in Figure 5.1, so that there is an oxygen atom lying above each outermost Ru atom. The p-orbitals of this apical oxygen are of the correct symmetry to facilitate tunnelling overlap between the $4d_{xz}/4d_{yz}$ out-of-plane orbitals and the tip, but not between the $4d_{xy}$ in-plane orbital and the tip, and thus $C_a = C_b \gg C_c$. Here we take $C_a = C_b = 1$ and $C_c = 0$, as is common [53]; this results in the effective spectral density visible via STS plotted in the upper left panel of Figure 5.5, where the hue represents the orbital contribution at a given momentum from the a and b orbitals (red and blue respectively).

We assume scattering due to a local perturbation in the potential of a single site in the lattice, i.e. a single potential scattering impurity; multiple independent, local scattering centres give rise to trivial, moiré-type interference patterns in the QPI [138, 34], as detailed in Section 4.4, but no qualitative effect on the observed QPI. This results in a t-matrix that is momentum-independent and diagonal in orbital space; in the first instance, we further simplify the problem, considering the case of a scalar impurity, corresponding to the weak-scattering (Born) limit potential scatterer.

Figure 5.5 compares the QPI measured via FT-STS (upper right) with that calculated via Eqs. 5.12 and 5.13 (lower right, calculated for a single scalar impurity, diagonal in orbital space) at the Fermi level ($\omega = 0$meV), plotted as $|g_{c,\text{expt.}}(\mathbf{q},\omega)|$ and $|\Delta g_c(\mathbf{q},\omega)|$ respectively. The out-of-plane spectral density (upper left panel) also depicts characteristic "nested" scattering vectors at which divergent (high intensity) features in the QPI are expected, following the arguments presented in Chapter 2 (specifically Section 2.3.1). Scattering between sections of the same hue (which denotes the orbital composition of states at a given momentum) dominates the theoretical QPI, in broad agreement with experiment. This is a result of the structure of the t-matrix, which is chosen to be diagonal in orbital space. These characteristic high-intensity features, marked by the purple, green and grey vectors in the experimental and theoretical QPI in Figure 5.5, are due to scattering between specific pairs of points on one (intra-band scattering) or two (inter-band scattering) CECs at which the group

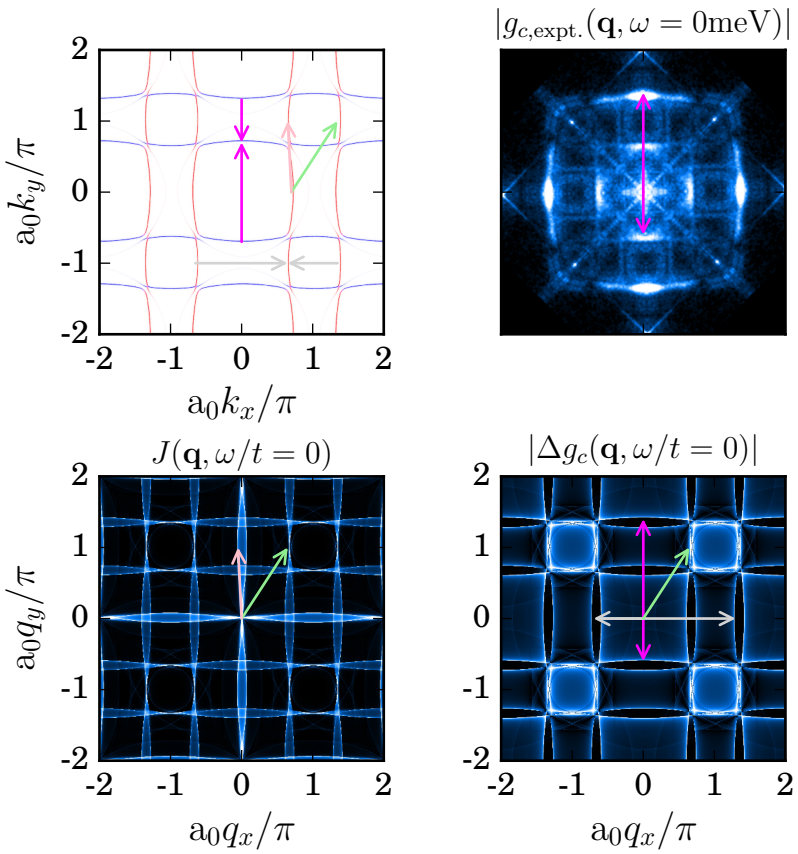

Fig. 5.5 Comparison of predicted dominant scattering vectors on the orbitally-resolved spectral density Im $G(\mathbf{k},\omega+\mathrm{i}0^+)$ (upper left panel; red (blue) corresponds to the $4d_{xz}$ ($4d_{yz}$) orbital), theoretical JDOS and QPI (lower panels) with the experimental FT-STS measured at the Fermi level (upper right panel).

velocities are antiparallel, and between which there is a non-zero scattering t-matrix element (see Section 2.3.1 for detailed explanation).

The experimental QPI is dominated by intra-band scattering on the β band, indicated by purple arrows in Figure 5.5. Inter-band scattering between α and β (inter-band but *intra-orbital*), as indicated by green arrows, is much weaker than predicted by the theoretical calculation. Intra-band scattering on the α band, denoted by the grey arrows in Figure 5.5, is almost absent in the experimental QPI, despite being of comparable strength to the β band contribution in theoretical calculation. This is puzzling at first sight, as the α and β bands are both largely derived from the a and b orbitals; we provide two possible explanations for this discrepancy in Section 5.2.1 and 5.2.2. The presence in the experimental QPI of additional, weak features centred around $a_0\mathbf{q} = (\pi, \pi)$, which appear to be replicas of the dominant (intra-β-band scattering) features denoted by the purple arrows, is addressed in Section 5.2.3.

The lower left panel of Figure 5.5 plots the JDOS $J(\mathbf{q}, \omega)$, calculated within the multi-band formalism detailed in Section 2.3 and taking into account the orbital texture via Eq. 2.35b, provided for comparison to the theoretical and experimental QPI. The discrepancy between the JDOS and the QPI in the multi-orbital case of Sr_2RuO_4 is substantial. The most striking difference is the presence in the JDOS of strong features along $q_x = 0$ and $q_y = 0$, which result from inter-band scattering processes between α and β, exemplified by the pink arrows in Figure 5.5. Such scattering vectors are expected to produce a strong QPI response within the simplistic picture of the "JDOS interpretation" (isotropic scattering between points on the CEC), as discussed in Section 2.2. However, due to the hole-like (particle-like) nature of the α (β) band such vectors connect points on the CEC for which the group velocities are parallel (rather than antiparallel, as is the case for the purple, grey and green vectors). In Section 2.2, it was demonstrated that such scattering vectors do not result in divergent features in the QPI.

5.2.1 Effect of scattering strength on QPI

In order to account for the discrepancy between the strength of signals in the QPI due to intra-band scattering on the α and β bands, we first consider the effect of changing the strength of the potential scattering in the theoretical calculation. Experimental bulk thermodynamic measurements for Ti-doped Sr_2RuO_4 [99] suggest that in-plane substitutional impurities act as strong potential scatterers. We therefore adopt the full

	$T_{aa}(\omega=0)$		$T_{bb}(\omega=0)$		$T_{cc}(\omega=0)$	
v_0/t	$\text{abs}(T)/t$	$\arg(T/v_0)/\frac{\pi}{2}$	$\text{abs}(T)/t$	$\arg(T/v_0)/\frac{\pi}{2}$	$\text{abs}(T)/t$	$\arg(T/v_0)/\frac{\pi}{2}$
-3.0	1.457	+0.612	1.593	+0.934	1.303	+0.748
-1.5	1.107	+0.420	1.335	+0.621	1.086	+0.518
-0.1	0.099	+0.035	0.102	+0.035	0.100	+0.038
+0.1	0.100	−0.038	0.971	−0.039	0.095	−0.044
+1.5	1.232	−0.437	0.985	−0.317	1.158	−0.415
+3.0	1.555	−0.682	1.280	−0.457	1.488	−0.632

Table 5.1 Variation with potential scattering strength v_0 in the magnitude $\text{abs}(T)$ and phase $\arg(T)$ of intra-orbital scattering matrix elements $T_{aa}(\omega=0)$, $T_{bb}(\omega=0)$ and $T_{cc}(\omega=0)$ at the Fermi level due to a single potential scatterer. NB. the phase is defined relative to that of v_0, such that the absolute phase for $v_0<0$ is given by $\pi+\arg(T/v_0)$.

expression for the (momentum-independent) t-matrix,

$$\begin{aligned}\mathbf{T}(\omega) =&\mathbf{V}\left(1+\sum_{\mathbf{k}}\mathbf{G}^0(\mathbf{k},\omega)\mathbf{V}\Big(1+\sum_{\mathbf{k}'}\mathbf{G}^0(\mathbf{k}',\omega)\mathbf{V}\,(1+\dots)\Big)\right)\\ =&\mathbf{V}(\mathbf{I}-\mathbf{G}^0_{\text{loc}}(\omega)\mathbf{V})^{-1}\,,\end{aligned}\tag{5.14}$$

where $\mathbf{G}^0_{\text{loc}}(\omega)=N_{\mathbf{k}}^{-1}\sum_{\mathbf{k}}\mathbf{G}^0(\mathbf{k},\omega)$ is the local Green function matrix in real space, and $\mathbf{V}=v_0\mathbf{I}$ the local scattering potential. Eq. 5.14 represents the exact t-matrix for arbitrary potential scattering strength (controlled by v_0); the Born series expansion is re-summed to infinite order, giving rise generically to a *dynamic* t-matrix, which reduces to $\mathbf{T}\sim\mathbf{V}$ in the weak-scattering (Born) limit, $v_0\ll t$.

Varying the strength of the local potential scatterer in Eq. 5.14 gives rise to orbital-dependent phase shifts and magnitudes in the elements of the scattering t-matrix. The dominant scattering matrix elements are found to be intra-orbital; Table 5.1 presents the magnitude and phase of the intra-orbital scattering matrix elements $T_{aa}(\omega)$, $T_{bb}(\omega)$ and $T_{cc}(\omega)$ for the $4d_{xz}$, $4d_{yz}$ and $4d_{xy}$ orbitals (respectively) for scattering potentials ranging from $v_0=-3t$ to $+3t$. While LDOS modulations in the $4d_{xy}$ orbital are not visible in the QPI due to the poor tunnelling between this orbital and the STM tip, intra-c-orbital scattering still contributes to the QPI as the orbitals are coupled via SOC. However, dominant contributions to the QPI are expected to result from intra-orbital scattering on the a and b orbitals, represented in the first two columns of Table 5.1. For small v_0 the Born limit holds, so that $T_{nn}(\omega)\ v_0$ is real and static. However, larger

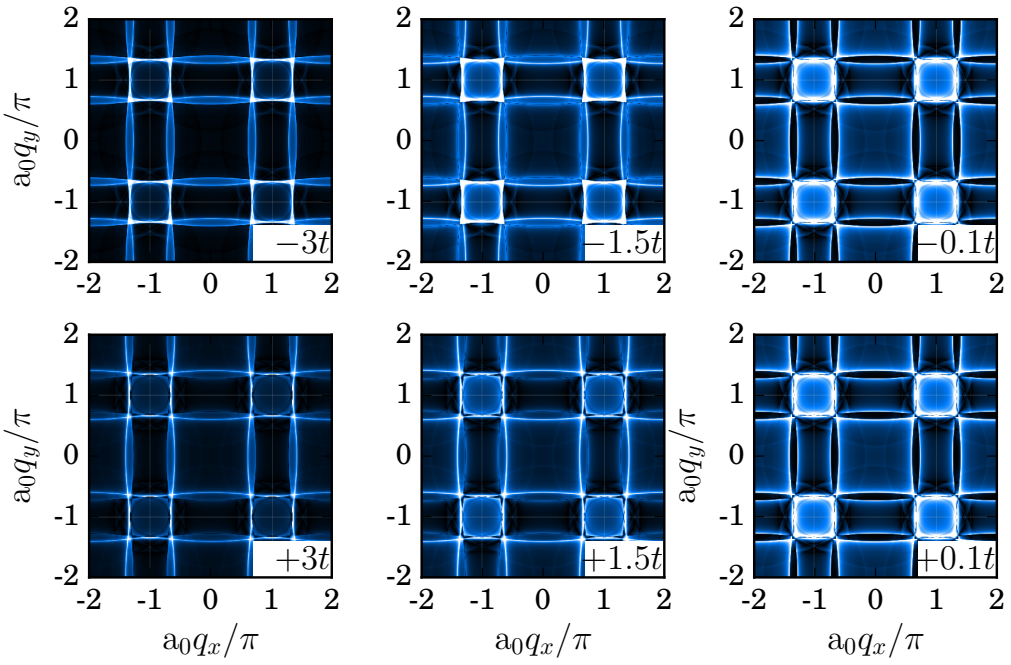

Fig. 5.6 Sr_2RuO_4 QPI calculated using the full t-matrix (Eq. 5.14) for a range of local scattering potential strengths, with v_0, noted in the inset of each figure, ranging from $-3t$ to $+3t$.

scattering potentials generate a significant scattering phase shift, which tends towards $\pi/2$ (the unitary limit of resonant bound-state scattering) as the magnitude of v_0 increases. The strong potential scattering suggested by experimental studies of in-plane substitutional impurities [99] therefore gives rise to a significant phase shift.

Moreover, the magnitude and sign of the phase shift (and indeed the magnitude of the scattering matrix element) is clearly dependent on the orbital for stronger scattering. As a result both the magnitudes of different contributions to the QPI and their relative phases depend on the strength of scattering, which can lead to changes in the relative intensity of features in total QPI. Figure 5.6 plots the QPI calculated for the range of local scattering potentials using in Table 5.1, from $v_0 = -3t$ to $+3t$. While varying the scattering strength does not change the topology of the important (divergent) **q**-space features in the QPI, it changes the detailed behaviour of the QPI around these divergent lines and thus has a qualitative effect on the observed QPI signal. Not only do the relative intensities of different regions of the QPI maps vary, but the strength of the divergent features is affected by the magnitude and sign of v_0.

This is most clearly demonstrated in the comparison of the QPI for potential scattering strengths of $v_0 = -1.5t$ and $+1.5t$, the upper and lower middle panels

respectively of Figure 5.6. For $v_0 = -1.5t$ the divergent features associated with intra-α-band scattering, which form a convex square centred at the origin and extending from $\sim -0.7\mathrm{a}_0/\pi \rightarrow +0.7\mathrm{a}_0/\pi$ in q_x and q_y, are dominant, while the concave square feature associated with intra-β-band scattering is suppressed. By contrast the QPI for $v_0 = +1.5t$ displays the reverse: the intra-β-band scattering is dominant, while the intra-α-band scattering is strongly suppressed. The link between the magnitude and phase of the scattering matrix element between orbitals and the interpretation in terms of scattering between states of the electron bands derived from these orbitals is non-trivial, and the phase of the scattering matrix elements in band space is highly complex due to the momentum-dependence of the t-matrix in band space (as discussed earlier in the section and in Section 2.3). However, the effect on the QPI resulting from intermediate or strong potential scattering, as displayed in Figure 5.6, is significant, and must be considered when seeking to understand experimental FT-STS measurements, as we turn to in Section 5.3. The suppression of features arising from intra-α-band scattering in the QPI, seen in the experimentally measured QPI in Figure 5.5, may be a result of intermediate or strong potential scattering, as demonstrated in Figure 5.6.

5.2.2 Wannier-basis QPI

In Section 3.5.3 we considered the effect of introducing a simple atomic-orbital-like Wannier basis to account for the spatial extension of the surface density of states beyond a simple lattice description. It was shown that a simple momentum-space cutoff results in the case of an isotropic (s-wave) Wannier basis. This can substantially change the detailed structure of the QPI calculated in this Wannier basis, but leaves the qualitative features of the QPI at low momenta (for example within the first Brillouin zone) unchanged in comparison with the "true" lattice QPI. However, many strongly correlated electronic materials consist of conduction bands derived from anisotropic atomic orbitals, in particular the d orbitals in transition metal oxides such as the cuprates and pnictides, and Sr_2RuO_4 investigated here. In these materials, the radial extension *and* angular form of the Wannier basis for the orbital or orbitals contributing to the LDOS at the surface must be considered. This is particularly challenging in the case of (binary) transition metal oxides such as Sr_2RuO_4, because the lattice models employed theoretically to understand their electronic structure are typically effective tight binding models for the transition metal atoms only, with the electronic degrees of freedom of other atoms in the lattice integrated out. Simple, heuristic forms for these Wannier orbitals can be estimated by an appropriate basis of atomic-like orbitals on each lattice site; however, for an accurate representation of the relevant Wannier

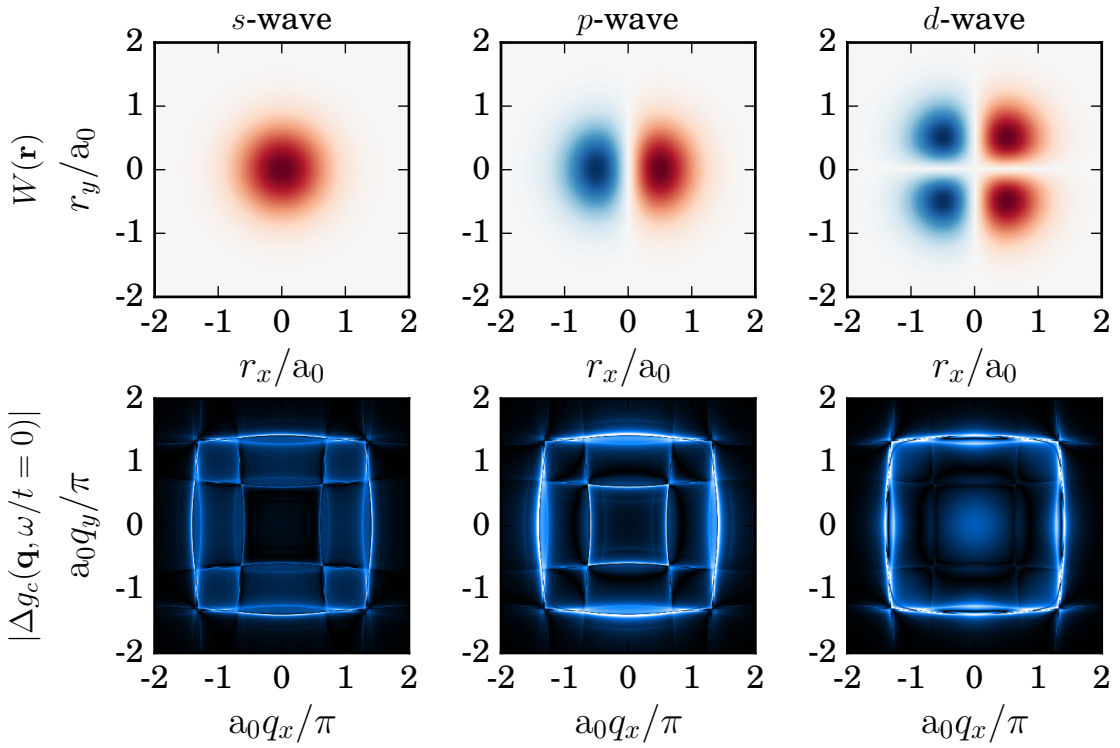

Fig. 5.7 QPI for Sr_2RuO_4 calculated at the Fermi level in the Wannier basis for three potential symmetries (s-wave, p-wave and d-wave). *Upper:* Illustrative Wannier functions $W(\mathbf{r})$ for the $4d_{xz}$ orbital in each of the three candidate bases of s-, p- and d-wave symmetry. The $4d_{yz}$ orbital Wannier function is given by a rotation of $\pi/2$, while the $4d_{xy}$ Wannier function is set to zero everywhere in keeping with the absence of tunnelling between the tip and the (in-plane) $4d_{xy}$ orbital. *Lower:* The QPI, plotted as the Fourier-transformed conductance, $|g_c(\mathbf{q}, \omega/t = 0)|$, for each candidate Wannier basis.

orbitals, more involved electronic structure methods considering the full-atom basis of the lattice unit cell, such as density functional theory, are required [106].

In Figure 5.7 we plot three possible Wannier bases for the $4d_{xz}$ orbitals of Sr_2RuO_4, and the resultant Wannier-basis QPI in each case. Representative atomic-orbital-like Wannier functions of s-wave, p-wave and d-wave symmetries are considered: the isotropic, s-wave basis is provided for reference, demonstrating the momentum-space cutoff effect, while the p- and d-wave bases are expected to be more appropriate for the $4d$ orbitals of Sr_2RuO_4, as we now explain.

Considering the shape of the $4d$ t_{2g} atomic orbitals in the (001) plane, the $4d_{xz}$ and $4d_{yz}$ orbitals are expected to be of p-wave symmetry, while the $4d_{xy}$ orbital is of d-wave symmetry in the (001) plane. However, as argued earlier in Section 5.2

the coupling between STM tip and the Ru $4d_{xz/yz}$ orbitals is facilitated by the apical oxygen atom $p_{x/y}$-orbitals, while there is no orbital of appropriate symmetry to facilitate coupling to the $4d_{xy}$ orbital, which is thus not seen in the surface LDOS and QPI (for example in Figure 5.5). We therefore set the Wannier function for the $4d_{xy}$ orbital to zero in each case. The Wannier functions for the $4d_{xz}$ orbital in the s-, p- and d-wave cases are given by $W_s(\mathbf{r}) = N_{s\mathbf{r}}\mathrm{e}^{-|\mathbf{r}|^2/2a^2}$, $W_p(\mathbf{r}) = N_{p,\mathbf{r}}r_x\mathrm{e}^{-|\mathbf{r}|^2/2a^2}$ and $W_d(\mathbf{r}) = N_{d,\mathbf{r}}\mathrm{sgn}(r_x)|r_xr_y|\mathrm{e}^{-|\mathbf{r}|^2/2a^2}$, with $a/\mathrm{a}_0 = 0.5$, 0.6 and 0.8 respectively (chosen to reproduce the momentum-space cutoff in the QPI as seen in experiment, as in Figure 5.5). The Wannier functions for the 4_{yz} orbitals are given by interchanging $r_x \leftrightarrow r_y$. The p-wave basis, depicted in Figure 5.7, is expected in the case that the coupling between STM tip and Ru orbitals is facilitated by the apical oxygen p orbitals, while the d-wave basis is appropriate if the coupling is facilitated by the (s-like) orbitals of the Sr surface atoms, situated at $\mathbf{r}/\mathrm{a}_0 = (0.5, 0.5)$.

The Wannier-basis QPI calculated for each symmetry, displayed in the lower panels of Figure 5.7, differ notably from the lattice QPI plotted in Figure 5.5. In all three cases the finite spatial extent of $W(\mathbf{r})$ results in a momentum-space cutoff in the QPI, as observed in Section 3.5.3, in good agreement with the experimental QPI measurement depicted in Figure 5.5, with the dominant feature in the QPI due to the intra-β-band scattering. Most notably, the momentum-space cutoff is seen to suppress the QPI signal due to intra-α-band scattering, which occurs between states at higher momenta, as well as the signal due to inter-band α-β scattering around $\mathrm{a}_0\mathbf{q} = (\pi, \pi)$. The angular form of the Wannier functions also has a significant impact on the appearance of the (Umklapp) QPI features due to intra-β-band scattering within the first Brillouin zone. Such Umklapp processes have the same intensity in the lattice QPI calculated in Figures 5.5 and 5.6, which is periodic over the first Brillouin zone, but have different intensities in the Wannier-basis QPI, which extends over a range twice that of the first Brillouin zone. Intra-β-band features inside the first Brillouin zone are suppressed for QPI calculations in the s-wave and d-wave Wannier bases, while these features are present in the p-wave basis result, albeit significantly weakened compared to the corresponding intra-β-band feature outside the first Brillouin zone.

The p-wave case most closely resembles the experimental result, and thus we adopt this Wannier basis when comparing calculations with experimental work in Section 5.3. In order to accurately match experimental calculations, an in-depth consideration of the Wannier basis is needed, necessitating a detailed calculation of the electronic structure in the full-atom basis of the Sr_2RuO_4 (001) surface, similar to that carried out for a cuprate superconductor in Ref. 106. The phenomenological Wannier basis suggested

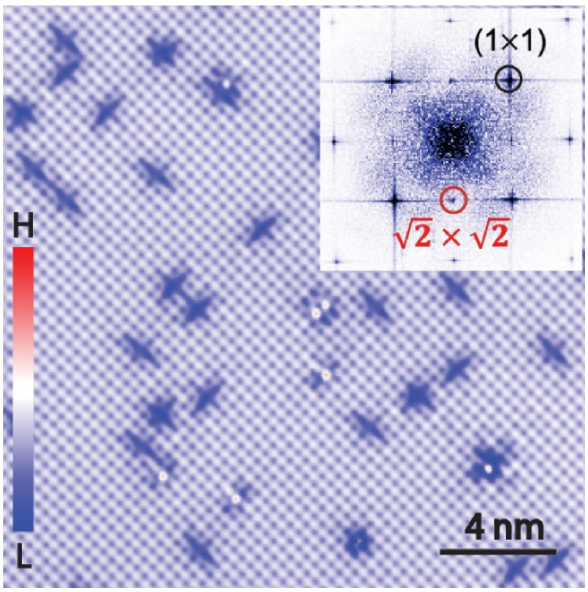

Fig. 5.8 Typical topographic image of Sr_2RuO_4 reproduced from Ref. 206 showing a uniform square lattice. *Inset:* Fourier transform of the topographic image, showing the Bragg peak (black circle) and the $\sqrt{2} \times \sqrt{2}$ reconstruction peak (red circle).

in this section illustrates the effect on the QPI, and gives reasonable agreement with experimental results; a more involved treatment is not attempted here.

5.2.3 Surface reconstruction & Brillouin zone folding

Cleaving the bulk Sr_2RuO_4 crystal to expose the (001) surface for study via STM results in a surface reconstruction in which the RuO_6 octahedra of the surface layer rotate by $\sim 6°$ in a checkerboard pattern, depicted in Figure 5.1, corresponding to the freezing out of a soft phonon mode of the bulk crystal. This reconstruction is reflected in the topographic map of the surface measured by STM, depicted in Figure 5.8 (reproduced from Ref. 206) which clearly shows the square lattice of the clean host with randomly distributed point-like defects. While the doubling of the unit cell is not clear to the naked eye, the Fourier transform of the topographic map demonstrates the presence of reconstruction in the form of additional Bragg peaks, as noted in Figure 5.8.

The surface reconstruction results in small changes in the topology of the FS in the conduction bands, as discussed in Section 5.1.1, accompanied by the doubling of the unit cell seen in Figure 5.8. The first Brillouin zone is therefore down-folded as depicted in Figure 5.2. Based on simple qualitative arguments the rotation of surface octahedra is expected to result in a weak hopping term between the two (inequivalent) sites of the doubled unit cell, which is staggered in real space, in similar fashion to the bilayer

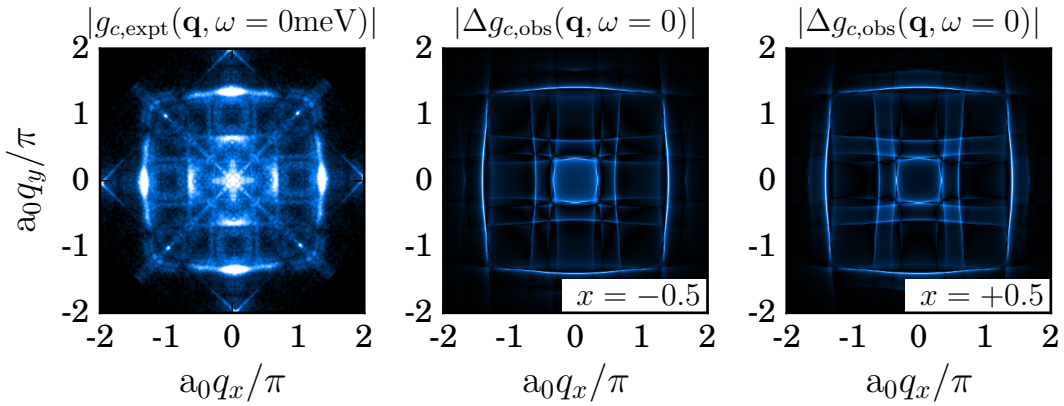

Fig. 5.9 Comparison of experimentally measured QPI with calculated QPI at the Fermi level, including the effects of surface reconstruction. *Left:* QPI measured experimentally via FT-STS,reproduced from Ref. 206. *Centre, Right:* Calculated Wannier-basis QPI (calculated as detailed in Section 5.2.2) for intermediate potential scattering strength (Section 5.2.1). The effects of surface reconstruction are included via the phenomenological approach of Eq. 5.16, with the mixing parameter $x = -0.5$ and $+0.5$ or the centre and right panels respectively. The choice of $x = -0.5$ gives the best agreement with experimental measurement.

$Sr_3Ru_2O_7$, which undergoes an equivalent static distortion in the bulk [116]. This perturbation weakly couples conduction band states at $\mathbf{k}$ and $\mathbf{k}+\mathbf{Q}$ for $\mathrm{a}_0\mathbf{Q} = (\pi,\pi)$ (where a_0 is the lattice constant of the undistorted crystal): as a result, shifted replicas of the un-reconstructed α, β and γ bands are expected at $\mathbf{k}+\mathbf{Q}$ where $\mathrm{a}_0\mathbf{Q} = (\pi,\pi)$, as observed in ARPES measurements [47, 196].

In order to see similar folded features in the QPI, however, the un-reconstructed and replica bands must be coupled by an appreciable scattering matrix element. A full and detailed consideration of the effect of surface reconstruction on the electronic structure is necessary to derive microscopically the scattering matrix element between un-reconstructed and replica bands. However, such a treatment is not possible within the effective tight binding description of the lattice, as relevant spatial structure and electronic degrees of freedom have already been integrated out. Instead of a complete treatment in the full atom basis the effects of surface reconstruction on the QPI are included on a phenomenological basis and by comparison with experimental results as depicted in Figure 5.5 and in more detail in Section 5.3.

Considering in the first case the lattice QPI (given by the Fourier transform of modulations in the lattice LDOS, periodic across the first Brillouin zone), the QPI contributions due to the scattering between un-reconstructed and replica bands is

simply the un-reconstructed QPI shifted by $\mathbf{Q}$. The total QPI response in the presence of the surface reconstruction is therefore approximated as

$$\Delta\rho_{i,\text{fold}}(\mathbf{q},\omega) = \Delta\rho_i(\mathbf{q},\omega) + x\Delta\rho_i(\mathbf{q}+\mathbf{Q},\omega)\,, \tag{5.15}$$

for $i = a, b, c$ orbitals, where $\Delta\rho(\mathbf{q},\omega)$ is the unfolded QPI response calculated via Eq. 5.12 and x is a mixing parameter dependent on the (relative) strength of the scattering between the un-reconstructed and replica bands. However, in order to consider the more realistic Wannier-basis QPI in the presence of the surface reconstruction a more involved calculation is required, such that

$$\Delta\rho_{i,\text{fold}}(\mathbf{q},\omega) = \Delta\rho_i(\mathbf{q},\omega) + x\Delta\rho'_{i,\mathbf{Q}}(\mathbf{q},\omega)\,, \tag{5.16}$$

where again $\Delta\rho_i(\mathbf{q},\omega)$ is the unfolded QPI response for orbital i, calculated this time in the Wannier basis as described in Sections 5.2.2 and 3.5.3, while the folded QPI response is given by

$$\Delta\rho'_{i,\mathbf{Q}}(\mathbf{q},\omega) = -\pi^{-1}\text{Im}\sum_{s,\mathbf{k}}\left[\mathbf{G}^0_s(\mathbf{k},\omega)\mathbf{T}(\mathbf{k},\mathbf{k}+\mathbf{q})\mathbf{G}^0_s(\mathbf{k}+\mathbf{Q}+\mathbf{q},\omega)\right]_{ii}\,. \tag{5.17}$$

In this phenomenological treatment, the mixing parameter x is chosen to match the folded features observed in experimental measurements. We note that not only the magnitude but also the sign of x is important, as this is in effect the interference of two different QPI signals, i.e. $|\Delta\rho_{i,\text{fold}}(\mathbf{q},\omega)| \neq |\Delta\rho_i(\mathbf{q},\omega)| + |x||\Delta\rho'_{i,\mathbf{Q}}(\mathbf{q},\omega)|$. Figure 5.9 displays the experimentally-measured QPI at the Fermi level, which clearly displays weaker, shifted replicas (centred around $\mathrm{a}_0\mathbf{q} = (\pi,\pi)$) of the dominant features centred around $\mathrm{a}_0\mathbf{q} = (0,0)$. The QPI calculated via Eq. 5.16 in the p-wave Wannier basis described in Section 5.2.2 for $x = -0.5$ and $+0.5$ are also plotted, demonstrating the same folded features with reasonable agreement. By setting $x = -0.5$ we see reasonable agreement with the experimentally-observed folded features. This value of x is adopted to match these folded features when comparing to experimental QPI measurements, as detailed in Section 5.3.

5.3 Normal state FT-STS: experimental measurements & theory

While the FS topology of Sr_2RuO_4 is well-known (from extensive experimental measurements, for example via ARPES [47, 20]), as well as the orbital character of the three Ru $4d$ t_{2g} derived conduction bands, a detailed and fulsome understanding of the normal state is still lacking. This is due to the multi-orbital structure with both 2D (γ band, largely derived from the $4d_{xy}$ orbital close to the Fermi level) and pseudo-1D electronic states (α and β bands, with predominantly $4d_{xz}$ and $4d_{yz}$ orbital character close the Fermi level), and the influence of substantial SOC effects [197] and electron-electron and electron-boson interactions [82, 85, 100]. The mixing of these degrees of freedom gives rise to the highly non-trivial triplet-SC state discussed in Section 5.1.2, believed to be driven by electron-electron interactions also responsible for significant spin fluctuations in the normal state. However, this mixing also makes disentangling the interaction effects on the three bands very challenging, and, as a result, uncertainty persists about the detailed SC pairing mechanism [152, 203, 166, 174], as detailed in Section 5.1.2.

The formidable complexity of the problem makes definitive, ab-initio theoretical progress all but impossible; experimental evidence is required in order to understand the balance of different possible effects and inform theoretical models. Detailed ARPES studies have revealed interaction effects in the 2D γ band [6, 82, 85, 100], but little detailed information about interactions in the pseudo-1D bands [84]. FT-STS has previously been used in the study of cuprate and pnictide SCs [78, 79, 55, 214] and heavy fermion compounds [193, 217, 9, 221], including recent work to probe electron-boson coupling in iron-based SCs [10]. Moreover, the very high energy resolution possible via FT-STS makes it an ideal technique to directly study the momentum-dependent SC OP $\Delta(\mathbf{k})$ with magnitude smaller than 1meV as is the case in Sr_2RuO_4, and similarly in heavy fermion SC systems [9, 221].

In Ref. 206 FT-STS was applied to Sr_2RuO_4 for the first time, in combination with momentum-resolved electron energy loss spectroscopy (M-EELS) – a powerful technique for measuring the energy and dispersion of collective excitations that couple strongly to electrons [103]. These measurements provide insight into the strength of correlations in the pseudo-1D β band, and thus potentially on the SC pairing mechanism (indirectly) via the interactions that may enhance or even facilitate pairing, as well as providing a basis for further, direct study of the SC state. From a theoretical perspective, their value is twofold. Firstly, such measurements provide the opportunity to benchmark and fit theoretical models for the electronic structure, and inform the

modelling of quasiparticle scattering processes in the material. Secondly, by comparison of experimental data to theoretical predictions for a free, non-interacting host material, deviations resulting from interaction effects may be identified and characterized. This gives insight and informs the development of theoretical (minimal) models in order to account for the most relevant interaction effects.

Figure 5.10 depicts high-resolution FT-STS measurements for a range of scanning energies around the Fermi level. Figure 5.10*a–c* show representative $dI/dV(\mathbf{r},\omega)$ maps on Sr_2RuO_4 at several different scanning energies, demonstrating the (approximately) point-like nature of the scattering centres giving rise to the LDOS modulations measured by FT-STS (and thus the QPI). The Fourier transforms of dI/dV maps, shown in Figure 5.10*d–l*, demonstrate a rich array of features and a strong energetic and momentum dependence. The lattice vector in reciprocal space is indicated by dashed white arrow, and a sequence of inequivalent $\mathbf{q}$-vectors corresponding to intense features in the QPI are labelled as $\mathbf{q}_i$, with $i = 0, 1, 2, 3, 4$. The (white) vector $\mathbf{q}_0$, found to be essentially non-dispersive over the energy range of interest, is potentially attributable to electronic states derived from "spectator" orbitals of the full material [206], which are neglected in the electronic structure deriving from the effective three-orbital considered in this chapter (see Section 5.1.1). As was the case for similar vectors identified in Figure 5.5, we assign the (dispersing) vectors $\mathbf{q}_1$-$\mathbf{q}_4$, which mark high-intensity features in the QPI to scattering between specific points on the CEC (or CECs) of the host conduction bands. Interpretation of QPI features in this way allows the detailed band dispersion to be mapped with very high energetic resolution via FT-STS.

By way of comparison with the experimental FT-STS measurements of Figure 5.10, Figure 5.11 provides the predicted QPI calculated (via Eq. 3.77) in the p-wave Wannier basis as detailed in Section 5.2.2, for a moderate-to-strong scattering potential as discussed in Section 5.2.1. At positive frequencies, folded features are observed in the experimental QPI in Figure 5.10, which we account for using the phenomenological method described in Section 5.2.3. The comparison of theoretical and experimental QPI maps shows reasonable qualitative agreement in the dominant features; however, the detailed dynamic structure of the experimental QPI in particular is not reproduced by the simplistic theoretical calculations. This may be the result of the basic treatment of the Wannier basis and folding effects in the QPI calculations, but may also point to more complex scattering processes. The richer structure of the experimental QPI may be a signature of correlation effects in the normal state, for example the presence of significant spin fluctuations, both FM and AFM (as discussed in Section 5.1).

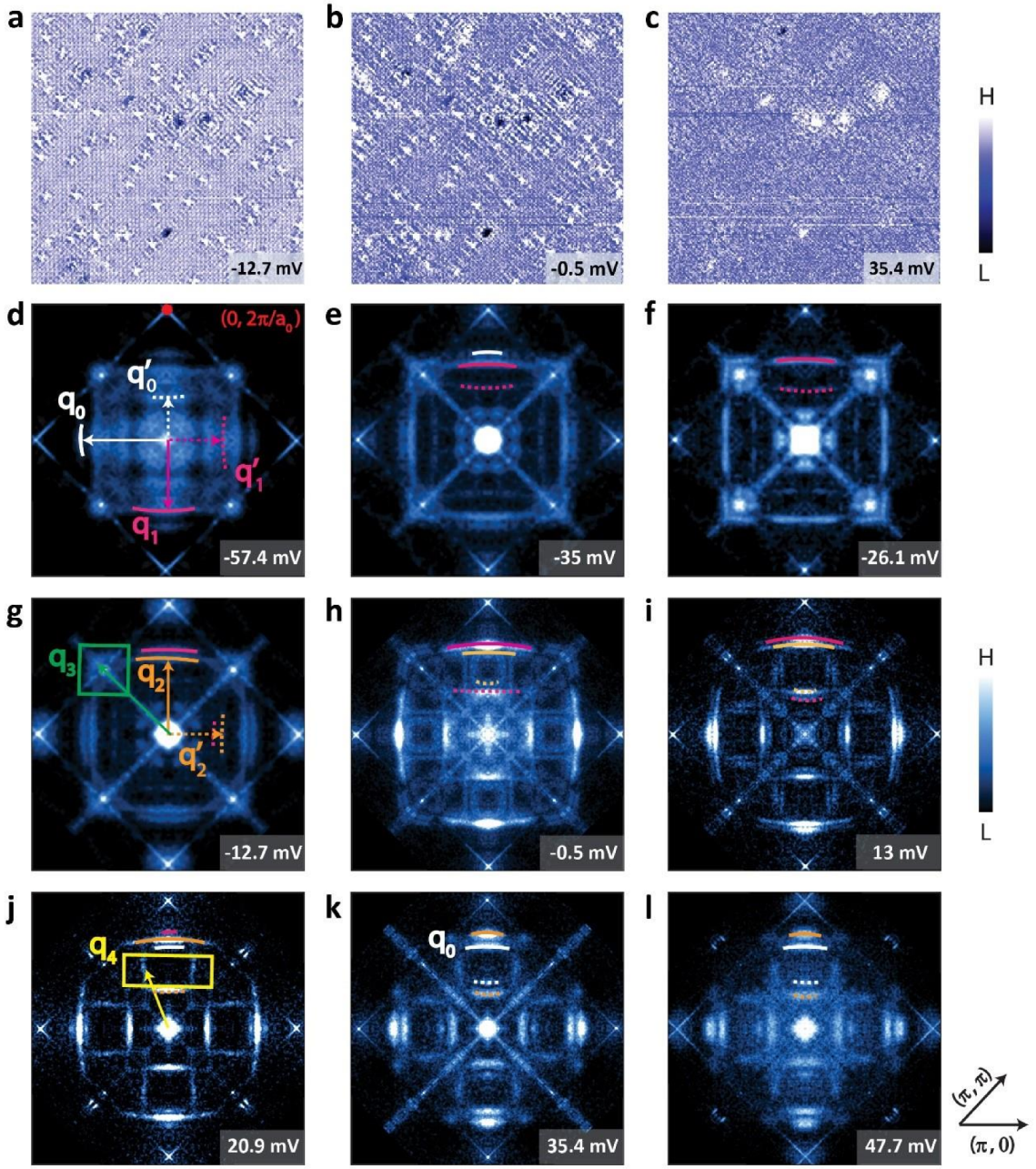

Fig. 5.10 Reproduced from Ref. 206. ***a*–*c*** Spatially resolved dI/dV conductance maps at -12.7meV, -0.5meV and $+35.4$meV. For clarity, a 34nm-square field of view (FOV) is cropped from a larger 78nm × 78nm FOV used to obtain the Fourier transform images. ***d*–*l*** Drift-corrected and symmetrized Fourier transforms of dI/dV conductance maps at a range of scanning energies above and below the Fermi level. The $(0, 2\pi/\mathrm{a}_0)$ Bragg peak is indicated by the red dot in ***d***. Dominant scattering vectors are indicated by q_i $(i = 0, 1, 2, 3, 4)$.

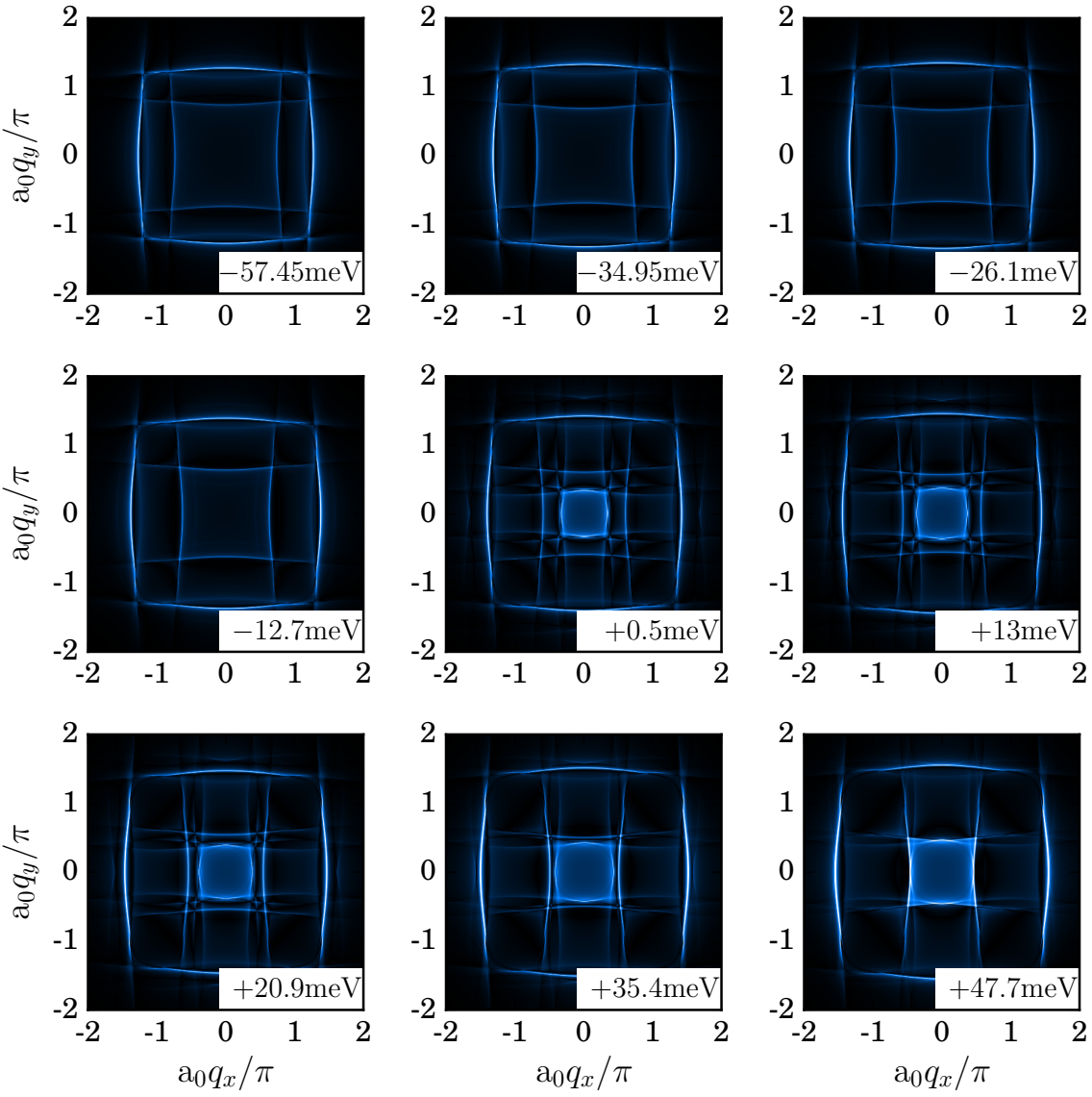

Fig. 5.11 QPI calculated in the p-wave Wannier basis (detailed in Section 5.2.2) for intermediate potential scattering strength (Section 5.2.1) at scanning energies matching the experimental measurements in Figure 5.10. For positive scanning energies, the folded features observed in the experimental QPI are replicated in the calculations using the phenomenological method described in Section 5.2.3.

In studies of the cuprates [200, 13], the proximity of a charge-ordering instability to the ground state has been argued to result in structured impurities in real space. Local potential scatterers may pin small charge-ordered patches, giving rise to extended impurities which may have complicated momentum and energy dependence. The existence of such extended impurities in Sr_2RuO_4 is plausible given the complicated nature of the correlated ground state in this case; moreover, the impurities imaged via STM, clearly seen in the topographical map in Figure 5.8, show some extended structure. Further theoretical and experimental investigations are needed to explore this possibility.

In comparison with the band structure depicted in Figure 5.2, it is immediately clear that the γ band is largely absent from the experimental QPI, in accordance with the planar nature of the d_{xy} orbital and resultant lack of overlap with the STM tip wavefunction as discussed in Section 5.2. The vectors $\mathbf{q}_1$ and $\mathbf{q}_1'$ (purple arrows) along the $(\pi, 0)$ direction are found to result from intra-β-band scattering (also depicted by purple arrows in Figure 5.5). A second, similar feature denoted by $\mathbf{q}_2$ (orange arrows) is found to have identical curvature to $\mathbf{q}_1$, in contrast to the convex curvature of the QPI feature resulting from intra-α-band scattering (depicted by the grey vectors in Figure 5.5), and $\mathbf{q}_2$ is therefore most likely *also* due to the β band. A secondary β band was also observed in ARPES measurements [196, 121], attributed to the surface band arising from the rotation of the RuO_6 octahedra in the surface layer (see Figure 5.1), as discussed in Section 5.1.1, the modified band structure for which is depicted in Figure 5.2. The feature around $a_0\mathbf{q}_X = (\pi, \pi)$ denoted by vector $\mathbf{q}_3$ (green arrow) has contributions from α-β inter-band scattering (green arrow in Figure 5.5), and intra-γ-band scattering, as the γ band acquires some $4d_{xz/yz}$ character around the $\Gamma \rightarrow X$ vector, and thus is "visible" to STS measurement, as seen in the upper left panel of Figure 5.5. Finally, the features highlighted the yellow box in Figure 5.10, and denoted by vector $\mathbf{q}_4$, are assigned as weak replicas of the intra-β-band scattering features denoted by $\mathbf{q}_1$(and $\mathbf{q}_2$), centred at $\mathbf{q}_X$. As discussed above in Section 5.2.3, such features are thought to arise from the folding of the Brillouin zone due to surface reconstruction although the exact mechanism of this QPI folding is unclear. The most compelling evidence for this assignment is from the dispersion of the $\mathbf{q}_4$ features, which is equivalent to the corresponding $\mathbf{q}_2$ feature, indicating that $\mathbf{q}_1$ is the bulk and $\mathbf{q}_2$ the surface band. Moreover, the folded $\mathbf{q}_4$ features are only observed close to and above the Fermi level, where the $\mathbf{q}_2$ features are also seen. This further validates the assignment of $\mathbf{q}_1(\mathbf{q}_2)$ as bulk (surface) bands respectively. Owing to the surface-sensitive nature of FT-STS, the question naturally arises as to how bulk bands may be observed at the

surface; one possible explanation is that the features arising from the "bulk" band are in fact due to areas of the surface for which the rotational reconstruction (known to be an energetically weak effect) is negligible [206].

To quantify the dispersion of the QPI features, line cuts are taken of the Fourier transforms in the two high symmetry directions, $\Gamma \rightarrow$ M and $\Gamma \rightarrow$ K, and the positions of the peaks corresponding to $\mathbf{q}_n$ found. The peak positions representing the energy and momentum resolved $\mathbf{q}$-vectors are plotted in Figure 5.12a, excluding $\mathbf{q}_4$ since it represents the folded $\mathbf{q}_1/\mathbf{q}_2$ band and is not an independent $\mathbf{q}$-vector – we emphasize the very fine energetic resolution of the FT-STS measurement that is apparent. The divergence in the QPI from theoretical prediction for the bulk (solid blue line) and surface (dashed blue line) is overlaid on the dispersion of experimentally recorded peak positions, showing good general agreement away from the Fermi level.

The most striking feature of the dispersion is the dramatic change in slope near the Fermi level along the $\Gamma \rightarrow$ M cut, revealed by the high energetic resolution of the FT-STS measurement. This indicates a strong mass renormalization resulting in much smaller values of the Fermi velocity at this point on the Fermi surface for the β band than obtained from de Haas-van Alphen oscillations [20] and from ARPES measurements [196]. Quantum oscillation measurements, while very precise, give an average value around the Fermi surface and thus the discrepancy with the value measured by FT-STS along the $\Gamma \rightarrow$ M cut is indicative of a momentum-dependent mass renormalization effect. Moreover, the corresponding mass renormalization appears weaker in the $\Gamma \rightarrow$ X cut, further supporting this possibility. It is clear that FT-STS measurements of the β band in Figure 5.12 reveal that the correlation effects on the β band are quite significant, and in fact much larger than previously thought [20]. The quasi-1D nature of the β band, clear from the shape of the FS in Figure 5.2, is expected to enhance the effect of correlations, in analogy to true 1D systems, although features are rounded by an eventual crossover to 2D Fermi liquid behaviour on a sufficiently low energy scale [36, 21]. Characteristic behaviours of 1D systems are observed via STM, including a zero-bias anomaly in the tunnelling DOS at an energy scale of about 10meV [206] and the previously discussed downward renormalization of the Fermi velocity over the same energy scale. These observations taken together support the scenario of enhanced correlation effects on the β band bolstered by its quasi-1D nature, and also suggest that this system may be close to a charge and/or spin density wave instability, as indicated by earlier neutron scattering data [181].

Comparison of the experimentally measured dispersion in Figure 5.12a with the free-electron theoretical calculation (overlaid) also reveals kinks at multiple energy

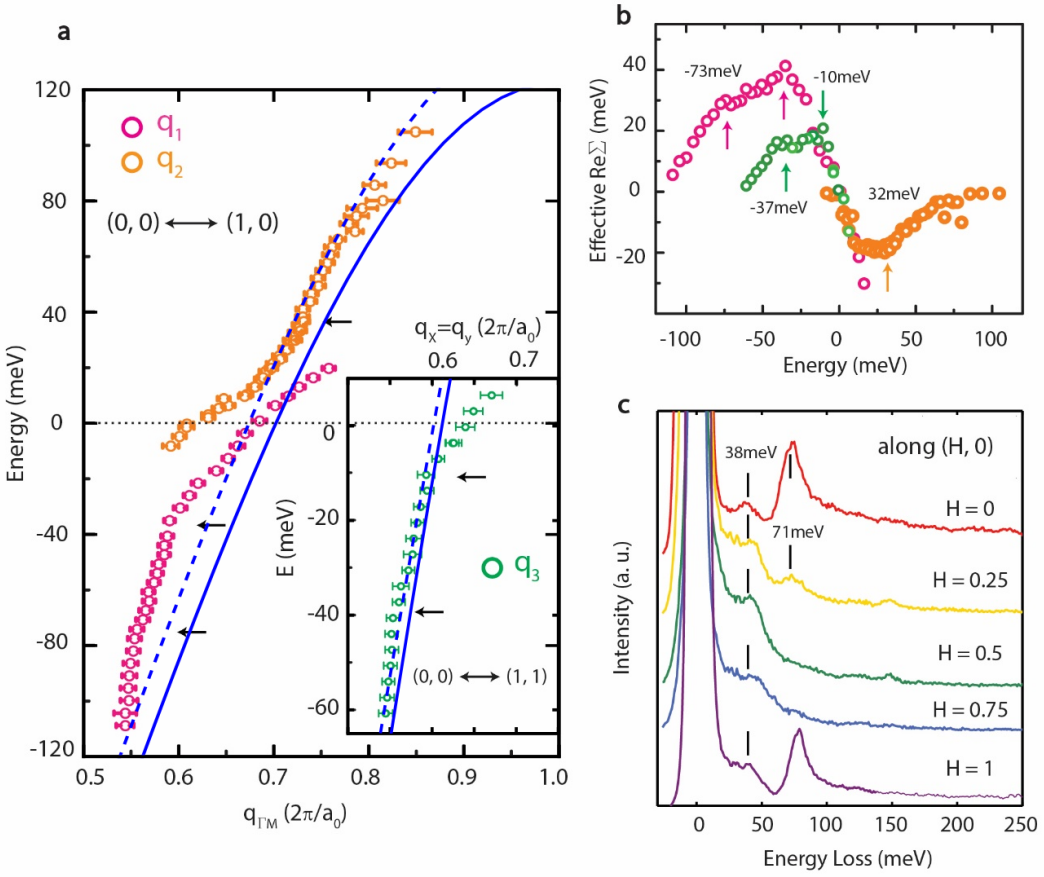

Fig. 5.12 ***a.*** Dispersions of β band $\mathbf{q}_1$ and secondary β band $\mathbf{q}_2$ extracted by fitting peaks in line-cut along $\Gamma \rightarrow$ M direction. These peaks reflect the dynamic nesting processes involving band structures as well as the quasiparticle self-energy. Kink features are seen at energies of about -35meV and -70meV for $\mathbf{q}_1$, and $+32$meV for $\mathbf{q}_2$, as shown by arrows. *Inset:* Dispersion of $\mathbf{q}_3$ along $\Gamma \rightarrow$ M direction. An additional kink at -10meV is found, which may be potentially related to coupling to a spin excitation. ***b.*** Corresponding effective real-part of quasiparticle self-energy (Re $\Sigma(\mathbf{k} = \mathbf{q}/2, \omega)$ given by $\Delta E = E_{\text{obs}} - E_{\text{bare}}$) for the measured dispersion. A straight line connecting two points at the Fermi level E_{F} and ± 110meV in the dispersion is used as the "bare" band for each $\mathbf{q}$ dispersion. Peaks at multiple energy scales are marked with arrows: -37meV and -73meV for β band, $+32$meV for secondary (surface) β band and -11meV and -37meV for $\mathbf{q}_3$. ***c.*** Momentum-resolved electron energy loss spectra taken along the $(2\pi/a_0, 0)$ direction. Two peaks at 38meV and 71meV are clearly revealed, which match the energy scales of kinks seen in QPI.

scales. Kinks are ubiquitous in many correlated electron systems and reflect (dynamic and momentum-dependent) contributions to the electronic self-energy, and contain important information about the effects of interactions. Among high-T_c superconductors for example, kinks in the dispersion and have been observed in cuprates [111, 35] and Fe-based superconductors [10, 205, 114]. In order to characterize the interactions giving rise to each kink in the self-energy, momentum-resolved electron energy loss spectroscopy (M-EELS) is employed to investigate specifically the effective electron-boson interactions (i.e. the effect of electron-phonon coupling). Kinks observed in FT-STS at energies of $\omega_1 \sim 35$meV and $\omega_2 \sim 70$meV in the dispersion of $\mathbf{q}_1$, and one at about ~ 32meV above Fermi level for $\mathbf{q}_2$, are clearly visible in the extracted self-energy Re $\Sigma(\mathbf{k}, \omega)$ shown in Figure 5.12b. The effective self energy Re $\Sigma(\mathbf{k}, \omega)$ was obtained by subtracting a "bare band" background from the observed dispersion in order to show the peak positions. The peak energies of ω_1 and ω_2 in extracted Re $\Sigma(\mathbf{k}, \omega)$ are ~ 37meV and ~ 73meV, while results of the M-EELS measurement along the $\Gamma \rightarrow$ M direction are shown in Figure 5.12c. Two dominant peaks are seen at ~ 38meV and 71meV, corresponding to ω_1 and ω_2 respectively. ω_1 disperses with momentum in a manner consistent with an optical phonon, while ω_2 shows anomalous momentum dependence, disappearing abruptly as we move away from the high symmetry point, suggestive of a surface phonon merging with a bulk band. The comparison of FT-STS with M-EELS provides clear evidence that ω_1 and ω_2 arise from collective bosonic modes that strongly couple with the pseudo-1D β band in Sr_2RuO_4. Moreover, similar modes were observed in ARPES studies of the 2D γ band [6, 85]; the similarity of these energy scales to the M-EELS data for the pseudo-1D β provides strong indication that the ARPES kinks at these energies also arise due to coupling of quasiparticles to the same bosonic modes.

The dispersion of $\mathbf{q}_3$ along the $\Gamma \rightarrow$ X direction, plotted in the inset in Figure 5.12a, shows an additional kink around $\omega_3 \sim 10$meV, also clearly seen in Figure 5.12b. The feature at $\mathbf{q}_3$ in the QPI is significantly less intense than those of $\mathbf{q}_1$, $\mathbf{q}_2$, and consists of contributions from both α-β scattering and intra-γ scattering, so assignment of the interaction effect due to the kink at ω_3 is less straightforward. As seen in Figure 5.5, the α-β scattering around X is enhanced by pronounced nesting. While the intensity of this response is reduced in the observed QPI (which we showed in Section 5.2.2 may be the result of the projection into the Wannier basis of the surface states), we still expect the α-β scattering to dominate as a result. Significant AFM spin fluctuations have been measured by inelastic neutron scattering [181, 134] at incommensurate momenta around $a_0\mathbf{q} = (2\pi/3, 2\pi/3)$; the imaginary part of the dynamical magnetic

susceptibility shows a broad peak near 8meV in the normal state [181], consistent with the energy of ω_3. If, instead, the kink at ω_3 arises from interaction effects for intra-γ-band scattering, it is possible that it corresponds to coupling to the Σ_3 soft phonon mode that corresponds to the RuO_6 octahedron rotation associated with the surface reconstruction (discussed in Section 5.1); further M-EELS measurements are needed to disambiguate between the two possibilities.

Overall, the picture that emerges from comparison of experimental FT-STS and theoretical QPI for the normal state in Sr_2RuO_4 is one in which the β band, arising from the Ru $4d_{xz}$ and $4d_{yz}$ orbitals, displays interaction effects significantly enhanced by the pseudo-1D nature of the band, and beyond those expected for a weakly-correlated 2D Fermi liquid metal. These same interactions may also be of central importance in the SC pairing mechanism [166, 175]. As previously discussed in Section 5.1.2, the detailed mechanism of triplet superconductivity in Sr_2RuO_4 has been a long-standing issue since its discovery. While compelling experimental evidence favors an odd parity (triplet) OP, and there is strong evidence that the SC order spontaneously breaks time reversal symmetry [127, 95], this latter question has remained controversial. The most direct way to distinguish between the various predictions involving pairing on either the quasi-1D bands (α,β) or the quasi-2D band (γ) is by determining the momentum dependent OP, a task not yet done due to the sub-meV magnitude of the gap and the multi-band structure. However, FT-STS measurements such as those presented here and in detail in Ref. 206 may provide a unique approach to directly confirm the gap structure on the pseudo-1D bands, and thus provide evidence for either the α/β-dominant [166, 174] or the γ-dominant [152, 203] SC pairing mechanism. The momentum dependence of the β band SC gap in each case results in complicated near-nodal structure in the Bogoliubov quasiparticle CECs, resulting in characteristic features in the QPI compared to that of the normal state, as discussed in Section 5.4. Importantly, the two potential pairing mechanisms described in Section 5.1.2, which result in the two SC OPs depicted in Figure 5.4, give rise to *different* nodal structures in the SC gap function around the FS, and thus different QPI signals for the two candidate OPs. Detailed information about $|\Delta(\mathbf{k})|$ on the β band can then be obtained by tracking the energy evolution of this pattern, enhancing the understanding of the microscopic pairing mechanism as we now consider.

5.4 QPI in the superconducting state

The addition of SC pairing to the normal state Hamiltonian results in a mean-field Bogoliubov-de Gennes Hamiltonian given by Eqs. 5.5 and 5.6. This pairing term mixes particle and hole excitations close to the Fermi level, yields Bogoliubov quasiparticles with a gapped excitation spectrum; the momentum-space distribution of these Bogoliubov quasiparticles reflects that of the SC gap function. The anisotropic SC gap functions proposed in Section 5.1.2 are plotted around the FS in Figure 5.4, displaying characteristic, near-nodal features. By measuring the QPI in the SC state, we aim to map the CECs of these quasiparticles, infer the symmetry and structure of the SC OP, and thus provide evidence for the candidate SC OP proposed from calculations for a particular microscopic pairing mechanism [174, 175, 203].

The calculation of the QPI is complicated somewhat by the SC pairing, due to the mixing of particle and hole states. In the Nambu spinor notation of Eqs. 5.5 and 5.6, the Green function matrix of the unperturbed host, $\mathbf{G}_{\mathrm{BdG}}(\mathbf{k},\omega) = ((\omega+\mathrm{i}0^+)\mathbf{I}-\mathbf{H}_{\mathrm{BdG}}(\mathbf{k}))^{-1}$, is given by

$$\mathbf{G}_{\mathrm{BdG}}(\mathbf{k},\omega) = \begin{pmatrix} \mathbf{G}(\mathbf{k},\omega) & \mathbf{F}(\mathbf{k},\omega) \\ \mathbf{F}(\mathbf{k},\omega)^\dagger & -\mathbf{G}(-\mathbf{k},-\omega) \end{pmatrix}, \tag{5.18}$$

where $\mathbf{G}(\mathbf{k},\omega)$ and $\mathbf{F}(\mathbf{k},\omega)$ are the normal and anomalous sectors of the (retarded) Green function matrix in spin and orbital space respectively [204, 34, 77]. In the notation of Zubarev [224], the propagators in these sections are respectively of the form $\langle\langle c_i; c_j^\dagger\rangle\rangle_\omega$ and $\langle\langle c_i; c_j\rangle\rangle_\omega$. We consider here the simplest case of a single (weak-scattering) scalar impurity, such that the (momentum-independent) scattering matrix $\mathbf{T}(\omega) \sim \mathbf{V}$, where the scattering potential is simply $\mathbf{V} = \boldsymbol{\tau}_3 \otimes (v_0\mathbf{I})$, where $\boldsymbol{\tau}_n$ denote the Pauli matrices in Nambu space. The STM conductance is related only to the normal sector of the Green function matrix, and is thus given by the trace over the upper left block of $\Delta\mathbf{G}_{\mathrm{BdG}}(\mathbf{k},\mathbf{k}+\mathbf{q},\omega)$ as defined by Eq. 5.18. Similar to Eqs. 5.12 and 5.13, it follows that

$$\Delta g_c(\mathbf{q},\omega) = \sum_{i=a,b,c} C_i \sum_{s=+1,-1} \Delta\rho_{(i,s)}(\mathbf{q},\omega)\,, \tag{5.19}$$

where

$$\begin{aligned}\Delta\rho_n(\mathbf{q},\omega) =& -\pi^{-1}\mathrm{Im}\ \left[\underset{\tau}{\mathrm{Tr}}\,(\boldsymbol{\tau}_0+\boldsymbol{\tau}_3)\mathbf{G}^0_{\mathrm{BdG}}(\mathbf{k},\omega)\mathbf{T}(\omega)\mathbf{G}^0_{\mathrm{BdG}}(\mathbf{k}+\mathbf{q},\omega)\right]_{nn} \\ =& -\frac{v_0}{\pi}\mathrm{Im}\ \left[\mathbf{G}^0(\mathbf{k},\omega)\mathbf{G}^0(\mathbf{k}+\mathbf{q},\omega)-\mathbf{F}^0(\mathbf{k},\omega)\mathbf{F}^0(\mathbf{k}+\mathbf{q},\omega)^\dagger\right]_{nn},\end{aligned} \tag{5.20}$$

and the coefficients $(C_a, C_b, C_c) = (1, 1, 0)$ to take into account the absence of tunnelling between the in-plane c orbital and the STM tip.

In analogy to the simpler multi-band case considered generally in Chapter 2 and for the specific case of the Sr_2RuO_4 normal state in Section 5.2, a subtlety arises when trying to interpret the QPI in terms of scattering between points on quasiparticle CECs for the SC state. The physical scattering process, which is local and diagonal in Nambu space, is more complicated in the Bogoliubov quasiparticle basis, giving rise to a momentum-dependent scattering matrix element, analogous to that arising due to orbital texture when considering multi-band systems in Section 2.3. This scattering matrix element is given by the product of "coherence factors" (particle and hole coefficients in the Bogoliubov quasiparticle state at a given momentum) [34, 77], analogous to the orbital coefficients for a given band in the multi-band problem. Nevertheless, the qualitative picture in which Bogoliubov quasiparticles are scattered between points on an appropriate CEC holds with these additional structures due to coherence factors.

The left panels of Figures 5.13 and 5.14 plot the Bogoliubov quasiparticle CECs for the two candidate SC OPs discussed in Section 5.1.2, $d^0_z(\mathbf{k})$ and $d^{\mathrm{RG}}_z(\mathbf{k})$ (respectively), for a range of scanning energies. The SC critical temperature measured experimentally is $T_\mathrm{c} \sim 1.5$K [127], corresponding to a SC gap scale of ~ 0.15meV. $\Delta_{\nu,0}$ and Δ_{RG}, which control the magnitude of the gap scale in each case, are adjusted to set the minima in the magnitude of the gap function to approximately $0.15\mathrm{meV} \sim 10^{-3}t$. The magnitudes of the SC gap functions around the FS for each band in both the "naive" and the RG-fit cases are plotted in Figure 5.4; the scanning frequencies plotted in Figures 5.13 and 5.14, $\omega/t = (0.001, 0.002, 0.003, 0.004, 0.01)$ correspond to $|\Delta(\mathbf{k})| = (0.2, 0.4, 0.6, 0.8, 2)$ for the naive SC gap and $|\Delta(\mathbf{k})| = (0.3, 0.6, 0.9, 1.2, 3)$ for the RG-fit SC gap on the scale of Figure 5.4 (in arbitrary units). The right panels of Figures 5.13 and 5.14 plot the QPI due to a single scalar impurity for each scanning energy, plotted as $|g_c(\mathbf{q},\omega)|$ defined in Eqs. 5.19 and 5.20, and calculated on an 8192×8192 grid over the first Brillouin zone ($\mathrm{a}_0(\delta k)/\pi \lesssim 10^{-4}$), with a finite broadening such that $\omega + \mathrm{i}0^+ \to \omega + \mathrm{i}\delta$ with $\delta \sim 0.1$meV. This smaller broadening parameter, which necessitates finer sampling of the Brillouin zone in calculations, is required in order to accurately capture in the

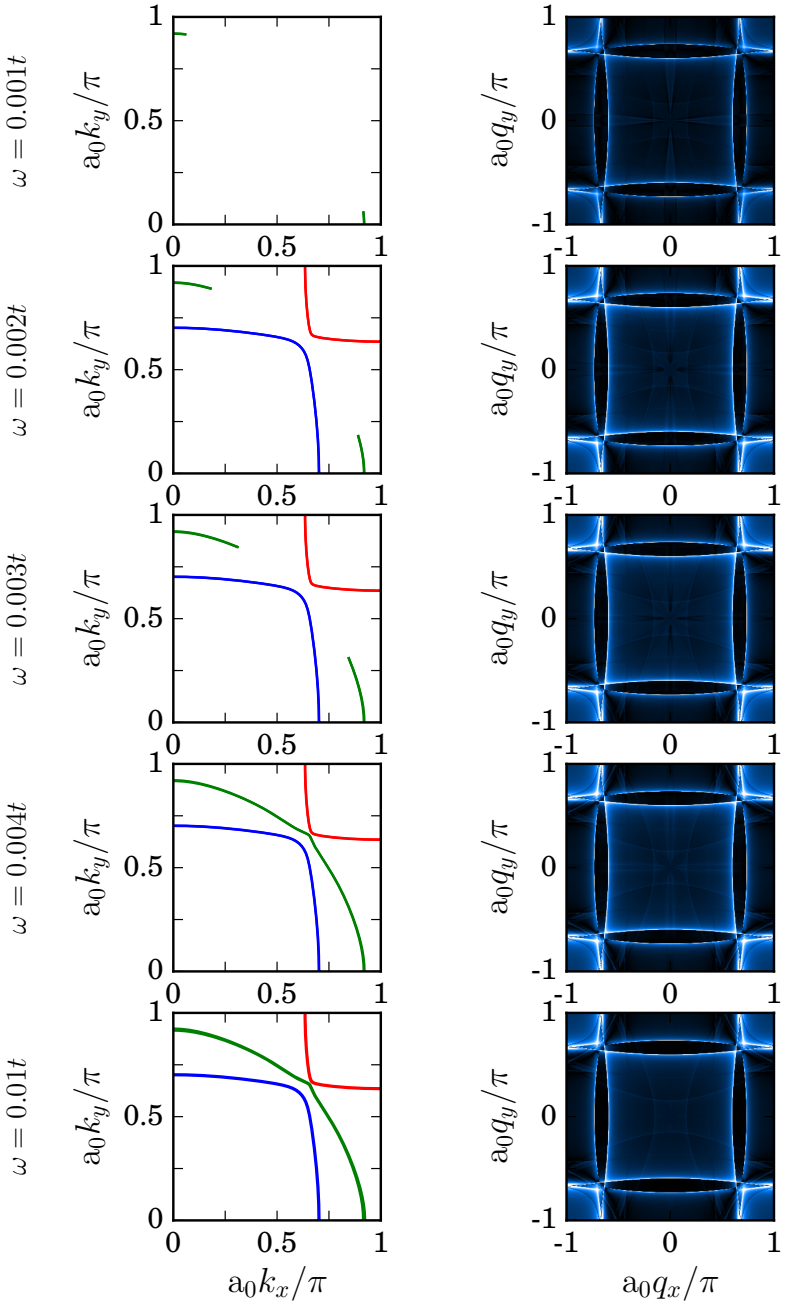

Fig. 5.13 Bogoliubov quasiparticle CECs (left panels) for the α, β and γ bands (red, blue and green contours respectively) and resultant QPI due to a single scalar impurity (right panels) in the SC state with OP given by $d_z^0(\mathbf{k})$ for a range of scanning frequencies around the absolute scale of the SC gap as depicted in Figure 5.4.

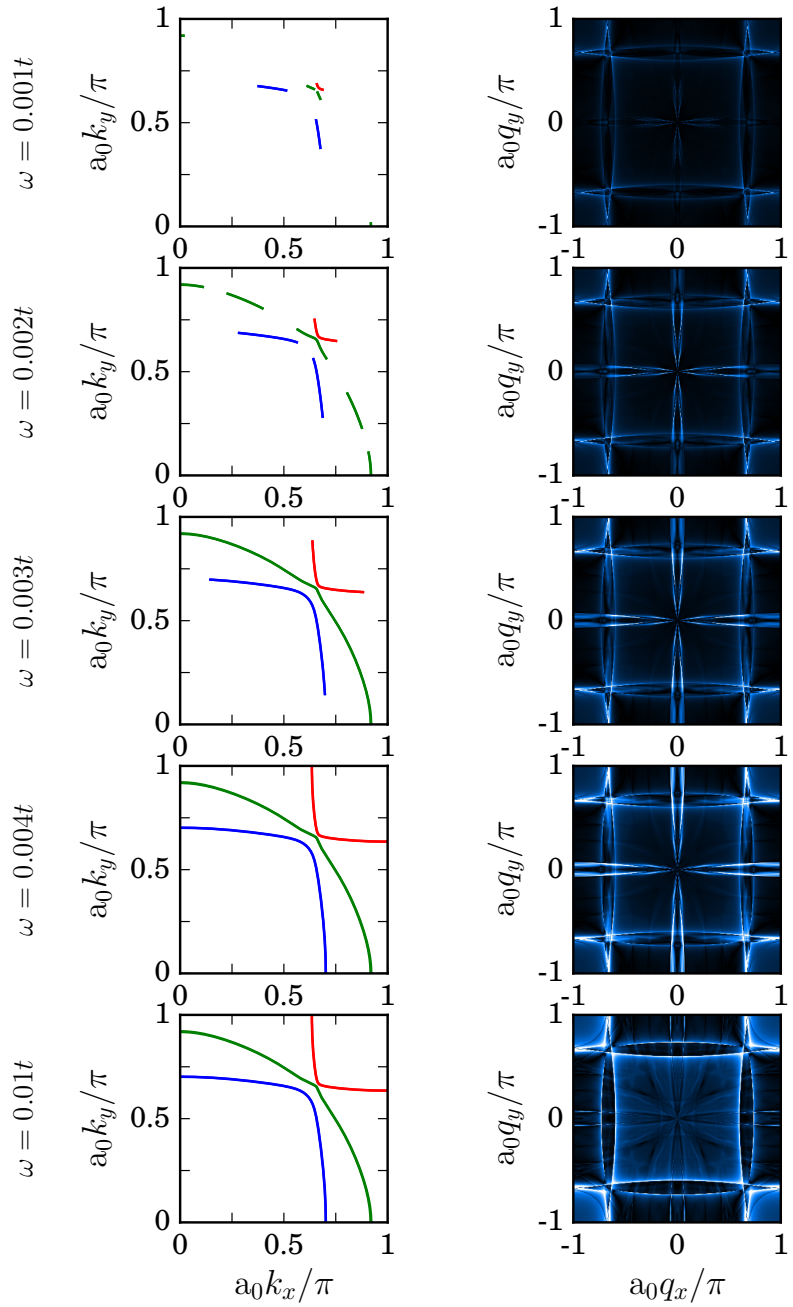

Fig. 5.14 Bogoliubov quasiparticle CECs (left panels) for the α, β and γ bands (red, blue and green contours respectively) and resultant QPI due to a single scalar impurity (right panels) in the SC state with OP given by $d_z^{\mathrm{RG}}(\mathbf{k})$ for a range of scanning frequencies around the absolute scale of the SC gap as depicted in Figure 5.4.

QPI the physics of the SC state, where the characteristic energy scale of the SC gap is of the same order of magnitude.

In the case of the naive SC OP, the dominant gap is on the γ band, with deep, near-nodal minima along the $\Gamma \rightarrow$ M direction, while smaller gaps on the α and β band are more uniform in magnitude around the FS. This is reflected in the Bogoliubov quasiparticle CECs, which form (Fermi) arcs around the FS as the scanning energy is increased from the bottom of the minima in the SC gap function, as seen for the (dominant) γ band in Figure 5.13. The resultant Fermi arcs form around the $\Gamma \rightarrow$ M direction, which are very narrow due to the small magnitude of the SC gap compared to t, the characteristic energy scale of the normal state electronic structure. These Fermi arcs coalesce to form continuous contours around the FS above the maxima in the magnitude of the SC gap. By contrast, the relatively uniform magnitude of the gap function in the α and β bands means that Fermi arcs are seen over a small energy window. The γ band arises almost completely from the c orbital (except around the $\Gamma \rightarrow$ X direction), and thus scattering between points on the γ band Fermi arcs manifests in modulations in the c orbital LDOS, not measured via STM due to the poor tip-orbital overlap with the in-plane $4d_{xy}$ orbital. The sub-dominant SC gap for the α and β bands means that the Bogoliubov quasiparticles of predominantly α and β character quickly resemble the normal state quasiparticles as the energy is increased, while the γ band remains (partially) gapped. As a result, the calculated QPI largely resembles that of the normal state, with the intensity and detailed structure affected by the SC pairing.

In contrast with the naive SC OP, the OP of higher Chern number proposed to fit the numerical weak-coupling RG results of Ref. 174 has comparable SC gap magnitudes on all three bands, with a more complex nodal gap structure, as depicted in Figure 5.4. The resultant Bogoliubov quasiparticle CECs, plotted in the left panels of Figure 5.14, display this more complicated form of the SC gap, resulting in Fermi arcs on all three bands. The γ band forms Fermi arcs around the $\Gamma \rightarrow$ M and $\Gamma \rightarrow$ X directions, as well as in between these two directions (at $\theta_1 \sim \pi/4$), in contrast to the naive SC OP case. Moreover the α and β bands have more pronounced anisotropy in the SC gap magnitude, with Fermi arcs forming around the $\Gamma \rightarrow$ X before coalescing at higher scanning energies. As the SC pairing on the α and β band is more significant in the RG-fit OP case, characteristic features are observed in the calculated QPI at scanning energies around the SC pairing scale. At low energy close to the SC gap minima, the quasiparticles are largely gapped and thus the magnitude of LDOS modulations is low, and the QPI intensity reduced compared to the normal state QPI (recovered at

high energies). As the scanning energy is increased, additional features are observed in the $q_x = 0$ and $q_y = 0$ directions, which disappear when the scanning energy is increased significantly above the SC gap scale as the quasiparticles reduce to those of the normal state. These intense features result from inter-band scattering between the α and β band Bogoliubov quasiparticles. Similar features are in fact observed in the JDOS of the normal state in Figure 5.5, but are cancelled by destructive interference in the normal state, as discussed in Section 5.2; the QPI contributions from these scattering events do not interfere destructively in the SC state, and are clearly visible in Figure 5.14.

Calculations of the QPI in the SC state indicate that FT-STS is sensitive to the detailed structure of the SC gap function, and the relative magnitudes of the SC gap in multi-band systems such as Sr_2RuO_4. In particular the distinctive inter-band scattering between α and β band Bogoliubov quasiparticles, which is seen in the SC state QPI in Figure 5.14 but not in the normal state QPI, is a strong indicator for significant SC pairing on these bands. The orbitally-selective nature of the conductance between the STM tip and host material, which arises due to the spatial anisotropy of the Ru $4d$ t_{2g} orbitals, further assists in distinguishing between the γ-dominant SC pairing scenario of the simplest proposed SC OP and the α/β dominant SC pairing of the RG-fit SC OP, as signatures of the Bogoliubov quasiparticle scattering on the γ band (with predominantly in-plane $4d_{xy}$ orbital character) are expected to be very weak in the measured QPI. FT-STS at temperatures below T_c may therefore offer direct insight into the SC pairing mechanism, in addition to the indirect information provided by measurements of the normal state as detailed in Section 5.3.

5.5 Conclusion

The layered ruthenate Sr_2RuO_4 is a fundamentally interesting quantum material that has attracted a great deal of interest as an interacting multi-orbital system in which orbital, spin and charge degrees of freedom are all relevant. This manifests in a spin-triplet SC whose order parameter appears to break time reversal invariance, thereby hosting half-quantized vortices with Majorana zero modes. While the nature of the superconducting state is still a matter of controversy, it has long been believed that the normal metallic state is well described by a weakly-interacting 2D Fermi liquid.

Previous QPI calculations for Sr_2RuO_4 [7, 59] have employed a simplified model of the host, neglecting SOC effects, and present results for only the most basic approximation to the true QPI. In order to provide more realistic QPI calculations, and

attempt to accurately simulate experimental measurements [206], we have calculated carefully the full QPI for Sr_2RuO_4 in the normal state within the effective model of Section 5.1. The nature of quasiparticle scattering, the anisotropy of the host orbitals to which the STM tip couples and the reconstruction of the host electronic structure at the surface have all been considered, giving rise to qualitative effects on the resultant QPI as demonstrated in Section 5.2.

Comparison of such theoretical results with experimental FT-STS measurements in Section 5.3 demonstrated significant departure from the non-interacting effective model for the electronic structure of Sr_2RuO_4 due to electron-phonon and electron-electron interactions. Theoretical investigations considering the effect of interactions on the conduction electrons of the host and the scattering of electrons due to structured, spatially-extended impurities are needed in order to provide further insight. Evidence of strong correlation effects in the normal state casts doubt on the conventional picture of a weakly-interacting 2D Fermi liquid, and has important implications for the SC state and the unconventional pairing mechanism, which is thought to be related to such correlations.

FT-STS also offers the possibility of directly probing the SC state due to the sub-meV energetic resolution of the technique. In Section 5.4 we presented QPI calculations for the SC state with two possible candidates for the SC pairing mechanism which realize different forms for the SC OP. The sensitivity of the QPI to the detailed form of the (anisotropic) SC gap function was demonstrated, indicating that future FT-STS measurements on the SC state may provide further evidence of the pairing mechanism, and help to resolve the long-standing controversy over the nature of the SC state in Sr_2RuO_4.

Chapter 6

Summary & outlook

In this thesis we have investigated the quasiparticle interference (QPI) arising due to the scattering of conduction electrons from local impurities embedded in a range of host materials. In particular we focused on the effect of electronic interactions, both in the host material and the impurities that cause scattering, on both the underlying host electronic structure and the scattering characteristics of the impurities. The QPI is measured experimentally using scanning tunnelling microscopy (STM), which is used to map modulations in the surface density of states of the host material caused by impurity scattering. Measuring the power spectrum of these spatial modulations gives the QPI , a technique known as Fourier transform scanning tunnelling spectroscopy (FT-STS).

The purpose of this thesis was two-fold. We studied the QPI in a number of interacting systems of fundamental interest in their own right, and for which the QPI is an experimentally accessible quantity that sheds light on the non-trivial physics arising due to strong correlations. In addition, we sought to develop a general framework for understanding and interpreting QPI results in simple physical terms where possible, and understand the capabilities and limitations of experimental QPI measurements in probing interaction effects in novel materials.

In Chapter 2 we developed the basic formalism of the QPI, starting from the real-space distribution of scattered conduction electron states of a 2D non-interacting host. The QPI was shown to be a two-particle quantity resulting from the interference of these scattered states, and therefore measures the amplitude of scattering between all pairs of conduction electron states separated by a given momentum, summed across the Brillouin zone. The interference of these contributions complicates the interpretation of the QPI at particular momentum vectors. We demonstrated that lines of divergence in the QPI are characteristic of scattering between particular pairs of points in momentum

space, but that the structure of the QPI away from these divergent lines is highly dependent on the details of the scattering, and thus the nature of impurities. Moreover, additional complicating factors that arise in realistic materials, such as the presence of multiple bands of conduction electrons, detailed spatial structure of the local surface orbitals of the host and electronic interactions, were shown to have a significant qualitative impact on the QPI. This sensitivity requires that careful calculations of the QPI are required in order to simulate accurately experimental measurements.

With a framework for understanding the QPI in place, we consider the effect of magnetic impurities on the QPI in Chapters 3 and 4. In Chapter 3 we considered the QPI due to a single magnetic impurity embedded on a range of host materials. The presence of strong on-site electronic interactions at the impurity was shown to affect the magnitude and phase of scattering, and thus directly affect the QPI. The interacting quantum impurity problem was treated exactly using numerical renormalization group (NRG). In stark contrast to the simpler case of a weak potential scatterer, strong dynamical features were observed in the QPI, which are characteristic of the interacting impurity state for each host material, including universal scaling in the magnitude of the QPI at low frequencies due to the Kondo effect.

The case of multiple magnetic impurities adsorbed on the (100) surface 3D cubic lattice is considered in Chapter 4. The scattering of conduction electrons from different impurities gives rise to interference between different contributions, which increases the complexity of the QPI. In the case of independent impurities, the QPI is the product of a structure factor, determined by the distribution of impurities, with the single-impurity QPI; this results in a "noisy" signal, which may be mitigated against by averaging over a number of different impurity distributions to recover the single-impurity result. However, inter-impurity correlations not only result in additional, non-local scattering channels, adding further contributions to the QPI, but also alter the nature of the local scattering. Significant inter-impurity interactions may therefore result in profound changes in the QPI, necessitating, in principle, a full treatment of the many-impurity system.

In order to better understand systems containing multiple magnetic impurities, in Chapter 4 we studied the two-impurity case, known as the Alexander Anderson model (AAM). This minimal model captures the competition between local impurity-host interactions and non-local inter-impurity interactions mediated by the conduction electrons of the host. The AAM is also amenable to treatment via NRG, with accurate calculations now possible due to recent technical and computational advances. Even

for this simple model, our calculations reveal a range of physics due to the interplay of the these local and non-local interactions, as investigated in Section 4.2.

The detailed exploration of the AAM in Chapter 4 also demonstrated that impurities behave essentially independently beyond a certain separation, as the local interactions with the host conduction electrons dominate the inter-impurity effects. For experimentally reasonable impurity parameters, this cutoff length scale was found to be of the order of only a few lattice sites. We were therefore able to establish a reasonable upper bound on the impurity concentration, below which the "dilute limit" (in which impurities behave independently) applies, for systems of many magnetic impurities. Utilizing exact two-impurity results from the AAM, we were able to go beyond this dilute limit with an "independent cluster approximation" for higher impurity concentrations. At higher concentrations this independent cluster approximation fails and more complicated models such as the diluted periodic Anderson model are required; this is expected not only to significantly affect the scattering of conduction electrons, but also alter the electronic structure of the conduction band itself for sufficiently high impurity density. Such models are often used to investigate heavy-fermion materials, for which the study of the QPI is an active area of research [193, 217].

Electronic interactions in the scattering centres exert an effect on the QPI by changing the magnitude and phase of local (and non-local, if applicable) scattering matrix elements. Interactions between electrons in the conduction band affect both the nature of the conduction electron states and the way in which they scatter, and hence the QPI. FT-STS experiments, which measure the QPI, aim to provide insight into the underlying conduction electron states of the material under study. These conduction electrons typically exhibit interesting or unusual properties due to interactions, such as superconductivity (SC) or unusual magnetic fluctuations. However, as demonstrated throughout this thesis, the QPI is a complicated superposition of many interfering scattering contributions, and is thus highly dependent on the detailed electronic structure of the material and the nature of scattering. In depth calculations of the QPI are needed in order to simulate experimental measurements, and provide an interpretation of experimental results.

In Chapter 5 we studied the QPI in one such experimentally-investigated material: the layered transition metal oxide Sr_2RuO_4, which undergoes a transition to an unusual SC state at $T_c \sim 1.5$K. The SC state is believed to consist of spin-triplet Cooper pairs, and thus an order parameter of p-wave symmetry. However, controversy remains as to the pairing mechanism, which is believed to be mediated by strong electron-electron or electron-phonon interactions. In the first instance we calculated the QPI

in the normal state, employing a non-interacting effective tight binding model for the electronic structure taking into account multiple conduction bands and spin-orbit coupling effects. We carefully considered the impact on the QPI of several experimentally relevant features of the host material in order to improve agreement with experimental measurements carried out by collaborators. These results were then used to interpret important features in the experimental QPI. The deviation of the experimental measurements from the calculations for a non-interacting model provide insight into the effect of interactions in the normal state, which may also be responsible for the SC pairing mechanism, and therefore shed light on the SC state indirectly. We also calculated the QPI in the SC state, demonstrating how the QPI measured via FT-STS may be used in the future to investigate the anisotropic structure of the SC gap and thus give further insight into the pairing mechanism.

A detailed theoretical treatment of the QPI demonstrated the profound influence that interactions exert on the QPI, in a wide range of systems. However, it has also demonstrated that the QPI is a very complicated and information-rich quantity, and that a direct and simple physical interpretation for the features present in the QPI is often not possible. The QPI was also shown to be very sensitive to a wide range of factors beyond the simple underlying structure of host conduction electrons. These factors, such as the nature and distribution of impurities and the strength of scattering, can qualitatively affect the resultant QPI, and furthermore are very hard to control or accurately determine. As a result, great care must be taken to consider the effect of all relevant, material-specific factors when calculating the QPI, in order to provide relevant and accurate interpretations of experimental measurements. However, with appropriately detailed calculations, the QPI offers a significant amount of insight into the nature of strong correlations in novel electronic condensed matter systems, and is expected to be of great use in understanding such materials in the future.

Appendix A

Lattice Green functions for generalized hypercubic tight binding models

The calculation of real-space Green functions (LGFs) for fermions on a tight binding (TB) lattice is a well-known problem encountered in many areas of condensed matter physics [198, 97, 67, 43]. The problem can in principle be formulated simply in terms of the eigenbasis Green functions,

$$G(\mathbf{r}, \mathbf{r}', z) = \sum_i \langle \mathbf{r}|i\rangle \frac{1}{z - \epsilon_i} \langle i|\mathbf{r}'\rangle, \tag{A.1}$$

where $z = \omega + \mathrm{i}0^{+/-}$ for the retarded/advanced Green function of the free (non-interacting) system, but could generally include a local self-energy $\Sigma(\omega)$ such that $\omega \to \omega - \Sigma(\omega)$. For systems possessing translational invariance, Eq. A.1 corresponds to an integral over the first Brillouin zone (1BZ) of the Green functions in momentum space:

$$G(\mathbf{r}, \mathbf{r}', z) = G(\mathbf{R}, z) = \int_{1\mathrm{BZ}} \frac{d^{\mathrm{D}}k}{\Omega_{\mathrm{BZ}}} \frac{\mathrm{e}^{\mathrm{i}\mathbf{k}.\mathbf{R}}}{z - \epsilon(\mathbf{k})} \tag{A.2}$$

where $\mathbf{R} = (\mathbf{r}' - \mathbf{r})$. Despite the simplicity of Eq. A.2, analytic calculation of LGFs via this direct methodology is possible only in the simplest cases and in low dimensions. Furthermore, numerical evaluation of Eq. A.2 is computationally intensive for 2D and 3D systems, owing to the high cost of numerical quadrature in multiple dimensions for integrands involving sharp features (e.g. first order poles, as in Eq. A.2). Several

alternative approaches have been developed in order to circumvent this problem, typically relying on recursive schemes [146, 18, 19, 71, 72, 162]. However, as discussed in Section 3.2.1, none of these methods provide a robust, numerically inexpensive way to calculate far non-local LGFs (between lattice points separated by tens or hundreds of sites) as a full function of frequency.

In order to calculate the modulations in the local density of conduction electron states due to impurities, which give rise to the QPI, we develop a novel technique for fast and accurate numerical calculation of LGFs on hypercubic-type lattices. In Section 3.5.1 we employ this technique to simulate the FT-STS procedure, while in Chapter 4 we use the non-local LGFs for the (100) 3D cubic surface in order to calculate the local and non-local hybridization functions for the Anderson Alexander model.

A.1 General formalism

We consider the TB lattice consisting of a general unit cell, with a local Hamiltonian $\hat{\varepsilon}$, on a N-dimensional hypercubic lattice with only NN hopping between unit cells, $\hat{t}_{ij}$. The Hamiltonian for the system is given by

$$\mathcal{H}_N = \sum_i \vec{\psi}_i^\dagger \hat{\varepsilon}\ \vec{\psi}_i + \sum_{\langle ij \rangle} \left(\vec{\psi}_i^\dagger \hat{t}_{ij} \vec{\psi}_j + \text{H.c.} \right) , \tag{A.3}$$

where $\langle ij \rangle$ runs over NN pairs of unit cells, and $\vec{\psi}_i = (c_{i,1},\, c_{i,2},\, c_{i,3}\, \dots)$ represents the local electronic states of the unit cell. As the lattice vectors for the hypercubic lattice form an orthogonal set, each non-local (hopping) term in the Hamiltonian only acts along one lattice vector,

$$\mathcal{H}_N = \sum_i \left\{ \vec{\psi}_{\mathbf{r}_i}^\dagger \hat{\varepsilon}\ \vec{\psi}_{\mathbf{r}_i} + \sum_{n=1}^{N} \left(\vec{\psi}_{(\mathbf{r}_i + \mathbf{a}_n)}^\dagger \hat{t}_{\mathbf{a}_n} \vec{\psi}_{\mathbf{r}_i} + \text{H.c.} \right) \right\} , \tag{A.4}$$

for $\mathbf{r} = (r_1, r_2, \dots, r_N) \in \mathbb{R}^N$. The NN TB lattice can thus be decomposed as a 1D stack of identical $(N-1)$D NN TB lattices:

$$\mathcal{H}_N = \sum_x \vec{\Psi}_x^\dagger \hat{\mathcal{E}}\ \vec{\Psi}_x + \left(\vec{\Psi}_{(x+1)}^\dagger \hat{T}\ \vec{\Psi}_x + \text{H.c.} \right) , \tag{A.5}$$

with $\vec{\Psi}_x = \bigoplus_i \vec{\psi}_{(x,\mathbf{s}_i)}$ where $\mathbf{s} \in \mathbb{R}^{N-1}$ such that $\mathbf{r}_i = (x_i, \mathbf{s}_i)$, and $\hat{\mathcal{E}}$, $\hat{T}$ span the $(N-1)$D subspace,

$$\hat{\mathcal{E}}_{ij} = \delta_{\mathbf{r}_i,\mathbf{r}_j}\hat{\varepsilon} \ + \sum_{n=2}^{N} \delta_{\mathbf{r}_i,\mathbf{r}_j+\mathbf{a}_n}\hat{t}_{\mathbf{a}_n} + \delta_{\mathbf{r}_i,\mathbf{r}_j-\mathbf{a}_n}\hat{t}^\dagger_{\mathbf{a}_n} \tag{A.6a}$$

such that

$$\begin{aligned}\vec{\Psi}^\dagger_x \hat{\mathcal{E}} \ \vec{\Psi}_x = \sum_i \Bigg\{ & \vec{\psi}^\dagger_{(x,\mathbf{s}_i)}\hat{\varepsilon} \ \vec{\psi}_{(x,\mathbf{s}_i)} \\ & + \sum_{n=2}^{N} \left(\vec{\psi}^\dagger_{((x,\mathbf{s}_i)+\mathbf{a}_n)}\hat{t}_{\mathbf{a}_n}\vec{\psi}_{(x,\mathbf{s}_i)} + \text{H.c.} \right) \Bigg\} \ ;\end{aligned} \tag{A.6b}$$

similarly

$$\hat{T} = \hat{I} \otimes \hat{t}_{\mathbf{a}_1}, \tag{A.7a}$$

such that

$$\vec{\Psi}^\dagger_{(x+1)} \hat{T} \ \vec{\Psi}_x = \sum_i \vec{\psi}^\dagger_{(x+1,\mathbf{s}_i)} \hat{t}_{\mathbf{a}_1} \vec{\psi}_{(x,\mathbf{s}_i)}. \tag{A.7b}$$

As $\mathcal{H}_{N-1} = \vec{\Psi}^\dagger_x \hat{\mathcal{E}} \ \vec{\Psi}_x$ is the Hamiltonian for a NN TB lattice, it is diagonalized by discrete Fourier transform in $(N-1)$D, $\hat{U} \otimes \hat{I}_M$ where M is the state space of the unit cell:

$$\begin{aligned}\mathcal{H}_N = & \sum_x \vec{\Phi}^\dagger_x \left(\hat{U} \otimes \hat{I}_M \right)^\dagger \hat{\mathcal{E}} \ \left(\hat{U} \otimes \hat{I}_M \right) \ \vec{\Phi}_x \\ & + \left(\vec{\Phi}^\dagger_{(x+1)} \hat{T} \ \vec{\Phi}_x + \text{H.c.} \right) \ ,\end{aligned} \tag{A.8}$$

where $\vec{\Phi}_x = \left(\hat{U} \otimes \hat{I}_M \right)^\dagger \vec{\Psi}_x$,

$$\vec{\Phi}_x = \bigoplus_i \vec{\phi}_{(x,\mathbf{k}_i)} \quad \text{and} \quad \vec{\phi}_{(x,\mathbf{k}_i)} = \sum_j \frac{\mathrm{e}^{\mathrm{i}\,\mathbf{k}_i \cdot \mathbf{s}_j}}{\sqrt{N_\mathbf{k}}} \vec{\psi}_{(x,\mathbf{s}_j)}. \tag{A.9}$$

This transformation, independent of the "stack index" x, leaves the hopping between unit cells ($\hat{t}_{\mathbf{a}_1}$) unchanged, while the unit cell Hamiltonian becomes

$$\left(\hat{U} \otimes \hat{I}_M \right)^\dagger \hat{\mathcal{E}} \ \left(\hat{U} \otimes \hat{I}_M \right) \ = \hat{I} \otimes \hat{\varepsilon}_{\mathbf{k}_j}, \tag{A.10}$$

where

$$\hat{\varepsilon}_{\mathbf{k}_j} = \hat{\varepsilon} + \sum_{n=2}^{N} \mathrm{e}^{\mathrm{i}\mathbf{k}_j\cdot\mathbf{a}_n}\hat{t}_{\mathbf{a}_n} + \mathrm{e}^{-\mathrm{i}\mathbf{k}_j\cdot\mathbf{a}_n}\hat{t}^{\dagger}_{\mathbf{a}_n}. \tag{A.11}$$

The transformation thus alters the local Hamiltonian of the unit cell in the new basis, rendering the full Hamiltonian, $\mathcal{H}_N$, as a bundle of uncoupled, 1D TB chains, $\mathcal{H}_N = \sum_j \mathcal{H}_{N,j}$ where

$$\mathcal{H}_{N,j} = \sum_x \vec{\phi}^{\dagger}_{(x,\mathbf{k}_j)}\hat{\varepsilon}_{\mathbf{k}_j}\vec{\phi}_{(x,\mathbf{k}_j)} + \left(\vec{\phi}^{\dagger}_{(x+1,\mathbf{k}_j)}\hat{t}_{\mathbf{a}_1}\vec{\phi}_{(x,\mathbf{k}_j)} + \mathrm{H.c.}\right). \tag{A.12}$$

Having recast the system Hamiltonian as Eq. A.12, the LGFs may be expressed in this new basis as

$$\begin{aligned}\mathbf{G}(\mathbf{r}_i,\mathbf{r}_j,z) =& |\vec{\psi}_{\mathbf{r}_i}\rangle(zI-\mathcal{H}_N)^{-1}\langle\vec{\psi}_{\mathbf{r}_j}| \\ =& \sum_{\mathbf{k}_l} U_{\mathbf{s}_i,\mathbf{k}_l}\,U^{\dagger}_{\mathbf{s}_j,\mathbf{k}_l}|\vec{\phi}_{(x_i,\mathbf{k}_l)}\rangle(zI-\mathcal{H}_{N,l})^{-1}\langle\vec{\phi}_{(x_j,\mathbf{k}_l)}|\,.\end{aligned} \tag{A.13}$$

$\hat{U}$ diagonalizes the $(N-1)$D NN TB model with a single-site unit cell, the (retarded) LGF for which is therefore

$$-\pi^{-1}\mathrm{Im}\,G(\mathbf{s}_i,\mathbf{s}_j,\omega+\mathrm{i}0^+) = \sum_{\mathbf{k}_l} U_{\mathbf{s}_i,\mathbf{k}_l}\,U^{\dagger}_{\mathbf{s}_j,\mathbf{k}_l}\delta\left(\omega'-\epsilon_{\mathbf{k}_l}\right), \tag{A.14}$$

where $\epsilon_{\mathbf{k}_l} = 2t\sum_{n=2}^{N}\cos(\mathbf{k}_l\cdot\mathbf{a}_n)$, so that

$$\begin{aligned}\sum_{\mathbf{k}_l} U_{\mathbf{s}_i,\mathbf{k}_l}\,U^{\dagger}_{\mathbf{s}_j,\mathbf{k}_l}\cdots &= \int_{-\infty}^{\infty} d\omega'\left\{\sum_{\mathbf{k}_l} U_{\mathbf{s}_i,\mathbf{k}_l}\,U^{\dagger}_{\mathbf{s}_j,\mathbf{k}_l}\delta\left(\omega'-\epsilon_{\mathbf{k}_l}\right)\right\}\ldots \\ &= -\pi^{-1}\int_{-\infty}^{\infty} d\omega'\mathrm{Im}\,G(\mathbf{s}_i,\mathbf{s}_j,\omega'+\mathrm{i}0^+)\ldots\end{aligned} \tag{A.15}$$

and therefore Eq. A.13 becomes

$$\mathbf{G}(\mathbf{r}_i,\mathbf{r}_j,z) = -\pi^{-1}\int_{-\infty}^{\infty} d\omega'\,\mathrm{Im}\,G(\mathbf{s}_i,\mathbf{s}_j,\omega'+\mathrm{i}0^+)\,\mathbf{G}^{\mathrm{1D}}_{\omega'}(x_i,x_j,z), \tag{A.16}$$

where $\mathbf{G}^{\mathrm{1D}}_{\omega'}(x_i,x_j,z)$ is the LGF between unit cells at x_i and x_j on a 1D TB chain described by $\mathcal{H}_{\mathrm{1D}}(\omega')$,

$$\mathbf{G}^{\mathrm{1D}}_{\omega'}(x_i,x_j,z) = |\vec{\phi}_{x_i}\rangle\left(zI-\mathcal{H}_{\mathrm{1D}}(\omega')\right)^{-1}\langle\vec{\phi}_{x_j}|, \tag{A.17}$$

where

$$\mathcal{H}_{1\mathrm{D}}(\omega') = \sum_i \vec{\phi}^{\dagger}_{x_i} \hat{\varepsilon}(\omega') \vec{\phi}_{x_i} + \left(\vec{\phi}^{\dagger}_{x_i+1} \hat{t}_{\mathbf{a}_1} \vec{\phi}_{x_i} + \mathrm{H.c.} \right) . \tag{A.18}$$

The simplest model amenable to this protocol for calculating LGFs is a 2D square lattice with a single-site unit cell, requiring only the knowledge of LGFs for the single-site 1D TB chain (known in closed form). LGFs for the single-site 3D (and higher-dimensional) hypercubic lattices may be calculated by applying the procedure recursively (e.g. calculating the 3D cubic LGFs via Eq. A.16 using 2D square LGFs calculated themselves via Eq. A.16). Edges (open boundary conditions in one or more dimensions) of such lattices can also be treated in this approach, allowing the calculation of surface LGFs with no increased computational difficulty.

We then consider the bulk and surface LGFs of the 2D honeycomb lattice via a two-site unit cell on the 2D square lattice. The formalism of Sec. A.1 yields a computationally efficient and accurate scheme for calculating the LGFs in this case, both in the infinite (bulk) system, relevant to bulk graphene, and for a finite strip, relevant to the graphene "nanoribbon" structure.

A.2 Monatomic hypercubic LGFs

For "monatomic" hypercubic TB lattices, the unit cell consists of a single site with a single orbital, taken here to be "s-like" such that the lattice is spatially isotropic (generalization to include anisotropy between spatial dimensions is straightforward). With only a single degree of freedom at each lattice point, the on-site and hopping Hamiltonians in the monatomic case are scalar, i.e. $\hat{\varepsilon} = \epsilon_0$ and $\hat{t}_{\mathbf{a}_n} = -t$ ($t > 0$), and thus $\hat{\varepsilon}_{\mathbf{k}} = \epsilon_0 + 2t \sum_{n=2}^{N} \cos(a_0 k_n)$, where $|\mathbf{a}_n| = a_0$ is the lattice spacing. Furthermore, the electronic structure is that of a single, particle-hole symmetric band of conduction electrons; such lattices are thus employed as a simple toy model for a (weakly-correlated) metal with no orbital or spin texture in Chapter 3 and 4 in this thesis.

2D square lattice

For the monatomic 2D square lattice, Eq. A.3 may be written as

$$\mathcal{H}_N = \epsilon_0 \sum_{x,y} c^{\dagger}_{(x,y)} c_{(x,y)} + t \sum_{x,y} \left(c^{\dagger}_{(x+1,y)} c_{(x,y)} + c^{\dagger}_{(x,y+1)} c_{(x,y)} + \mathrm{H.c.} \right) . \tag{A.19}$$

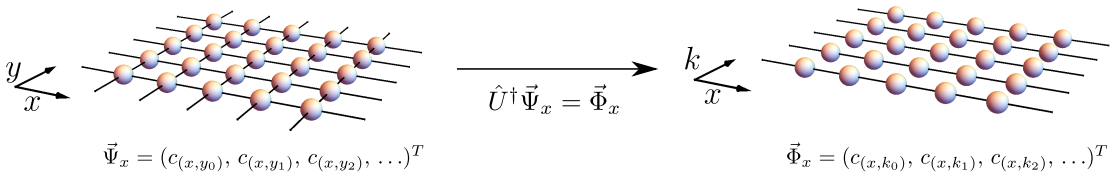

Fig. A.1 Schematic representation of the transformation described in Section A.1 applied the 2D square lattice TB Hamiltonian, given by Eq. A.19, yielding a bundle of uncoupled 1D TB chains described by Eq. A.20.

Despite the simplicity of the 2D square lattice, a complication arises due to the presence of the van Hove singularity at $\omega - \epsilon_0 = 0$. The "critical points" $\mathbf{k} = (\pm\pi, \pm\pi)$, where $|\nabla\epsilon_{\mathbf{k}}| = 0$ for dispersion $\epsilon_{\mathbf{k}} = \epsilon_0 - 2t[\cos(k_x a_0) + \cos(k_y a_0)]$ are saddle points; the density of states (DOS) is thus expected to diverge logarithmically, as confirmed by direct integration of Eq. A.2, as demonstrated in Ref. 147. Under the transformation described in Section A.1, the Hamiltonian is rendered in the form of a Eq. A.12,

$$\mathcal{H}_{\text{sq}} = \sum_k \sum_x \varepsilon_k \phi^\dagger_{(x,k)} \phi_{(x,k)} - \left(t\phi^\dagger_{(x+1,k)} \phi_{(x,k)} + \text{H.c.} \right), \tag{A.20}$$

where $\varepsilon_k = \epsilon_0 - 2t\cos(a_0 k)$. This transformation is represented schematically in Figure A.1. The uncoupled 1D chains described by Eq. A.20 are simply single-site 1D TB chains with uniform hopping matrix elements t and on-site energies ε_k, for which $G^{\text{1D}}_{\omega'}(x, x', z) = G^{\text{1D}}(x, x', z - \omega')$. These LGFs are obtained in closed form via direct integration of Eq. A.2, or via equations of motion,[224] yielding

$$tG^{\text{1D}}(x, x', z - \omega') = \left[f_{\text{semi}}\left(\frac{z - \omega'}{2t} \right) \right]^{|x'-x|} \times f_{\text{inf}}\left(\frac{z - \omega'}{2t} \right), \tag{A.21}$$

where

$$f_{\text{semi}}(\tilde{z}) = \tilde{z} - \begin{cases} \text{sgn}(\text{Re}\,\tilde{z})\,\text{sgn}(\text{Im}\,\tilde{z})\sqrt{\tilde{z}^2 - 1} & |\tilde{z}| > 1 \\ \text{i}\sqrt{1 - \tilde{z}^2} & |\tilde{z}| \leq 1 \end{cases}, \tag{A.22a}$$

and

$$f_{\text{inf}}(\tilde{z}) = \begin{cases} \text{sgn}(\text{Re}\,\tilde{z})\,\text{sgn}(\text{Im}\,\tilde{z})/\sqrt{\tilde{z}^2 - 1} & |\tilde{z}| > 1 \\ -\text{i}/\sqrt{1 - \tilde{z}^2} & |\tilde{z}| \leq 1 \end{cases}. \tag{A.22b}$$

Using this closed form expression for 1D TB chain LGFs, together with Eq. A.16, the retarded LGFs ($z = \omega + \mathrm{i}0^+$) for the 2D square lattice are expressed in terms of the linear convolution of two 1D TB chain LGFs, known in closed form:

$$\begin{aligned} G_{\mathrm{sq}}(\mathbf{r}, \mathbf{r}', z) = -\pi^{-1} \int_{-\infty}^{\infty} d\omega' \mathrm{Im}\, G^{\mathrm{1D}}(r_y, r'_y, \omega' + \mathrm{i}0^+) \\ \times G^{\mathrm{1D}}(r_x, r'_x, (\omega - \omega') + \mathrm{i}0^+). \end{aligned} \tag{A.23}$$

The convolution theorem gives the linear convolution of two functions in terms of the product of their Fourier transforms,

$$\begin{aligned} (f * g)(\omega) = &\int_{-\infty}^{\infty} d\omega' f(\omega') g(\omega - \omega') \\ = &\mathcal{F}^{-1} \left[\mathcal{F} \left[f(\omega) \right] \times \mathcal{F} \left[g(\omega) \right] \right], \end{aligned} \tag{A.24}$$

such that advantage may be taken of numerically efficient fast Fourier transform (FFT) algorithms to calculate LGFs for the 2D square lattice to high accuracy.

*N*D hypercubic lattice: open and periodic boundary conditions

The LGFs for higher-dimensional (ND) hypercubic lattices are obtained from the 2D square lattice LGFs recursively, via the convolution of an appropriate 1D TB chain LGF with the LGF for the hypercubic lattice in $(N-1)$ dimensions. The 3D cubic lattice offers a toy model for a metallic system with a single conduction band. The density of states is essentially constant close to the Fermi level (at energy scales significantly below the hopping amplitude t) and is therefore appropriate as a minimal model for simple materials such as the alkali metals. Higher-dimensional LGFs are also of interest, as non-interacting two-particle LGFs may be expressed in terms of single-particle LGFs in higher dimension (for example 3D two-particle LGFs in terms of single-particle LGFs in 6D [19]).

In addition to the infinite hypercubic lattices (with periodic boundary conditions) considered thus far, the method described in Section A.1 is also applicable to the calculation of LGFs for the semi-infinite case (open boundary conditions), and even the LGFs of a strip geometry (a finite system with open boundary conditions), with no change in the structure of the calculation. Eqs. A.13 and A.16 define the LGFs of the ND system in terms of a sum/integral (respectively) over the LGFs of a 1D TB system, weighted by the imaginary part of an appropriate LGF for the $(N-1)$D

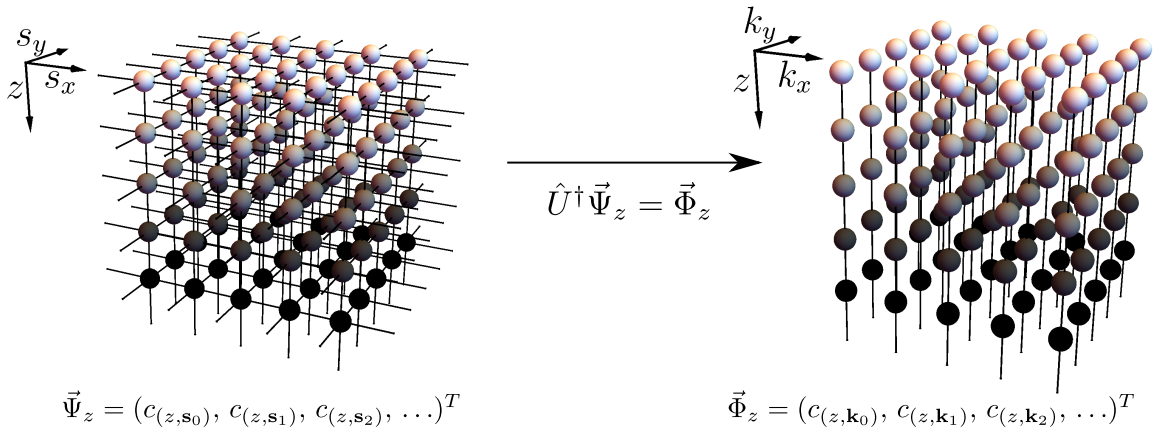

Fig. A.2 Schematic representation of the transformation described in Section A.1 applied the 3D cubic lattice TB Hamiltonian with open boundary conditions in the z direction, given by Eq. A.25, which yields a bundle of uncoupled 1D TB chains described by Eq. A.26.

system, given by Eq. A.14. The 1D LGF to be calculated for the TB system defined by Eq. A.18; by specifying the bounds of the 1D chain index i defined in this Hamiltonian, infinite systems with periodic and open boundary conditions in the one dimension of the ND system may be treated, with the 1D chain LGFs of Eq. A.18 to be calculated. Open boundaries in multiple dimensions of the ND system follow simply by employing $(N-1)$D LGFs for a system with open boundary conditions in Eq. A.16. Finite systems with open boundary conditions may be calculated via Eq. A.13, where the imaginary part of the 1D chain LGF employed is a sum of discrete poles.

In order to illustrate this procedure for higher-dimensional lattices, we consider the (infinite) 3D cubic lattice case (with periodic or open boundary conditions). The general Hamiltonian given by Eq. A.3 becomes

$$\mathcal{H}_N = \sum_{i,z} \epsilon c^\dagger_{(\mathbf{s}_i,z)} c_{(\mathbf{s}_i,z)} + t \sum_{<ij>} \left(c^\dagger_{(\mathbf{s}_i,z)} c_{(\mathbf{s}_j,y)} + \text{H.c.} \right) + t \left(\sum_z c^\dagger_{(\mathbf{s}_i,z)} c_{(\mathbf{s}_i,z+1)} + \text{H.c.} \right) , \tag{A.25}$$

defined in terms of a stack of 2D square lattice planes, indexed by z, where each site in the plane is indexed by $\mathbf{s} = (s_x, s_y)$. Each 2D square lattice plane is diagonalized by the same transformation, as argued in Section A.1. The transformation to a bundle of

uncoupled 1D chains yields

$$\mathcal{H}_{\text{cubic}} = \sum_{\mathbf{k}} \sum_{z} \varepsilon_{\mathbf{k}} \phi^{\dagger}_{(z,\mathbf{k})} \phi_{(z,\mathbf{k})} - \left(t \phi^{\dagger}_{(z+1,\mathbf{k})} \phi_{(z,\mathbf{k})} + \text{H.c.} \right) , \tag{A.26}$$

where the site energies on the $\mathbf{k}$-th chain are given by $\varepsilon_{\mathbf{k}} = \epsilon_0 + 2t(\cos(\mathrm{a}_0 k_x) + \cos(\mathrm{a}_0 k_y))$, and the range of the index z depends on the periodic ($z \in (-\infty, \infty)$) or open ($z \in (0, \infty)$) boundary conditions of the system. This transformation is represented schematically in Figure A.2 for the case of open boundary conditions in the z direction. The LGFs for the 3D cubic lattice are therefore given by Eq. A.16, which becomes

$$\begin{aligned} G_{\text{cub}}(\mathbf{r}, \mathbf{r}', z) = -\pi^{-1} \int_{-\infty}^{\infty} d\omega' \, \text{Im}\, G_{\text{sq}}(\mathbf{s}\,, \mathbf{s}', \omega' + \text{i}0^+) \\ \times G^{\text{1D}}(r_z, r'_z, (\omega - \omega') + \text{i}0^+) \, . \end{aligned} \tag{A.27}$$

where the LGF $G_{\text{sq}}(\mathbf{s}_i, \mathbf{s}_j, \omega' + \text{i}0^+)$ is calculated on the infinite 2D square lattice with periodic boundary conditions, and $G^{\text{1D}}_{\omega'}(r_z, r'_z, z)$ is the 1D LGF between sites z and z' on the 1D TB chain for which the site energies are given by ω'.

This new methodology for the calculation of LGFs for hypercubic lattices is employed in Chapter 3 in the calculation of real-space modulations in the electronic density of states (LDOS), given by the imaginary part of the local LGF at a given site, due to a magnetic impurity embedded on the (100) surface 3D cubic lattice. Such calculations require both the local and non-local LGFs of the impurity-free host, as detailed in Section 3.2.1. By calculating the spatial modulations in LDOS, the QPI may be obtained in direct analogy with the experimental measurement procedure. The low computational cost of this convolution technique for calculation of LGFs allows the LDOS modulations to be simulated on large plaquettes of the surface consisting of several hundred lattice sites, as would be carried out in experiment; using other, more expensive techniques (discussed earlier) to calculate accurately $\sim 100 \times 100$ LGFs for a range of energies would not be possible due to the significant computational cost.

A.3 2D honeycomb LGFs

The simple 2D honeycomb lattice of single-orbital sites is bipartite, consisting two coupled, interpenetrating triangular lattices of "A" and "B" sites. The NN TB 2D honeycomb lattice is commonly employed as a minimal model for graphene, as it (largely) captures the electronic structure at low energies, which is approximately

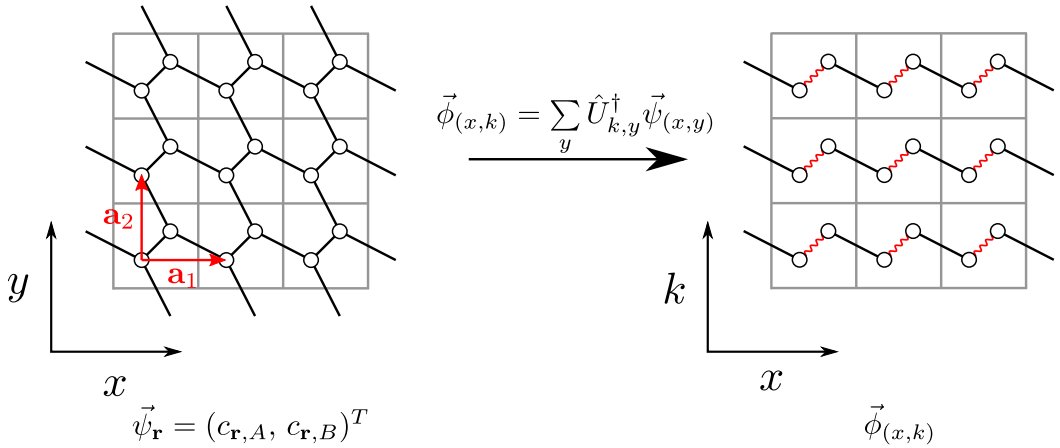

Fig. A.3 Schematic representation of the 2D honeycomb lattice as a square lattice of two-site unit cells, described by Eq. A.28, transformed under partial diagonalization to a bundle of 1D TB chains for which the Hamiltonian is Eq. A.30.

described in terms of massless Dirac fermions [37]. This unusual property of graphene results in a bulk semi-metal, with a vanishing electronic density of states at the Fermi level. In Chapter 3 this is shown to result in non-trivial local-moment physics when a magnetic impurity is adsorbed on the 2D honeycomb lattice; moreover, the sublattice structure results in significant complications in calculating the QPI. There are many other properties of graphene that deviate from those of typical metallic systems as a result of this low-energy electronic structure, for example the transport of heat and current, and the inter-impurity interactions of adsorbed magnetic impurities. The decomposition technique introduced in this appendix offers a numerically inexpensive methodology for calculating the LGFs of the 2D honeycomb lattice, which are of significant importance in the calculation of other dynamical properties of the lattice (such as transport and magnetic interactions).

An alternative spatial representation for the 2D honeycomb lattice, depicted in Figure A.3, consists of a square lattice of unit cells, each containing two orbitals (one A and one B site) of the bipartite lattice; inter-cell coupling is nearest-neighbour only, and so the lattice can be treated using the general approach of Sec. A.1. In this representation, the Hamiltonian for the 2D honeycomb lattice is given by Eq. A.4,

$$\mathcal{H}_{\text{hc}} = \sum_i \left\{ \vec{\psi}^\dagger_{\mathbf{r}_i} \hat{\varepsilon}\ \vec{\psi}_{\mathbf{r}_i} + \sum_{n=1,2} \left(\vec{\psi}^\dagger_{(\mathbf{r}_i+\mathbf{a}_n)} \hat{t}_{\mathbf{a}_n} \vec{\psi}_{\mathbf{r}_i} + \text{H.c.} \right) \right\} \tag{A.28}$$

with $\mathbf{r}_i$ the position of the i-th unit cell and $\vec{\psi}^{\dagger}_{\mathbf{r}_i} = \left(c^{\dagger}_{i,A},\, c^{\dagger}_{i,B}\right)$ such that

$$\hat{\varepsilon} \;= \begin{pmatrix} \epsilon_0 & -t \\ -t & \epsilon_0 \end{pmatrix} \quad \text{and} \quad \hat{t}_{\mathbf{a}_{1,2}} = \begin{pmatrix} 0 & 0 \\ -t & 0 \end{pmatrix} . \tag{A.29}$$

Figure A.3 represents schematically the partial diagonalization of the 2D honeycomb lattice given by Eqs. A.8 and A.9, yielding a bundle of uncoupled 1D TB chains, cf. Eq. A.12, with the Hamiltonian for each chain given by

$$\mathcal{H}_{\mathrm{hc,j}} = \sum_x \vec{\phi}^{\dagger}_{(x,k_j)} \hat{\varepsilon}_{k_j} \vec{\phi}_{(x,k_j)} + \left(\vec{\phi}^{\dagger}_{(x+1,k_j)} \hat{t}\; \vec{\phi}_{(x,k_j)} + \mathrm{H.c.}\right), \tag{A.30}$$

where

$$\hat{\varepsilon}_{k_j} = \begin{pmatrix} \epsilon_0 & -t(1+\mathrm{e}^{-\mathrm{i}\tilde{a}_0 k_j}) \\ -t(1+\mathrm{e}^{\mathrm{i}\tilde{a}_0 k_j}) & \epsilon_0 \end{pmatrix} . \tag{A.31}$$

Eqs. A.30 and A.31 describe a two-site 1D TB chain in which the inter-cell hopping, t_E is constant, while the intra-cell hopping, t_I depends (both magnitude and phase) on k_j. This is a variation on the well-known Su Schrieffer Heeger (SSH) model for polyacetylene [189, 188] in the Born-Oppenheimer limit, where the Peierls instability at half-filling causes dimerization of the single-site 1D TB chain, resulting in alternating hoppings $t_{\pm} = -(t \pm \delta t)$, corresponding to alternating single and double bonds. We emphasize that the transformation of the 2D honeycomb lattice to a bundle of 1D TB chains described by Eq. A.30 is exact, and independent of filling fraction; moreover, the modulation in hopping amplitudes is only in the intracellular hopping, as discussed.

The LGFs for the 2D honeycomb lattice,

$$\mathbf{G}_{\mathrm{hc}}(\mathbf{r},\mathbf{r}',z) = \begin{pmatrix} G^{AA}_{\mathrm{hc}}(\mathbf{r},\mathbf{r}',z) & G^{AB}_{\mathrm{hc}}(\mathbf{r},\mathbf{r}',z) \\ G^{BA}_{\mathrm{hc}}(\mathbf{r},\mathbf{r}',z) & G^{BB}_{\mathrm{hc}}(\mathbf{r},\mathbf{r}',z) \end{pmatrix}, \tag{A.32}$$

can be written via Eq. A.13 in terms of the sum over LGFs for the SSH-like 1D TB chains described by Eq. A.30,

$$\mathbf{G}_{\mathrm{hc}}(\mathbf{r},\mathbf{r}',z) = \sum_{k_j} \mathrm{e}^{\mathrm{i}k_j(r_y - r'_y)} |\vec{\phi}_{(r_x,k_j)}\rangle (zI - \mathcal{H}_{N,j})^{-1} \langle \vec{\phi}_{(r'_x,k_j)}| \,, \tag{A.33}$$

which must now be determined. Considering the A-B sublattice symmetry of the 2D honeycomb lattice, it follows that $G^{AA}_{\mathrm{hc}}(\mathbf{r},\mathbf{r}',z) = G^{BB}_{\mathrm{hc}}(\mathbf{r},\mathbf{r}',z)$ and $G^{AB}_{\mathrm{hc}}(\mathbf{r},\mathbf{r}',z) = G^{BA}_{\mathrm{hc}}(\mathbf{r}',\mathbf{r},z)$. Translational symmetry dictates that $\mathbf{G}_{\mathrm{hc}}(\mathbf{r},\mathbf{r}',z) = \mathbf{G}_{\mathrm{hc}}(\mathbf{0},\mathbf{r}'-\mathbf{r},z)$,

so that calculation of the "AA" and "AB" LGFs for general (positive *and* negative) $\mathbf{R} = \mathbf{r}' - \mathbf{r}$ is sufficient.

A.3.1 LGFs for the 1D TB chain with alternating hopping

Here we consider a 1d lattice in which the unit cell consists of two sites (A and B sites), with an inter-cellular hopping matrix element t_E between neighboring unit cells, an intracellular hopping matrix element t_I and uniform site energies, $\epsilon_A = \epsilon_B = 0$, a generalization of the Su Schrieffer Heeger (SSH) model,

$$\mathcal{H}_{\text{SSH}} = \sum_i \epsilon_0 \left(c^\dagger_{i,A} c_{i,A} + c^\dagger_{i,B} c_{i,B} \right) + \left(t_I c^\dagger_{i,B} c_{i,A} + t_E c^\dagger_{i+1,A} c_{i,B} \right) + \text{H.c.} \,. \tag{A.34}$$

It is necessary to consider t_I and t_E as complex, and thus the $L \to R$ directionality of the hopping amplitudes indicated in Eq. A.34 is emphasized.

Local LGF

Considering an A site in the bulk of the SSH model, the local LGF may be written simply via equations of motion as

$$G_{AA}(x, x, z) = \left[z - |t_I|^2 g(t_E, t_I, z) - |t_E|^2 g(t_I^*, t_E^*, z) \right]^{-1}, \tag{A.35}$$

where $g(t_1, t_2, z)$ is the local LGF for the surface site of a SSH model with open boundary conditions, alternating (complex) hopping matrix elements t_1 and t_2, and uniform site energies (c.f. Eq. A.34). An equations of motion treatment gives $g(t_1, t_2, z)$ in closed form:

$$|t_2| g(t_1, t_2, z) = f_{\text{semi}} \left(\frac{z}{2|t_2|} + Q(t_1, t_2) \frac{2|t_2|}{z} \right), \tag{A.36}$$

where

$$Q(t_1, t_2) = \frac{|t_2|^2 - |t_1|^2}{4|t_2|^2} \tag{A.37}$$

and $f_{\text{semi}}(x)$ is given by Eq. A.22a.

For the retarded LGF ($z = \omega + \mathrm{i}\eta$),

$$\begin{aligned}\frac{z}{2|t_2|} + Q(t_1,t_2)\frac{2|t_2|}{z} =& \frac{\omega}{2|t_2|} + Q(t_1,t_2)\,\mathrm{P}\left(\frac{2|t_2|}{\omega}\right) \\ &+\mathrm{i}\,\frac{\eta/2|t_2|}{(\omega/2|t_2|)^2 + (\eta/2|t_2|)^2}\left(\left(\frac{\omega}{2|t_2|}\right)^2 - Q(t_1,t_2)\right),\end{aligned} \tag{A.38}$$

so that

$$|t_2|g(t_1,t_2,\omega+\mathrm{i}\eta) = \tilde{x} - \begin{cases}\mathrm{sgn}(\tilde{x})\,\mathrm{sgn}(\tilde{\eta})\sqrt{\tilde{x}^2-1} & |\tilde{x}| > 1 \\ \mathrm{i}\left(\sqrt{1-\tilde{x}^2} + \theta(Q(t_1,t_2)) \times \pi\delta(\tilde{x}) \times 2Q(t_1,t_2)\right) & |\tilde{x}| \le 1\end{cases} \tag{A.39}$$

where

$$\tilde{x} = \frac{\omega}{2|t_2|} + Q(t_1,t_2)\,\mathrm{P}\left(\frac{2|t_2|}{\omega}\right) \quad \text{and} \quad \tilde{\eta} = \left(\frac{\omega}{2|t_2|}\right)^2 - Q(t_1,t_2)\,. \tag{A.40}$$

Using these expressions, noting that $|t_2|^2 Q(t_1,t_2) = -|t_1|^2 Q(t_2,t_1)$, Eq. A.35 becomes

$$G_{AA}(x,x,z) = f_{\mathrm{inf}}\left(\frac{z}{2|t_2|} + Q(t_1,t_2)\frac{2|t_2|}{z}\right), \tag{A.41}$$

with $f_{\mathrm{inf}}(x)$ given by Eq. A.22b.

The parameter, $Q(t_1,t_2)$, thus controls the (topological) phase of the SSH system. For $Q(t_1,t_2) = 0$ and, $|t_1| = |t_2|$ and Eqs. A.41 and A.39 reduce to the expressions for local LGF on a single-site 1D TB chain with periodic or open boundary conditions respectively, giving a metallic state; the complex phase of t_I in Eq. A.34 is only relevant in non-local LGFs (considered shortly). $Q(t_1,t_2) < 0$ and $Q(t_1,t_2) > 0$, by contrast, give rise to insulating states, with a gap (whose magnitude is $2\Big||t_2| - |t_1|\Big|$) between conduction and valence bands. For periodic boundary conditions these phases are indistinguishable, but for open boundary conditions, Eq. A.39 reveals a zero-frequency pole in the density of states at the edge (the imaginary part of $g(t_1,t_2,\omega+\mathrm{i}\eta)$) for $Q(t_1,t_2) > 0$ ($|t_1| < |t_2|$). This corresponds to the localized edge state of the SSH model in the topological insulating phase, adiabatically connected to the limiting case of $|t_2| \neq |t_1| = 0$, where the TB chain consists of pairs of dimers with isolated, uncoupled sites at the boundaries of the chain. respectively, giving a metallic state; the complex phase of t_I in Eq. A.34 is only relevant in non-local LGFs (considered shortly). $Q(t_1,t_2) < 0$ and $Q(t_1,t_2) > 0$, by contrast, give rise to insulating states,

with a gap (whose magnitude is $2\big||t_2| - |t_1|\big|$) between conduction and valence bands. For periodic boundary conditions these phases are indistinguishable, but for open boundary conditions, Eq. A.39 reveals a zero-frequency pole in the density of states at the edge (the imaginary part of $g(t_1, t_2, \omega + \mathrm{i}\eta)$) for $Q(t_1, t_2) > 0$ ($|t_1| < |t_2|$). This corresponds to the localized edge state of the SSH model in the topological insulating phase, adiabatically connected to the limiting case of $|t_2| \neq |t_1| = 0$, where the TB chain consists of pairs of dimers with isolated, uncoupled sites at the boundaries of the chain.

Non-local LGFs

Treating the non-local LGFs for the SSH model via equations of motion, the phase and hence directionality of the hopping elements t_I and t_E is important, with

$$\begin{aligned} G_{AB}(x, x, z) &= (t_I g(t_E, t_I, z))\, G_{AA}(x, x, z) \\ G_{BA}(x, x+1, z) &= (t_E g(t_I, t_E, z))\, G_{BB}(x, x, z), \end{aligned} \tag{A.42}$$

while

$$\begin{aligned} G_{AB}(x, x-1, z) &= (t_E^* g(t_I^*, t_E^*, z))\, G_{AA}(x, x, z) \\ G_{BA}(x, x, z) &= (t_I^* g(t_E^*, t_I^*, z))\, G_{BB}(x, x, z). \end{aligned} \tag{A.43}$$

From consideration of the local LGF above, we know that $g(t_1, t_2, z)$ and $G_{AA}(x, x, z)$ are independent of the phase of t_1 and t_2, so that the general expression for the LGFs for the SSH model is given by:

$$G_{AA}(x, x', z) = \mathrm{e}^{\mathrm{i}\phi_{AA}(x,x')} \left(|t_I| g(t_E, t_I, z)\right)^{|x'-x|} \left(|t_E| g(t_I, t_E, z)\right)^{|x'-x|} G_{AA}(x, x, z) \tag{A.44a}$$

$$G_{AB}(x, x', z) = \mathrm{e}^{\mathrm{i}\phi_{AB}(x,x')} \left(|t_I| g(t_E, t_I, z)\right)^{|x'-x|-\theta(x-x')} \left(|t_E| g(t_I, t_E, z)\right)^{|x'-x|-\theta(x'-x)} G_{AA}(x, x, z), \tag{A.44b}$$

with

$$\phi_{AA}(x, x') = (x' - x) \arg(t_I) + (x' - x) \arg(t_E) \tag{A.45a}$$

$$\phi_{AB}(x, x') = (x' - x - \theta(x - x')) \arg(t_I) + (x' - x - \theta(x' - x)) \arg(t_E). \tag{A.45b}$$

Expressions for the local and non-local LGFs for this generalized SSH model reveal that only the phase of the LGF is dependent on the phase of the intra- and inter-cell hopping elements. The zero-frequency pole in $g(t_1, t_2, z)$, corresponding to the edge state of the SSH model with open boundary conditions, also contributes to the non-local LGFs in the case of periodic boundary conditions.

A.3.2 LGFs for the 2D honeycomb lattice

Having found closed-form expressions for the LGFs of the generalized SSH model arising from the partial diagonalization of the 2D honeycomb lattice, the LGFs for the full 2D honeycomb lattice may be written

$$G_{\mathrm{hc}}^{AA(AB)}(\mathbf{r}, \mathbf{r}', z) = \sum_{k_j} \mathrm{e}^{\mathrm{i}k_j(r_y - r'_y)} G_{AA(AB)}(r_x, r'_x, z), \tag{A.46}$$

with $G_{AA(AB)}(r_x, r'_x, z)$ defined by Eqs. A.44 and A.45, and Eq. A.39. From Eqs. A.29 and A.31, $t_I = -t(1 + \exp(\mathrm{i}\tilde{a}_0 k_j))$ and $t_E = -t$ such that $\arg(t_I) = \mathrm{a}_0 k_j/2$ and $\arg(t_E) = 0$, resulting in

$$\phi_{AA}(x, x') = \mathrm{a}_0(x' - x)k_j/2 \tag{A.47a}$$

$$\phi_{AB}(x, x') = \mathrm{a}_0(x' - x - \theta(x - x'))k_j/2\,. \tag{A.47b}$$

Eq. A.46 may therefore be rewritten as

$$G_{\mathrm{hc}}^{AA}(\mathbf{r}, \mathbf{r}', z) = \sum_{k_j} \mathrm{e}^{\mathrm{i}k_j(r_y - r'_y)} \mathrm{e}^{-\mathrm{i}k_j(r_x - r'_x)/2} \times \left(G_{AA}(r_x, r'_x, z) / \mathrm{e}^{\mathrm{i}\phi_{AA}(r_x, r'_x)} \right) \tag{A.48a}$$

$$G_{\mathrm{hc}}^{AB}(\mathbf{r}, \mathbf{r}', z) = \sum_{k_j} \mathrm{e}^{\mathrm{i}k_j(r_y - r'_y)} \mathrm{e}^{-\mathrm{i}k_j(r_x - r'_x - \theta(r_x - r'_x))/2} \times \left(G_{AB}(r_x, r'_x, z) / \mathrm{e}^{\mathrm{i}\phi_{AB}(r_x, r'_x)} \right). \tag{A.48b}$$

We note that the bracketed terms in Eqs. A.48a and A.48b are independent of the phase of t_I. Introducing $\epsilon_{k_j} = 2t\cos(\mathrm{a}_0 k_j)$, we write

$$|t_I| = \sqrt{2}t\sqrt{\cos(\mathrm{a}_0 k_j) + 1} = \sqrt{2}t\sqrt{\frac{\epsilon_{k_j}}{2t} + 1}\,, \tag{A.49}$$

and as such rewrite Eqs. A.48a and A.48b in terms of an integral,

$$G_{\rm hc}^{AA}(\mathbf{r},\mathbf{r}',z) = \int_{-\infty}^{\infty} d\omega' \left\{ \sum_{k_j} \mathrm{e}^{\mathrm{i}k_j[(r_y-r'_y)-(r_x-r'_x)/2]}\delta(\omega-\epsilon_{k_j})\right\} \times \mathfrak{f}_{AA}(r_x,r'_x,z,\omega') \tag{A.50a}$$

$$G_{\rm hc}^{AB}(\mathbf{r},\mathbf{r}',z) = \int_{-\infty}^{\infty} d\omega' \left\{ \sum_{k_j} \mathrm{e}^{\mathrm{i}k_j[(r_y-r'_y)-(r_x-r'_x-\theta(r_x-r'_x))/2]}\delta(\omega-\epsilon_{k_j})\right\} \times \mathfrak{f}_{AB}(r_x,r'_x,z,\omega')\,, \tag{A.50b}$$

for which $\mathfrak{f}_{AA(AB)}(r_x,r'_x,z,\omega') = G_{AA(AB)}(r_x,r'_x,z)/\exp(\mathrm{i}\phi_{AB}(r_x,r'_x))$. The sum over k_j in Eqs. A.50a and A.50b can be evaluated directly (in the thermodynamic limit, where that sum converges to an integral) as the half-integer Chebyshev polynomial of the first kind [2, 60], $T_{n/2}(x)$; for integer values, the Chebyshev polynomials simply give the imaginary parts of the simple, single-site 1D TB chain LGFs, such that $-\pi^{-1}t\mathrm{Im}\; G^{\rm 1D}(r'-r,\omega) = T_{r'-r}(\omega/2t)$. The honeycomb LGFs are therefore evaluated for each value of frequency with $z=\omega+\mathrm{i}\eta$ as

$$G_{\rm hc}^{AA}(\mathbf{r},\mathbf{r}',z) = \int_{-\infty}^{\infty} d\omega'\, T_{[(r_y-r'_y)-(r_x-r'_x)/2]}(\omega'/2t)\mathfrak{f}_{AA}(r_x,r'_x,z,\omega') \tag{A.51a}$$

$$G_{\rm hc}^{AB}(\mathbf{r},\mathbf{r}',z) = \int_{-\infty}^{\infty} d\omega'\, T_{[(r_y-r'_y)-(r_x-r'_x-\theta(r_x-r'_x))/2]}(\omega'/2t)\mathfrak{f}_{AB}(r_x,r'_x,z,\omega')\,. \tag{A.51b}$$

These equations allow the calculation of local and non-local LGFs for the infinite 2D honeycomb lattice, with no significant increase in computational demand for far non-local LGFs. The structure of the calculation is more complex than in the simple, monatomic hypercubic lattice case, and as a result the integrals required (given by Eqs. A.51a and A.51b) are not simple convolutions, and the FFT algorithm cannot be used. However, the calculation of LGFs is still significantly more computationally efficient than direct integration via Eq. A.2. In contrast with recursive calculations of the LGF [117], the method described here is formally in the thermodynamic limit, calculating the LGF for the infinite system. In addition, the technique developed here can be extended to treat the LGFs of the semi-infinite 2D honeycomb lattice and those of a finite-strip or "nanoribbon", treating the open boundary conditions in a manner exactly analogous to that employed in the monatomic hypercubic lattice case. The use of this technique to study the properties of the 2D honeycomb lattice is the subject of future work.

Appendix B

Pinning condition for the Fermi-level spectrum in the AAM

The Anderson Alexander model (AAM) consists of two single-level Anderson impurities coupled to a common conduction band of non-interacting electrons, as introduced in Chapter 4:

$$\mathcal{H}_{AA} = \mathcal{H}_{\text{host}} + \sum_{\alpha=1,2} \sum_{\sigma} \left(\epsilon_d + \frac{U}{2} d^\dagger_{\alpha\bar{\sigma}} d_{\alpha\bar{\sigma}} \right) d^\dagger_{\alpha\sigma} d_{\alpha\sigma} + V \left(d^\dagger_{\alpha\sigma} c_{(\mathbf{r}_\alpha,0)\sigma} + \text{H.c.} \right) . \tag{B.1}$$

We consider the two impurities at particle-hole symmetry, such that $\epsilon_d = -U/2$, here and throughout Chapters 3 and 4; however, these findings are also expected to hold away from particle-hole symmetry, provided the impurities are deep in the singly-occupied regime (with ϵ_d, $U \gg V$). The impurities couple locally to the host conduction band via the (effective) orbital represented by $c_{(\mathbf{r}_\alpha,0)\sigma}$, where $(\mathbf{r}_\alpha, 0)$ denotes the position of the impurity on the surface with $\alpha = 1, 2$, and $\mathbf{r}_1 \neq \mathbf{r}_2$. The impurities are spatially-separated by the vector $\mathbf{R} = \mathbf{r}_2 - \mathbf{r}_1$, so that there is an indirect, host-mediated coupling between the two impurities which depends on the relative position of the two impurities as well as the on-site impurity parameters (the interaction strength U and hybridization strength V). The interplay between local impurity-band and non-local inter-impurity correlations gives rise to several different regimes, detailed in Section 4.2.3, depending on the relative strength and sign of these two effective interactions. Despite this, the ground state of the model is necessarily a Fermi liquid, with the (possible) non-Fermi liquid quantum critical point (present in the simpler 2IKM) destabilized as a result of the inter-channel charge transfer due to the through-lattice coupling between the impurities, as argued in Section 4.2.6. As a result, the

impurity spectral function follows a low-frequency asymptotic form characteristic of a Fermi liquid, given by Eq. 4.16:

$$-\Gamma_0 \mathrm{Im}\; G_d^{11}(\omega) \overset{|\omega|\ll T_\mathrm{K}}{\sim} p - q\left(\frac{\omega}{T_\mathrm{K}}\right)^2 . \tag{B.2}$$

In this appendix, we derive the form of the pinning condition p for the AAM, which differs from the single-impurity result ($p = 1$) away from $|\mathbf{R}| \neq \infty$, the limit that the impurities are infinitely separated.

Considering the matrix Dyson equation for the impurity Green functions,

$$[\mathbf{G}_d(\omega)]^{-1} = (\omega + \mathrm{i}0^+ - \epsilon_d)\mathbf{I} - \mathbf{\Gamma}(\omega) - \mathbf{\Sigma}(\omega)\,, \tag{B.3}$$

where $[\mathbf{G}_d(\omega)]_{\alpha,\beta} = \langle\!\langle d_{\alpha\sigma}; d^\dagger_{\beta\sigma}\rangle\!\rangle_\omega$ are the retarded impurity Green functions between impurity α and β, and $[\mathbf{\Gamma}(\omega)]_{\alpha,\beta} = V^2 G^0_\mathrm{surf}(\mathbf{r}_\alpha, \mathbf{r}_\beta, \omega)$ the hybridization matrix element, given by the "clean" lattice Green function in the absence of impurities between sites $\mathbf{r}_\alpha$ and $\mathbf{r}_\beta$. $\mathbf{\Sigma}(\omega)$ is the self-energy matrix, embodying the effects due to interactions, such that for $U = 0$, $\mathbf{\Sigma}(\omega) = \mathbf{0}$. In the case of a translationally-invariant, inversion-symmetric host, $\Gamma_{11}(\omega) = \Gamma_{22}(\omega) \equiv \Gamma_\mathrm{loc}(\omega)$ and $\Gamma_{12}(\omega) = \Gamma_{21}(\omega) \equiv \Gamma_\mathrm{nl}(\omega)$. As a result, the non-interacting impurity Green function matrix is diagonalized by a transformation to the even/odd basis,

$$c_{e/o\,\sigma}(d_{e/o\,\sigma}) = \frac{1}{\sqrt{2}}\left(c_{\mathbf{r}_1\sigma}(d_{1\sigma}) \pm c_{\mathbf{r}_2\sigma}(d_{1\sigma})\right)\,, \tag{B.4}$$

yielding

$$\mathbf{G}_d(\omega) = \begin{pmatrix} G_{d,e}(\omega) & 0 \\ 0 & G_{d,o}(\omega) \end{pmatrix}\,, \tag{B.5}$$

where

$$[G_{d,p}(\omega)]^{-1} = \omega + \mathrm{i}0^+ - \epsilon_d - \Gamma_p(\omega) - \Sigma_p(\omega)\,, \tag{B.6}$$

for $p = e, o$ such that $\mathcal{O}_{e/o} = \mathcal{O}_{11} \pm \mathcal{O}_{12}$ defines the even/odd combinations for a given quantity. Writing $\mathcal{O}_{e/o}(\omega) = \mathcal{O}^\mathrm{R}_{e/o}(\omega) - \mathrm{i}\mathcal{O}^\mathrm{I}_{e/o}(\omega)$, it follows from Eq. B.6 that

$$-\mathrm{Im}\; G_{d,p}(\omega) = \frac{\Gamma^\mathrm{I}_p(\omega) + \Sigma^\mathrm{I}_p(\omega)}{[\omega - \epsilon_d - \Gamma^\mathrm{R}_p(\omega) - \Sigma^\mathrm{R}_p(\omega)]^2 + [\Gamma^\mathrm{I}_p(\omega) + \Sigma^\mathrm{I}_p(\omega)]^2}\,. \tag{B.7}$$

As the system is in a Fermi liquid phase, $\Sigma_p^{\mathrm{I}}(\omega \to 0) \to 0$ [74], and thus

$$-\Gamma_p^{\mathrm{I}}(\omega=0)\,\mathrm{Im}\;G_{d,p}(\omega=0) = \frac{1}{1+\left[\frac{\epsilon_p^*+\Gamma_p^{\mathrm{R}}(\omega=0)}{\Gamma_p^{\mathrm{I}}(\omega=0)}\right]^2} \leq 1\,, \tag{B.8}$$

with $\epsilon_p^* = \epsilon_d + \Sigma_p^{\mathrm{R}}(\omega=0)$ denoting the renormalized level energy, such that the even/odd impurity spectral function is pinned at the Fermi level, analogous to the Friedel sum rule for a single impurity [74]. Eq. B.8 is a general result for the AAM with a translationally-invariant host, and results from the Fermi liquid nature of the ground state for all parameters. However, the pinning condition in the even and odd channels separately, and are dependent (respectively) on the even and odd impurity renormalized level energies $\epsilon_{e/o}^*$ – themselves related to the (non-trivial) impurity self-energy, which must be calculated by considering the full interacting system, for example via NRG. Relating these pinning conditions in the even/odd basis to one of the form $\mathrm{Im}\;\Gamma_{11}(\omega=0)\,\mathrm{Im}\;G_d^{11}(\omega=0) \sim p - q(\omega/T_{\mathrm{K}})^2$ for the local impurity spectral function is not necessarily straightforward.

For a host material which is particle-hole symmetric, such as the (100) surface 3D cubic lattice employed in Chapter 4, the clean host lattice Green functions have well-defined symmetry with respect to frequency, which depends on the parity of the Manhattan distance $d_{\mathrm{M}}(\mathbf{R}) = R_x + R_y$, such that

$$G_{\mathrm{surf}}^0(\mathbf{R},-\omega) = (-1)^{(d_{\mathrm{M}}(\mathbf{R})+1)}\,G_{\mathrm{surf}}^0(\mathbf{R},\omega)^*\,. \tag{B.9}$$

In Section 4.2.4 it was explained that this well-defined parity symmetry resulted in the effective inter-impurity RKKY interaction being sign-definite with respect the Manhattan distance: impurities separated by an odd Manhattan distance experience an antiferromagnetic RKKY interaction, while even Manhattan distances result in a ferromagnetic RKKY interaction. As a result, the hybridization functions in the local/non-local basis $[\mathbf{\Gamma}(\omega)]_{\alpha,\beta} = V^2 G_{\mathrm{surf}}^0(\mathbf{r}_\alpha, \mathbf{r}_\beta, \omega)$ obey

$$\Gamma_{11}(-\omega) = -\Gamma_{11}(\omega)^*\,, \tag{B.10}$$

while

$$\Gamma_{12}(-\omega) = \begin{cases} -\Gamma_{12}(\omega)^* & d_{\mathrm{M}}(\mathbf{R}) \text{ even} \\ +\Gamma_{12}(\omega)^* & d_{\mathrm{M}}(\mathbf{R}) \text{ odd} \end{cases}\,. \tag{B.11}$$

Considering first the case of even impurity separation, in the even/odd basis, for which $\Gamma_{11}(\omega)$ and $\Gamma_{12}(\omega)$ have the *same* parity with respect to frequency, such that $\Gamma_{e/o}(\omega) = \Gamma_{11}(\omega) \pm \Gamma_{12}(\omega)$ has the same well-defined symmetry and Re $\Gamma_{11/12}(\omega \to 0) \to 0$, so

$$\Gamma_{e/o}(\omega = 0) = 0 + \mathrm{i}\left(\mathrm{Im}\ \Gamma_{11}(\omega) \pm \mathrm{Im}\ \Gamma_{12}(\omega)\right) . \tag{B.12}$$

In the non-interacting limit (particle-hole symmetric, such that $U = -\epsilon_d/2 = 0$), the impurity Green function, given by Eq. B.6, is given in terms of functions whose real (imaginary) parts are odd (even) with respect to frequency, and thus the real (imaginary) parts of $G^0_{d,e/o}(\omega)$ are themselves odd (even) in frequency. Introducing interactions does not break this well-defined symmetry, and the renormalized level energy $\epsilon^*_{e/o} = \epsilon_d + \Sigma^{\mathrm{R}}_{e/o}(\omega)$ therefore vanishes at the Fermi level, while $\Sigma^{\mathrm{I}}_{e/o}(\omega \to 0) \to 0$ in keeping with the Fermi-liquid nature of the ground state. Inspecting Eq. B.8, all dynamic terms in the denominator therefore vanish at the Fermi level, so that the pinning condition is simply $-\Gamma^{\mathrm{I}}_{e/o}(\omega = 0)\mathrm{Im}\ G_{d,e/o}(\omega = 0) = 1$. Defining $\Gamma_0 = V^2\rho_0 = -\mathrm{Im}\ \Gamma_{11}(\omega = 0)$, in terms of the local conduction band Fermi level density of states ρ_0 at each impurity, the local impurity spectral function is therefore

$$\begin{aligned} -\Gamma_0 \mathrm{Im}\ G^{11}_d(\omega = 0) &= -\frac{1}{2}\Gamma_0 \mathrm{Im}\left[G_{d,e}(\omega = 0) + G_{d,o}(\omega = 0)\right] \\ &= \frac{1}{2}\mathrm{Im}\ \Gamma_{11}(0)\left[\frac{1}{\mathrm{Im}\ \Gamma_{11}(0) + \mathrm{Im}\ \Gamma_{12}(0)} + \frac{1}{\mathrm{Im}\ \Gamma_{11}(0) - \mathrm{Im}\ \Gamma_{12}(0)}\right] . \end{aligned} \tag{B.13}$$

For even impurity separation, we find that the pinning condition for the local impurity spectral function is in fact related solely to the non-interacting hybridization functions,

$$\begin{aligned} -\Gamma_0\, \mathrm{Im}\ G^{11}_d(\omega = 0) &= \frac{\mathrm{Im}\ \Gamma_{11}(0)^2}{\mathrm{Im}\ \Gamma_{11}(0)^2 - \mathrm{Im}\ \Gamma_{12}(0)^2} \\ &= \frac{1}{1 - \frac{\mathrm{Im}\ \Gamma_{12}(0)^2}{\mathrm{Im}\ \Gamma_{11}(0)}} \geq 1 . \end{aligned} \tag{B.14}$$

In particular, we note that the value of the (appropriately scaled) impurity spectral function at the Fermi level can exceed the unitary limit that holds in the single-impurity case; such behaviour is indeed seen for $\mathbf{R}/\mathrm{a}_0 = (1, 1)$ in Figure 4.4.

In the case of odd impurity separation, $\Gamma_{11}(\omega)$ and $\Gamma_{12}(\omega)$ have *different* parity with respect to frequency, such that $\Gamma_{e/o}(\omega) = \Gamma_{11}(\omega) \pm \Gamma_{12}(\omega)$ have a more complicated

symmetry in frequency. Instead $\Gamma_o(\omega) = -\Gamma_e(-\omega)^*$ and Im $\Gamma_{12}(\omega \to 0) \to 0$, so that

$$\Gamma^{\mathrm{I}}_{e/o}(\omega = 0) = -\mathrm{Im}\ \Gamma_{11}(\omega) \quad \text{and} \quad \Gamma^{\mathrm{R}}_{e/o}(\omega = 0) = \mathrm{Re}\ \Gamma_{12}(\omega)\,. \tag{B.15}$$

The renormalized level energy for the even/odd impurity is $\epsilon^*_{e/o} = \epsilon_d + \Sigma^{\mathrm{R}}_{e/o}(\omega) = \epsilon_d + \mathrm{Re}[\Sigma_{11}(\omega) + \Sigma_{12}(\omega)]$. At the Fermi level, it is known that $\epsilon_d + \mathrm{Re}\ \Sigma_{11}(\omega = 0) = 0$ at particle-hole symmetry in analogy to the single-impurity case (and confirmed via NRG calculations). The even/odd impurity renormalized level energy is therefore given by

$$\epsilon^*_{e/o} \overset{\omega \to 0}{=} \pm \mathrm{Re}\ \Sigma_{12}(\omega = 0) \equiv \epsilon^*\,. \tag{B.16}$$

The even/odd impurity spectral functions are therefore subject to a pinning condition, Eq. B.8, such that

$$-\Gamma^{\mathrm{I}}_{e/o}(\omega = 0)\,\mathrm{Im}\ G_{d,e/o}(\omega = 0) = \frac{1}{1 + \left[\frac{\pm\epsilon^* \pm \mathrm{Re}\ \Gamma_{12}(0)}{\mathrm{Im}\ \Gamma_{11}(0)}\right]^2}\,; \tag{B.17}$$

considering the local impurity spectral function, with $\Gamma_0 = -\mathrm{Im}\ \Gamma_{11}(\omega = 0)$ as before, we find

$$\begin{aligned} -\Gamma_0\,\mathrm{Im}\ G_{11}(\omega = 0) &= -\frac{1}{2}\Gamma_0\,\mathrm{Im}\left[G_{d,e}(\omega = 0) + G_{d,e}(\omega = 0)\right] \\ &= \frac{1}{1 + \left[\frac{\epsilon^* + \mathrm{Re}\ \Gamma_{12}(0)}{\mathrm{Im}\ \Gamma_{11}(0)}\right]^2} \leq 1\,. \end{aligned} \tag{B.18}$$

For odd impurity separations, the spectral pinning condition given by Eq. B.18 depends on the strength of interactions via the renormalized level energy, which does not vanish due to the non-local self-energy contribution Re $\Sigma_{12}(\omega = 0)$, and as such must be determined for the full interacting system, for example via NRG calculations. This pinning condition in the odd-separation case, for which the RKKY interaction is antiferromagnetic is analogous to a similar effect found in the simpler two-impurity Anderson model with featureless hybridization functions and a direct inter-impurity hopping, described in Ref. 86. For both even and odd impurity separation (corresponding to antiferromagnetic and ferromagnetic effective RRKY interactions) the independent impurity limit $|\mathbf{R}| \to \infty$ recovers the single-impurity pinning condition, as $\Gamma_{12}(\omega) \to 0$ and $\Sigma_{12}(\omega) \to 0$.

References

[1] E. Abrahams. "Kondo effect, one and two Kondo impurities: implications for the lattice problem". In: *J. Magn. Magn. Mater.* **63** (1987), pp. 234–238 (cit. on pp. 82, 91).

[2] M. Abramowitz and I. A. Stegun. *Handbook of mathematical functions*. 1964, p. 958 (cit. on p. 180).

[3] I. Affleck, L. Borda, and H. Saleur. "Friedel oscillations and the Kondo screening cloud". In: *Phys. Rev. B* **77** (2008), p. 180404 (cit. on p. 101).

[4] I. Affleck and A. W. W. Ludwig. "Exact critical theory of the two-impurity Kondo model". In: *Phys. Rev. Lett.* **68** (1992), pp. 1046–1049 (cit. on pp. 82, 102, 103).

[5] I. Affleck, A. W. W. Ludwig, and B. A. Jones. "Conformal-field-theory approach to the two-impurity Kondo problem: Comparison with numerical renormalization-group results". In: *Phys. Rev. B* **52** (1995), pp. 9528–9546 (cit. on pp. 82, 83, 88, 91, 92, 102, 103).

[6] Y. Aiura et al. "Kink in the dispersion of layered strontium ruthenates". In: *Phys. Rev. Lett.* **93** (2004), p. 117005 (cit. on pp. 145, 152).

[7] A. Akbari and P. Thalmeier. "Multiorbital and hybridization effects in the quasiparticle interference of the triplet superconductor Sr_2RuO_4". In: *Phys. Rev. B* **88** (2013), p. 134519 (cit. on pp. 35, 123, 159).

[8] S. Alexander and P. W. Anderson. "Interaction between localized states in metals". In: *Phys. Rev.* **133** (1964), A1594–A1603 (cit. on pp. 81, 82).

[9] M. P. Allan et al. "Imaging Cooper pairing of heavy fermions in $CeCoIn_5$". In: *Nat. Phys.* **9** (2013), p. 14 (cit. on p. 145).

[10] M. P. Allan et al. "Identifying the 'fingerprint' of antiferromagnetic spin fluctuations in iron pnictide superconductors". In: *Nat. Phys.* **11** (2014), pp. 177–182 (cit. on pp. 20, 24, 145, 152).

[11] A. Allerdt et al. "Kondo versus indirect exchange: the role of the lattice and the actual range of RKKY interactions in real materials". In: *Phys. Rev. B* **91** (2015), p. 085101 (cit. on pp. 82, 83, 88, 100).

[12] F. B. Anders and A. Schiller. "Real-time dynamics in quantum-impurity systems: a time-dependent numerical renormalization-group approach". In: *Phys. Rev. Lett.* **95** (2005), p. 196801 (cit. on pp. 36, 77, 86).

[13] B. M. Andersen and P. J. Hirschfeld. "Extinction of quasiparticle interference in underdoped cuprates with coexisting order". In: *Phys. Rev. B* **79** (2009), p. 144515 (cit. on p. 149).

[14] P. W. Anderson. "Localized magnetic states in metals". In: *Phys. Rev.* **124** (1961), pp. 41–53 (cit. on pp. 31, 33).

[15] P. W. Anderson. "A poor man's derivation of scaling laws for the Kondo problem". In: *J. Phys. C* **3** (1970), p. 2346 (cit. on p. 92).

[16] P. W. Anderson and W. F. Brinkman. "Anisotropic superfluidity in ^{3}He: a possible interpretation of its stability as a spin-fluctuation effect". In: *Phys. Rev. Lett.* **30** (1973), pp. 1108–1111 (cit. on p. 127).

[17] P. W. Anderson and P. Morel. "Generalized Bardeen-Cooper-Schrieffer states and the proposed low-temperature phase of liquid ^{3}He". In: *Phys. Rev.* **123** (1961), pp. 1911–1934 (cit. on p. 127).

[18] M. Berciu. "On computing the square lattice Green's function without any integrations". In: *J. Phys. A: Mathematical and Theoretical* **42** (2009), p. 395207 (cit. on pp. 40, 166).

[19] M. Berciu and A. M. Cook. "Efficient computation of lattice Green's functions for models with nearest-neighbour hopping". In: *Europhys. Lett.* **92** (2010), p. 40003 (cit. on pp. 40, 166, 171).

[20] C. Bergemann et al. "Quasi-two-dimensional Fermi liquid properties of the unconventional superconductor Sr_2RuO_4". In: *Adv. Phys.* **52** (2003), pp. 639–725 (cit. on pp. 123, 124, 127, 128, 145, 150).

[21] S. Biermann et al. "Deconfinement transition and Luttinger to Fermi liquid crossover in quasi-one-dimensional systems." In: *Phys. Rev. Lett.* **87** (2001), p. 276405 (cit. on p. 150).

[22] G. Binnig and H. Rohrer. "Scanning tunneling microscopy". In: *Physica B+C* **127** (1984), pp. 37–45 (cit. on p. 5).

[23] G. Binnig and H. Rohrer. "Scanning tunneling microscopy — from birth to adolescence". In: *Rev. Mod. Phys.* **59** (1987), pp. 615–625 (cit. on p. 5).

[24] M. Bode et al. "Imaging magnetic nanostructures by spin-polarized scanning tunneling spectroscopy". In: *J. Electron. Spectrosc. Relat. Phenom.* **114-116** (2001), pp. 1055–1062 (cit. on p. 22).

[25] D. A. Bonnell. *Scanning probe microscopy and spectroscopy : theory, techniques, and applications*. Wiley-VCH, 2001, p. 493 (cit. on p. 6).

[26] A. Bouhon and M. Sigrist. "Current inversion at the edges of a chiral p-wave superconductor". In: *Phys. Rev. B* **90** (2014), 220511(R) (cit. on p. 129).

[27] I. Brihuega et al. "Quasiparticle chirality in epitaxial graphene probed at the nanometer scale". In: *Phys. Rev. Lett.* **101** (2008), p. 206802 (cit. on p. 38).

[28] R. Bulla, A. C. Hewson, and T. Pruschke. "Numerical renormalization group calculations for the self-energy of the impurity Anderson model". In: *J. Phys. Condens. Matter* **10** (1998), p. 8365 (cit. on pp. 36, 86).

[29] R. Bulla, T. A. Costi, and T. Pruschke. "Numerical renormalization group method for quantum impurity systems". In: *Rev. Mod. Phys.* **80** (2008), pp. 395–450 (cit. on pp. 27, 33, 36, 37, 74, 77, 84, 85, 89).

[30] R. Bulla et al. "The soft-gap Anderson model: comparison of renormalization group and local moment approaches". In: *J. Phys. Condens. Matter* **12** (2000), p. 4899 (cit. on p. 34).

[31] C. A. Busser, G. B. Martins, and A. E. Feiguin. "Lanczos transformation for quantum impurity problems in $d-$dimensional lattices: application to graphene nanoribbons". In: *Phys. Rev. B* **88** (2013), p. 245113 (cit. on p. 33).

[32] C. Büsser et al. "Numerical analysis of the spatial range of the Kondo effect". In: *Phys. Rev. B* **81** (2010), p. 45111 (cit. on p. 101).

[33] V. Campo and L. Oliveira. "Thermodynamics for the two-impurity Kondo model". In: *Phys. Rev. B* **70** (2004), p. 153401 (cit. on pp. 83, 92).

[34] L. Capriotti, D. J. Scalapino, and R. D. Sedgewick. "Wave-vector power spectrum of the local tunneling density of states: Ripples in a $d-$wave sea". In: *Phys. Rev. B* **68** (2003), p. 014508 (cit. on pp. 16, 17, 31, 32, 39, 46, 47, 71, 75, 115, 134, 154, 155).

[35] J. P. Carbotte, T. Timusk, and J. Hwang. "Bosons in high-temperature superconductors: an experimental survey". In: *Rep. Prog. Phys.* **74** (2011), p. 066501 (cit. on p. 152).

[36] E. W. Carlson et al. "Dimensional crossover in quasi-one-dimensional and high-T_c superconductors". In: *Phys. Rev. B* **62** (2000), pp. 3422–3437 (cit. on p. 150).

[37] A. H. Castro Neto et al. "The electronic properties of graphene". In: *Rev. Mod. Phys.* **81** (2009), pp. 109–162 (cit. on pp. 35, 44, 56, 174).

[38] C. J. Chen. *Introduction to scanning tunneling microscopy*. Oxford University Press, 2007, p. 423 (cit. on pp. 6, 22).

[39] T. A. Costi et al. "Kondo decoherence: finding the right spin model for iron impurities in gold and silver". In: *Phys. Rev. Lett.* **102** (2009) (cit. on pp. 33, 81).

[40] M. F. Crommie. "Observing electronic scattering in atomic-scale structures on metals". In: *J. Electron. Spectrosc. Relat. Phenom.* **109** (2000), pp. 1–17 (cit. on p. 6).

[41] M. F. Crommie, C. P. Lutz, and D. M. Eigler. "Confinement of electrons to quantum corrals on a metal surface". In: *Science* **262** (1993), pp. 218–220 (cit. on pp. 6, 7).

[42] M. F. Crommie, C. P. Lutz, and D. M. Eigler. "Imaging standing waves in a two-dimensional electron gas". In: *Nature* **363** (1993), p. 524 (cit. on pp. 6, 16).

[43] J. Cserti. "Application of the lattice Green's function for calculating the resistance of an infinite network of resistors". In: *Am. J. Phys.* **68** (2000), pp. 896–906 (cit. on pp. 40, 165).

[44] P. J. Curran et al. "Search for spontaneous edge currents and vortex imaging in Sr_2RuO_4 mesostructures". In: *Phys. Rev. B* **89** (2014), p. 144504 (cit. on p. 128).

[45] E. G. Dalla Torre et al. "Friedel oscillations as a probe of fermionic quasiparticles". In: *Phys. Rev. B* **93** (2016), p. 205117 (cit. on pp. 26, 71, 73).

[46] A. Damascelli, Z. Hussain, and Z. Shen. "Angle-resolved photoemission studies of the cuprate superconductors". In: *Rev. Mod. Phys.* **75** (2003), pp. 473–541 (cit. on p. 8).

[47] A. Damascelli et al. "Fermi surface, surface states, and surface reconstruction in Sr_2RuO_4". In: *Phys. Rev. Lett.* **4** (2000), p. 4 (cit. on pp. 122, 126, 134, 143, 145).

[48] P. G. Derry, A. K. Mitchell, and D. E. Logan. "Quasiparticle interference from magnetic impurities". In: *Phys. Rev. B* **92** (2015), p. 035126 (cit. on pp. 20, 27, 32, 77, 80, 90, 106, 107, 109).

[49] S. Doniach. "The Kondo lattice and weak antiferromagnetism". In: *Physica B+C* **91** (1977), pp. 231–234 (cit. on pp. 81, 94).

[50] H. E. Ekström and H. P. Myers. "The magnetic susceptibility of dilute CuFe alloys in the temperature range 1.7–300 K". In: *Physik der Kondensierten Materie* **14** (1972), pp. 265–274 (cit. on p. 112).

[51] L. M. Falicov and F. Yndurain. "Model calculation of the electronic structure of a (111) surface in a diamond-structure solid". In: *J. Phys. C: Solid State Physics* **8** (1975), p. 147 (cit. on p. 40).

[52] R. M. Feenstra, J. A. Stroscio, and A. P. Fein. "Tunneling spectroscopy of the Si(111)2 x 1 surface". In: *Surf. Sci.* **181** (1987), pp. 295–306 (cit. on pp. 6, 31, 38, 133).

[53] I. A. Firmo et al. "Evidence from tunneling spectroscopy for a quasi-one-dimensional origin of superconductivity in Sr_2RuO_4". In: *Phys. Rev. B* **88** (2013), p. 134521 (cit. on pp. 20, 121, 123, 128, 134).

[54] K. Fischer. "Absence of two energy scales in the two-impurity Kondo model". In: *Phys. Rev. B* **57** (1998), R6771–R6774 (cit. on p. 93).

[55] O. Fischer et al. "Scanning tunneling spectroscopy of high-temperature superconductors". In: *Rev. Mod. Phys.* **79** (2007), pp. 353–419 (cit. on pp. 14, 27, 38, 145).

[56] L. Fritz and M. Vojta. "The physics of Kondo impurities in graphene". In: *Rep. Prog. Phys.* **76** (2013), p. 32501 (cit. on pp. 34, 35, 50, 60).

[57] J. Gan. "Solution of the two-impurity Kondo model: critical point, Fermi-liquid phase, and crossover". In: *Phys. Rev. B* **51** (1995), pp. 8287–8309 (cit. on pp. 102, 103).

[58] J. Gan. "Mapping the critical point of the two-impurity Kondo model to a two-channel problem". In: *Phys. Rev. Lett.* **74** (1995), pp. 2583–2586 (cit. on p. 102).

[59] Y. Gao et al. "Probing active/passive bands by quasiparticle interference in Sr_2RuO_4". In: *Phys. Rev. B* **88** (2013), p. 094514 (cit. on pp. 123, 159).

[60] J. García Ravelo et al. "Chebyshev functions of half-integer order". In: *Integral Transforms and Special Functions* **18** (2007), pp. 743–749 (cit. on p. 180).

[61] S. Gardonio et al. "Excitation spectra of transition-metal atoms on the Ag (100) surface controlled by Hund's exchange". In: *Phys. Rev. Lett.* **110** (2013), p. 186404 (cit. on p. 33).

[62] A. Georges et al. *Dynamical mean-field theory of strongly correlated fermion systems and the limit of infinite dimensions*. 1996 (cit. on p. 27).

[63] M. T. Glossop and D. E. Logan. "Magnetic impurities in gapless Fermi systems: perturbation theory". In: *Eur. Phys. J. B* **13** (2000), pp. 513–525 (cit. on p. 50).

[64] M. T. Glossop and D. E. Logan. "Single-particle dynamics of the Anderson model: a local moment approach". In: *J. Phys. Condens. Matter* **14** (2002), p. 6737 (cit. on pp. 61, 77, 96).

[65] C. Gonzalez-Buxton and K. Ingersent. "Renormalization-group study of Anderson and Kondo impurities in gapless Fermi systems". In: *Phys. Rev. B* **57** (1998), pp. 14254–14293 (cit. on pp. 33, 34, 49, 50, 60).

[66] H. M. Guo and M. Franz. "Theory of quasiparticle interference on the surface of a strong topological insulator". In: *Phys. Rev. B* **81** (2010), p. 041102 (cit. on pp. 23, 67).

[67] A. J. Guttmann. "Lattice Green's functions in all dimensions". In: *J. Phys. A: Mathematical and Theoretical* **43** (2010), p. 305205 (cit. on pp. 40, 165).

[68] C. V. Haesendonck, J. Vranken, and Y. Bruynseraede. "Resonant Kondo scattering of weakly localized electrons". In: *Phys. Rev. Lett.* **58** (1987), pp. 1968–1971 (cit. on p. 112).

[69] M. Hanl et al. "Iron impurities in gold and silver: comparison of transport measurements to numerical renormalization group calculations exploiting non-Abelian symmetries". In: *Phys. Rev. B* **88** (2013) (cit. on pp. 33, 81, 110).

[70] M. Hanson. "Magnetic susceptibility and single-impurity effects in dilute AgMn alloys". In: *J. Phys. F: Metal Physics* **8** (1978), pp. 1225–1242 (cit. on p. 112).

[71] R. Haydock, V. Heine, and M. J. Kelly. "Electronic structure based on the local atomic environment for tight-binding bands". In: *J. Phys. C: Solid State Physics* **5** (1972), p. 2845 (cit. on pp. 40, 166).

[72] R. Haydock, V. Heine, and M. J. Kelly. "Electronic structure based on the local atomic environment for tight-binding bands. II". In: *J. Phys. C: Solid State Physics* **8** (1975), pp. 2591–2605 (cit. on pp. 40, 166).

[73] A. Heinrich and S. Loth. "A logical use for atoms". In: *Science* **332** (2011), pp. 1039–1040 (cit. on p. 32).

[74] A. C. Hewson. *The Kondo Problem to Heavy Fermions*. Cambridge University Press, 1997 (cit. on pp. 7, 27, 31, 32, 35, 49, 60, 61, 63, 64, 74, 77, 81, 82, 90, 93, 94, 96, 99, 183).

[75] C. W. Hicks et al. "Limits on superconductivity-related magnetization in Sr_2RuO_4 and $PrOs_4Sb_{12}$ from scanning SQUID microscopy". In: *Phys. Rev. B* **81** (2010), p. 214501 (cit. on p. 128).

[76] P. J. Hirschfeld, M. M. Korshunov, and I. I. Mazin. "Gap symmetry and structure of Fe-based superconductors". In: *Rep. Prog. Phys.* **74** (2011), p. 124508 (cit. on p. 24).

[77] P. J. Hirschfeld et al. "Robust determination of the superconducting gap sign structure via quasiparticle interference". In: *Phys. Rev. B* **92** (2015) (cit. on pp. 9, 20, 24, 132, 154, 155).

[78] J. E. Hoffman et al. "Imaging quasiparticle interference in $Bi_2Sr_2CaCu_2O_{8+\delta}$". In: *Science* **297** (2002), pp. 1148–1151 (cit. on pp. 9, 14, 20, 25, 27, 35, 38, 39, 54, 64, 66, 72, 122, 145).

[79] C. Howald et al. "Periodic density-of-states modulations in superconducting $Bi_2Sr_2CaCu_2O_{8+\delta}$". In: *Phys. Rev. B* **67** (2003), p. 14533 (cit. on pp. 27, 38, 145).

[80] L. Huang, T. O. Wehling, and P. Werner. "Electronic excitation spectra of the five-orbital Anderson impurity model: from the atomic limit to itinerant atomic magnetism". In: *Phys. Rev. B* **89** (2014), p. 245104 (cit. on p. 33).

[81] C. M. Hurd. "Further evidence of Nagaoka's bound state for conduction electrons in dilute alloys". In: *Phys. Rev. Lett.* **18** (1967), pp. 1127–1129 (cit. on p. 112).

[82] N. J. C. Ingle et al. "Quantitative analysis of Sr_2RuO_4 angle-resolved photoemission spectra: Many-body interactions in a model Fermi liquid". In: *Phys. Rev. B* **72** (2005), p. 205114 (cit. on pp. 127, 145).

[83] K. Ishida et al. "Spin-triplet superconductivity in Sr_2RuO_4 identified by ^{17}O Knight shift". In: *Nature* **396** (1998), pp. 658–660 (cit. on p. 127).

[84] H. Iwasawa et al. "Orbital selectivity of the kink in the dispersion of Sr_2RuO_4". In: *Phys. Rev. B* **72** (2005), p. 104514 (cit. on p. 145).

[85] H. Iwasawa et al. "Interplay among Coulomb interaction, spin-orbit interaction, and multiple electron-boson interactions in Sr_2RuO_4". In: *Phys. Rev. Lett.* **105** (2010), p. 226406 (cit. on pp. 127, 145, 152).

[86] W. Izumida and O. Sakai. "Two-impurity Kondo effect in double-quantum-dot systems: effect of interdot kinetic exchange coupling". In: *Phys. Rev. B* **62** (2000), pp. 10260–10267 (cit. on p. 185).

[87] C. Jayaprakash, H. R. Krishna-murthy, and J. W. Wilkins. "Two-impurity Kondo problem". In: *Phys. Rev. Lett.* **47** (1981), pp. 737–740 (cit. on pp. 78, 82, 86, 91, 92).

[88] C. Jayaprakash, H. R. Krishna-murthy, and J. W. Wilkins. "Thermodynamic scaling theory for the two-impurity Anderson model". In: *J. Appl. Phys.* **53** (1982), pp. 2142–2144 (cit. on p. 93).

[89] F. Jayatilaka, M. Galpin, and D. Logan. "Two-channel Kondo physics in tunnel-coupled double quantum dots". In: *Phys. Rev. B* **84** (2011), p. 115111 (cit. on pp. 83, 84, 103).

[90] B. A. Jones and C. M. Varma. "Study of two magnetic impurities in a Fermi gas". In: *Phys. Rev. Lett.* **58** (1987), pp. 843–846 (cit. on pp. 78, 82, 86, 91, 92).

[91] B. A. Jones and C. M. Varma. "Critical point in the solution of the two magnetic impurity problem". In: *Phys. Rev. B* **40** (1989), pp. 324–329 (cit. on pp. 82, 102).

[92] B. A. Jones, C. M. Varma, and J. W. Wilkins. "Low-temperature properties of the two-impurity Kondo Hamiltonian". In: *Phys. Rev. Lett.* **61** (1988), pp. 125–128 (cit. on pp. 81, 83).

[93] W. J. Kaiser and R. C. Jaklevic. "Scanning tunneling microscopy study of metals: Spectroscopy and topography". In: *Surf. Sci.* **181** (1987), pp. 55–68 (cit. on p. 6).

[94] C. Kallin and A. J. Berlinsky. "Is Sr_2RuO_4 a chiral p-wave superconductor?" In: *J. Phys. Condens. Matter* **21** (2009), p. 164210 (cit. on p. 128).

[95] C. Kallin. "Chiral p-wave order in Sr_2RuO_4". In: *Rep. Prog. Phys.* **75** (2012), p. 042501 (cit. on pp. 122, 127, 153).

[96] T. Kasuya. "A theory of metallic ferro-and antiferromagnetism on Zener's model". In: *Progr. Theor. Phys.* **16** (1956), pp. 45–57 (cit. on pp. 81, 82).

[97] S. Katsura et al. "Lattice Green's function: introduction". In: *J. Math. Phys.* **12** (1971), pp. 892–895 (cit. on pp. 40, 165).

[98] A. A. Khajetoorians et al. "Realizing all-spin-based logic operations atom by atom". In: *Science* **332** (2011), pp. 1062–4 (cit. on p. 32).

[99] N. Kikugawa et al. "Effects of in-plane impurity substitution in Sr_2RuO_4". In: *J. Phys. Soc. Jpn.* **72** (2003), pp. 237–240 (cit. on pp. 136, 138).

[100] C. Kim et al. "Self-energy analysis of multiple-bosonic mode coupling in Sr_2RuO_4". In: *J. Phys. Chem. Solids*. Vol. 72. 2011, pp. 556–558 (cit. on p. 145).

[101] N. Knorr et al. "Kondo effect of single Co adatoms on Cu surfaces". In: *Phys. Rev. Lett.* **88** (2002), p. 96804 (cit. on pp. 90, 100, 112).

[102] O. Kodra and W. A. Atkinson. "Many-impurity effects in Fourier transform scanning tunneling spectroscopy". In: *Phys. Rev. B* **73** (2006), p. 45404 (cit. on pp. 46, 47, 71, 75, 115).

[103] A. Kogar et al. "Temperature-resolution anomalies in the reconstruction of time dynamics from energy-loss experiments". In: *J. Phys. B: Atomic, Molecular and Optical Physics* **47** (2014), p. 124034 (cit. on p. 145).

[104] G. Kotliar and D. Vollhardt. "Strongly correlated materials: insights from dynamical mean-field theory". In: *Physics Today* **57** (2004), p. 53 (cit. on p. 27).

[105] G. Kotliar et al. "Electronic structure calculations with dynamical mean-field theory". In: *Rev. Mod. Phys.* **78** (2006), pp. 865–951 (cit. on p. 27).

[106] A. Kreisel et al. "Interpretation of scanning tunneling quasiparticle interference and impurity states in cuprates". In: *Phys. Rev. Lett.* **114** (2015), p. 217002 (cit. on pp. 25, 26, 71, 73–75, 140, 141).

[107] H. R. Krishna-Murthy and C. Jayaprakash. "Thermodynamic scaling theory for impurities in metals". In: *Phys. Rev. B* **30** (1984), pp. 2806–2827 (cit. on p. 93).

[108] H. R. Krishnamurthy, J. W. Wilkins, and K. G. Wilson. "Renormalization-group approach to the Anderson model of dilute magnetic alloys. I. Static properties for the symmetric case". In: *Phys. Rev. B* **21** (1980), pp. 1003–1043 (cit. on pp. 36, 77, 84, 89).

[109] H. R. Krishna-murthy, J. W. Wilkins, and K. G. Wilson. "Renormalization-group approach to the Anderson model of dilute magnetic alloys. II. Static properties for the asymmetric case". In: *Phys. Rev. B* **21** (1980), pp. 1044–1083 (cit. on pp. 36, 84).

[110] D. C. Langreth. "Friedel sum rule for Anderson's model of localized impurity states". In: *Phys. Rev.* **150** (1966), pp. 516–518 (cit. on p. 96).

[111] A. Lanzara et al. "Evidence for ubiquitous strong electron-phonon coupling in high-temperature superconductors." In: *Nature* **412** (2001), pp. 510–514 (cit. on p. 152).

[112] B. Lechtenberg and F. B. Anders. "Spatial and temporal propagation of Kondo correlations". In: *Phys. Rev. B* **90** (2014), p. 045117 (cit. on pp. 82, 86, 88, 93).

[113] S. Lederer et al. "Suppression of spontaneous currents in Sr_2RuO_4 by surface disorder". In: *Phys. Rev. B* **90** (2014), pp. 1–6 (cit. on p. 129).

[114] J. J. Lee et al. "Significant T_c enhancement in FeSe films on $SrTiO_3$ due to anomalous interfacial mode coupling". In: *Nature* **515** (2014), p. 245 (cit. on p. 152).

[115] J. Lee et al. "Heavy *d*-electron quasiparticle interference and real-space electronic structure of $Sr_3Ru_2O_7$". In: *Nat. Phys.* **5** (2009), pp. 1–5 (cit. on p. 121).

[116] W. C. Lee, D. P. Arovas, and C. Wu. "Quasiparticle interference in the unconventional metamagnetic compound $Sr_3Ru_2O_7$". In: *Phys. Rev. B* **81** (2010), p. 184403 (cit. on pp. 121, 143).

[117] C. H. Lewenkopf and E. R. Mucciolo. "The recursive Green's function method for graphene". In: *J. Comput. Electron.* **12** (2013), pp. 203–231 (cit. on p. 180).

[118] J. Li et al. "Kondo scattering observed at a single magnetic impurity". In: *Phys. Rev. Lett.* **80** (1998), pp. 2893–2896 (cit. on pp. 6, 32, 33, 77).

[119] C.-Y. Lin, A. H. Castro Neto, and B. A. Jones. "First-principles calculation of the single impurity surface Kondo resonance". In: *Phys. Rev. Lett.* **97** (2006), p. 156102 (cit. on pp. 49, 90).

[120] Q. Liu, X. L. Qi, and S. C. Zhang. "Stationary phase approximation approach to the quasiparticle interference on the surface of a strong topological insulator". In: *Phys. Rev. B* **85** (2012), p. 125314 (cit. on pp. 20, 67).

[121] S. Liu et al. "Fermi surface sheet-dependent band splitting in Sr_2RuO_4 revealed by high-resolution angle-resolved photoemission spectroscopy". In: *Phys. Rev. B* **86** (2012), p. 165112 (cit. on p. 149).

[122] D. E. Logan, A. P. Tucker, and M. R. Galpin. "Common non-Fermi liquid phases in quantum impurity physics". In: *Phys. Rev. B* **90** (2014), p. 75150 (cit. on pp. 34, 49, 50, 60).

[123] J. M. Longo. "Magnetic Properties of $SrRuO_3$ and $CaRuO_3$". In: *J. Appl. Phys.* **39** (1968), p. 1327 (cit. on p. 121).

[124] A. Ludwig et al. "Integer quantum Hall transition: an alternative approach and exact results". In: *Phys. Rev. B* **50** (1994), pp. 7526–7552 (cit. on p. 35).

[125] G. M. Luke et al. "Time-reversal symmetry-breaking superconductivity in Sr_2RuO_4". In: *Nature* **394** (1998), pp. 558–561 (cit. on p. 128).

[126] A. P. Mackenzie et al. "Quantum oscillations in the layered perovskite superconductor Sr_2RuO_4". In: *Phys. Rev. Lett.* **76** (1996), pp. 3786–3789 (cit. on p. 125).

[127] A. P. Mackenzie and Y. Maeno. "The superconductivity of Sr_2RuO_4 and the physics of spin-triplet pairing". In: *Rev. Mod. Phys.* **75** (2003), pp. 657–712 (cit. on pp. 121, 125, 127–129, 153, 155).

[128] V. Madhavan, W. Chen, and T. Jamneala. "Tunneling into a single magnetic atom: spectroscopic evidence of the Kondo resonance". In: *Science* **280** (1998), pp. 567–569 (cit. on pp. 6, 31–33, 77).

[129] V. Madhavan et al. "Local spectroscopy of a Kondo impurity: Co on Au(111)". In: *Phys. Rev. B* **64** (2001), pp. 1–11 (cit. on pp. 6, 31–33, 77).

[130] H. Manoharan, C. Lutz, and D. Eigler. "Quantum mirages formed by coherent projection of electronic structure". In: *Nature* **403** (2000), pp. 512–5 (cit. on pp. 32, 90, 100, 112).

[131] R. S. Markiewicz. "Bridging k and q space in the cuprates: comparing angle-resolved photoemission and STM results". In: *Phys. Rev. B* **69** (2004) (cit. on pp. 8, 31, 38, 47).

[132] R. Matzdorf et al. "Ferromagnetism stabilized by lattice distortion at the surface of the p-wave superconductor Sr_2RuO_4". In: *Science* **289** (2000), pp. 746–748 (cit. on p. 122).

[133] R. Matzdorf et al. "Surface structural analysis of the layered perovskite Sr_2RuO_4 by LEED $I(V)$". In: *Phys. Rev. B* **65** (2002), pp. 1–6 (cit. on p. 123).

[134] I. Mazin and D. Singh. "Competitions in layered ruthenates: ferromagnetism versus antiferromagnetism and triplet versus singlet pairing". In: *Phys. Rev. Lett.* **82** (1999), pp. 4324–4327 (cit. on pp. 121, 122, 152).

[135] K. McElroy et al. "Elastic scattering susceptibility of the high temperature superconductor $Bi_2Sr_2CaCu_2O_{8+x}$: a comparison between real and momentum space photoemission spectroscopies". In: *Phys. Rev. Lett.* **96** (2006), p. 67005 (cit. on pp. 32, 38).

[136] A. K. Mitchell, M. Becker, and R. Bulla. "Real-space renormalization group flow in quantum impurity systems: Local moment formation and the Kondo screening cloud". In: *Phys. Rev. B* **84** (2011), p. 115120 (cit. on pp. 77, 101).

[137] A. K. Mitchell and R. Bulla. "Validity of the local self-energy approximation: application to coupled quantum impurities". In: *Phys. Rev. B* **92** (2015), p. 155101 (cit. on pp. 84, 89).

[138] A. K. Mitchell, P. G. Derry, and D. E. Logan. "Multiple magnetic impurities on surfaces: scattering and quasiparticle interference". In: *Phys. Rev. B* **91** (2015), p. 235127 (cit. on pp. 20, 78, 81, 134).

[139] A. K. Mitchell and L. Fritz. "Kondo effect with diverging hybridization: possible realization in graphene with vacancies". In: *Phys. Rev. B* **88** (2013), p. 75104 (cit. on pp. 33, 49, 50).

[140] A. K. Mitchell and L. Fritz. "Signatures of Weyl semimetals in quasiparticle interference". In: *Phys. Rev. B* **93** (2016), p. 035137 (cit. on pp. 10, 67, 78).

[141] A. K. Mitchell and E. Sela. "Universal low-temperature crossover in two-channel Kondo models". In: *Phys. Rev. B* **85** (2012), p. 235127 (cit. on pp. 83, 103).

[142] A. K. Mitchell, E. Sela, and D. E. Logan. "Two-channel Kondo physics in two-impurity Kondo models". In: *Phys. Rev. Lett.* **108** (2012), p. 086405 (cit. on pp. 82, 83, 102, 103).

[143] A. K. Mitchell et al. "Kondo effect on the surface of three-dimensional topological insulators: Signatures in scanning tunneling spectroscopy". In: *Phys. Rev. B* **87** (2013), p. 75430 (cit. on pp. 23, 33, 34, 49, 77).

[144] A. K. Mitchell et al. "Quantum phase transitions and thermodynamics of the power-law Kondo model". In: *Phys. Rev. B* **88** (2013), p. 195119 (cit. on pp. 33, 35, 49, 50).

[145] A. K. Mitchell et al. "Generalized Wilson chain for solving multichannel quantum impurity problems". In: *Phys. Rev. B* **89** (2014), 121105(R) (cit. on pp. 89, 90, 110).

[146] T. Morita. "Useful procedure for computing the lattice Green's function - square, tetragonal, and bcc lattices". In: *J. Math. Phys.* **12** (1971), pp. 1744–1747 (cit. on pp. 40, 166).

[147] T. Morita and T. Horiguchi. "Lattice Green's functions for the cubic lattices in terms of the complete elliptic integral". In: *J. Math. Phys.* **12** (1971), pp. 981–986 (cit. on pp. 40, 170).

[148] J. Mysliveček et al. "Structure of the adatom electron band of the Si(111)-7x7 surface". In: *Phys. Rev. B* **73** (2006), p. 161302 (cit. on p. 62).

[149] C. Nayak et al. "Non-Abelian anyons and topological quantum computation". In: *Rev. Mod. Phys.* **80** (2008), pp. 1083–1159 (cit. on p. 128).

[150] K. D. Nelson et al. "Odd-parity superconductivity in Sr_2RuO_4". In: *Science* **306** (2004), p. 1151 (cit. on p. 127).

[151] A. H. Nevidomskyy and P. Coleman. "Kondo resonance narrowing in d- and f-electron systems". In: *Phys. Rev. Lett.* **103** (2009), p. 147205 (cit. on p. 97).

[152] T. Nomura and K. Yamada. "Perturbation theory of spin-triplet superconductivity for Sr_2RuO_4". In: *J. Phys. Soc. Jpn.* **69** (2000), pp. 3678–3688 (cit. on pp. 145, 153).

[153] T. Nomura and K. Yamada. "Detailed investigation of gap structure and specific heat in the p-wave superconductor Sr_2RuO_4". In: *J. Phys. Soc. Jpn.* **71** (2002), pp. 404–407 (cit. on p. 125).

[154] P. Nozières and A. Blandin. "Kondo effect in real metals". In: *J. Phys. (Paris)* **41** (1980), p. 193 (cit. on pp. 92, 97).

[155] A. F. Otte et al. "Spin excitations of a Kondo-screened atom coupled to a second magnetic atom". In: *Phys. Rev. Lett.* **103** (2009), p. 107203 (cit. on pp. 90, 100, 112).

[156] J. T. Park et al. "Electronic phase separation in the slightly underdoped iron pnictide superconductor $Ba_{(1-x)}K_xFe_2As_2$". In: *Phys. Rev. Lett.* **102** (2009), p. 117006 (cit. on pp. 24, 27, 38).

[157] C. A. Paula, M. F. Silva, and L. N. Oliveira. "Low-energy spectral density for the Alexander-Anderson model". In: *Phys. Rev. B* **59** (1999), pp. 85–88 (cit. on p. 83).

[158] Y. Pennec et al. “Cleaving-temperature dependence of layered-oxide surfaces”. In: *Phys. Rev. Lett.* **101** (2008), p. 216103 (cit. on pp. 122, 134).

[159] R. Peters, T. Pruschke, and F. B. Anders. “Numerical renormalization group approach to Green’s functions for quantum impurity models”. In: *Phys. Rev. B* **74** (2006), p. 245114 (cit. on pp. 36, 77, 85, 86).

[160] L. Petersen et al. “Direct imaging of the two-dimensional Fermi contour: Fourier-transform STM”. In: *Phys. Rev. B* **57** (1998), R6858–R6861 (cit. on pp. 38, 105).

[161] L. Petersen et al. “Fourier transform-STM: determining the surface Fermi contour”. In: *J. Electron. Spectrosc. Relat. Phenom.* **109** (2000), pp. 97–115 (cit. on pp. 38, 105).

[162] D. G. Pettifor and D. L. Weaire. *The recursion method and its applications*. Vol. 58. Springer Series in Solid State Sciences. Springer, 1985 (cit. on pp. 40, 166).

[163] F. Pierre et al. “Dephasing of electrons in mesoscopic metal wires”. In: *Phys. Rev. B* **68** (2003), p. 085413 (cit. on p. 112).

[164] J. Pollmann and S. Pantelides. “Scattering-theoretic approach to the electronic structure of semiconductor surfaces: The (100) surface of tetrahedral semiconductors and SiO2”. In: *Phys. Rev. B* **18** (1978), p. 5524 (cit. on p. 40).

[165] T. Pruschke, M. Jarrell, and J. Freericks. “Anomalous normal-state properties of high-T_c superconductors: intrinsic properties of strongly correlated electron systems?” In: *Adv. Phys.* **44** (1995), pp. 187–210 (cit. on p. 27).

[166] S. Raghu, A. Kapitulnik, and S. A. Kivelson. “Hidden quasi-one-dimensional superconductivity in Sr_2RuO_4”. In: *Phys. Rev. Lett.* **105** (2010), p. 136401 (cit. on pp. 128, 145, 153).

[167] S. Reich et al. “Tight-binding description of graphene”. In: *Phys. Rev. B* **66** (2002), p. 35412 (cit. on pp. 50, 55).

[168] P. Roushan et al. “Topological surface states protected from backscattering by chiral spin texture”. In: *Nature* **460** (2009), pp. 1106–1109 (cit. on pp. 14, 23, 25, 38).

[169] M. A. Ruderman and C. Kittel. “Indirect exchange coupling of nuclear magnetic moments by conduction electrons”. In: *Phys. Rev.* **96** (1954), pp. 99–102 (cit. on pp. 81, 82).

[170] O. Sakai and Y. Shimizu. “Excitation spectra of the two-impurity Anderson model. I. Critical transition in the two magnetic impurity problem and the roles of the parity splitting”. In: *J. Phys. Soc. Jpn.* **61** (1992), pp. 2333–2347 (cit. on pp. 83, 103).

[171] O. Sakai and Y. Shimizu. “Excitation spectra of the two-impurity Anderson model. II. Interplay between the Kondo effect and the inter site interactions”. In: *J. Phys. Soc. Jpn.* **61** (1992), pp. 2348–2358 (cit. on pp. 83, 103).

[172] M. P. L. Sancho, J. M. L. Sancho, and J. Rubio. “Quick iterative scheme for the calculation of transfer matrices: application to Mo (100)”. In: *J. Phys. F: Metal Physics* **14** (1984), pp. 1205–1215 (cit. on p. 40).

[173] J. A. Sauls. "Surface states, edge currents, and the angular momentum of chiral p-wave superfluids". In: *Phys. Rev. B* **84** (2011), p. 214509 (cit. on p. 129).

[174] T. Scaffidi, J. C. Romers, and S. H. Simon. "Pairing symmetry and dominant band in Sr_2RuO_4". In: *Phys. Rev. B* **89** (2014), 220510(R) (cit. on pp. 76, 125, 128–131, 145, 153, 154, 158).

[175] T. Scaffidi and S. H. Simon. "Large Chern number and edge currents in Sr_2RuO_4". In: *Phys. Rev. Lett.* **115** (2015) (cit. on pp. 128, 130, 132, 153, 154).

[176] A. Schiller and S. Hershfield. "Theory of scanning tunneling spectroscopy of a magnetic adatom on a metallic surface". In: *Phys. Rev. B* **61** (2000), pp. 9036–9046 (cit. on p. 33).

[177] J. R. Schrieffer. "The Kondo effect - the link between magnetic and nonmagnetic impurities in metals?" In: *J. Appl. Phys.* **38** (1967), pp. 1143–1150 (cit. on p. 97).

[178] J. R. Schrieffer and P. A. Wolff. "Relation between the Anderson and Kondo Hamiltonians". In: *Phys. Rev.* **149** (1966), pp. 491–492 (cit. on pp. 93, 103).

[179] E. Sela, A. K. Mitchell, and L. Fritz. "Exact crossover Green function in the two-channel and two-impurity Kondo models". In: *Phys. Rev. Lett.* **106** (2011), p. 147202 (cit. on p. 83).

[180] P. Sessi et al. "Direct observation of many-body charge density oscillations in a two-dimensional electron gas." In: *Nat. Commun.* **6** (2015), p. 8691 (cit. on pp. 16, 20).

[181] Y. Sidis et al. "Evidence for incommensurate spin fluctuations in Sr_2RuO_4". In: *Phys. Rev. Lett.* **83** (1999), pp. 3320–3323 (cit. on pp. 122, 128, 150, 152, 153).

[182] J. Silva et al. "Particle-hole asymmetry in the two-impurity Kondo model". In: *Phys. Rev. Lett.* **76** (1996), pp. 275–278 (cit. on p. 83).

[183] L. Simon, F. Vonau, and D. Aubel. "A phenomenological approach of joint density of states for the determination of band structure in the case of a semimetal studied by FT-STS". In: *J. Phys. Condens. Matter* **19** (2007), p. 355009 (cit. on pp. 9, 14, 66, 67).

[184] L. Simon et al. "Fourier-transform scanning tunnelling spectroscopy: the possibility to obtain constant-energy maps and band dispersion using a local measurement". In: *J. Phys. D: Applied Physics* **44** (2011), p. 464010 (cit. on pp. 9, 14, 32, 38, 55, 66, 67, 70, 105).

[185] I. V. Solovyev, A. I. Liechtenstein, and K. Terakura. "Is Hund's second rule responsible for the orbital magnetism in solids?" In: *Phys. Rev. Lett.* **80** (1998), pp. 5758–5761 (cit. on p. 90).

[186] K. M. Stadler et al. "Dynamical mean-field theory plus numerical renormalization-group study of spin-orbital separation in a three-band Hund metal". In: *Phys. Rev. Lett.* **115** (2015), p. 136401 (cit. on p. 110).

[187] K. M. Stadler et al. "Interleaved numerical renormalization group as an efficient multiband impurity solver". In: *Phys. Rev. B* **93** (2016), p. 235101 (cit. on pp. 81, 82, 84, 90, 110).

[188] W. P. Su and J. R. Schrieffer. "Soliton excitations in polyacetylene". In: *Phys. Rev. B* **22** (1980) (cit. on p. 175).

[189] W. P. Su, J. R. Schrieffer, and A. J. Heeger. "Solitons in polyacetylene". In: *Phys. Rev. Lett.* **42** (1979), pp. 1698–1701 (cit. on p. 175).

[190] S. Sykora and P. Coleman. "Quasiparticle interference in an iron-based superconductor". In: *Phys. Rev. B* **84** (2011), p. 054501 (cit. on p. 24).

[191] M. Ternes, A. J. Heinrich, and W.-D. Schneider. "Spectroscopic manifestations of the Kondo effect on single adatoms". In: *J. Phys. Condens. Matter* **21** (2009), p. 053001 (cit. on pp. 32, 33, 77, 90, 100).

[192] J. Tersoff and D. R. Hamann. "Theory and application for the scanning tunneling microscope". In: *Phys. Rev. Lett.* **50** (1983), pp. 1998–2001 (cit. on pp. 6, 31, 38, 133).

[193] F. P. Toldin et al. "Disorder and quasiparticle interference in heavy-fermion materials". In: *Phys. Rev. B* **88** (2013), p. 81101 (cit. on pp. 38, 39, 122, 145, 163).

[194] M. Tsuchiizu et al. "Spin-triplet superconductivity in Sr_2RuO_4 due to orbital and spin fluctuations: Analyses by two-dimensional renormalization group". In: *Phys. Rev. B* **91** (2015), p. 155103 (cit. on p. 128).

[195] O. Újsághy et al. "Theory of the Fano resonance in the STM tunneling density of states due to a single Kondo impurity". In: *Phys. Rev. Lett.* **85** (2000), pp. 2557–2560 (cit. on pp. 33, 49, 90).

[196] C. N. Veenstra et al. "Determining the surface-to-bulk progression in the normal-state electronic structure of Sr_2RuO_4 by angle-resolved photoemission and density functional theory". In: *Phys. Rev. Lett.* **110** (2013), p. 097004 (cit. on pp. 122, 126, 143, 149, 150).

[197] C. N. Veenstra et al. "Spin-orbital entanglement and the breakdown of singlets and triplets in Sr_2RuO_4 revealed by spin- and angle-resolved photoemission spectroscopy". In: *Phys. Rev. Lett.* **112** (2014), p. 127002 (cit. on pp. 121, 125, 145).

[198] J. Velev and W. Butler. "On the equivalence of different techniques for evaluating the Green function for a semi-infinite system using a localized basis". In: *J. Phys. Condens. Matter* **16** (2004), R637 (cit. on pp. 40, 165).

[199] I. M. Vishik et al. "A momentum-dependent perspective on quasiparticle interference in $Bi_2Sr_2CaCu_2O_{8+\delta}$". In: *Nat. Phys.* **5** (2009), pp. 718–721 (cit. on pp. 8, 10, 14, 38).

[200] M. Vojta. "Electronic properties of disordered valence-bond stripes in cuprate superconductors". In: *Phys. Rev. B* **78** (2008), p. 144508 (cit. on p. 149).

[201] G. E. Volovik. "Fermion zero modes on vortices in chiral superconductors". In: *JETP Lett.* **70** (1999), p. 609 (cit. on p. 130).

[202] P. Wahl et al. "Kondo temperature of magnetic impurities at surfaces". In: *Phys. Rev. Lett.* **93** (2004) (cit. on pp. 33, 49, 62, 77, 90, 100, 112).

[203] Q. H. Wang et al. "Theory of superconductivity in a three-orbital model of Sr2RuO4". In: *Euro. Phys. Lett.* **1305:2317** (2013), pp. 1–6 (cit. on pp. 122, 125, 128, 145, 153, 154).

[204] Q.-H. Wang and D.-H. Lee. "Quasiparticle scattering interference in high-temperature superconductors". In: *Phys. Rev. B* **67** (2003), p. 020511 (cit. on pp. 9, 31, 35, 54, 67, 71, 154).

[205] Q.-Y. Wang et al. "Interface-induced high-temperature superconductivity in single unit-cell FeSe films on $SrTiO_3$". In: *Chin. Phys. Lett.* **29** (2012), p. 037402 (cit. on p. 152).

[206] Z. Wang et al. "Quasiparticle interference and strong electron-mode coupling in the quasi-one-dimensional bands of Sr_2RuO_4". *Nat. Phys.* (2017). (*Accepted for publication - preprint arXiv:1701.02773*) (cit. on pp. 21, 25, 72, 76, 123, 127, 142, 143, 145–147, 150, 153, 160).

[207] T. O. Wehling, A. I. Lichtenstein, and M. I. Katsnelson. "Transition-metal adatoms on graphene: influence of local Coulomb interactions on chemical bonding and magnetic moments". In: *Phys. Rev. B* **84** (2011), p. 235110 (cit. on p. 55).

[208] T. O. Wehling et al. "Orbitally controlled Kondo effect of Co adatoms on graphene". In: *Phys. Rev. B* **81** (2010) (cit. on pp. 50, 55).

[209] A. Weichselbaum. "Non-Abelian symmetries in tensor networks: a quantum symmetry space approach". In: *Ann. Phys.* **327** (2012), pp. 2972–3047 (cit. on p. 110).

[210] A. Weichselbaum and J. von Delft. "Sum-rule conserving spectral functions from the numerical renormalization group". In: *Phys. Rev. Lett.* **99** (2007), p. 76402 (cit. on pp. 36, 77, 85, 86).

[211] K. G. Wilson. "The renormalization group: critical phenomena and the Kondo problem". In: *Rev. Mod. Phys.* **47** (1975), pp. 773–840 (cit. on pp. 27, 36, 77, 84, 89).

[212] D. K. Wohlleben and B. R. Coles. "Magnetic Properties of Metallic Alloys". In: *Magnetism Vol. 5: Magnetic Properties of Metallic Alloys*. Ed. by H. Suhl and G. T. Rado. NewYork: Academic Press, 1973 (cit. on p. 90).

[213] J. Xia et al. "High resolution polar Kerr effect measurements of Sr_2RuO_4: evidence for broken time-reversal symmetry in the superconducting state". In: *Phys. Rev. Lett.* **97** (2006), p. 167002 (cit. on p. 128).

[214] Y. Yin et al. "Scanning tunneling spectroscopy and vortex imaging in the iron pnictide superconductor $BaFe_{1.8}Co_{0.2}As_2$". In: *Phys. Rev. Lett.* **102** (2009), p. 97002 (cit. on pp. 24, 25, 27, 38, 122, 145).

[215] Y. Yin et al. "Scanning tunneling microscopy and spectroscopy on iron-pnictides". In: *Physica C: Supercond.* **469** (2009), pp. 535–544 (cit. on pp. 14, 24, 27, 38).

[216] K. Yosida. "Magnetic properties of Cu-Mn alloys". In: *Phys. Rev.* **106** (1957), pp. 893–898 (cit. on pp. 81, 82).

[217] T. Yuan, J. Figgins, and D. K. Morr. "Hidden order transition in URu_2Si_2: evidence for the emergence of a coherent Anderson lattice from scanning tunneling spectroscopy". In: *Phys. Rev. B* **86** (2012), p. 35129 (cit. on pp. 20, 38, 39, 145, 163).

[218] V. B. Zabolotnyy et al. "Effective tight-binding model for renormalized band structure of Sr_2RuO_4". In: *J. Electron. Spectrosc. Relat. Phenom.* **191** (2012), pp. 1–5 (cit. on pp. 124, 125).

[219] T. Zhang et al. "Experimental demonstration of topological surface states protected by time-reversal symmetry". In: *Phys. Rev. Lett.* **103** (2009), p. 266803 (cit. on pp. 20, 38).

[220] Y. Zhang et al. "Origin of spatial charge inhomogeneity in graphene". In: *Nat. Phys.* **5** (2009), pp. 722–726 (cit. on pp. 25, 38).

[221] B. B. Zhou et al. "Visualizing nodal heavy fermion superconductivity in $CeCoIn_5$". In: *Nat. Phys.* **9** (2013), pp. 474–479 (cit. on p. 145).

[222] L. Zhu and J.-X. Zhu. "Coherence scale of coupled Anderson impurities". In: *Phys. Rev. B* **83** (2011), p. 195103 (cit. on pp. 83, 86).

[223] R. Žitko. "Kondo resonance lineshape of magnetic adatoms on decoupling layers". In: *Phys. Rev. B* **84** (2011), p. 195116 (cit. on pp. 33, 90).

[224] D. N. Zubarev. "Double-time Green functions in statistical physics". In: *Sov. Phys. Usp.* **3** (1960), p. 320 (cit. on pp. 37, 154, 170).